Remote Monitoring of Land Degradation in Arid/Semiarid Regions

Thesis by

Terrill Wylie Ray

In Partial Fulfillment of the Requirements

for the Degree of

Doctor of Philosophy

California Institute of Technology

Pasadena, California

1995

(Submitted May 11, 1995)

"The history of civilizations is a record of struggles against the progressive desiccation of civilized lands. The more ancient the civilization, the drier and more wasted, usually, are the supporting countries....Recently, the archeologists have turned back the pages of history, not merely centuries, but thousands of years. Their post-mortems on buried civilizations suggest that it has been the hand of man, more than climatic change, which has reduced once rich and populous regions to desolation and poverty. After long struggles, a civilization either died or its people migrated to more productive regions. Many ancient civilizations, once reveling in a golden age of prosperity, are crumbling in ruins or lie buried in sands and debris, largely caused by the destructive treatment of the lands on which they were dependent for sustenance. If modern peoples are to escape a similar fate by man-induced impoverishment and the desiccation of their lands, it would seem well to take a measure of these destructive processes and forces, and by intelligent land planning and land use provide for the sustained productivity of agricultural lands and the protection of grasslands and forests for food, textiles, raw materials and continued water supply."
(Lowdermilk, **Man-Made Deserts**, 1935)

Acknowledgements

This thesis would not have occurred if Bruce Murray had not said "I have this project which I think will interest you," when I first arrived at Caltech. I would like to thank Dan McCleese and Moustafa Chahine at JPL for providing the initial impetus for this project. Many people at JPL have provided immense quantities of aid during the time that this research was underway: Tom Farr, Jakob van Zyl, Ron Blom, Robert Crippen, Eric De Jong, Rob Green, Curtiss Davis (now at the Naval Research Laboratory), Eni Njoku, JoBea Way, Oliver Chadwick, Elsa Abbott, Simon Hook, Cindy Grove, Pascale DuBois, Ghani Chehbouni (now at LERTS), Mark Helmlinger, Pavel Hajek, Shigeru Suzuki, Jeffrey Hell, Edith Huang, Sharon Okonek, and Marguerite Schier. Bruce Murray and Arden Albee deserve a great deal of thanks for wading through the early drafts of this thesis, and I also thank Dewey Muhleman for providing a final review of the radar sections. Thanks also to Arden Albee, Bruce Murray, Dewey Muhleman, Peter Wyllie, Don Anderson, and Ron Blom for serving on my thesis committee.

Arnold Selivanov of the Institute of Space Devices Engineering in Moscow was kind enough to supply the 1991 RESOURCE data. Dar Roberts at UC-Santa Barbara provided invaluable help with the calibration of the MSS data to apparent reflectance. Jim Westphal at Caltech and Chris Elvidge at the Desert Research Institute (University of Nevada at Reno) provided very useful advice on collecting the field spectra of desert plants. I also profited from several discussions with Roberta Yuhas, Joe Boardman, and Alex Goetz (all at the University of Colorado at Boulder). I would like to thank Caltech undergraduate student Cailin Henderson for her work with the aerial photos and SeaWIFS

bandpasses, and I thank Caltech undergraduates Becky Zaske and Lisa Gaskell for helping collect field spectra Thanks are also due to Cathy Weitz, Elizabeth Duxbury and Stephanie Brachfeld for their aid during the first year of this project when they were graduate students at Caltech. Thanks also to the Division of Geological and Planetary Sciences Staff, especially Leona Kershaw, Mike Black, Kay Campbell, Irma Betters, Donna Sackett, and Annette McCusker. Special thanks go to Al Hibbs for narrating the videotape which was released by JPL and is included in this thesis. Parts of the work presented in this thesis were performed using the Spectral Image Processing System (SIPS) created at the University of Colorado at Boulder's Center for the Study of Earth from Space. Substantial funding for this work was provided by NASA Graduate Student Fellowship NGT-50891.

A large number of people deserve my gratitude for the non-technical aid they have given to me during my work at Caltech. Foremost among these are my mother, Marvaline Ray and my siblings: Robin, Marcy, and Arlyn. I also thank Bill Anderson, Laszlo Keszthelyi, Bruce Betts, and Mark Hofstadter for their friendship. Thanks also to all of the people at Theatre Arts at Caltech for providing me with a distraction from my research, especially Shirley Marneus, Karen Young, Todd Brun, Dan Dilling, Cara King, and Doug Smith.

Finally, thanks to Caltech Graphic Arts, the Caltech Photo Lab, the JPL Photo Lab, and the JPL Digital Animation Laboratory for invaluble aid in assembling the manuscript and videotape.

Abstract

Land degradation is a serious and growing problem on a world-wide scale -- 11% of the Earth's vegetated surface having suffered serious damage in the last 45 years. Human activity, especially sprinkler irrigation agriculture, can cause dramatic changes in arid regions as the fragile natural plant cover is stripped off and its root system destroyed in the process of cultivation. Satellite and airborne remote sensing data covering the Manix Basin of Eastern California over the last two decades shows that abandoned fields there suffered progressive degradation, as the topsoil eroded due to the lack of protective plant cover. Blowing sand buried and disrupted the downwind plant cover, which caused the downwind area to lose its protection against wind erosion and expanded the region of damage.

Because the amount and kind of plant cover is an important marker both of where wind erosion has occurred and where it is likely to occur in the future, especially designed satellite monitoring systems should be able to sense to signatures of undisturbed and disturbed vegetation cover in arid regions. However, this problem cannot be addressed by standard vegetation indices, because of the adaptation of arid region plants to the scarcity of water. Furthermore, weekly to monthly sampling will be necessary because blowing sand visible to satellite remote sensing is highly dependent on the local weather, and this can change within a few months. A new vegetative index suitable for arid regions is proposed for the wavelength region from 0.4–1.0 μm.

The detection and identification of arid region plant communities requires a highly calibrated remote sensing system with higher spectral resolution than that currently offered

by Landsat Thematic Mapper. The way in which regions of blowing sand can appear and disappear with rapidity demonstrates the need for a remote monitoring system that can survey large areas on a regular basis. Such a system must be supported by focused ground observations and a continuing analysis of the satellite data.

Table of Contents

List of Figures

List of Plates

List of Tables

Chapter 1: *Introduction*

> *"To gain control over the soil is the greatest achievement of which mankind is capable. The organization of civilized societies is founded upon the measures taken to wrest control of the soil from wild Nature, and not until complete control has passed into human hands can a stable superstructure of what we call civilization be erected on the land....Soil erosion is altering the course of world history more radically than any war or revolution. Erosion is humbling mighty nations, re-shaping the domestic and external policies and once and for all it has barred the way to the El Dorado that a few years ago seemed almost within reach."* (Jacks, 1939)

During the early part of the 20th century a proto-Green Revolution occurred as many nations, including the United States, attempted to "reclaim" arid regions for agriculture. The Dust Bowl which afflicted the Great Plains of the United States during the 1930's provided a shocking example of the magnitude of wind erosion which could be triggered by a combination of poorly-planned agriculture and drought. The research presented in this thesis provides a scientific basis for the use of satellite remote sensing for monitoring land degradation caused by human activity in arid and semiarid regions.

In this introduction, land degradation is defined and the extent of the problem is discussed. The processes by which arid lands degrade are then examined. The sparse vegetation cover in arid regions is an important factor for both controlling land degradation and showing where degradation has occurred. Lastly, this chapter shows how the discontinuous nature of land degradation in both time and space strongly argues for the use of satellite remote sensing for monitoring arid land degradation.

Part 1.1: *The Land Degradation Problem*

Part 1.1.1: *Defining Land Degradation*

As early as 1949, the scientist Aubreville noticed land degradation that seemed to be extending north into semi-arid and sub-humid regions of North Africa from the more arid zones of the Sahara (Aubreville, 1949). The term Aubreville coined for this process was "desertification." The problem had been observed in the Mediterranean World nearly two millennia before by the Roman senator Cicero who spoke of the destruction of the north African forests and their replacement by barren, desert-like areas. The devastating Sahel droughts of 1968–73 and the apparent accelerated southward advance of the Sahara Desert led to extensive international discussion of the problem and the formation of the United Nations Conference on Desertification (UNCOD).

At a meeting convened during 1977 in Nairobi, Kenya, UNCOD defined desertification as follows:

> *"Desertification is the diminution or destruction of the biological potential of land, and can lead ultimately to desert-like conditions. It is an aspect of the widespread deterioration of ecosystems, and has diminished or destroyed the biological potential, i.e. plant and animal production, for multiple use purposes at a time when increased productivity is needed to support growing populations in quest of development."* (UNEP, 1978)

During the following years various agencies, scientific institutions and individual scientists found the above definition to be inadequate (UNEP, 1992). In response various groups developed their own definition, which, not unexpectedly, led to a significant amount of confusion. Additionally, cyclic oscillations of vegetation productivity related to climate fluctuations had been observed in satellite data, and there was a need to differentiate between desertification and these cyclic climatic oscillations (UNEP, 1992). In 1992 UNCOD settled upon the following definition of desertification:

> *"Desertification is land degradation in arid, semi-arid, and dry sub-humid areas resulting mainly from adverse human impact."* (UNEP, 1992)

Perhaps the most significant aspect of this definition of desertification is its focus on "human impact." This differentiates the issue of desertification from simple climatic fluctuations such as drought, but it should be noted that drought can cause an exacerbation of damage derived from human activities. The definition of desertification offered by Mainguet (1994) states that desertification is "*revealed* by drought," but "*caused* by human activities." Nearly one-quarter of the vegetated land area of the Earth

has been highly disturbed by human activity and an additional 28 percent has been moderately disturbed (World Resources Institute [WRI], 1993). This massive level of human disturbance suggests that there are large areas of the Earth's surface that have either been degraded through human activity or have a significant potential of being degraded through human activity.

Part 1.1.2: *Extent of the Problem*

> *"In fact, so devastating seems the occupation of man that, with a few striking exceptions, a desert or near-desert condition is often associated with his long habitation of a region. Two major factors are believed to account for the growth of man-made deserts. In the first place, semi-arid to semi-humid regions proved the most favorable sites for the early development of human culture. Such areas, however, stand in a condition of delicate ecological balance between humid and true desert climates. In the second place, processes of soil erosion are accelerated by the exposure of soil surfaces hitherto protected by complete mantles of vegetation, whether grass or forest, by heavy grazing and cultivation. It is only within the past decade that experimental studies of these processes have been made. So enormous have been the differences in soil wastage and superficial runoff of rain waters from bared sloping lands, as compared with similar surfaces protected by a complete coverage of vegetation, that new light is thrown on the problem of the decadence of former civilizations."* (Lowdermilk, 1935)

The World Resources Institute (1992) reports that "over the past 45 years, about 11 percent of the Earth's vegetated soils became degraded to the point that their original biotic functions are damaged, and reclamation may be costly or in some cases impossible." UNCOD stated that as of 1992 desertification affects 70 percent of the world's drylands (3.6 billion hectares) or nearly one-fourth of the total land area of the planet (UNEP,

1992). However, UNCOD estimates have been questioned by workers such as Warren and Agnew (1988) who pointed out that about half of the arid area being used for the estimates is too arid for any form of agriculture. In fact, the UNEP (1992) definition of "rangeland" includes "non-agricultural, largely unoccupied drylands that are unused or used only occasionally by nomadic pastoralists," which suggests that the estimated area of degraded rangeland may be inflated, but, since the estimate of total rangeland would also be inflated, this may not change the fraction of *usable* arid lands that has been degraded. Even if the area of usable arid lands is only half of the value quoted by UNCOD, the region at risk represents one-sixth of the Earth's surface, and the reduced area of arid lands still included are those most used by humans.

The second important aspect of the extent of land degradation is the question of the potential for reversing the degradation. Nelson (1988) expressed the view that "the extent of desertification as an irreversible state has probably been exaggerated, although it is correct to classify it as a serious problem." Topsoil lost to erosion can usually be rebuilt given time, and the well-known process of biological succession shows that a forest ecosystem can replace an abandoned field in a few centuries. However, on the scale of people's need to use the land for sustenance, a few centuries is forever. Human effort can accelerate the regeneration of topsoil or ecosystems, shortening the time need for regeneration, but this may require considerable economic expense. In extreme cases of degradation where the clay fraction of the soil is nearly completely lost or invading flora becomes too firmly entrenched, natural recovery to the *original* ecosystem will not occur.

Warren and Agnew (1988) point out lack of the knowledge needed to assess the resilience or recoverability of soils and plant communities.

Although the effects of land degradation have been less severe in the United States than they have been in areas such as the Sahel or Western Rajasthan (India), the United States itself has a great potential for the degradation of drylands. The historian Walter Prescott Webb once said of the Western United States:

> *"Draw a line anywhere from the region's eastern boundary to the Pacific, stand on its mid-point and you will find yourself either in the desert or near it. If we do not understand the West it is because we perversely refuse to recognize this fact...When the desert pokes a hot finger into the border regions, the people speak of a drought; when it pulls the finger back, they say "the country is getting more seasonable." At the heart of the desert there is no drought, there is only an occasional mitigation of dryness."* (Webb, 1957)

The Western U.S. has been one of the most rapidly growing regions of the country over the last 100 years (Sheridan, 1981). Agricultural output from this region comprised more than 18 percent of the total agricultural output of the United States in 1977 (Sheridan, 1981). That year the arid lands produced 66 percent of the nation's cotton, 39 percent of US barley, and 21 percent of the total wheat production (Sheridan, 1981).

The annual rainfall in much of the West averages less than 51 cm (20 inches). This has long been considered to be below the threshold of successful agriculture without irrigation, and it was predicted that "these lands will maintain but a scanty population" (Powell, 1879). In order to support the large population and agricultural output of the West groundwater has been pumped out of the ground faster than it can be recharged, most of the region's rivers have been dammed to make water available on demand, and water has been transported over long distances from where it is more plentiful to where it

is scarce (Sheridan, 1981). In 1893, John Wesley Powell told the International Irrigation Congress in Los Angeles, (Stegner, 1954) "you are piling up a heritage of conflict and litigation over water rights for there is not sufficient water to supply the land." This prophecy has been borne out as witnessed by the conflicts over water that have increased in intensity over the last few decades.

Given the large potential area of the United States in which degradation of drylands can occur and the unprecedented stresses due to its large population and vast agricultural output, it should not be a surprise to find that significant desertification has occurred in North America. Dregne (1983) reported that nearly 1.3 million square kilometers of North American drylands have been "severely" or "very severely" degraded. Over the last 100 years the Sonoran and Chihuahuan deserts have become perceptibly more barren, even though these areas have been deserts for a very long time (Sheridan, 1981). This problem is likely to get worse, not better: "The introduction of sprinkler irrigation systems, especially the center pivot systems, has enabled previously unsuitable rolling sandy lands to be cropped successfully. If and when those soils are abandoned, for reasons of economy or shortage of water, the United States will face an even greater wind erosion threat than it has had to cope with in the past" (Dregne 1983).

We can see the double-edged nature of the water problem here. The rate at which the water is being used in these arid regions around the world for irrigated agriculture is not sustainable, and for that reason the environmentally prudent thing would seem to be to severely curtail irrigation in these areas. When the irrigation is stopped, the area that had

been under cultivation may become a source of blowing sand which further damages the environment of the drylands.

Part 1.1.3: *The Processes of Land Degradation*

Another significant item in the current UNCOD definition of desertification listed above is the idea of "land degradation." UNCOD defined land degradation as follows:

> *"Degradation implies reduction of resource potential by one or a combination of processes acting on the land. These processes include water erosion, wind erosion and sedimentation by those agents, long-term reduction in the amount or diversity of natural vegetation, where relevant, and salinization and sodication."* (UNEP, 1992)

Sheridan (1981) characterized the affliction of land degradation as having the following symptoms: declining groundwater tables, salinization of topsoil and water, reduction of surface waters, unnaturally high soil erosion, and the desolation of native vegetation. Dregne (1983) indicates the major processes of desertification in arid regions as: water erosion, wind erosion, salinization, waterlogging, and soil compaction. Additionally, the mechanical destruction of desert pavements and calcrete (caliche) makes the soil more vulnerable to erosion. Through these different processes, the land is made more barren, and it may become effectively like a desert, even without climate changes. Before continuing further to consider how to assess and monitor land degradation, we should look briefly at some of these processes.

Part 1.1.3.1: *Soil Compaction*

Soil compaction is caused by the pressure exerted on the soil by raindrops, animal hooves, repetitive large changes in the water state of the soil, and from the pressure exerted on the soil by tractors and other agricultural machinery (USDA, 1993). Compaction caused solely by repetitive large changes in the water state of the soil is called "water compaction," while compaction caused by the pressure of machines and animals, as well as the impact of raindrops, is called "mechanical compaction" by the United States Department of Agriculture Soil Conservation Service (USDA, 1993). Compacted layers of soil constrict the infiltration of water into the soil, and help accelerate sheet erosion of the soil during periods of rain (Hillel, 1982; Dregne, 1983). If the compacted layer is very near the surface, water may not penetrate to the level of buried seedlings or to deeper plant roots (Hillel, 1982; Dregne, 1983). The lack of water penetration into the soil will make the soil effectively more arid than would be expected due to climate alone (Dregne, 1983). Compacted surface layers may prevent seedlings from penetrating the soil surface, while deeper compacted layers restrict root growth into the deeper layers of the soil (Hillel, 1982; Dregne, 1983).

Part 1.1.3.2: *Leaching, Waterlogging and Salinization*

The soils in drylands have developed in an environment of limited rainfall and significant periods of drying. This excess of evapotranspiration to rainfall draws water from depth and causes many soluble minerals to accumulate in the upper soil horizons. In the southwestern United States this leads to the formation of cemented deposits of calcium carbonate known as caliche or calcrete (Millar *et al.*, 1951).

The low amount of rainfall characteristic of arid and semiarid regions often requires the use of some form of irrigation, and the continuing additions of water that occur under irrigation are a dramatic departure from the natural state. The irrigation water dissolves the calcium carbonate and soluble salts and transports them downward in the soil profile. The relative insolubility of calcium carbonate means that the calcrete layer is driven down relatively slowly compared to the more soluble salts.

If the calcrete is not driven well below the root zone of the crops, several problems can arise. Colloidal clay particles which are being transported down the soil profile by the irrigation water may be deposited on top of the relatively impermeable calcrete producing a much more impermeable layer in the soil. At this point the irrigation water pools in the root-zone soils. The water may fill all of the pore space in the soil (waterlogging), restricting gas exchange between the soil and the atmosphere which causes the buildup of chemicals toxic to most terrestrial plants (Hillel, 1982; Fitter and Hay, 1987; Mainguet, 1994).

Much of the water in the root-zone soils in arid regions will be lost by evaporation rather than downward transport. Therefore, any soluble salts which were present in the water will be deposited in the root-zone soils. Even if the irrigation water is only slightly saline, repeated cycles of evaporation lead to build-up of toxic salt levels in the soil (Millar *et al.*, 1951; Dregne, 1983; Fitter and Hay, 1987; Mainguet, 1994). Even if the impermeable layer is deep enough that the root-zone soil is not waterlogged, evaporation will draw the added water from the water table and cause the salinization of the near-surface soils.

This salinization occurs with nearly any type of irrigation. Before the construction of the High Aswan Dam in the 1960's the annual Nile floods would flush the salts which accumulated in the near-surface during the year, but the High Dam made year-round irrigation possible and prevented the annual floods, which led to increased salinization in the land irrigated by the canal system (Dregne, 1983; El Baz, 1988; Goossens *et al.*, 1994; Mainguet, 1994). In Iraq, there is a historical record of salinization caused by canal irrigation between 2400 and 1700 B.C., and this problem has recurred at intervals through the present (Dregne, 1983). Sheridan (1981) stated that about 162,000 hectares in the San Joaquin Valley of California were affected by high brackish water tables, and that if this area continued to expand at the rates noted in 1981, by 2080 455,00 hectares would become unproductive. In both western Texas and the Welton-Mohawk area of Arizona the irrigation water being applied by sprinkler irrigation systems is saline, and relatively impermeable subsurface soil layers hold the irrigation water near the surface which contributes to waterlogging and to salinization (Sheridan, 1981).

Part 1.1.3.3: *Water Erosion*

Reports by the World Resources Institute (1992, 1993) indicate that water erosion is the most serious form of land degradation on a global scale. Water erosion begins with raindrops striking the ground. The World Meteorological Organization (1983) stated that a 4 mm diameter raindrop strikes the ground with enough energy to throw a 0.1 cm^3 volume of sand having a density of 2.65 g/cm^3 to a height of 6 cm.

The USDA Soil Conservation Service (1993) recognizes four styles of erosion by runoff: sheet, rill, gully, and tunnel (piping). Sheet erosion is an approximately uniform removal of soil from an area without the development of conspicuous water channels, and it is less apparent than rill or gully erosion in early stages. Sheet erosion can be serious at slopes of only 1 to 2 percent, but it is generally most serious at steep soil gradients. Rill erosion is soil removal caused by the cutting of many small, conspicuous channels where the runoff is concentrated. The small channels can be easily obliterated by tillage. More serious is gully erosion where the water cuts down into the soil along the line of flow. The resulting channels, which often form along plow furrows, vehicle ruts, animal trails, and the rows between crops, cannot be obliterated by ordinary tillage and they may become impassable to farm machinery (Dregne, 1983; USDA, 1993; Mainguet, 1994).

The last, and perhaps most unusual, type of water erosion is tunnel erosion, which is more commonly called "piping." This type of erosion occurs when subsurface layers are more susceptible to entrainment in moving free water than the surface layer. Water gains

entry into the subsurface through such things as rodent burrows and desiccation cracks. Water entrains the subsurface soil material and moves it downward within the soil or, if some sort of outlet is present, completely out of the soil. This forms a series of enlarging and coalescing tunnels (or pipes), and inlets to the tunnels may enlarge into a funnel-shaped feature known as a "jug" (USDA, 1993). This type of erosion is quite dangerous since it undermines the ground surface which can then collapse under the weight of a person walking across the surface, a grazing animal, or a piece of farm machinery. Several fields in the Manix Basin Area studied in this thesis suffer from tunnel erosion, which makes walking across those fields hazardous to field workers. Except in the cases where obvious jugs have formed this type of erosion cannot be immediately discerned by surface observation.

In Mediterranean North Africa, the Romans developed excellent water conservation and irrigation techniques through the use of extensive systems of terraces, enabling them to effectively cultivate this low rainfall area. When the empire collapsed, the irrigation and terrace systems fell into disuse. Some of the land returned to its original state, but most of the cropland was eroded away leaving wasteland riddled by dunes and gullies (Bennett, 1939). Terrace systems are designed to concentrate water in areas with low rainfall and control water erosion (Dregne, 1983; Mainguet, 1994), but terraces which are not kept in good repair will cause erosion more serious than there would have been if no terraces had been built (Dregne, 1983). The Egyptians and Phoenecians also developed terrace systems that fell into disrepair and suffered severe degradation (Stallings, 1957).

Part 1.1.3.4: *Wind Erosion*

On a global scale, wind erosion is not as serious a problem as water erosion (Holý, 1980, WRI 1992, WRI 1993), but it affects many arid and semiarid regions. Like water erosion, wind erosion involves the removal of soil particles by a moving fluid. In this case, the fluid is air. As with water erosion, the finer particles are typically lost first which leads to the loss of the organic matter and nutrients that are generally attached to those particles, and this will diminish the productivity of the soil (Dregne, 1983). The potential final result of continued wind erosion is an area of active barren dunes (Dregne, 1983). The classic study of wind and sand was performed by Bagnold (1942), who focused on sand in the open deserts in areas where vegetation was generally absent. He pointed out that the vast majority of the movement of sand by wind occurred very close to the level of the ground. He also concluded that the sand-sized particles were not actually in suspension, but that they "move like Ping-Pong balls," that is, by bouncing and rolling (saltation). Sometimes the sand grain striking the surface will cause a splash that throws other sand grains into the air.

If the surface is covered by objects that cannot be removed by the wind, such as pebbles or vegetation, the roughness produced by these objects will restrict the ability of the wind to mobilize and transport sand. Saltating sand grains will drop into the spaces between pebbles or into the vegetation and be trapped. A surface of pebbles can be filled by sand in this way until no more sand can be trapped. Bagnold (1942) found that the

movement of a sand sheet would be accelerated as it passed over a surface of sand-saturated pebbles, because when the pebbles could no longer trap sand the saltating grains would bounce more vigorously off of the pebbly surface than they would from a surface of pure sand. Bagnold (1942) suggested that this would never happen with vegetation since the vegetation would continually grow and add to the sand-trapping ability of the vegetated patch.

The weird rock formations formed from the continued abrasion of blowing sand in desert areas attest the power of blowing sand as an agent of erosion. Vegetation is also affected by the abrasive action of sand grains. Fryrear *et al.* (1973) performed laboratory experiments on grass seedlings under conditions of blowing sand and found that blowing sand ruptures plant cells, dried out the exposed tissue, and led to increased damage by insects and disease. Mainguet (1994) stated that the abrasive effect of blowing sand created microscratches on the surface of the leaves. The thick waxy epidermis of arid plant leaves and the presence of fine hairs and thorns on the leaves of arid plants may provide a first line of defense against this abrasion, but most cultivated crops do not have the luxury of these protections. The abrasive action of blowing sand can also to serious damage to man-made objects as witnessed by the following statement by a farmer in the Manix Basin Area of California's Mojave Desert as reported by Gorman (1993):

> *"I used to grow alfalfa on 40 acres, but my fields have been sandblasted. All my equipment is destroyed. The sand has ruined the magnetic switches in my irrigation equipment."*

Part 1.2: *The Vital Role of Vegetation*

When most people think of deserts, they think of barren wastelands filled only with drifting sands, but this picture is only true of the extremely hyperarid regions such as the Saharan Desert, the Empty Quarter of the Arabian Desert and the core of the Gobi. Many deserts look more like plate 1 — areas with relatively widely spaced shrubs, succulents such as agave and cacti, and small dry grasses. This vegetation is highly adapted to the hot, dry environment in which it lives, and it is remarkably resistant to the harsh conditions found in arid regions. Although it is fashionable in the environmental movement to speak of the fragility of the desert ecosystem, Mainguet (1994) stated quite clearly that the prominent feature of dryland vegetation (and soil) is resilience and not fragility. One measure of land degradation is the degradation of vegetation (Dregne, 1983), and a brief examination reveals that the state of vegetation is a powerful indicator of where additional degradation is occurring and will occur.

The most important property of plants in erosion control is their ability to break the flow of erosive agents and prevent energy that would cause erosion from being delivered to the soil. The discussion of water erosion in part 1.1.3.3 above showed that the impact of raindrops on the soil surface was one of the fundamental causes of soil degradation. As early as 1877, the German soil scientist Wollny recognized that plant canopies and surface mulch protected soil from water erosion primarily by breaking the fall of raindrops (Mainguet, 1994). In the case of wind erosion, Bagnold (1942) stated that the main effect of a vegetated surface was to raise the height above the soil at which

the mean wind speed would be zero. This serves to decrease the stress applied to the soil surface by the wind. As mentioned previously, Bagnold (1942) also discussed the sand-trapping ability of vegetation, and pointed out that continually growing vegetation would provide a permanent sand trap. Of course, if the sand fell into the vegetation fast enough to bury and kill the vegetation, this sand trap would be lost, and the full wind stress would be applied directly to the previously trapped sand.

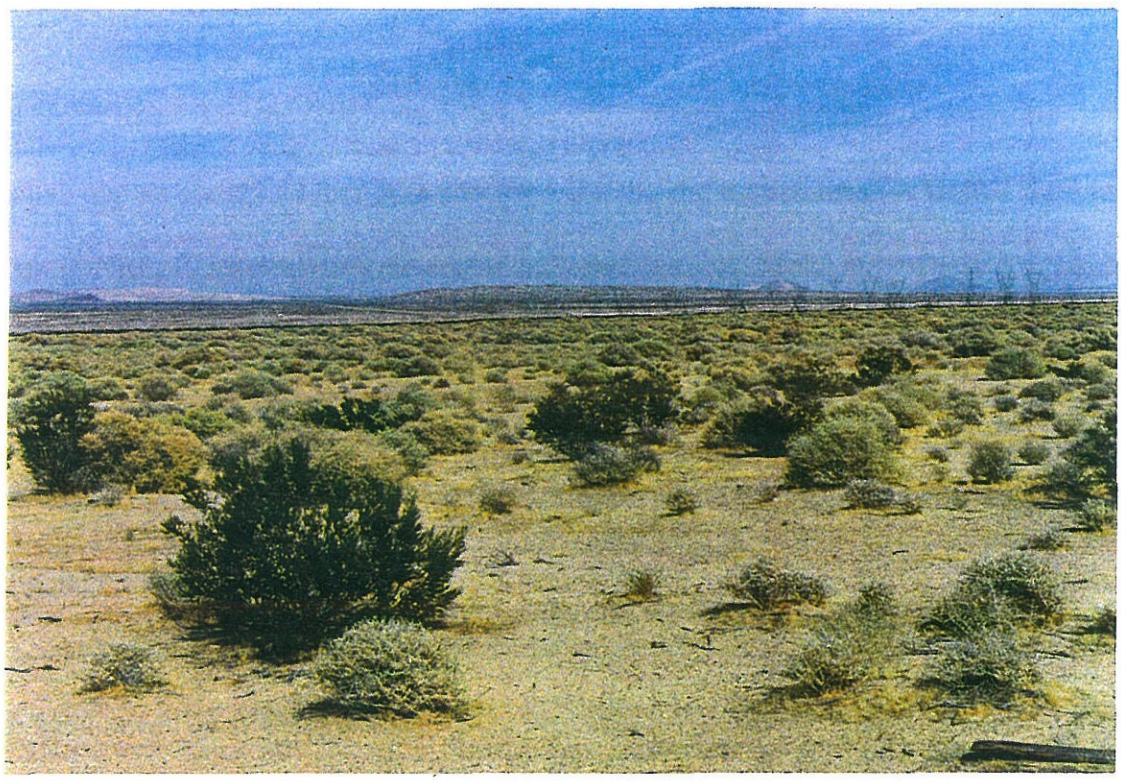

Plate 1: Mojave Desert landscapes showing numerous widely-spaced shrubs and short dry grass.

Part 1.3: *The Challenge of Monitoring Desertification*

> *"...the image created has too often been of inexorably advancing sands, as opposed to more subtle, more complex, pulsating deteriorations, sometimes with reversals, but at least, with substantial periodic remissions, radiating out from centers of excessive population pressure."* Nelson (1988)

Desertification is not, as sometimes envisioned, an invasion of non-desert areas from a desert core. Sheridan (1981) compares desertification to guerrilla warfare with no real "front line." Dregne (1983) describes desertification as a patch of land degraded through human abuse that then spreads outward if the abuse continues. A United Nations report (UNEP, 1978) describes the spread of desertification as follows: "These degraded patches, like a skin disease, link up to carry the process over extended areas." Mainguet (1994) clearly states, "The theory of the encroaching desert, which has now been scientifically rejected, is still a fixed idea in the minds of governments, donors, and journalists; this must change."

The extent of this "subtle and insidious process" (UNEP, 1978) of land degradation can be difficult to assess from observations on the ground. Ground observations may quickly show that soil is blowing from a farmer's field or the salinization is beginning in the soil; however, this single observation does not indicate the state of degradation a few miles away. Each site requires manpower-intensive biomass surveys and soil sampling. Furthermore, as indicated by the quotation from Nelson (1988) above, the desertification processes fluctuate over time, so repeated and ongoing observations are required to determine if progressive degradation is actually occurring and to track its

progress. Warren and Agnew (1988) stated that one of the main problems in our understanding of land degradation was "the ignorance in establishing trends and speeds, because trends and speeds require sequential surveys." In addition, sequential surveys are of limited use if baselines for comparison are not established (Nelson, 1988; Rodenberg, 1991; Murray *et al.*, 1994).

Remote sensing from satellites offers a potential means to survey all arid regions of the globe. However, remote sensing can not entirely supplant the use of ground observations as was widely believed in the 1970's and early 1980's (Mainguet, 1994). Still, satellite remote sensing can provide a powerful adjunct to ground observations by extending in time and space field observations made at a single point in a given region. Satellite remote sensing thus can monitor much larger areas than ground surveys and aid in targeting key ground observations. In this way, ground observation anchors satellite observations, with the satellite remote sensing effectively multiplying the value of the data acquired on the ground and identifying the specific localities where additional and repeat ground surveys are most needed.

Mainguet (1994) cites the importance of "remote sensing supported by verifications on the ground for a better perception of the extent and processes of degradation." Dregne and Tucker (1988) indicate that 30 to 40 years of observation by satellites and ground studies will be required to confidently determine any permanent changes in the boundaries of the Sahel.

This thesis investigation demonstrates how remote sensing can be used to understand and monitor land degradation in a marginal agricultural area that is being used

for center-pivot agriculture and is undergoing progressive abandonment of cultivated fields. The area studied is within the Manix Basin of the Mojave Desert in Eastern California. A review of its geological, ecological and historical background will be presented in chapter 2. A valuable feature of this area is that the progressive abandonment of fields there has produced a series of abandoned fields in various stages of degradation which makes it possible to record temporal effects in any single remote sensing observation. The value of this feature to single overflights of airborne remote sensing instruments will be shown in chapters 3 and 4 with airborne data acquired in the summer of 1990. First, the unique fingerprints of human cultivation and wind erosion in polarimetric synthetic aperture radar, using data acquired with the Jet Propulsion Laboratory (JPL) Airborne SAR (AIRSAR), will be examined and used to infer the progress of land degradation due to wind erosion. Subsequently, the view will shift to the use of imaging spectroscopy in the visible and near-infrared, acquired with the JPL Advanced Visible/Infrared Imaging Spectrometer (AVIRIS), to examine changes in the land surface and to observe how vegetative cover is affected by the presence of abandoned fields and the length of time the field has been abandoned.

The importance of vegetation in the desertification has been outlined in this introduction, and the importance of monitoring the vegetation is clear. However, arid region monitoring differs intrinsically from the more developed practice of remote sensing of humid vegetated areas. The plants of arid regions are uniquely adapted to survive in their environment, and these adaptations tend to degrade the ability of conventional remote sensing to measure the plant cover. Chapter 5 reveals problems with the current

techniques of measuring vegetation with remote sensing. Important features of the path towards the effective monitoring of arid region vegetation will be illuminated. Chapter 6 demonstrates the value of a true temporal sequence of remote sensing data, even at the poor spectral resolution of the Landsat Multispectral Scanner, and the same chapter demonstrates the importance of connecting meteorological data and ground observations to remote sensing data will be shown. These data will show the truth in the statement made above about the fact that desertification is revealed by drought. Finally, the parameters needed for an effective satellite monitoring instrument and system will be elucidated in chapter 7.

Chapter 2: *The Manix Basin*

Most geologists love the desert since everything geological is so well exposed; no false eyelashes, no cosmetics, no fancy clothes, just pure plain naked geology with a good coat of tan. (Sharp, 1976)

Effective use of remote sensing data requires knowledge of the area under observation. Chapter 1 discussed many of the processes involved in land degradation, and prior knowledge of the area being observed identifies those processes likely to be important in that area. This chapter briefly describes the geologic setting of the study area and the soils which exist in the area. The history of human activity in the area is important since, as we saw in chapter 1, human activity is the primary driving force behind land degradation. Climatological features of the area, especially rainfall and winds, control how degradation due to human activity proceeds. Finally, knowledge of the vegetation native to the area is necessary in order to effectively make assessments of vegetation cover using remote sensing.

Part 2.1: *Geologic Setting*

The primary area examined in this study is within the Manix Basin area of Eastern California's Mojave Desert. This area derives its name from a railroad siding which was known as "Manix Siding." Figure 1 shows the general location of the Manix Basin and its location with respect to the Los Angeles Metropolitan area.

The Manix Basin is located on the western edge of the eastern Mojave Desert. This area was the site of a series of perennial freshwater lakes during the late Pleistocene and early Holocene (Jefferson *et al.*, 1982). The largest of these, known as Lake Manix, may have covered an area of 77,700 hectares and was as much as 61 meters deep. The lake supported an abundant and diverse fauna as demonstrated by the fossils of pelicans, flamingos, bison, camels, mammoths, cats, canines, bears, horses, antelopes, sheep, fish, shellfish, turtles and beetles which have been recovered from the lake bed and shore deposits. Lake Manix was eventually drained along Afton Canyon about 15,000 years ago (Jefferson *et al.*, 1982; Meek, 1989), and the course of the Mojave River then divided the basin into two smaller lakes, which were responsible for forming the playas now known as Troy Dry Lake to the south of the Mojave River and Coyote Dry Lake to the north.

In the late Pleistocene the Mojave river flowed from the San Bernardino Mountains to Death Valley through a series of lakes, including lakes occupying the Manix Basin (Jefferson *et al.*, 1982). Today, there is above ground flow in the Mojave River ephemerally after storms and perennially where natural underground barriers force the water to the surface (Tugel and Woodruff, 1986). The amount of water flowing in the Mojave River averaged 81 million cubic meters per year between 1936 and 1961, but levels as high as 392 million cubic meters and as low as 13 million cubic meters have been reported (McIntire, 1986b).

This study focuses on that part of the Manix Basin bounded by the Calico Mountains on the west, the Alvord Mountains and Coyote Dry Lake to the north, a major alluvial fan originating in the Alvord Mountains on the east, and the course of the Mojave

River on the south. This area is centered at 35°00'N latitude 116°36'W longitude and is shown in figure 2. The Calico Mountains are named for the variegated appearance produced by the complex structure of strongly-colored Tertiary sedimentary and volcanic rocks. The Alvord Mountains are composed of granitic intrusions of Mesozoic age overlain by dark Tertiary volcanics which are in turn overlain by lighter-colored Miocene fanglomerates (Buwalda, 1914; Woodburne *et al.*, 1985).

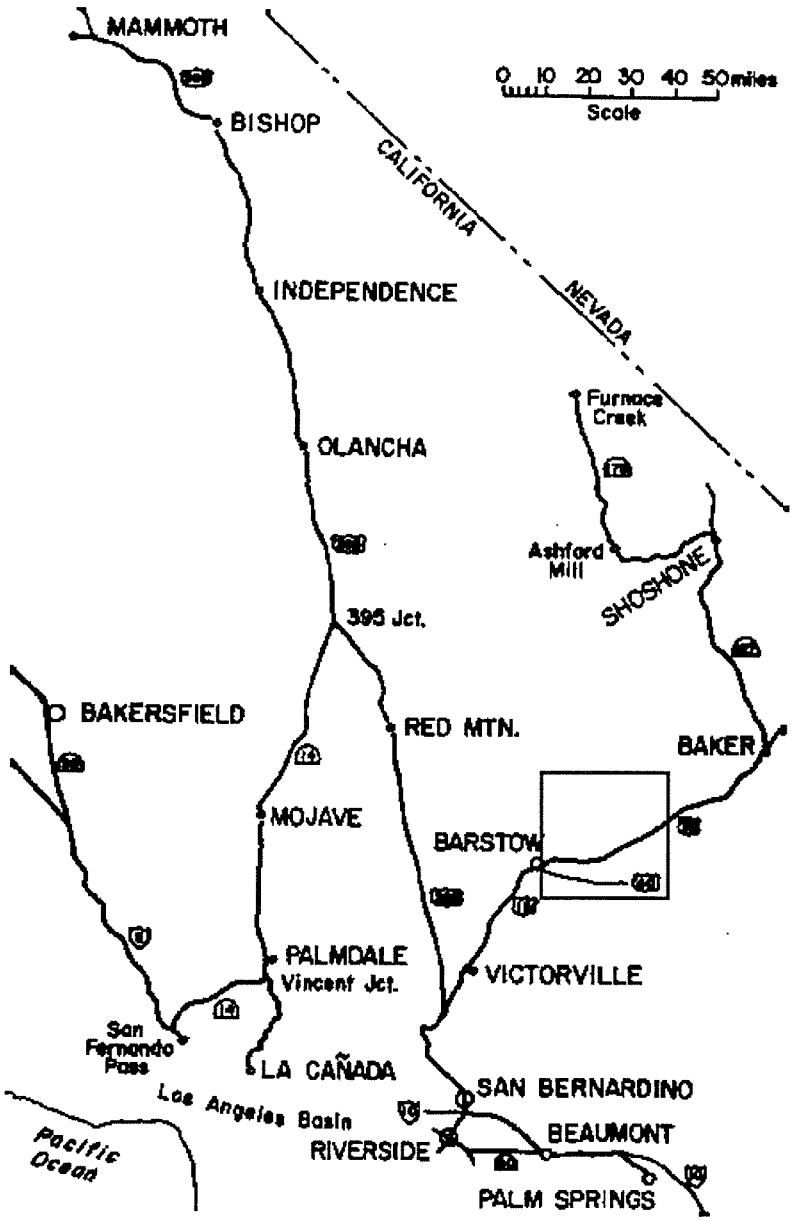

Figure 1: General sketch map of the southern 2/3 of California showing major highways and the Manix Basin Area (box). Adapted from Sharp, **Geology Field Guide: Southern California**, © 1976 Kendall/Hunt, reproduced by permission.

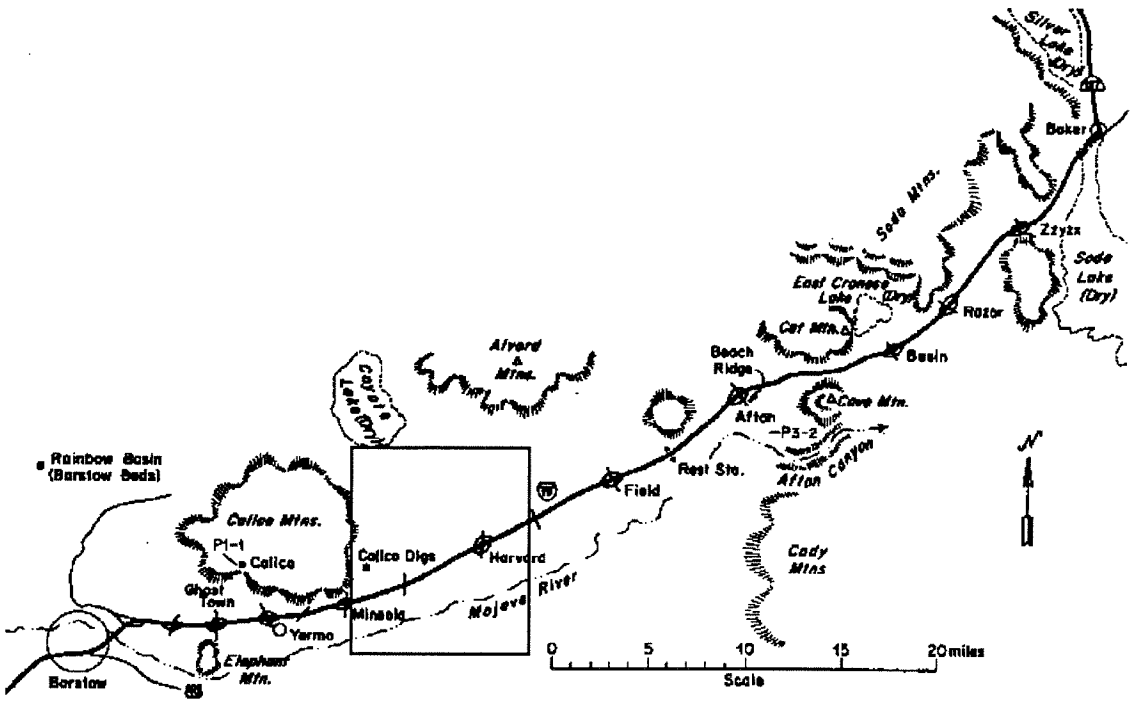

Figure 2: Map of Manix Basin area showing several geological features of importance. Primary study area indicated by box. Adapted from Sharp, **Geology Field Guide: Southern California**, © 1976 Kendall/Hunt, reproduced by permission..

The primary soils of the study area are of the Cajon Series, which are very deep, somewhat excessively drained soils on alluvial fans and river terraces (Tugel and Woodruff, 1986). A "somewhat excessively drained" soil means that water is removed from the soil rapidly and internal free water is either very rare or very deep (USDA, 1993). These soils formed in alluvial material derived from granitic source rock, and the soil surface slope ranges from 0–15 % and they have a 0–25 cm thick A horizon (Tugel and Woodruff, 1986).

All of the Cajon topsoils in the study area are generally either undesirably gravelly or sandy. Most of the soils in the area are considered to be very highly wind erodible, requiring intensive measures to control wind erosion. The small amount of gravelly sand is only moderately wind erodible. The hazard of water erosion is generally slight, but the Cajon loamy sand is listed as unsuitable for embankments, dike, and levees because of the potential for piping. These soils are considered to be non-saline by the Soil Conservation Survey (Tugel and Woodruff, 1986; USDA, 1993), which means that the conductivity of the saturation extract is less than 2 dS/m (deciSiemens per meter).

Analysis of four samples of soil from a part of the study area not on or immediately downwind of abandoned or active fields (referred to as "undisturbed desert") are summarized in table 1, along with corresponding data on the three dominant soil types of the area from Tugel and Woodruff (1986). These four soil samples were collected from an area approximately 0.1 km north of the limit of the UDSA Soil Conservation Service Survey at approximately 34° 59' 45" N latitude and 116° 39' 30" W longitude.

Table 1: Comparison of Soil Data for the Study Area

	Cajon Sand	Cajon Gravelly Sand	Cajon Loamy Sand	4 Samples Outside USDA Survey Area
Gravel (> 2mm)	25–50%	0–25%	0–25%	2–12%
Coarse Sand[†]	0–50%	15–60%	0–50%	27–36%
Fine Sand[†]	0–50%	15–55%	20–70%	50–58%
Silt and Clay[†]	5–25%	5–25%	10-30%	8–12%
pH	7.4–8.4	7.4–8.4	7.4–8.4	7.8–8.2
Salinity (dS/m)[‡]	<2	<2	<2	0.3

[†] "Coarse sand" here is the "medium sand" class from the unified system and "coarse sand" from the USDA system. "Fine Sand" here is the "fine sand" class from the unified system and it combines the "very fine," "fine," and "medium" sand classes from the USDA system. The particle size analyses reported by Tugel and Woodruff (1986) use the Unified particle size system. Particle size analyses on soils collected in this study were performed using the USDA (1993).

The four soil samples from the undisturbed desert yield a particle size distribution which classifies the soil as a "sand" (USDA, 1993). The silt and clay fraction is too small for the soil to be considered "loamy," and the gravel fraction is too small for the soil to be considered "gravelly." These soils are most likely Cajon sand with slopes under 2%. The dominance of fine sand in these soil samples indicates strong susceptibility to wind erosion.

Part 2.2: *Climate*

The processes of land degradation depend strongly on rainfall and the wind regime. Temperature is important to the rate at which water is lost from the soil through evapotranspiration, and the water content of the soil is very important to the processes of wind erosion. The state of the vegetation is highly dependent on rainfall and evapotranspiration. For these reasons, climatic data for the area are very important.

A small municipal airport located just southeast of Barstow near the town of Daggett has provided daily climatological data extending back to before 1961 and hourly wind speed and direction data extending back to 1961 (NREL, 1991a, 1991b). In addition, some rainfall and temperature data have been collected by stations located in the city of Barstow (NCDC, 1986a; NCDC, 1972-1991). The field area is part of the California Southeastern Desert Basins climatological division (NCDC, 1990a; NCDC, 1972–1991) for which the National Climate Data Center has released monthly and annual temperature, precipitation, and Palmer Hydrological Drought Index data covering 1895–1990 (NCDC, 1990a). Since this climatological division covers an area extending from the Lee Vining, California station near Mono Lake in the north to the Calexico station at the U.S.-Mexico border in the south (NCDC, 1972–1991), these climatological division data probably do not give a good representation of the conditions in the study area or for any particular location in the climatological division. This strongly suggests that climate data used as part of a monitoring program should be taken from the nearest station to the area of interest.

NCDC (1986a) gives the average annual precipitation for Barstow over the period 1951–1977 as 9.65 cm, with extreme rainfalls of more than 13.2 cm or less than 5.23 cm each expected 2 years in each decade. The average daily temperature at Barstow for this period was 63.8°F with an average daily minimum of 47.6°F and average daily maximum of 80.3°F (NCDC, 1986a). The length of the growing season at Barstow where the daily temperature does not drop below 32°F ranges between 201 and 262 days, and it is slightly longer in the Daggett-Yermo-Newberry area (NCDC, 1986a), which is nearer to the study area than Barstow itself.

Strong winds are common in the study area (NCDC, 1986a; NREL 1991b). The strongest wind ever recorded in the area was 40.5 m/s from the west recorded in June 1959 (NCDC, 1986a) The average wind speed at Daggett is 5 m/s (NREL, 1991b), which is only 0.56 m/s lower than the standard wind speed where sand begins to be lifted and carried (NCDC, 1986a). NCDC (1986a) data on the average percentage of time that wind speeds exceed the sand mobilization threshold of 5.56 m/s are shown in table 2.

The direction from which these highly erosive winds blow is summarized by data from NCDC (1986a) shown in figure 3. Figure 3 shows that 92.8% of the erosive winds blow towards directions between SE and NE, and that 82.7% of the erosive winds blow towards directions between ESE and ENE. It is important to realize that the Calico Mountains which are positioned just to the west of the study area may modify the wind regime compared to Daggett Airport which has no such features nearby.

Table 2: Average Percentage of Time Winds Exceed 5.56 m/s at Daggett Airport	
Month	**Percentage of Time**
January	16
February	31
March	45
April	50
May	65
June	54
July	41
August	39
September	33
October	24
November	21
December	12
Annual	36

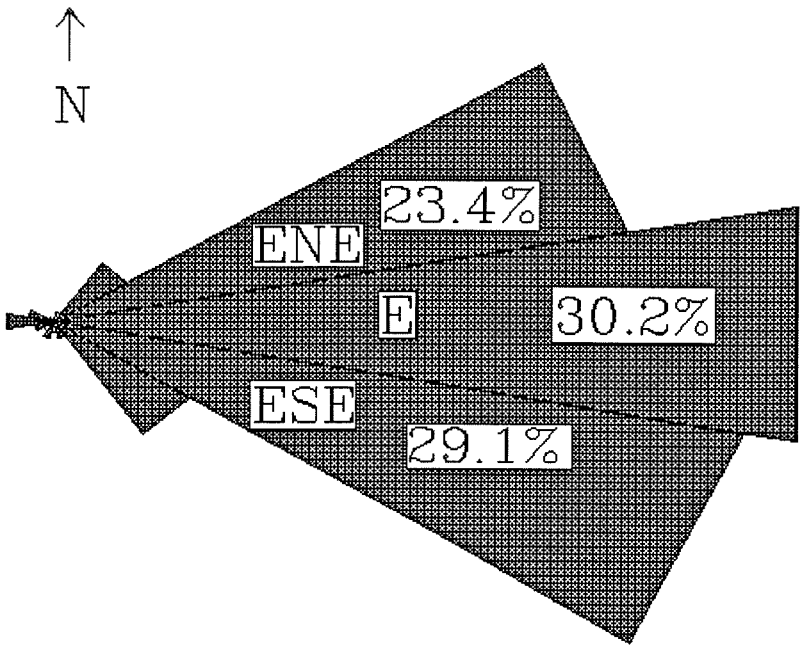

Figure 3: Rose diagram showing the percentage of erosive winds blowing *towards* each compass point at the Daggett Airport which is located about 20 miles SSE of the Manix Basin field area. Erosive winds are winds exceeding 5.56 m/s. Meteorologists typically define winds in terms of the direction the winds is blowing *from*. As shown in this figure, 30.2% of the erosive winds blow from West to East.

Part 2.3: *Vegetation*

The vegetation of this climatically harsh area is strikingly different from that of more humid areas, which has important consequences for remote sensing. The vegetation of the field area is dominated by a creosote bush and white bursage community (*Larrea-Ambrosia*). The creosote bush is the species *Larrea tridentata*, which is sometimes known as "gobernadora" which is the only one of the five *Larrea* species present in North America (Abrams, 1951; Hunziker *et al.*, 1977). The other four species of *Larrea* occur in South America, and two of them, *Larrea divaricata* ("jarillo") and *Larrea cuneifolia,* are as ubiquitous in arid and semi-arid regions in South America as *Larrea tridentata* is in arid and semi-arid areas in North America. The creosote bush (Plate 2) is an evergreen shrub with small green leaves which have a thick cuticle covered by a sticky resin (Mabry *et al.*, 1977; Fitter and Hay, 1987). A principal component of the sticky resin is a substance known as NGDA (nordihydroguaiaretic acid) which was an important food preservative in the early to mid 1900's (Mabry *et al.*, 1977). The creosote bush is capable of shedding leaves and even twigs and branches during extremely dry conditions (Fitter and Hay, 1987).

The other dominant shrub in the study area is the white bursage (*Ambrosia dumosa*), which is sometimes called burro bush (Abrams, 1960). The white bursage is a short shrub whose canopy is composed of a dense thicket of twigs (Plate 3). The leaves are generally very small and remained tightly curled during dry conditions. During wet conditions, fully developed leaves, sometimes with very complex edges will be present.

The leaves are covered with fine, white hairs and have a gray-green to silvery appearance. Seeds are contained in small burrs which can catch on the fur or feathers of animals which come in contact with the plant.

A small desert grass is ubiquitous in this area. As shown in plate 4, this grass is typically dry and yellow, and has never been observed to be green during any of the on-site investigations. A potted sample of this which was returned to Caltech produced green blades when water was added, but it was unclear if this was new growth or a greening of existing blades. Tugel and Woodruff (1986) list Indian ricegrass (*Oryzopsis hymenoides*) as the grass species occurring on the soils in this area, but the 10 cm tall blades observed in the field seem quite inconsistent with the 30–60 cm height quoted by Hitchcock (1935). The height of fluffgrass (*Erioneuron pulchellum*) at less than 15 cm (Hitchcock, 1935) seems more consistent with the observed height, and the appearance of the small clumps of grass is consistent with illustrations in Hitchcock (1935).

The last major species encountered here is the classic symbol of desert desolation in the American West, the tumbleweed. The tumbleweed, or Russian thistle (*Salsola kali*) is actually an import from Eurasia which is extremely common in disturbed areas (Abrams, 1944). Despite its shrubby appearance (Plate 5) this is an annual plant, which will soon dry up and break free from the ground to be driven across the landscape by the wind, scattering its ripe seeds as it rolls. The shrubby appearance of this plant can easily mislead the casual observer into comparing tumbleweed cover on a badly disturbed area to the cover of perennial shrubs in an undisturbed area and concluding that the disturbed area has recovered or is recovering.

Plate 2: Photograph of typical creosote bush (*Larrea tridentata*), notice small evergreen leaves and sparse canopy.

Plate 3: Photograph of typical white bursage (*Ambrosia dumosa*) shrub, notice the gray-green color and the dense thicket of twigs.

Plate 4: Photograph of typical patch of dry desert grass, notice the yellow color.

Plate 5: Photograph of typical tumbleweed or Russian Thistle (*Salsola kali*), which is a common annual plant. This is a species common in areas which have been distubed by human activity. Although it looks like a shrub, it is an annual weed.

Other plants have also been occasionally observed in the area such as woolly daisy (*Eriophyllum wallacei*), chinchweed (*Pectis papposa*), desert velvet (*Psathyrotes ramoisissima*), and smoke tree (*Dalea spinosa*). The succulents, such as cactus and yucca, which are common in many desert areas are virtually absent in this area. However, the amount of area covered by all of these minor species combined is dwarfed by that covered by any of the four dominant plant types, creosote bush, bursage, tumbleweed, and desert grass (the grass and tumbleweed can drop to very low levels under conditions of heavy drought, and at certain times of year).

Part 2.4: *Humans in the Manix Basin*

Human activity initiates land degradation, so the length of time humans have been active in the region is important, as is the nature of their activities. Humans have been in the Manix Basin area since prehistoric times as revealed by the Calico archeological site (Leakey and Simpson, 1972; Jefferson, 1982) located just at the western edge of the study area. Pedro Fages commanded Spanish forces who were the first Europeans to explore parts of the Mojave River Valley and encounter the Serrano (a branch of the Shoshone Indians) and the Chemehuevi (a branch of the Paiute Indians) who lived in the area (California Interstate Telephone Company, 1961). In the 1860's, the U.S. Army established Camp Cady on the Mojave River 15 miles downriver of Daggett to protect cattle ranchers living in the area as well as travelers (Tugel and Woodruff, 1986). Camp Cady also provided the garrison for Fort Piute and perhaps other posts which protected the route between San Bernardino and Fort Mojave in Arizona (Frazer, 1972). The

location of Camp Cady would place it just southeast of the study area, and the site reportedly had an abundant water supply

In 1882, the Calico mining camp began producing silver from the Calico Mountains, and the Southern Pacific Railroad started a line from Mojave, California to the Colorado River (Tugel and Woodruff, 1986). Daggett became an important supply and transportation center for mining operations, but this began to change when the Santa Fe Railroad line running from San Diego through the Cajon pass joined in 1885 with the Atlantic and Pacific Railroad at the site of what became Barstow, 15 km west of Daggett, (Tugel and Woodruff, 1986). In 1905, the San Pedro, Los Angeles, and Salt Lake Railroad was constructed to run from Riverside to Daggett and on to Salt Lake City, and after this line was purchased by the Union Pacific Railroad, Yermo became a division point (Tugel and Woodruff, 1986).

The area around Daggett became the first large area of the Mojave Desert to be irrigated through the construction of the Daggett Ditch over the period 1884–1902 (Mead, 1901; Tugel and Woodruff, 1986). The Daggett Ditch was built by the Marysville and Nevada Power Company at a cost of more than $3,000 (1901 dollars), and it diverted water from the Yuba River in northern California to Daggett (Mead, 1901). In 1913, the United States Department of Agriculture (USDA) reported that the amount of irrigated land in the Mojave River area exceeded 4,000 hectares (Adams, 1913). At that time, the USDA estimated that 45,200 hectares of the Mojave Desert could ultimately be irrigated (Adams, 1913). By 1917 there were 1,238 hectares of land in the Mojave River and Victor Valley areas irrigated by water diverted from the Mojave River, and 2702 hectares

irrigated by water from wells (Tugel and Woodruff, 1986), giving a total of 3,940 hectares of irrigated land. By 1934 the total irrigated area had dropped to 2620 hectares, with between 80 and 120 hectares irrigated by water diverted from the Mojave River (Tugel and Woodruff, 1986). The area of irrigated land exploded during the 1940's to 7,200 hectares by 1951, and the irrigated area remained relatively steady from that time through the mid-1980's (Tugel and Woodruff, 1986).

Most of the early irrigation systems using water pumped from wells were flood-type irrigation systems. Figure 4 shows a segment of a partially excavated flood irrigation system on a field abandoned prior to 1972. The pipes would typically have been buried until the vertical pipes ("risers") were flush with the ground. Each of the vertical pipes is topped with an alfalfa valve (basically a cap) which can be opened to allow water to flow from the pipe. This pipe would be buried along the highest part of the field and the water would then flow over and flood the field (Robinson and Humpherys, 1967). This type of system is not discussed in Houk (1951), so it seems likely that this system came into service during the late 1950's. Figure 5 shows the most deeply buried riser along this system. The 1970's saw the introduction of sprinkler irrigation systems, which were installed on land newly developed for cultivation and used to replace some of the flood irrigation systems (Tugel and Woodruff, 1986). Some of these sprinkler systems were designed to operate on rectangular fields but many were of the center-pivot type which ultimately became the dominant type of system.

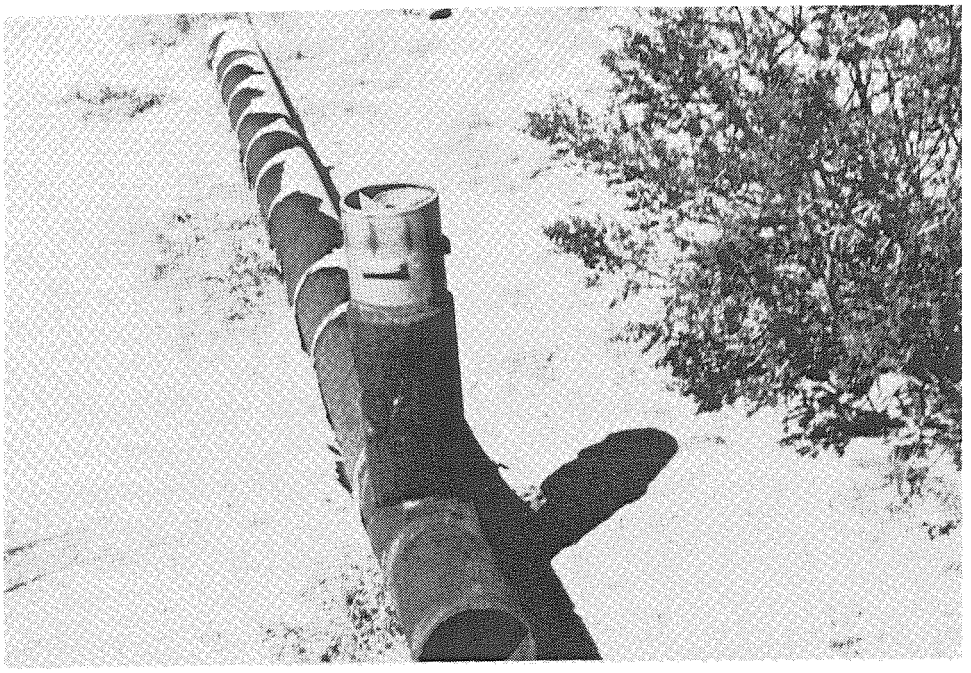

Figure 4: Photograph of old abandoned flood irrigation system in primary study area. When this system was being used, there would be a cap at the top of the vertical pipe forming an alfalfa valve which could be opened an closed to regulate the water flow.

Figure 5: Photograph of the most deeply-buried vertical pipe on the flood irrigation system shown in figure 4.

During the 1920's there was a flirtation with growing deciduous fruit in the Mojave Valley, and by 1929 fruit represented nearly 13% of the total crop value in the area (Tugel and Woodruff, 1986). However, by 1934 most of the orchards and vineyards were abandoned and only 1% of the crop value produced in the Mojave River area resulted from fruit (Tugel and Woodruff, 1986). By 1934, nearly 90% of the irrigated land was being used to grow alfalfa, and alfalfa hay remained the main agricultural product well into the 1980's (Tugel and Woodruff, 1986).

Beginning in the early 1970's, center-pivot irrigation fields in the study area north of the Mojave River began to be abandoned. Additional fields were abandoned at an increasing rate during the 1980's. Interviews with local residents revealed that the primary reason for abandoning these fields was that the cost of electricity necessary to pump the irrigation water increased to uneconomical levels. (Some of the residents hinted that some environmentalistic persons were also agitating against the irrigated fields in the area.) Over the last decade, some people have planted pistachio orchards, but nearly all of the abandoned center-pivot fields are unused. This progressive abandonment of center-pivot fields means that a series of fields at various stages in their evolution may be observed at any one time.

Chapter 3 will show how human activity produces features which can be observed and characterized using satellite and airborne data. Chapter 3 will also show how radar data can be used to infer the existence and nature of features smaller than the pixel resolution. The value of the series of abandoned fields in the Manix Basin will be shown in chapter 4 with snapshots taken by airborne instruments. These snapshots will show the

importance of wind erosion as the primary land degradation process, and the close relationship between plant cover and erosion will also be demonstrated.

Chapter 3: *The Marks of Human Activity*

Human activity produces characteristic marks on the Earth which can be recognized with both satellite and airborne remote sensing techniques. Agricultural activity in arid regions produces geometrical areas of high vegetation cover, clearly distinct in Landsat Thematic Mapper images. Viewing two images taken a year apart shows that the most significant changes occur in the zones of human activity. These zones of human activity also produce unusual features in polarimetric Synthetic Aperture Radar (SAR) data, and the radar return can be used to infer features smaller than the resolution cell of the SAR image.

Part 3.1: *Orientation*

Airborne remote sensing images cover small areas on the ground compared to satellite remote sensing images, and before moving to the close view provided by AIRSAR a broader view with satellite data is needed to provide a background for airborne data. The broader temporal view provided by using satellite images taken annually reveals that the significant changes occur over time where humans are interacting with the environment. Plate 6 shows the Manix Basin area of the Mojave Desert as seen from a satellite platform. This image was constructed by Robert Crippen at JPL by merging data from Landsat Thematic Mapper collected on July 28, 1985 and from with that from the French SPOT (Systeme Pour l'Observation de la Terre) instrument. Table 3 summarizes the features of the Landsat Thematic Mapper. The TM data are displayed as band ratios.

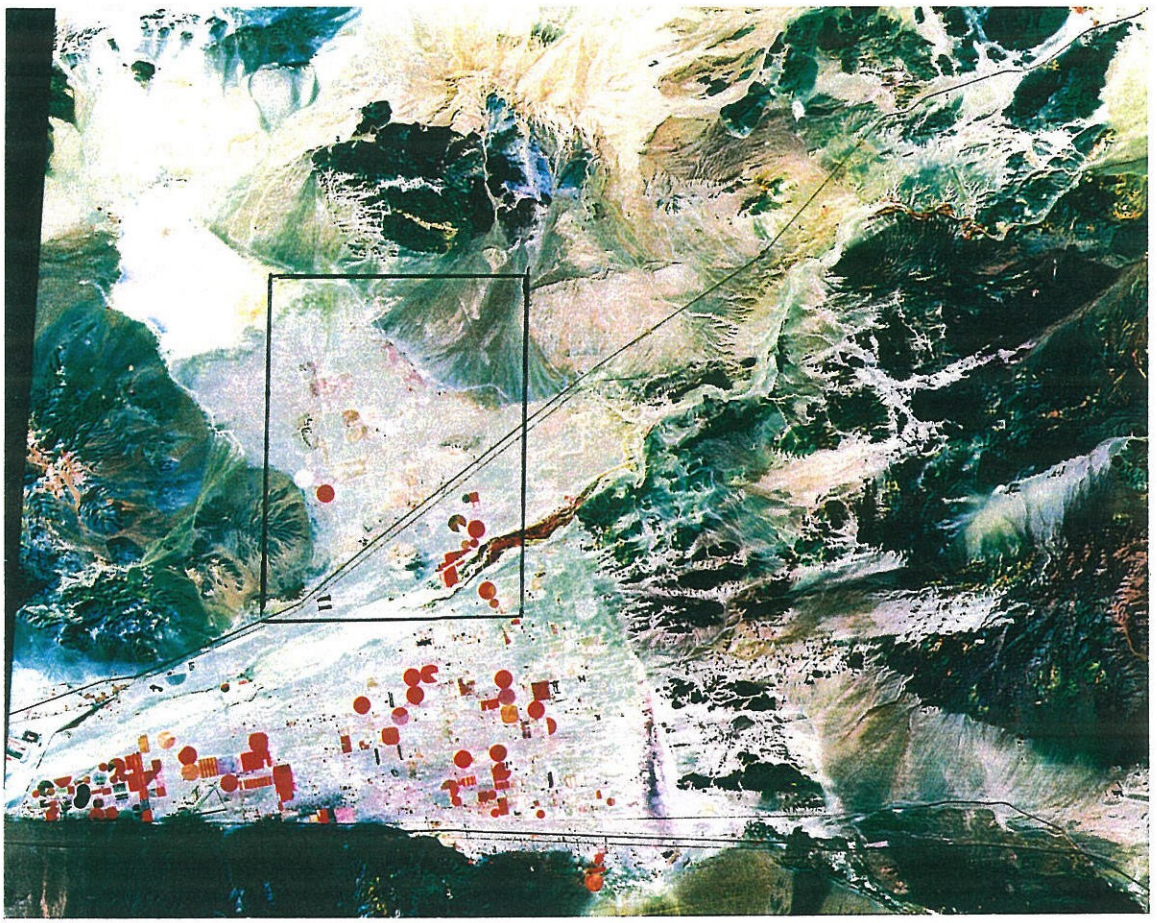

Plate 6: Landsat Thematic Mapper image of the Manix Basin taken on July 28, 1985. This image has been enhanced by Robert E. Crippen at Jet Propulsion Laboratory using SPOT panchromatic data. Red is the ratio of TM band 5 to TM band 7, green is the ratio of TM band 5 to TM band 4, and blue is the ratio of TM band 3 to TM band 1. The geometric red patches are actively irrigated fields. The boxed area is enlarged in plate 7.

Plate 7: An enlargement of the boxed area in plate 6 covering the primary study area.

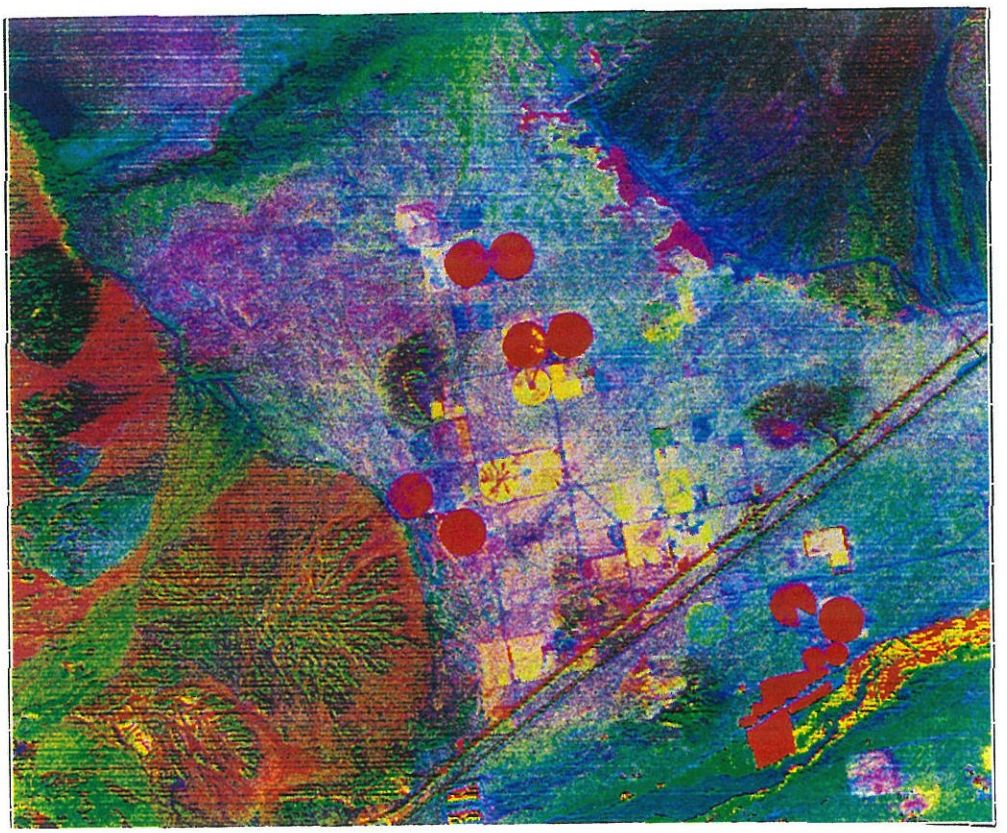

Plate 8: a) Landsat TM image taken on March 23, 1984. Red is TM Band 5/TM Band 7, green is TM Band 5/TM Band 4, and blue is TM Band 3/TM Band 1. This image has not been enhanced using SPOT data. Compare to plate 8b, and note how many of the geometrical red areas (irrigated fields) in this image are not red in plate 8b.

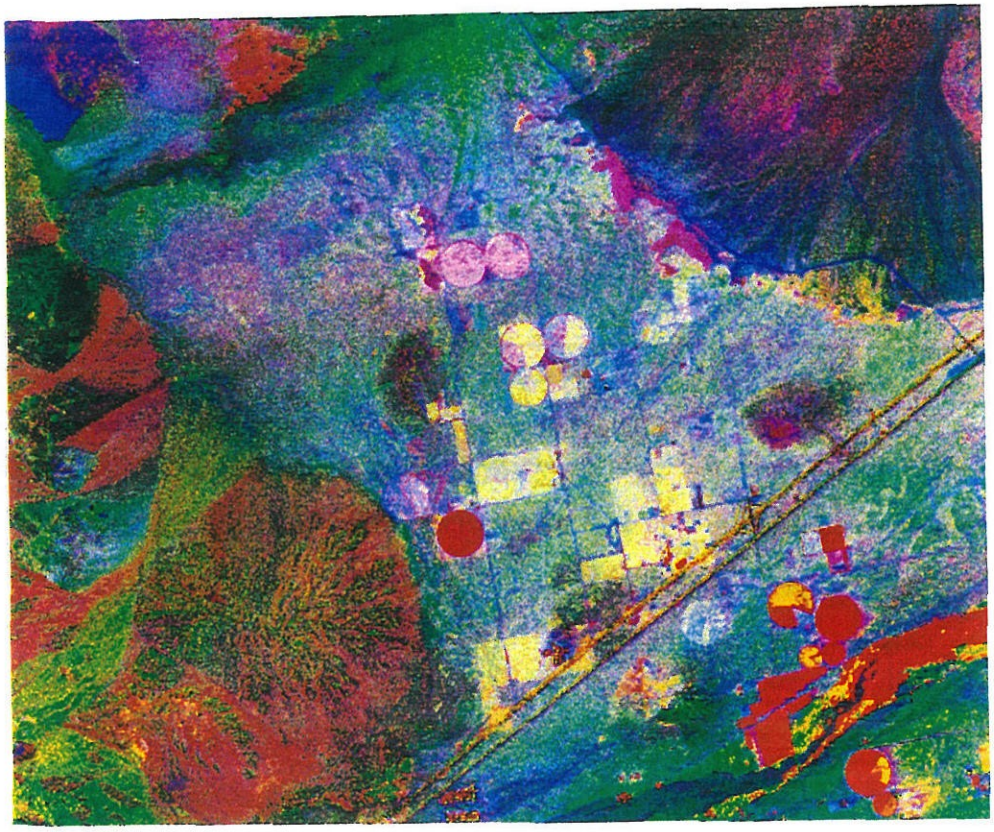

Plate 8: b) TM image taken on July 28, 1985. Red is TM Band 5/TM Band 7, green is TM Band 5/TM Band 4, and blue is TM Band 3/TM Band 1. This image has not been enhanced using SPOT data. Compare to plate 8a, and note how many of the geometrical red areas (irrigated fields) in this plate 8a are not red in this image.

The red in plate 6 is the ratio of TM band 5 with TM band 7, which should be sensitive to the presence of vegetation and the presence of green plants, since TM band 7 includes the strong water absorption band near 2.0 μm. Data from the 10 m resolution SPOT panchromatic band, which covers the spectra range from 0.51–0.73 μm, were used as a general albedo to give higher resolution texture to the TM band ratios (Ford *et al.*, 1990).

Table 3: Landsat Thematic Mapper (TM) Characteristics

Platform	Satellite	
Operation Altitude	705 km	
Repeat Cycle	16 days	
Spectral Coverage	Band Number	Range (μm)
	Band 1	0.45–0.52
	Band 2	0.52–0.6
	Band 3	0.63–0.69
	Band 4	0.76–0.90
	Band 5	1.55–1.75
	Band 6	10.4–12.5
	Band 7	2.08–2.35
Swath Width	185 km	
Ground Resolution	Band 1–5, 7	30 m
	Band 6	120 m
Quantization Level	8 bits	
Instrument Type	Whiskbroom Scanner	

The two interstates shown in figures 1 and 2 can be clearly seen on this image. Barstow California lies just off the lower left side of the image, where the two interstates would intersect. The Mojave River runs roughly parallel to Interstate-15 from the lower

left to upper right. Coyote Dry Lake can be seen as a nearly white patch in the upper left part of the image. There are also many geometric patches of red, which are irrigated fields with a great deal of plant cover. Abandoned fields can also be seen on this image as circular and rectangular patches which differ in color from the surrounding desert, sometimes only subtly.

The enlargement of plate 6 focusing on the primary study area in plate 7 shows the active and abandoned fields more clearly. Coyote Dry Lake occupies the upper left corner, with the Calico Mountains and a large alluvial fan occupying the lower left and upper right corners, respectively. A small segment of the Mojave River can be seen cutting across the lower right corner of the image. The trail which can be seen snaking up onto and then along the alluvial fan is a path used by U.S. Army tanks since World War Two to travel across the desert to Fort Irwin, located just north of the Manix Basin.

Plate 8 shows two TM images using the same band ratios as in plates 6 and 7. Plate 8a is a TM image acquired on March 23, 1984, and plate 8b is the July 28, 1985 image. A comparison of plates 8a and 8b show relatively little variation in the images in areas not occupied by agricultural fields. There are a few changes in the surface of the Coyote Dry Lake playa, and a segment of the Mojave River seems to be much more heavily vegetated in 1985 than in 1984, but the areas not directly altered by man have changed little (the greening in the Mojave River may have been due to human activity). Five fields north and two fields south of I-15 are inactive in 1985 after being active in 1984, while three fields south of I-15 are active in 1985 after being inactive in 1984. (These two images have not been inter-calibrated, so differences in atmospheric

properties, instrument characteristics, and solar geometry between these two images have not been removed which could give the appearance of ephemeral change where no real change on the surface has occurred.)

Part 3.2: *A First Look with Radar*

The nature of the radar return from a surface provides a great deal of information about the roughness and orientation of the surface being observed. The modifications of the Earth's surface through human activities can be readily seen in radar data. Plate 9 is a three color total power image of JPL Airborne Synthetic Aperture Radar (AIRSAR) data. In this image the total backscattered power received by the instrument in the C-band (5.7 cm) is shown in blue, the total power in the L-band (24 cm) is shown as green, and the total power in the P-band (68 cm) as red. AIRSAR is an airborne instrument which flies at about 8 km altitude, while the Landsat satellite flies at 705 km altitude. Additionally, AIRSAR is a side-looking radar (SLR), which introduces distortions caused by the changing incidence angle across the instrument swath. Nominal AIRSAR characteristics are summarized in table 4.

Table 4: Nominal AIRSAR Characteristics

Platform	Airplane (DC-8)
Operational Altitude	7.9 km
Radar Wavelength	C-Band (5.7 cm) L-Band (24 cm) P-Band (68 cm)
Polarization	Full Stoke's Matrix
Swath Width	12.8 km
Ground Resolution	10 m

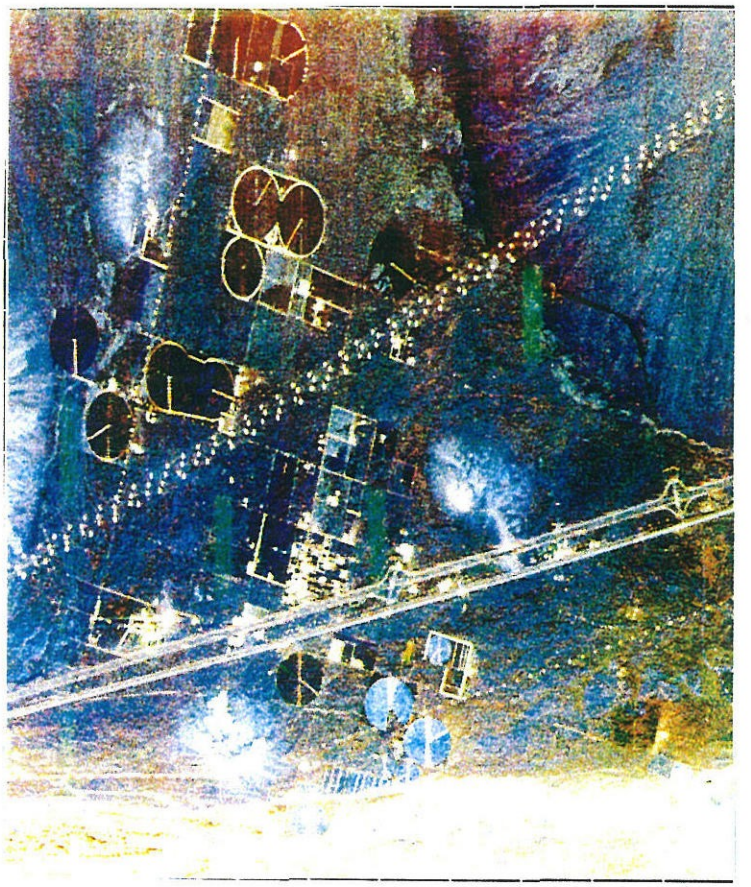

Plate 9: Three-color composite of JPL AIRSAR total backscattered power images. The blue is the 5.6 cm C-band data, the green is the 24 cm L-band data, and the red is the 68 cm P-band data. AIRSAR flew from left to right across the bottom (south) edge of this image.

The most important characteristic of the target which affects the radar return is the surface roughness. A smooth, mirror-like surface (sometimes called a "facet") strongly reflects radar energy in accordance with the law of reflection. Since the radar is side-looking, the only way in which energy reflecting from facets can be detected is if the facet happens to be oriented at an angle perpendicular to the incoming radar signal. Radar return from facets is typically referred to as "specular" scattering.

The radar return from most natural targets is caused by scattering caused by small-scale surface roughness. There are two simple ways in which this has been modeled. The first model is the point scattering model which assumes that the surface behaves as a series of uncoupled isotropically radiating points. This model leads to the Lambertian scattering law:

$$\sigma(\theta) = N\sigma_0 \cos^2\theta \qquad (1),$$

where θ is the incidence angle and σ_o is the ratio of energy received by the sensor from the scatterer to the energy that would have been received from an isotropic scatterer which scatters energy equally in all directions (backscatter cross section).

The other alternative is the Bragg scattering model which divides the surface into its Fourier components, and then assumes that the backscatter is mainly due to the spectral component leading to Bragg resonance with the incoming radar wavelength (λ):

$$\Lambda = \frac{n\lambda}{2\sin\theta} \qquad n = 1,2,... \qquad (2)$$

The $n = 1$ term gives the strongest scattering. The practical result of both the point scattering and Bragg models is that radar backscatter, for constant dielectric constant and

in the absence of specular scattering, is directly proportional to the amount of surface roughness close to the scale of the radar wavelength.

Polarization, which defines how the electric field vector is oriented, can provide information on the nature of the surface roughness. Two angles are used to define polarization, the orientation angle (ψ) and the ellipticity angle (χ) which are related to each other as shown in figure 6. Table 5 summarizes the definitions of the four fundamental polarizations in terms of χ and ψ. For linear polarization, $\chi=0°$, and $\chi=\pm45°$ for circular polarization. The method of describing handedness used in this study is the standard for the Institute of Electrical and Electronics Engineers (IEEE, 1979). This is a more "natural" way of describing the handedness of polarization than the traditional optics form because the IEEE standard defines the handedness based on the rotation direction of the electric field vector in space(Jackson, 1975; Born and Wolf, 1980). It should also be noted that the orientation angle is rotated 90° counter-clockwise by some authors (e.g., Ulaby and Elachi, 1987), making $\psi=0°$ vertical polarization.

Table 5: Basic Polarizations

Polarization	**Orientation Angle: ψ**	**Ellipticity Angle: χ**
Linear Horizontal (H) (Generally parallel to the Earth's surface.)	0° or 180°	0°
Linear Vertical (V) (Perpendicular to H polarization.)	90°	0°
Right Hand Circular (R)	0°	-45°
Left Hand Circular (L)	0°	+45°

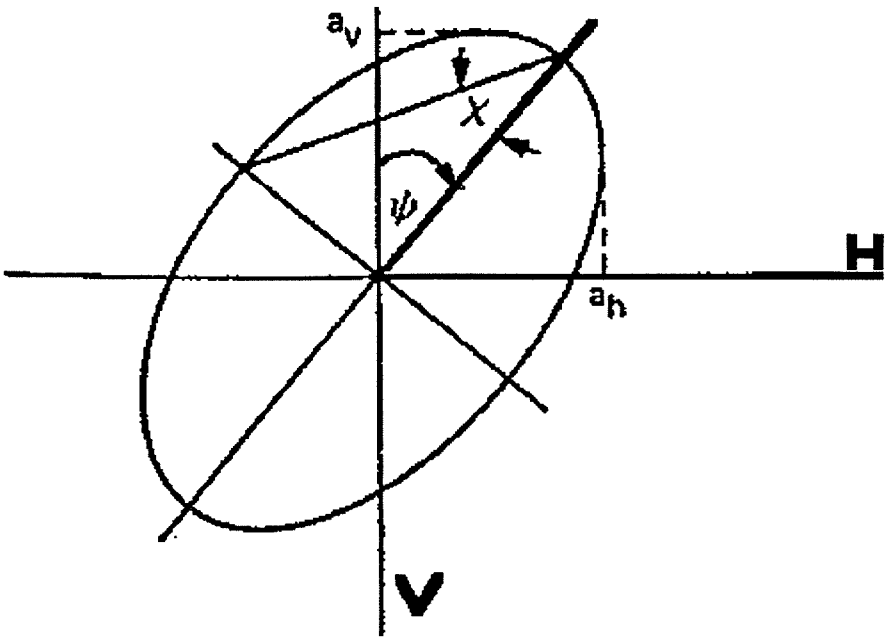

Figure 6: The polarization ellipse showing the relationship between the orientation angle ψ and the ellipticity angle χ. The amplitudes of the horizontal and vertical components of the electric field vector are shown by a_h and a_v. The tip of the electric field vector traces out the ellipse shown in the plane perpendicular to the wave propagation.

In active remote sensing, such as radar, the polarization of both transmitted and received signals can be chosen, so "polarization" in radar is defined by both the transmitted and received polarizations. Pairs of letters are used for radar polarizations with the first letter indicating the transmitted polarization and the second letter indicating the received polarization. For either circular or linear polarizations there are four mutually orthogonal radar polarizations — VV, HH, VH, and HV for linear polarizations; RR, LL, RL, and LR for circular polarizations.

If complex scattering amplitudes are known for all of the orthogonal radar polarizations, it is then possible to synthesize the scattering for any combination of transmitted and received polarizations (van Zyl *et al.*, 1987a, 1987b; Zebker *et al.*, 1987a,

1987b). This provides a complete description of the polarization response of the target for a given incidence angle and look direction. Zebker and Norikane (1987) demonstrated the power of using the polarization response to gather information about the orientation of the observed target.

The AIRSAR instrument measures all four complex scattering amplitudes by first transmitting an H-polarized pulse and then receiving the HH and HV responses simultaneously. The antenna then switches electronically to V polarization and transmits a V-polarized pulse. Table 6 summarizes some of the characteristics of the AIRSAR data used in this study. There are differences between this table and the nominal AIRSAR characteristics given in table 4, which shows how the nominal values may not be the same as the real values. The characteristics not listed in table 6 are the same as those in table 4.

Table 6: Characteristics of Manix Basin AIRSAR Data for June 28, 1990

Characteristic	Value
Instrument Altitude	7826 m
Resolution (cross-track)	6.66 m
Resolution (along-track)	12.10 m

The AIRSAR data were calibrated using the technique described in van Zyl (1990). In this technique, a single trihedral corner reflector boresighted on the AIRSAR instrument (which causes the trihedral corner reflector to have the same polarization response as a large sphere) and a natural target are used. For the AIRSAR data in this study, there was no corner reflector in the image, but data analyzing trihedral corner

reflector data were available for a flight on June 24, 1990. According to van Zyl (1991, personal communication), the AIRSAR instrument is sufficiently stable to allow the use of the analysis data from June 24, 1990 along with a natural target in the image for data calibration. This calibration corrects for errors in the phase relationship between polarization channels, errors due to imperfections in the radar antenna which cause imperfections in the polarization states ("crosstalk"), absolute amplitude and channel gain balance (Zebker *et al.*, 1987a). The trihedral corner reflector data are only needed for the absolute amplitude and channel gain balance calibrations (Zebker *et al.*, 1987a). The calibration was performed with a JPL program called POLCAL, which was written by Jakob van Zyl and runs on a VMS-based VAX.

Looking at plate 9 which represents the total backscattered power in all polarizations in each wavelength, many human constructions can be seen. There are three parallel lines of bright points crossing the image diagonally and another single line of points running diagonally across the lower part of the image. All four of these lines of bright points are cause by a series of metal towers supporting power lines.

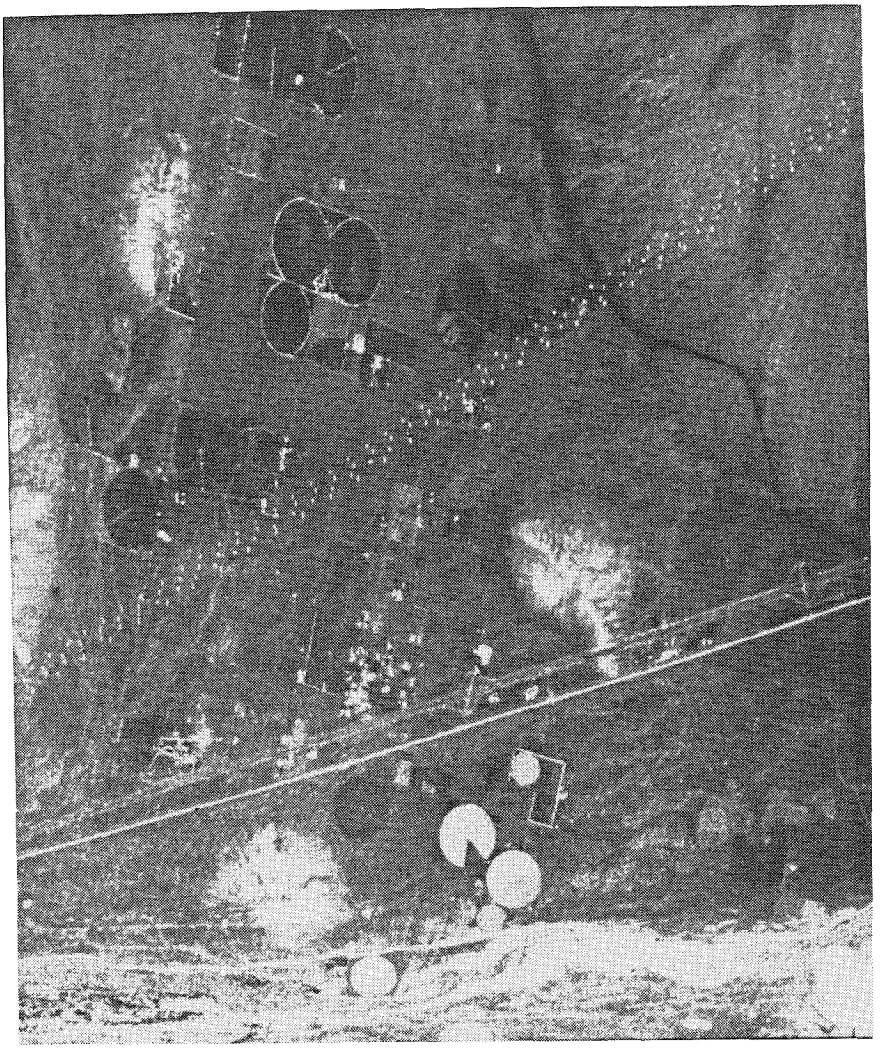

Figure 7: The three single-band total power images which comprise plate 9. The elliptical appearance of the dark abandoned fields in the upper part of the image is due to the fact that the incidence angle of the radar increases from the bottom of the image to the top of these images. The radar flew left-to-right (west to east) across the bottom of the image. Bright regions are typically rougher than dark regions. Very bright pixels are usually caused by metal objects, specular reflections, or resonance. **a)** C-band (5.6 cm) total power image. Notice that the active fields at the bottom of the image are nearly uniformly bright.

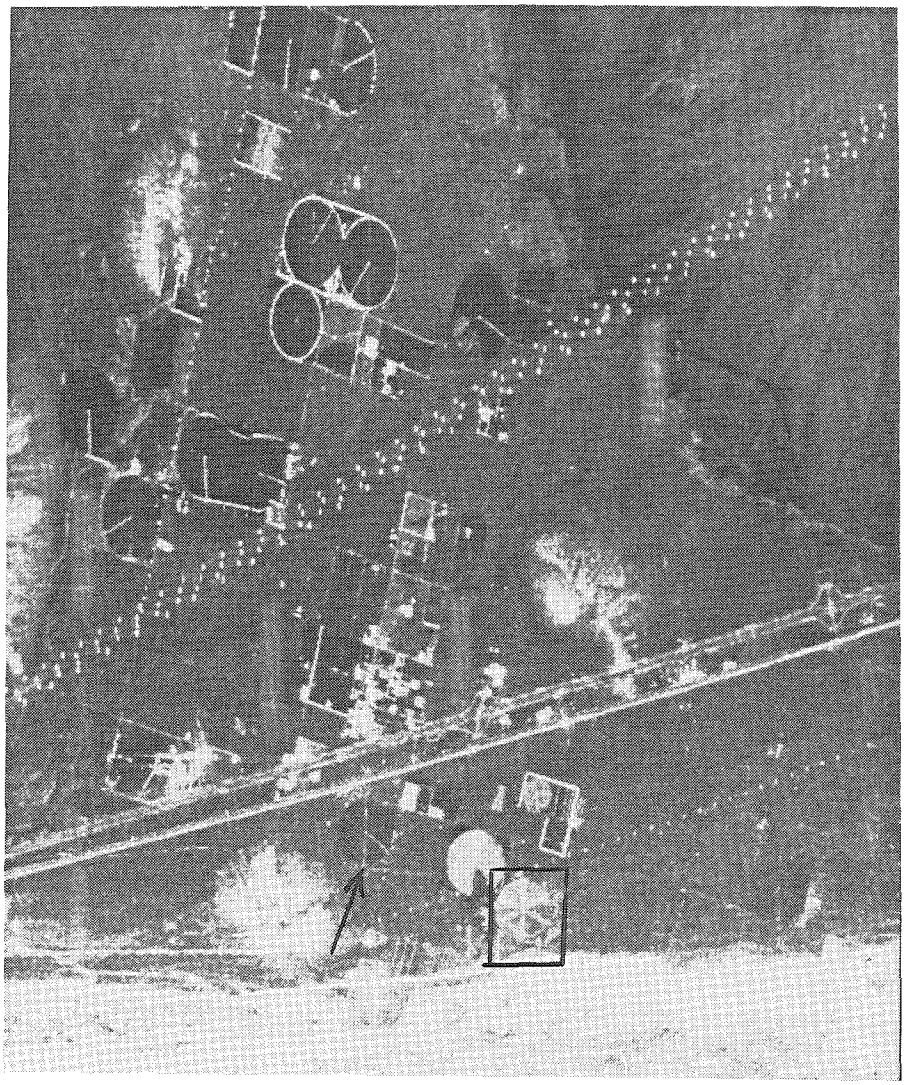

Figure 7b): L-band (24 cm) total power image. Notice that the bright diameter indicated by the arrow is made of very bright pixels separated by dimmer pixels giving the appearance of a string of pearls. Notice also the three bright diameters on the active field in the box near the bottom of the image. The boxed area is enlarged for figure 10b.

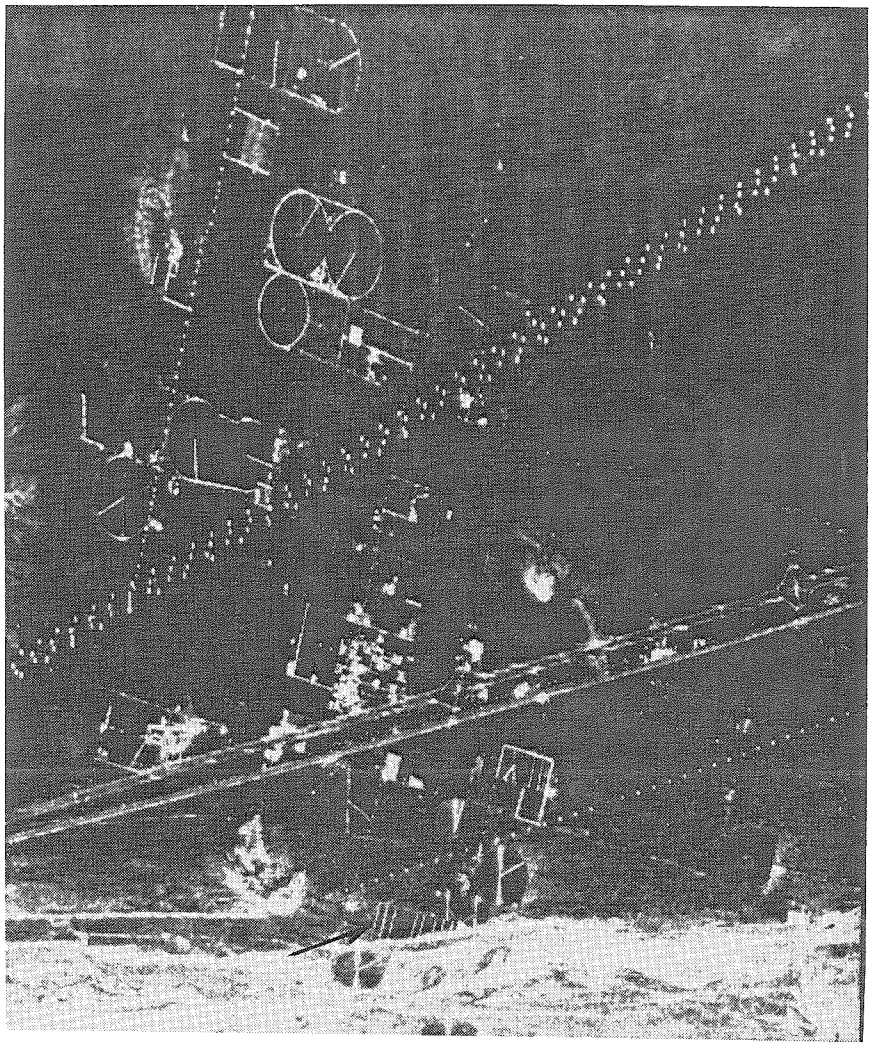

Figure 7c): P-band (68 cm) total power image. Notice the indicated straight irrigation systems on rectangular fields.

Active fields can be seen in the lower part of the image as bluish circular and elliptical patches, while abandoned fields can be seen as similarly-shaped dark patches The blue color of the active fields indicate that they are rough at the scale of the C-band radar, meaning there are many scatterers in the range of 5–6 cm in size. Many of the abandoned fields are surrounded by circular fences, and some linear fences can be seen in the images. All of the active fields and all but one abandoned field have a single bright radius that is caused by the overhead pipe of the center-pivot irrigation system. The distorted elliptical shape of many of the abandoned fields is caused by the changing antenna footprint. The low altitude of the aircraft causes pixels to get compressed in the look direction of the radar and expanded in the direction parallel to the line of flight as the incidence angle of the radar varies.

The three parts of figure 7 show the three bands which were combined to form plate 9. In figure 7a, the active fields at the bottom of the image are entirely bright, which shows that the alfalfa plants on these active fields are very strong scatterers on the 5–6 cm scale. Figures 7b and 7c show these active fields as substantially fainter which occurs because of the greater ability of the longer wavelengths to penetrate through the vegetation canopy and the decrease in the effective roughness of the vegetation as the radar wavelength increases.

The irrigation systems used for these fields can be seen very clearly in 7b and 7c, and slightly less well in figure 7a. All but one of the circular, center-pivot fields have a single bright radius, which delineates the overhead pipe used for center-pivot sprinkler irrigation. The relatively weak response in the C-band is due to the fact that the pipes

have a smooth, curved surface. A close look at some of these center pivot fields as indicated in figure 7b, shows that the bright radius is composed of a series of very bright points separated by slightly fainter pixels. This response shows that most of the strong scattering from the irrigation systems is due to the wheeled supports which hold the pipes overhead. In figure 7c several irrigation systems on rectangular fields are indicated. The one indicated north of the diagonally-running triple power lines is an old flood irrigation system as described in chapter 2. Looking at the various parts of figure 7, this system is most clearly visible in the P-band. The irregular visibility of this system is caused by the fact that it is partially buried. The fact that the system appears most continuous in the P-band is most likely due to the greater penetration of the longer radar wavelengths.

Plates 10, 11, and 12 are three color composite images for each band where different polarizations are used for the different colors. In each case, the blue color is the cross-polarized VH polarization, green is the co-polarized VV polarization, and red is the co-polarized HH polarization. In the C-band image, plate 10, most of the undisturbed desert is bright green, which indicates that the dominant polarization is VV. The Bragg model for rough surface scattering predicts that VV polarization will be the strongest polarization for a slightly rough natural surface (Kuga *et al.*, 1987). Notice the area pointed out by the arrow on the relatively dark center-pivot field. The indicated bright patch is a region of heavily-clumped white bursage. Note that the upper center part of the image has a slightly red tinge indicating a stronger HH response. This may indicate a different substrate than exists in the rest of the image, but the Bragg model predicts a more equal balance between HH and VV at large incidence angles.

Plate 10: A three-color composite composed of single polarization images in the C-band (5.6 cm). The blue is VH polarization, the green is VV polarization, and the red is HH polarization. The general green (VV) background is what Bragg scattering of slightly rough surfaces predicts.

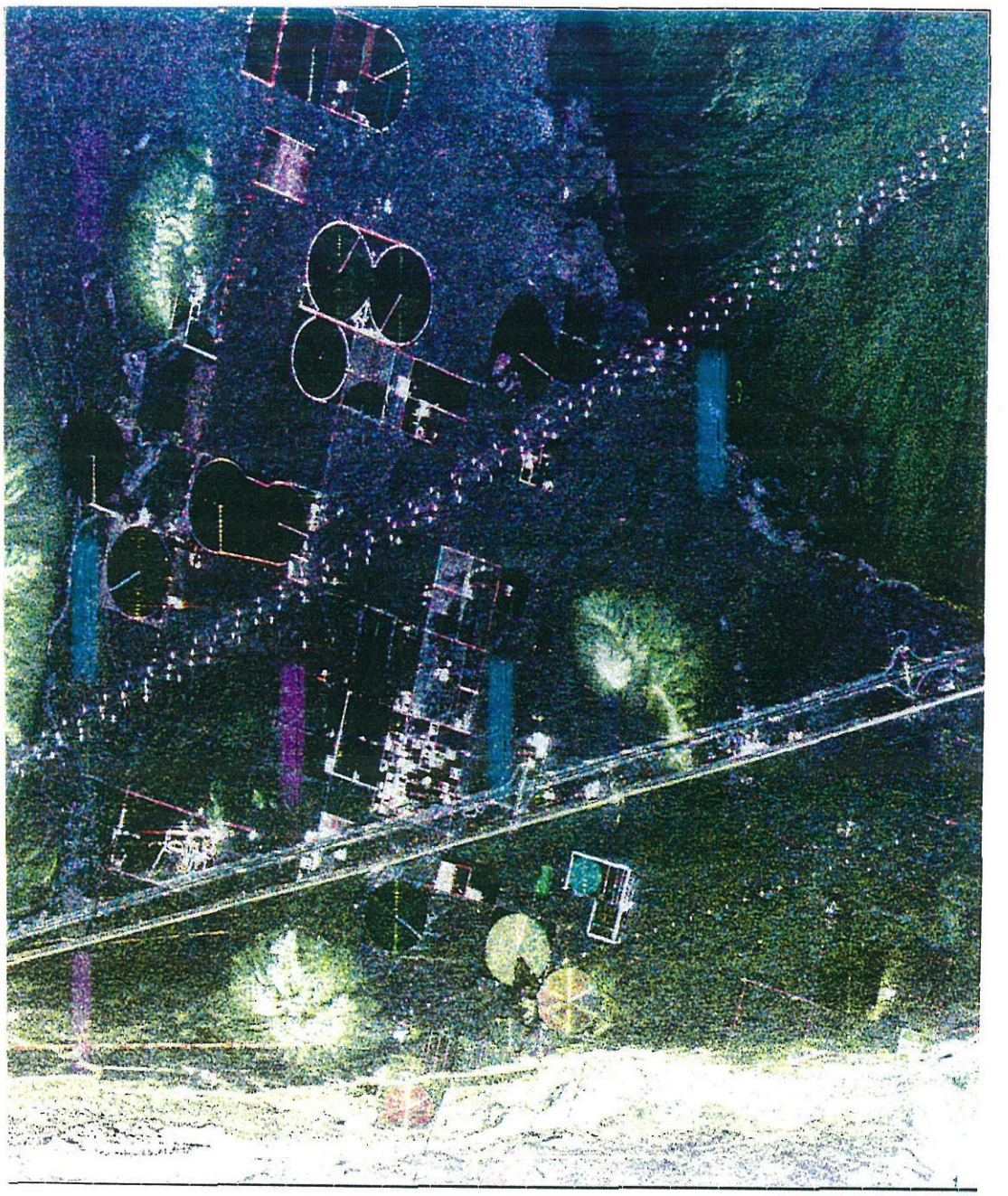

Plate 11: A three-color composite composed of single polarization images in the L-band (24 cm). The color scheme is the same as in plate 10. Notice the purple and green-blue chirps of L-band noise and the exceptionally strong VV (green) return on the small circular field.

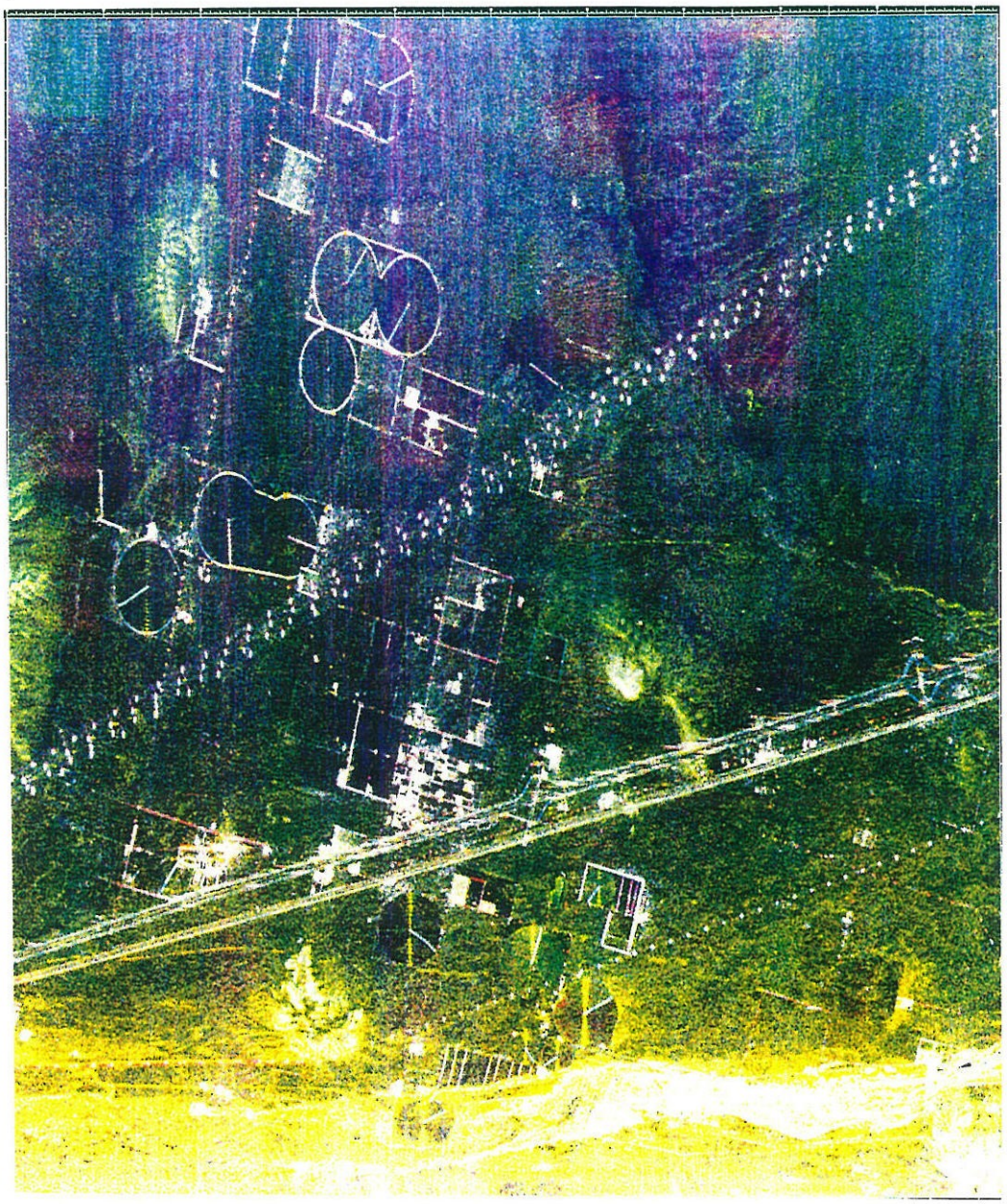

Plate 12: A three-color composite composed of single polarization images in the P-band (68 cm). The color scheme is the same as in figure 20. Notice the strong HH (red) interference in the upper half of the image caused by radar at Fort Irwin which is located just north of this image.

A series of strange features are present in plate 11 as short, vertically-oriented strips of pink and blue-green. These strips are clearly due to some sort of L-band radar transmitting from either the Daggett Airport to the southwest or Fort Irwin to the north. The changing color either indicates a single radar changing polarizations or at least two radars with different polarizations. It is also possible that the interfering radar is mounted on civilian or military aircraft. Fortunately, all of the pulses miss the areas of interest, active and abandoned fields. The small center-pivot field in the l-shaped patch south of I-15 exhibits a very strong VV return, which may indicate that tall plants were growing on this field.

The P-band polarization image shown in plate 12 clearly has a serious problem. There are a large number of red streaks extending from the north edge of the image, which swamp virtually all other returns. This is clearly due to some sort of P-band radar located on Fort Irwin. This strong signal renders the upper half of the image virtually unusable, especially for the abandoned fields which have very weak returns.

Figure 8: Photograph of center-pivot irrigation system in the Manix Basin. Notice the wheeled supports which scatter radar strongly, producing most of the return observed from the center-pivot irrigation system..

Part 3.3: *The Great Compact Discs of the Desert*

In plates 9–12 and figure 7, many of the fields have a single bright radius aligned parallel to the radar look direction (Ray *et al.*, 1991; Ray *et al.*, 1992a; Ray *et al.*, 1992b). This phenomenon was discussed by Ulaby *et al.* (1982), and it has been observed on center-pivot fields in France by DuBois *et al.* (1992). As shown in figure 8, center-pivot irrigation systems are supported by several sets of struts on wheels. The repeated travel of these fields around the field ultimately wear ruts into the surface of the field. The sides of these ruts generate specular reflections at the point along the circumference of the circle

where the tangent line to the circle is perpendicular to the look direction of the radar (Ulaby *et al.*, 1982).

These active fields have a set of features which were not present on the fields in France studied by DuBois *et al.* (1992). The French fields were plowed straight across in linear rows, while the fields in the Manix Basin study area, as well as in other areas of the arid and semi-arid western U.S., are plowed with furrows in concentric furrows. This has at least two advantages. One advantage is the fact that the crop rows are not cut and crossed by the irrigation system furrows. Another advantage is related to the problem of wind erosion. Wind erosion is decreased by plants in rows which are perpendicular to the direction of expected erosive winds, and a concentric pattern of crop rows provides protection from winds blowing in any direction. We will see in chapter 4 how the concentric circles also provide the greatest protection for the part of the field which has the potential of losing the most soil The undulations produced by this concentric pattern of furrows can also add to the specular reflections causing the bright diameter parallel to the look direction (Ulaby *et al.*, 1982; Ray *et al.*, 1991; Ray *et al.*, 1992b, 1992b).

In plate 11, the active field located just southeast of the Pacman-shaped field has two bright diameters oriented about 45° from the look direction. These are analogous to the diffraction pattern that can be seen from a compact disc when light strikes it at some angles. From figure 7, it is clear that these spokes are L-band phenomena, which suggests that they are due to a surface feature of a scale similar to the L-band wavelength of 24 cm. This differs from the diameters parallel to the radar look direction which are strong in both

the L- and P-band wavelengths. A reasonable candidate for a surface feature of scale comparable to the 24 cm L-band wavelength is the concentric pattern of crop rows.

Part 3.4: *Modeling the Spokes*

Part 3.4.1: *A Diffraction Model*

[The principal results of this section were originally presented in Ray and van Zyl (1994).]

As suggested in part 3.2, the bright diameters, or spokes, look similar to the diffraction patterns seen in reflections from compact discs. In view of this similarity, a diffraction model of the scattering from the surface should be investigated. It is important to bear in mind that SAR illuminates and receives scattered radar energy from an area much larger than the size of a single pixel, so that the entire field is "seen" by the radar at once.

There are two different limits of diffraction theory. The first limit is Frauenhofer diffraction which occurs when the diffraction pattern is observed at distances which are large compared to the size of the diffracting system and the illumination is also at a distance much larger than the diffracting system. The Frauenhofer limit is also valid when the light source and observer are near a line perpendicular to the plane of the diffracting system passing through the center of the diffracting system. The case of these center-pivot fields and the side-looking radar system clearly lies outside of the Frauenhofer case (the radar would need to be more than 10,000 km away from the center of the field before Frauenhofer diffraction would apply). Therefore, a Fresnel diffraction model must be considered.

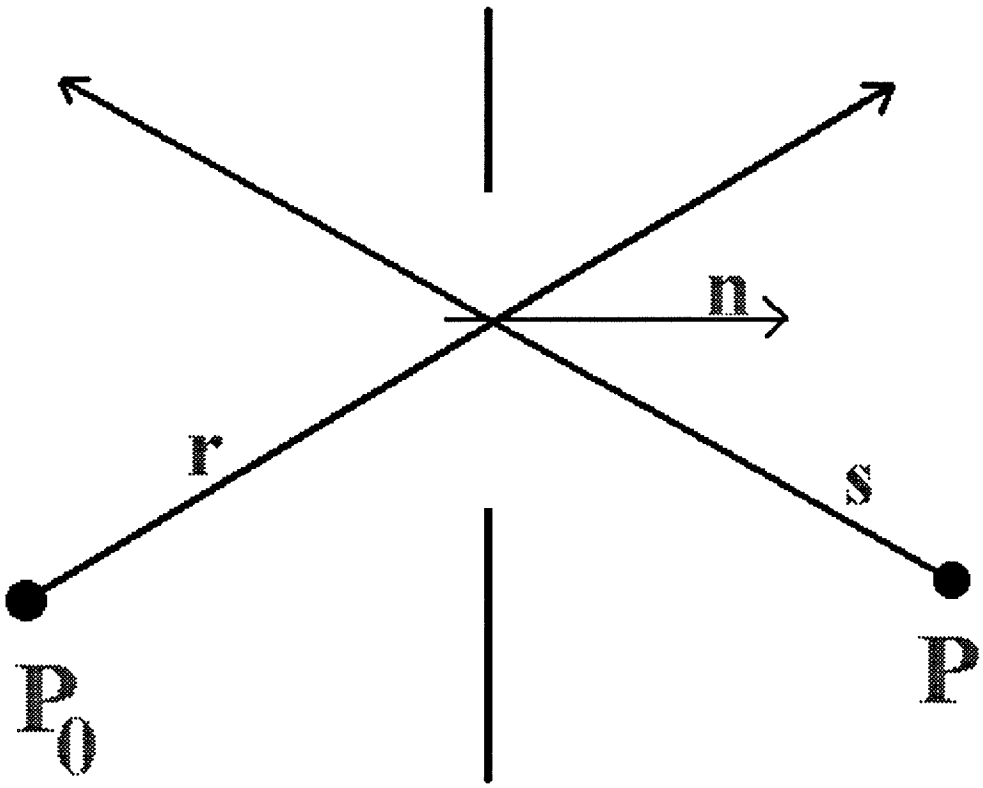

Figure 9: Geometry for the Fresnel diffraction model. P_0 is the radiation source and P is the point at which the diffracted field is observed. The surface normal is **n**, the vector from the source to the diffracting system is represented by **r** and the vector from the observation point to the diffracting system is represented by **s**.

The geometry used for the Fresnel diffraction model is shown in figure 9. In order to keep the diffraction model simple, the field is considered as a flat disc with reflectivity that varies as $\cos(a\rho)$, where ρ is the radial distance from the center of the field, and the constant a defines the wavelength of the "undulations" in the reflectivity function. The diffracted field is evaluated at point P in figure 9, which corresponds to the location of the light source according to the Helmholtz reversion (or reciprocity) theorem (Born and Wolf, 1980). The Fresnel-Kirchhoff diffraction formula for the intensity U at a point P is given by Born and Wolf (1980):

$$U(P) = -\frac{iA}{2\lambda}\iint_A \frac{e^{ik(r+s)}}{rs}[\cos(n,r) - \cos(n,s)]dS \qquad (3)$$

Figure 10a shows the results of numerically evaluating this integral with the radial sinusoidal reflectivity function for the case when the platform is flying at 10,000 m altitude in a straight line which is 7000 m from the center of the field at closest approach. The wavelength of the surface "undulations" is 30 cm and the radar wavelength is 24 cm (the same as AIRSAR L-band). The plot is a polar plot of the total intensity received along each radius of the field. There is a region of strong return offset about 45° from the line parallel to the radar look direction which can be compared to the bright spokes in figure 10b. Figure 11 shows how the pattern varies as the center of the field is moved closer and closer to the flight line. The "spokes" open up further and further as the incidence angle approaches the nadir. Simple experiments with a flashlight and compact disk in a dark room will reveal a very similar result.

There are two obvious problems with this model. The first problem is that a surface with physical undulations is being treated as a flat surface of varying reflectivity. While there may be some justification for this from the results of diffraction modeling of gratings having physically undulating surfaces and no true slits (Born and Wolf, 1980), how well this extends to the case considered here is questionable. Second, Kirchhoff theory assumes that the dimensions of the "opening" (in this case the wavelength of the undulations) are large compared to the wavelength of the radiation, which is clearly not the case here.

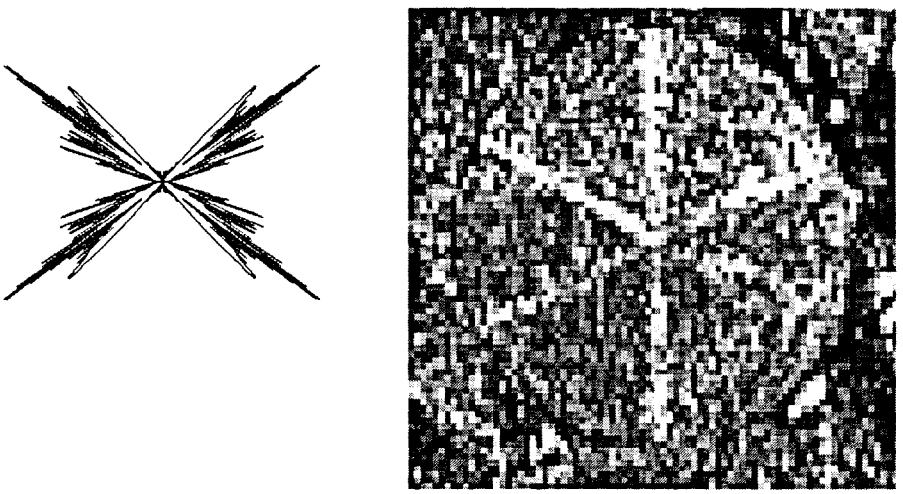

a) b)

Figure 10: a) Intensity for the diffraction from a disk of radially sinusoidal reflectance with a wavelength of 30 cm and an illumination wavelength of 24 cm at an incidence angle of 35°. The distance of the point from the radial center is the total returned power. **b)** Enlargement of active fields with bright diameters offset from the look direction. In both cases observation is from the bottom edge of the figures.

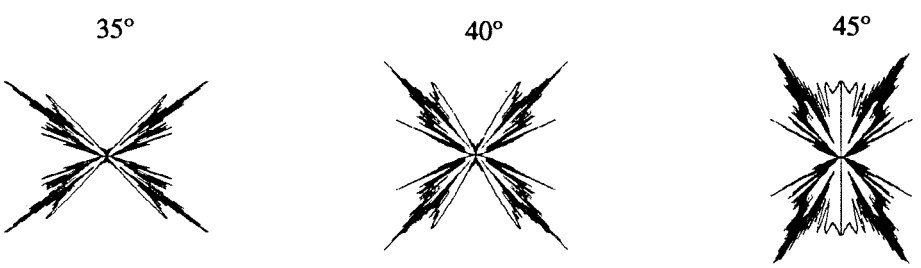

Figure 11: A series of plots similar to figure 10a showing how the bright returns narrow and increase in angular offset from the look direction as the incidence angle approaches vertical. The further the point is from the center of the figure, the stronger the backscattered return. Again, all three of these figures are observed from the bottom edge of the figure.

Part 3.4.2: *Small-Perturbation Model*

In view of the preceding problems with the simple diffraction model, a different approach to modeling the surface was used. The second approach involves an approximation of scattering from a rough surface by assuming small perturbations from a smooth surface. This is known as the "small perturbation" technique (or model), and it can be viewed as analogous to a Taylor's series expansion.

The small perturbation technique begins by using the Rayleigh approximation (which is the same as the first Born approximation) to describe the scattered and transmitted fields in terms of waves propagating away from the interface (Jackson, 1975; Born and Wolf, 1980; Kuga *et al.*, 1987). In the region between the minimum and maximum height of the rough surface there are scattered waves moving both up away from the interface and down towards the interface. The Rayleigh approximation ignores scattered waves that are traveling towards the interface (Jackson, 1975; Born and Wolf, 1980; Kuga *et al.*, 1987), so any model using this hypothesis as its basis will not be able to deal with double scattering. From this point, there are two different approaches to formulating the small perturbation model (Kuga *et al.*, 1987).

Either of the techniques result in the following expressions for the scattering elements for the first-order scattered fields.:

$$
\begin{aligned}
&< S_{HH} S_{HH}^{*} >= k_0^4 \cos^3\theta \left| \frac{\varepsilon - 1}{\left[\varepsilon \cos\theta + \sqrt{\varepsilon - \sin^2\theta}\right]^2} \right|^2 W(2k_0 \sin\theta, 0) \\
&< S_{VV} S_{VV}^{*} >= k_0^4 \cos^3\theta \left| \frac{\left[\varepsilon(1+\sin^2\theta) - \sin^2\theta\right](\varepsilon - 1)}{\left[\varepsilon \cos\theta + \sqrt{\varepsilon - \sin^2\theta}\right]^2} \right|^2 W(2k_0 \sin\theta, 0) \\
&< S_{HH}^{*} S_{VV} >= k_0^4 \cos^3\theta \left\{ \frac{\varepsilon - 1}{\left(\cos\theta + \sqrt{\varepsilon - \sin^2\theta}\right)^2} \right\}^{*} \times \\
&\qquad \left\{ \frac{(\varepsilon - 1)\left[\varepsilon(1+\sin^2\theta) - \sin^2\theta\right]}{\left(\varepsilon \cos\theta + \sqrt{\varepsilon - \sin^2\theta}\right)^2} \right\} W(2k_0 \sin\theta, 0)
\end{aligned}
\qquad \textbf{(4)}
$$

where k_0 is the wavenumber of the incident wave, θ is the incidence angle, and ε is the complex dielectric constant. The function W(p,q) is the power spectrum of the surface which is given by the Fourier transform of the surface. The first-order small perturbation model attributes the scattering to Bragg-type scattering, and it predicts that the linear polarizations are the maximum co-polarized returns for any given orientation angle (ψ) with VV being the strongest and HH the weakest. The predicted cross-polarization signature is a maximum at the circular polarizations and a minimum at the linear polarizations, and the cross-polarization signature is constant at any ellipticity angle (χ).

In order to model the agricultural field with concentric furrows, the power spectrum for a radial sinusoid must be computed. The properties of Fourier transforms in a radial system state that a radially symmetric function has a radially symmetric Fourier transform (Papoulis, 1962), which simplifies the problem to finding a one-dimensional Fourier transform. The form of the Fourier transform for monochromatic sinusoids is well known, and the resulting power spectrum consists of delta functions located at $\pm\omega$, where

ω is the frequency of the sinusoid. However, the Fourier transform of cos(kρ) is not simply an annular delta function at distance k from the origin of the two dimensional wavenumber space, which is what results from rotating the one-dimensional transform of the sinusoid about the origin. The radial sinusoid is actually a band-limited sinusoid, which is zero for negative values, rotated about the origin, so the Fourier transform needed is the Fourier transform for the band-limited sinusoid. The band-limited sine function with wavenumber k_0 has the following Fourier transform:

$$F(\omega) = \frac{\pi}{2i}\left(\delta\,(k - k_0) + \delta\,(k + k_0)\right) + \frac{k_0}{k - k_0} \qquad (5)$$

while the Fourier transform for the cosine is:

$$F(\omega) = \frac{\pi}{2}\left(\delta\,(k - k_0) + \delta\,(k + k_0)\right) + i\frac{k}{k - k_0}. \qquad (6)$$

Flying in a straight line past one of these fields of concentric circles basically means that the incidence angle of the radar on the field is changing. Figure 12 shows how the power returned from a radially symmetric cosine surface with a wavelength twice that of the radar. The smooth curve which decreases as the incidence angle increases is a classic result of Bragg scattering. In figure 13, the result for a radially symmetric cosine surface with a wavelength equal to the radar plotted on the same scale as figure 12. Now a very strong spike is obvious at an incidence angle of 30°. Varying the wavelength of the surface causes this spike to move to larger incidence angles as the wavelength of the surface decreases and to smaller incidence angles as the wavelength of the surface increases. For surface wavelengths longer than 1.4 times the radar wavelength, the response looks similar to figure 12, while surface wavelengths shorter than 0.5 times the

radar wavelength the response curve looks like figure 14. This large spike in backscattered power would lead to bright spokes like those in the L-band radar images (figure 7b and plate 11).

Why does the result in figure 12 occur? The reason can be seen in equation (2) which gives the Bragg resonance criteria. In this case, the scale of the scatter and the radar wavelength are the same. Notice that the sine of 30° is 0.5, so the incidence angle of 30° leads to the fundamental (n=1) Bragg resonance for a surface with undulations of scale equal to that of the radar. The strong return spike is simply Bragg resonance.

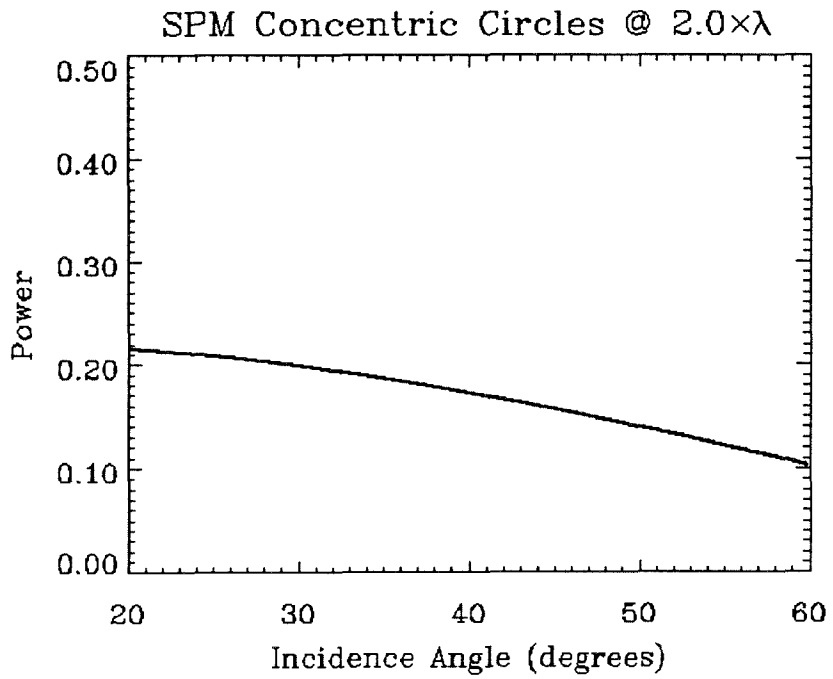

Figure 12: The total power response predicted by the first-order small perturbation model from a surface with a radially sinusoidal undulation with a wavelength twice of the radar plotted against incidence angle in degrees. The surface has a dielectric constant of 2.0.

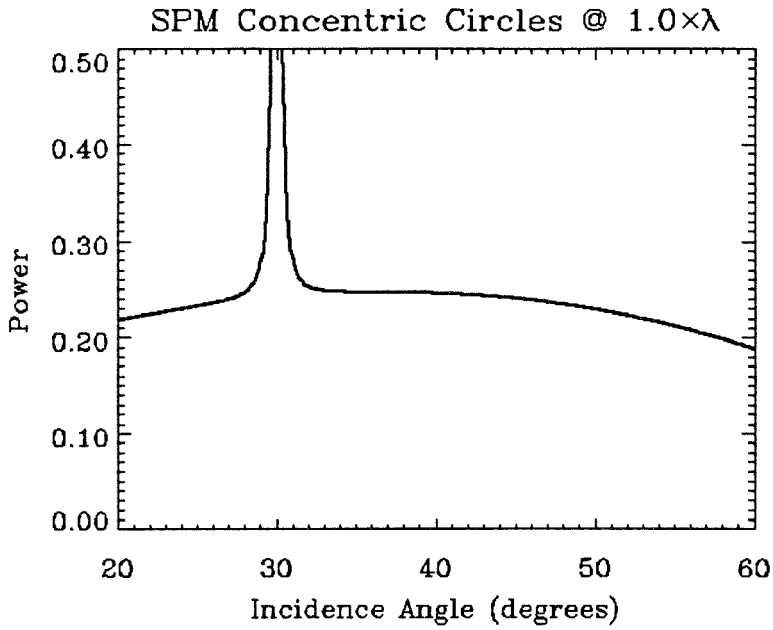

Figure 13: The total power response predicted by the first-order small perturbation model from a surface with a radially sinusoidal undulation with a wavelength equal to that of the radar plotted against incidence angle in degrees. Notice the strong return driven by Bragg resonance at and incidence angle of 30°.

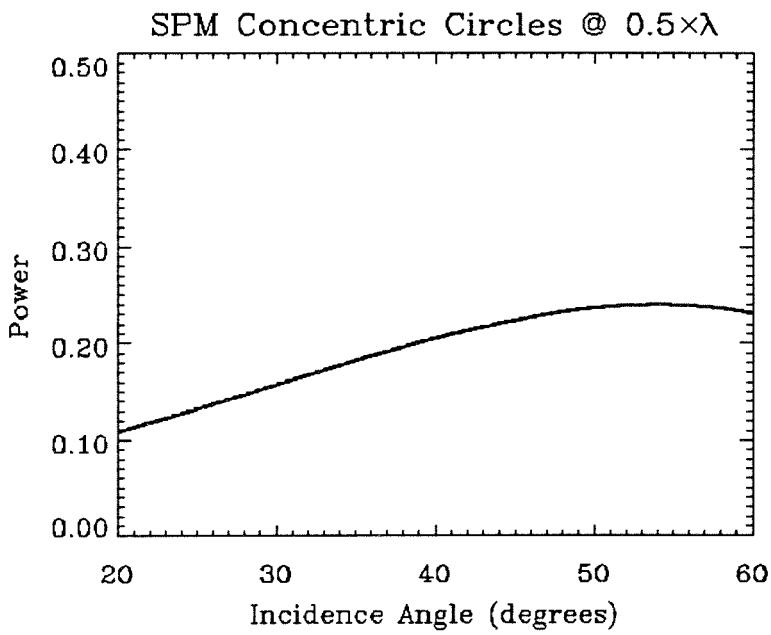

Figure 14: The total power response predicted by the first-order small perturbation model from a surface with a radially sinusoidal undulation with a wavelength twice of the radar plotted against incidence angle in degrees. Notice that the weakest returns occur at near-normal incidence and the strongest ones occur at the largest incidence angles.

There are problems with the small perturbation model of these surfaces as well. The small perturbation model expects that the slopes of the surface be small with respect to the radar wavelength (van Zyl *et al.*, 1987b), which is not true when the surface wavelength is smaller than about twice that of the radar. Also, the variations in surface height must be smaller than about 0.1 times the radar wavelength, and the undulations that occur due to these planting furrows are on the order of 2 cm, which is close to the limit of this criterion.

Part 3.4.3: *Conclusions*

Although both of the scattering models discussed above have significant problems, an important conclusion about the two bright spokes which are not parallel to the look direction can still be made. These spokes can only arise when there are concentric undulations which have a wavelength very similar to the wavelength of the radar. An estimate of the wavelength undulations can be made by using the orientation of the spokes.

From the incidence angle of the center of the field at the closest approach of the platform (36°) and the altitude of the instrument (7826 m) the perpendicular distance from the radar flight line to the center of the field can be found (5686 m). The orientation of the bright spokes is about 45° from the look direction, which make the incidence angle when the spokes were observed 45.8°. Substituting this result into the equation for Bragg resonance with the radar wavelength on 24 cm the wavelength of the surface undulations is found to be 16.7 cm, which is consistent with the spacing of the furrows on active fields in the area.

A consequence of the above results is the fact that fields any closer to the AIRSAR flight line will have spokes open at broader angles than the 46.8° indicated above, which will probably place them outside the radar beam. The small circular field directly north of the field with the spokes may also fall outside the radar beam before the required angle is reached. The Pacman-shaped field just northwest of the field with the spokes is a more serious problem. According to the calculation from the field with the spokes, bright spokes would be expected on this field at 38° from the look direction. The absence of spokes may be due to the alfalfa on that field being higher and wetter which would prevent the L-band signal from penetrating the canopy. The Pacman-shaped field is brighter in the L-band overall than the other active fields in the image. It is possible that the field was irrigated more recently than the other fields, which would make the canopy wetter and prevent radar penetration.

Part 3.5: *A Lasting Impression*

The AIRSAR data also reveal that the marks made by human activity persist for many years after the human activity ceases. Many of the abandoned fields have the single bright diameter parallel to the radar look direction. These are also caused by specular reflection from the ruts caused by the irrigation systems. The ruts are nearly 5 cm deep and 15 cm wide, and formed of heavily packed dirt. This makes them a very persistent feature of the surface which cannot be removed without a good deal of reworking of the abandoned field surface. This means that the fields which lack the spokes have

experienced erosion, deposition or both to sufficient to eradicate the ruts. This provides a measure of the degree to which the surface has been eroded and may give an indication of the length of time the field has been abandoned.

Surprisingly, the concentric pattern of the planting furrows can also survive for at least 6 years after the abandonment of the field. Consider figure 35, which is a ground level photograph of the abandoned field located immediately northeast of the Pacman-shaped field taken on October 15, 1992. The plant in this photograph is the small, yellow desert grass which is ubiquitous in the study area. As clearly shown in the photograph, the desert grass is growing in concentric circles, just like the alfalfa on the actively irrigated fields. The L-band images (figure 7b and plate 11) do not show the bright spokes caused by Bragg resonance from the concentric furrows. This may be due to the undulations of the field surface actually being smaller than when the field was being cultivated, and the fact that the grass is a much drier plan than irrigated alfalfa may also weaken the signal. On the other hand, the small perturbation model results were based on a dielectric constant $\varepsilon = 2.0 + 0.0i$ for the surface which represents a dry soil.

Another reason for the absence of the spokes on this field is the fact that the field looked more like figure 16, which was taken on April 13, 1991. The photograph still shows a concentric circle habit for the desert plants, but they are much more sparse. Additionally, in-situ examination of the field surface showed that there were only broken segments of circles and not completely intact concentric undulations. This corroborates with the above suggestion that the surface undulations were too small to be seen by the

Figure 15: Ground level photograph of recently abandoned field taken October 15, 1992. Notice the desert grass growing in concentric circles like cultivation furrows.

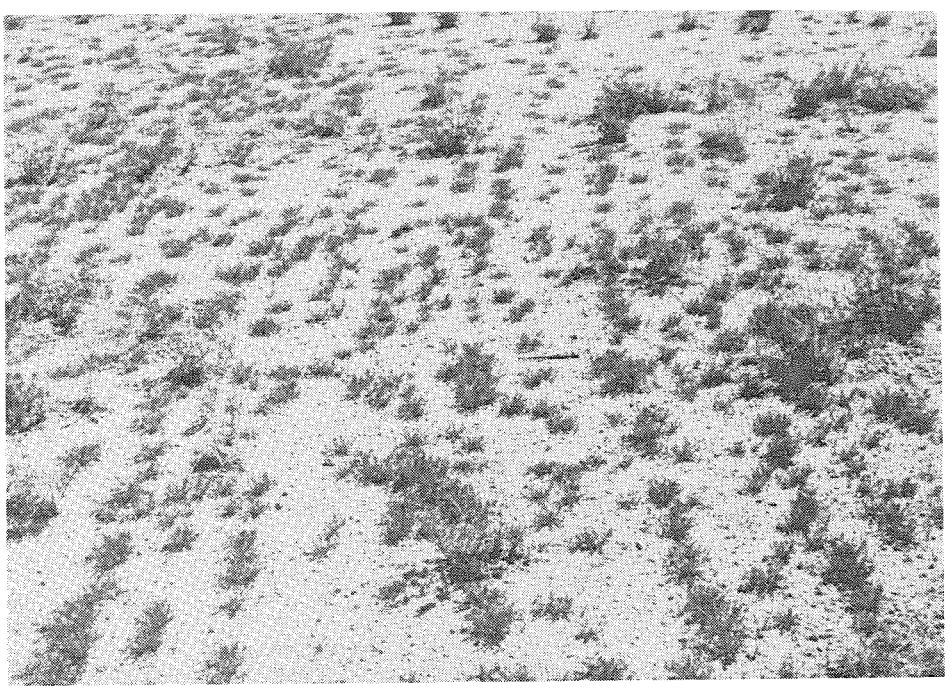

Figure 16: Photograph of same field as in figure 15 taken April 13, 1991. Note that the field is considerably more barren than shown in figure 15 even though a concentric habit of plant growth is visible. Notice also the large amount of dead plant material on the field.

radar. The small desert grass itself is almost certainly too small and dry to provide much L-band return.

This growth of the wild desert plants in the concentric circles may be due to several factors. First, when the field is abandoned, the alfalfa stubble remains standing in concentric circles which may help to trap the seeds from desert plants in concentric circular rows. Second, the undulations in the surface due to cultivation may provide the same trapping effect, and the furrows may help channel water to where the seeds are concentrated. Third, there are likely to be chemicals which can help plant growth where the original alfalfa plants had been growing. The decaying deep root systems of the alfalfa would release important nutrients for the use of wild desert plants, and alfalfa is a plant which adds fixed nitrogen to the soil through the symbiotic bacteria which grow on the roots of the alfalfa. These factors attribute to the persistence of human scratches on the Earth's surface for several years after the humans have stopped actively using the area.

Chapter 4: *A Snapshot of Abandonment*

The sequence of abandoned fields in the Manix Basin Area provides the opportunity to observe fields in various stages of degradation each time a remote sensing instrument collects data over the area. Chapter 3 showed how scratching by humans on the Earth's surface can be detected and characterized with a snapshot of data covering the area. This chapter shows how these snapshots of abandonment provide a view of land degradation showing that abandoned fields are experiencing continued land degradation, primarily due to wind erosion, even after human activity has been suspended. There is also evidence of land degradation in the form of wind erosion from active fields. These snapshots of degradation also show the close tie between wind erosion and vegetation cover.

Part 4.1: *Introduction*

The abandonment of center-pivot irrigation systems in the Manix Basin began in 1972, according to local residents of the area.[†] Use of the temporal Landsat MSS dataset discussed in Chapter 6 allowed confirmation of some of the dates given by local residents and corrected others. In one case, a field reported as abandoned in 1978 by one local resident and in 1982 by another, was shown by the MSS images to be uncultivated during 1979 and 1980, cultivated over the period 1981–1983, and then abandoned, explaining the four-year discrepancy between the local residents' reports. In another case, three

[†] However, in some cases two different dates of abandonment were reported for certain fields.

neighboring fields belonging to the same owner were reported by the local residents as having been abandoned in 1984, but the MSS data revealed that one of the three fields was recultivated in 1988.

Figure 17 is a sketch map showing the arrangement and relative locations of the abandoned center-pivot irrigation in the study area. Three active center-pivot fields are also shown, including the Pacman-shaped field, which provides a good point for orientation due to its unique shape. The fields are labeled with numbers which will be used to refer to the fields in the text. The last year that the field was observed to be active in MSS imagery is also listed for each field.

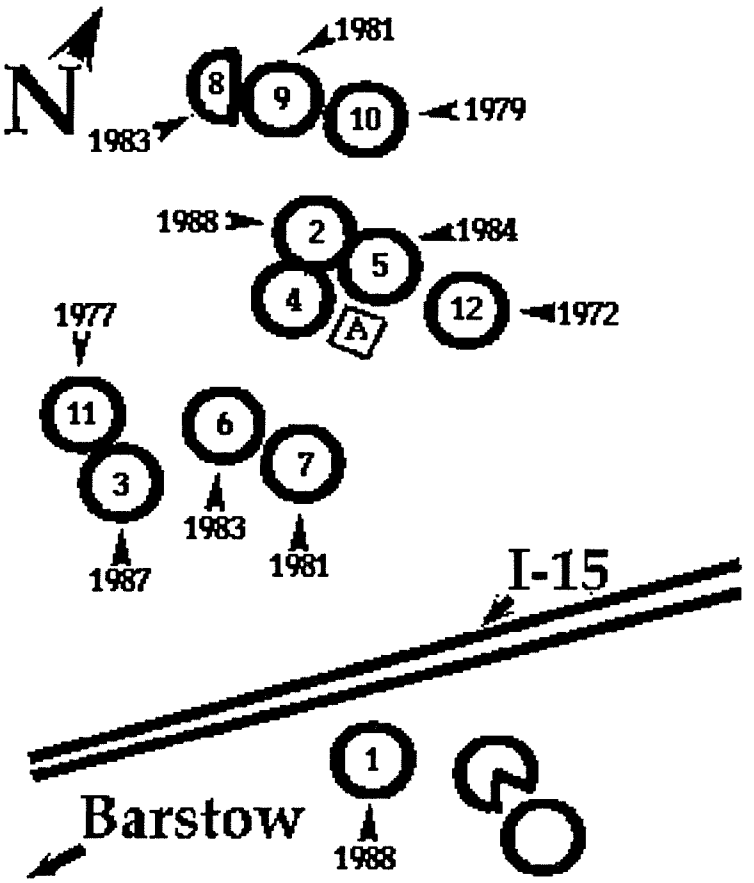

Figure 17: Sketch map showing relative locations and arrangement of abandoned center-pivot fields in the primary study area. The numbers on each field will be used to refer to the fields in the text. The year given for each field is the last year in which the field is observed to be active in Landsat MSS images.

The varying times at which each field was abandoned means that any observation of the area provides a look at abandoned field in different stages of evolution. This provides a way to do temporal analyses with data collected by an instrument that can only be flown over a study area occasionally or once. However, there are differences between the individual fields which may cause them to evolve differently, and this adds some complication to performing temporal analysis from a single look at this area. In this chapter we will use data collected from single AIRSAR and AVIRIS flights to look for evidence of degradation, and use the semi-temporal nature of the data to establish temporal trends.

Part 4.2: *The Radar View*

[Many of the results of this section were originally presented in Ray *et al.*, 1991; Ray *et al.*, 1992a, Ray *et al.*, 1992b; and Ray and van Zyl, 1994]

Part 4.2.1: *Introduction*

Chapter 3 showed how roughness produced by human cultivation can be detected by using radar, and suggested that the destruction of human scratches on the land's surface could potentially be used to measure the degree to which natural processes had modified the surface. Vegetation provides much of the roughness seen by radar on many natural surfaces, so radar data will reveal changes in the surface roughness caused by changes in vegetation cover. Erosion of the surface will also alter the roughness seen by radar, and the creation of rippled surfaces by wind erosion produces unusual signatures in AIRSAR data which can be used to detect their presence even though their scale is far below the pixel resolution of the radar.

An examination of plates 9–12 and figure 7 shows that the abandoned fields are generally "darker" and therefore smoother than the surrounding desert. This is indicated by the fact that the abandoned fields are darker than the surrounding desert. Recall that the backscattered energy detected by radar is generally proportional to the roughness of the surface being imaged at scales close to the wavelength of the radar. Plates 9–12 show that the fields are smooth in all three of the AIRSAR wavelengths and at all three of HH, VV and HV polarizations. The P-band data was so badly corrupted by the strong interference that more-analysis of the data proved futile.

More sophisticated techniques to determine both the degree and nature of surface roughness are available using the AIRSAR data because of the polarimetric nature of the instrument. The polarimetric capabilities of AIRSAR provide a great deal of information for each pixel, and this immediately leads to the problem of displaying this new wealth of information. One solution to this for polarimetric radar is the "polarization signature" (van Zyl, 1985; van Zyl *et al.*, 1987b; Zebker *et al.*, 1987b) which is a graphical representation of the variation of scattering cross section as a function of polarization. Figure 18a & b shows the co-polarization and cross-polarization signatures for the response of a large conducting sphere (or for a conducting trihedral corner reflector illuminated along its boresight, which has an identical polarization signature). The scattering cross section, σ, is normalized as indicated in the figure. Figure 18c shows a top-down view of the two axes defining the base of the polarization signature. The point where the orientation angle, ψ, is 180° and the ellipticity angle, χ, is -45° is the corner

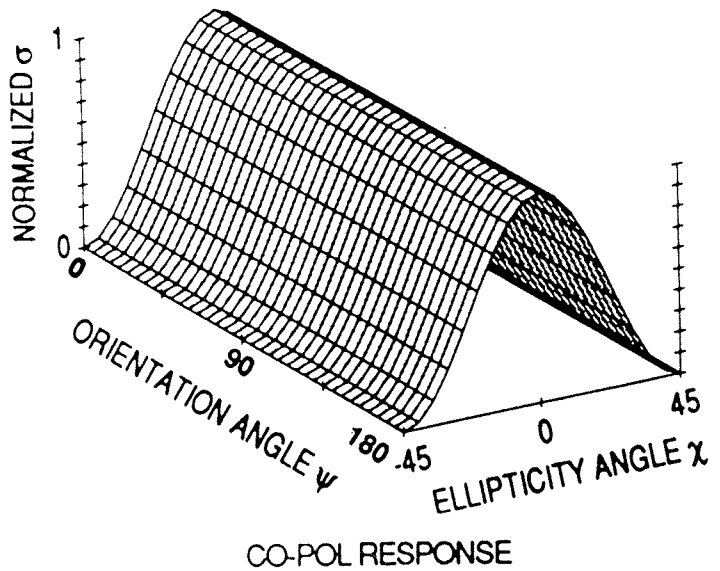

a)

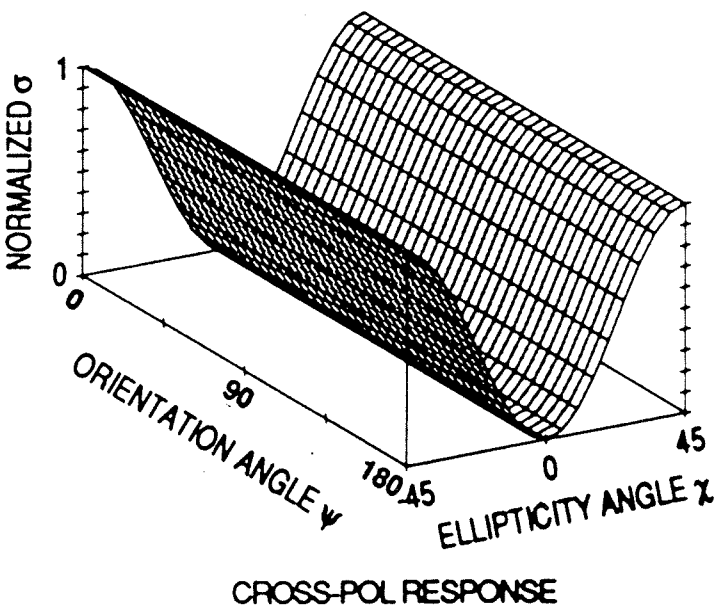

b)

Figure 18: The basics of polarization signatures. **a)** The co-polarization signature for a large conducting sphere. Note how the edges of the polarization signature actually touch the base. **b)** The cross-polarization signature for a large conducting sphere. The central minimum of the cross-polarization signature touches the base of the signature. The scattering cross-section is always normalized to be equal to 1.0 in these polarization signatures. (See Appendix E for more on polarization signatures.)

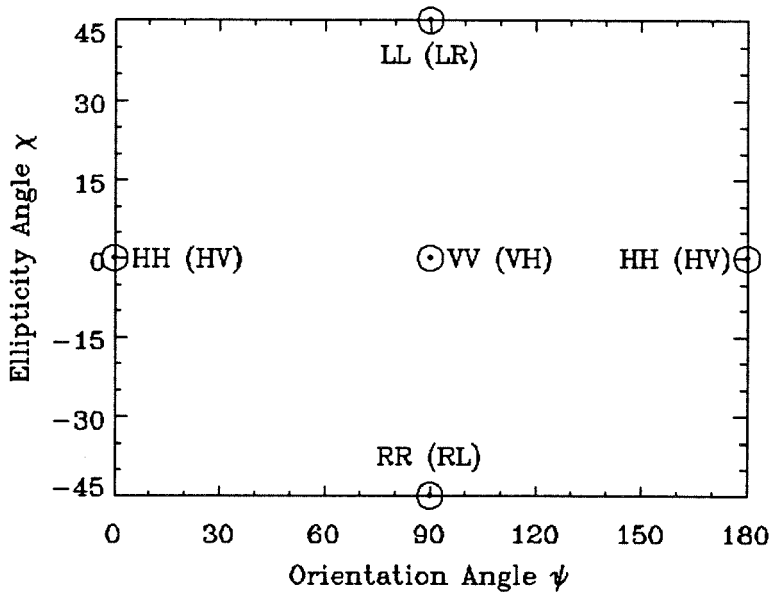

c)

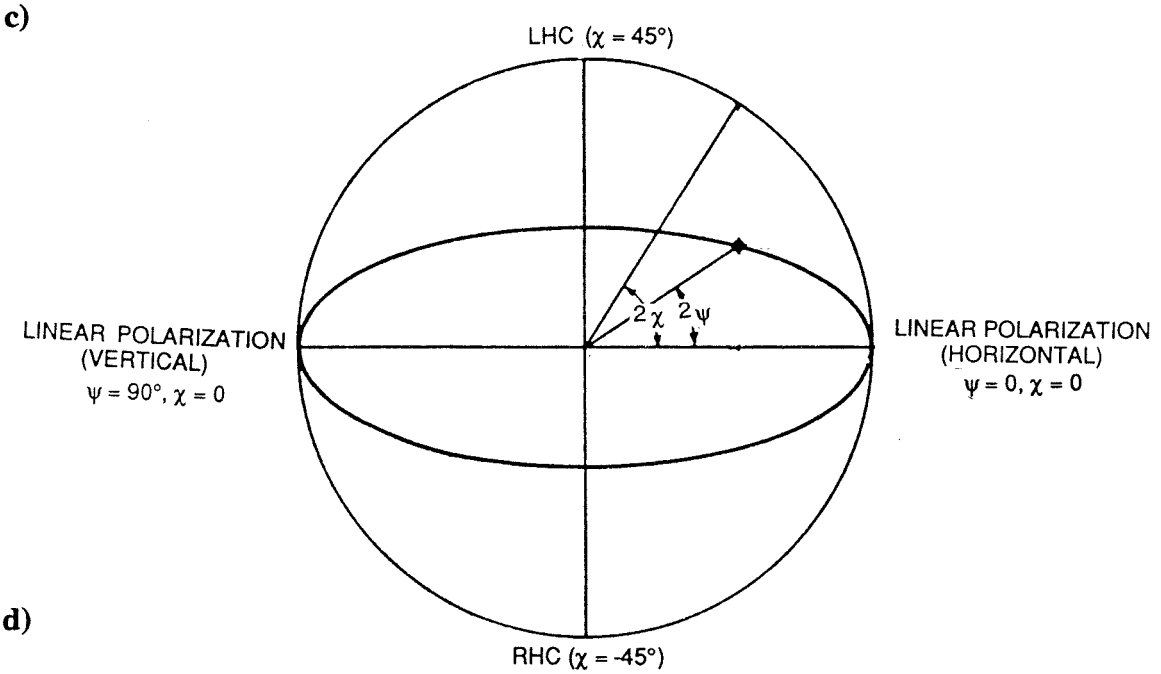

d)

Figure 18: The basics of polarization signatures. **c)** The ψ and χ axes which define the base of the polarization signatures, along with significant locations of co-polarizations and (cross-polarizations). H is horizontal polarization, V is vertical, R is right-hand circular, and L is left-hand circular. The first letter is the transmit polarization and the second letter is the receive polarization. **d)** The Poincaré sphere. The circular polarization edges (χ=±45°) of the polarization signature degenerate into the north and south poles, and the two edges defining horizontal polarizations (ψ=0° and 180°) form a single line on the sphere. (See Appendix E for more on polarization signatures.)

nearest the view in the perspective views. The points at which some interesting polarizations are located in the polarization signatures are indicated in figure 18c with the cross-polarized values in parenthesis, and it should be noted that the location at which the scattering cross section is plotted is the point defined by the transmitted polarization. A further important thing to bear in mind is shown in figure 18d. The sphere shows that the two edges where the circular polarizations are plotted are actually the north and south poles of the Poincaré sphere. Furthermore, the edges of the polarization signature where ψ=0° and 180° form a single line on the sphere.

In the case of the polarization signatures displayed in figure 18, note that the polarization signature "rests" on the base formed by the χ and ψ axes which means that the minimum co-polarized scattering cross section is zero. The deepest point in the "trough" of the cross-polarized signature indicates that the minimum value of the cross-polarization scattering cross section is also zero. The scattering from all simple targets (van Zyl and Ulaby, 1987) as predicted by the simple scattering models for rough surfaces, such as the first-order small perturbation model (Kuga *et al.*, 1987), predict that the minimum value in each polarization signature will be zero.

The ratio of the minimum value of the scattering cross section to the maximum value is known as the "coefficient of variation" (van Zyl *et al.*, 1987b). When there is more than one type of scatterer in a given pixel, the polarization signature of the pixel will be the sum of the polarization signatures of the individual scatterers (van Zyl *et al.*, 1987b). Unless all of the scatterers have at least some minima in the same locations, the minimum of the resulting polarization signature will not be zero. In this case, the

coefficient of variation will be greater than zero. This non-zero minimum of the polarization signature means that the polarization signature does not touch the $\chi-\psi$ base and the entire signature seems to sit on a "pedestal," and the coefficient of variation is sometimes referred to as the "pedestal height" (van Zyl *et al.*, 1987b; Zebker *et al.*, 1987b). Multiple scattering will also increase the pedestal height for a given pixel (van Zyl *et al.*, 1987b; Zebker *et al.*, 1987b), and, since rougher surfaces tend to produce more multiple scattering, this means that the pedestal height can serve as a measurement of the roughness of the surface. Pedestal height is the parameter most useful for the analysis here. It should be noted that multiple scattering of waves penetrating into a partially transparent medium, such as a dry sand, will also contribute to the "roughness" seen by the pedestal height.

Figures 19 and 20 are plots of the C- and L-band pedestal heights on the abandoned fields versus the number of years since the field was last irrigated (also called the "length of abandonment"). There does not appear to be any relationship between the pedestal height and the length of abandonment for each field. However, pedestal height is sensitive to the incidence angle of the radar effect (van Zyl *et al.*, 1987b; Zebker *et al.*, 1987b), so it is more appropriate to compare pedestal heights for fields at similar incidence angles. The variance in pedestal height seen in figures 19 and 20 (and also 21 and 22) are due to "speckle," which is caused by random constructive and destructive interference of the coherent radar waves.

Figures 21 and 22 show the results when fields are grouped with fields of similar incidence angle. In figure 21, the fields at approximately 57° incidence, show a trend of

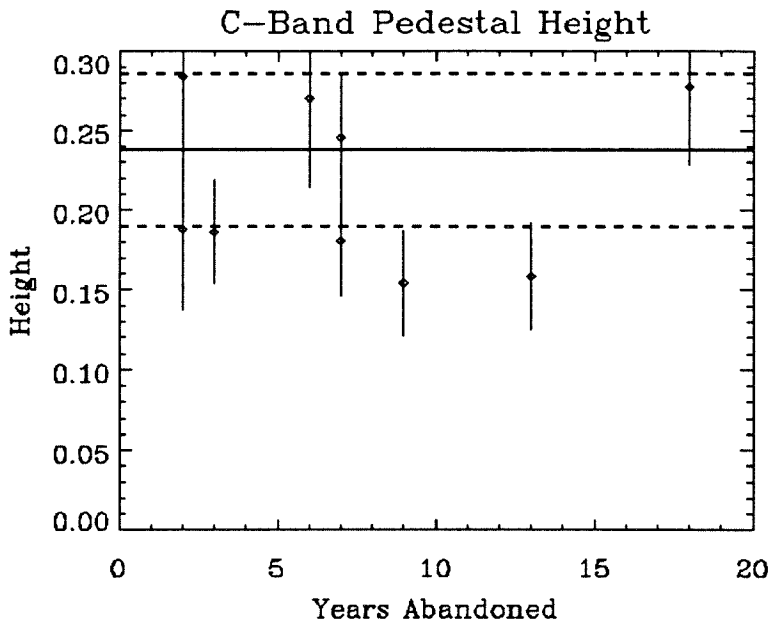

Figure 19: Plot of C-band pedestal height (ratio of the maximum co-polarized backscatter to the minimum co-polarized backscatter) for abandoned fields as a function of the number of years since last irrigation. The bars show 1σ variance. The solid line is the mean value for areas of the desert which are not near active or abandoned fields, and the two dotted lines show 1σ variance from the desert mean.

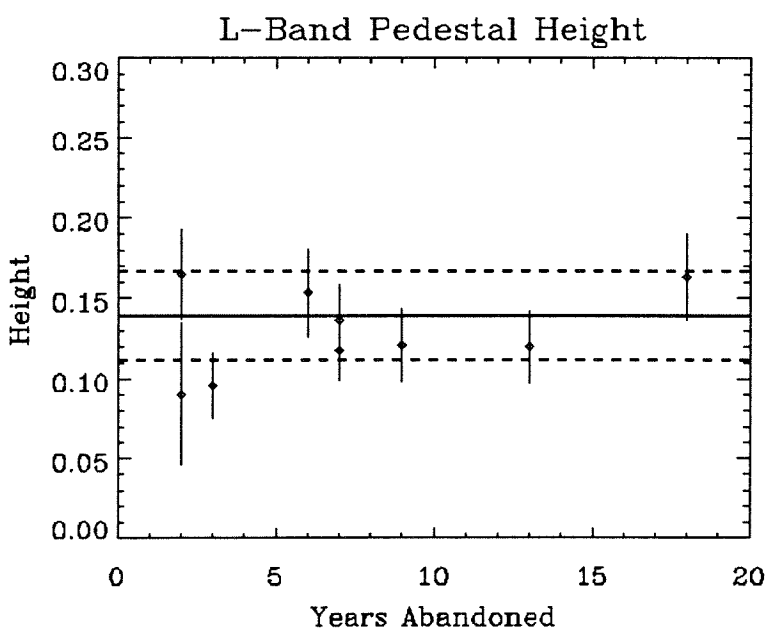

Figure 20: Plot of L-band pedestal height (ratio of the maximum co-polarized backscatter to the minimum co-polarized backscatter) for abandoned fields as a function of the number of years since last irrigation. The bars show 1σ variance. The solid line is the mean value for areas of the desert which are not near active or abandoned fields, and the two dotted lines show 1σ variance from the desert mean.

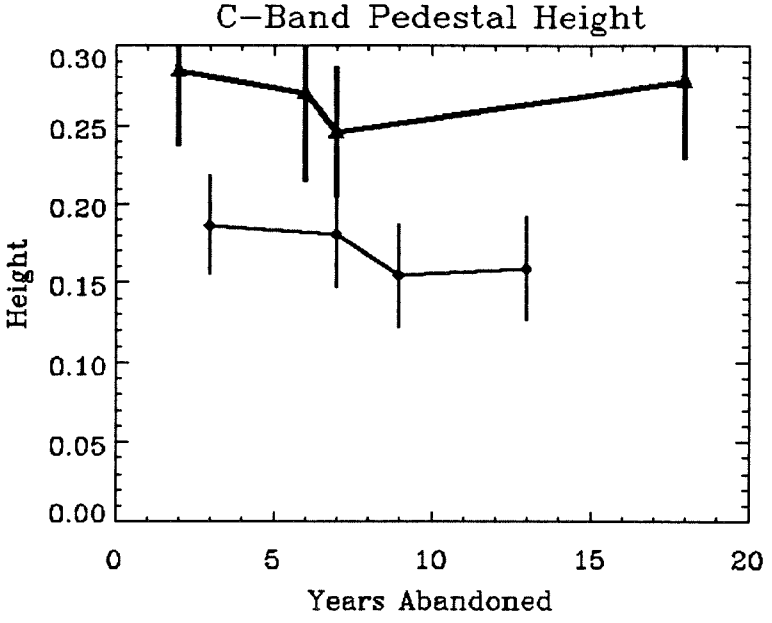

Figure 21: Plot of C-band pedestal height (ratio of the maximum co-polarized backscatter to the minimum co-polarized backscatter) as a function of number of years since last irrigation for fields at similar incidence angles. The bars show 1σ variance. The thick line is for fields located at 57° incidence (fields 2, 4, 5, and 12), and the thin line is for fields located at 52° incidence (fields 2, 6, 7, 11).

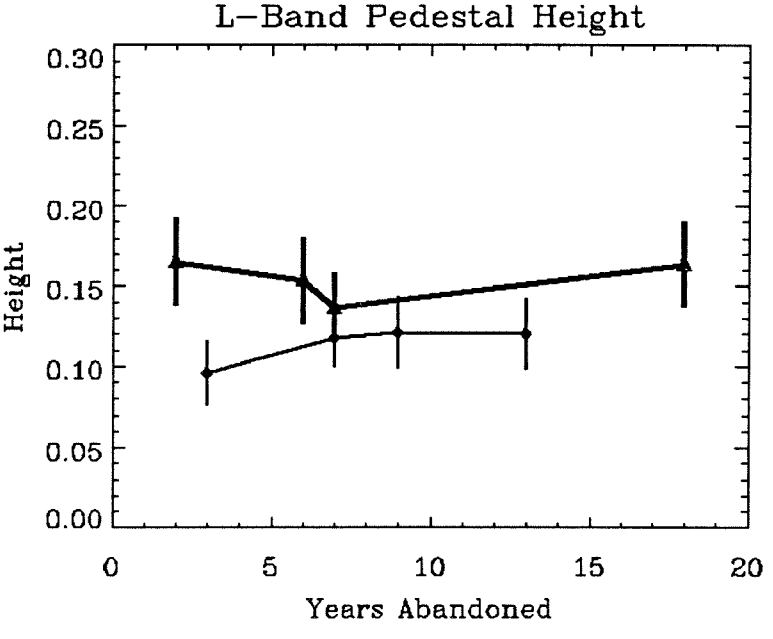

Figure 22: Plot of L-band normalized pedestal height (ratio of the maximum co-polarized backscatter to the minimum co-polarized backscatter) for abandoned fields as a function of the number of years since last irrigation. The bars show 1σ variance. The thick line is for fields located at 57° incidence (fields 2, 4, 5, and 12), and the thin line is for fields located at 52° incidence (fields 2, 6, 7, 11).

initially decreasing C-band pedestal height with increasing length of abandonment, and this trend also occurs for the fields at 52° incidence. The initial decrease in pedestal height is followed in both cases by an increase in the pedestal height. These changes of pedestal height suggests that the fields get smoother at the C-band (5.7 cm) scale during the first decade after the field's abandonment, and that this is then followed by increasing roughness. The initial decrease in roughness is probably due to a general decrease in the amount of small vegetation, like the dry desert grass which occurs in this area, growing on the field as the length of abandonment increases. The increase in roughness after the initial smoothing may be due to either a later increase in vegetation cover or increasing surface roughness produced by wind erosion from a nearly vegetationless surface.

The L-Band pedestal heights in figure 22 show similar but slightly different trends. The fields at 57° incidence (thick line) have a nearly identical trend in the L-band as in the C-Band. However, the fields at 52° show a monotonic increase in pedestal height with increasing length of time abandoned. The trend for the fields at 57° incidence is consistent with the interpretation from the C-Band, but something different is clearly happening on the fields at 52° incidence. The youngest three fields in the group at 57° incidence are protected from wind erosion by a shelter belt of trees. By contrast, the fields at 52° incidence have no such protection.

The pedestal height data suggest a smoothing of the abandoned fields at the C-band scale (5.7 cm) over time as vegetation cover on the surface decreases. After the first decade of abandonment, either wind erosion or an increase in the vegetation cover of the fields causes an increase in small-scale roughness. The 24 cm roughness seems to be

dominated by wind erosion, with unprotected fields immediately increasing in roughness from wind erosion after abandonment. Protected fields initially get smoother from the loss of vegetation cover, and wind erosion eventually causes an increase in roughness. The speckle noise in the radar images accounts for much of the variance shown in figures 19-22, and it is very constant across fields at similar incidence angles, so the trends in these figures are probably real and significant. Also, figures 21 and 22 clearly show that the pedestal height is dependent on the incidence angle, with the fields at 57° incidence having consistently large pedestal heights than those at 52° incidence.

Part 4.2.2: *The Polarization Shift*

Although the pedestal height data discussed in the previous section provide a measure of the degree of surface roughness, those data do not provide information on the nature of the roughness. However, the polarimetric information collected by AIRSAR does provide information on the nature of the surface roughness. We will now see that the polarimetric radar data can characterize the nature of the roughness so that features produced by wind erosion, which are an order of magnitude smaller in scale than the pixel resolution, can be inferred. In figure 23 three L-band polarization signatures of the background desert are shown. The top signature was extracted from an area of the desert near 40° incidence, the middle signature from near 50° incidence, and the bottom signature is from the alluvial fan in the northeast part of the study area at an incidence angle of 55°. The strongest return in the co-polarized signature is near VV polarization, which places it

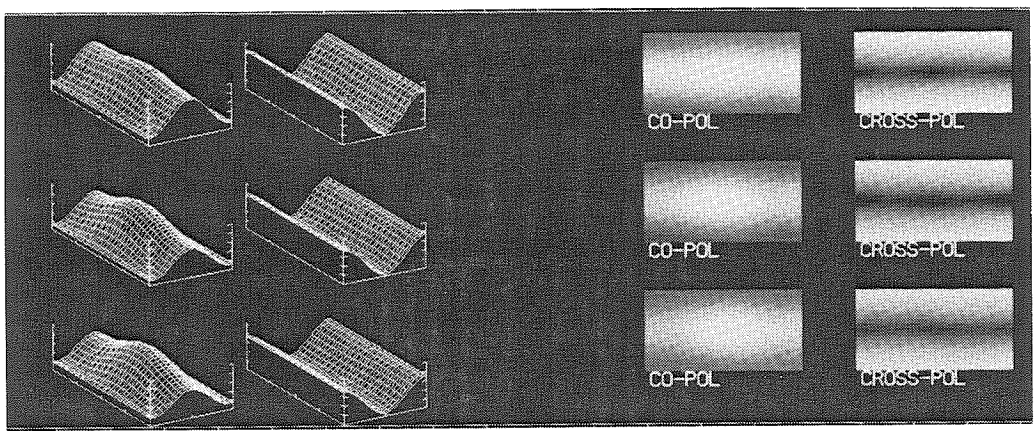

Figure 23: Three L-band polarization signatures of the background desert. The top signature is from a region of desert at 40° incidence and the middle signature is from an area of desert at 50°. The bottom signature is from the alluvial fan in the northeast part of the study area at an incidence angle at 55°. Note that the maximum of the co-polarization signatures are all near VV polarization at the center of the co-polarization signatures.

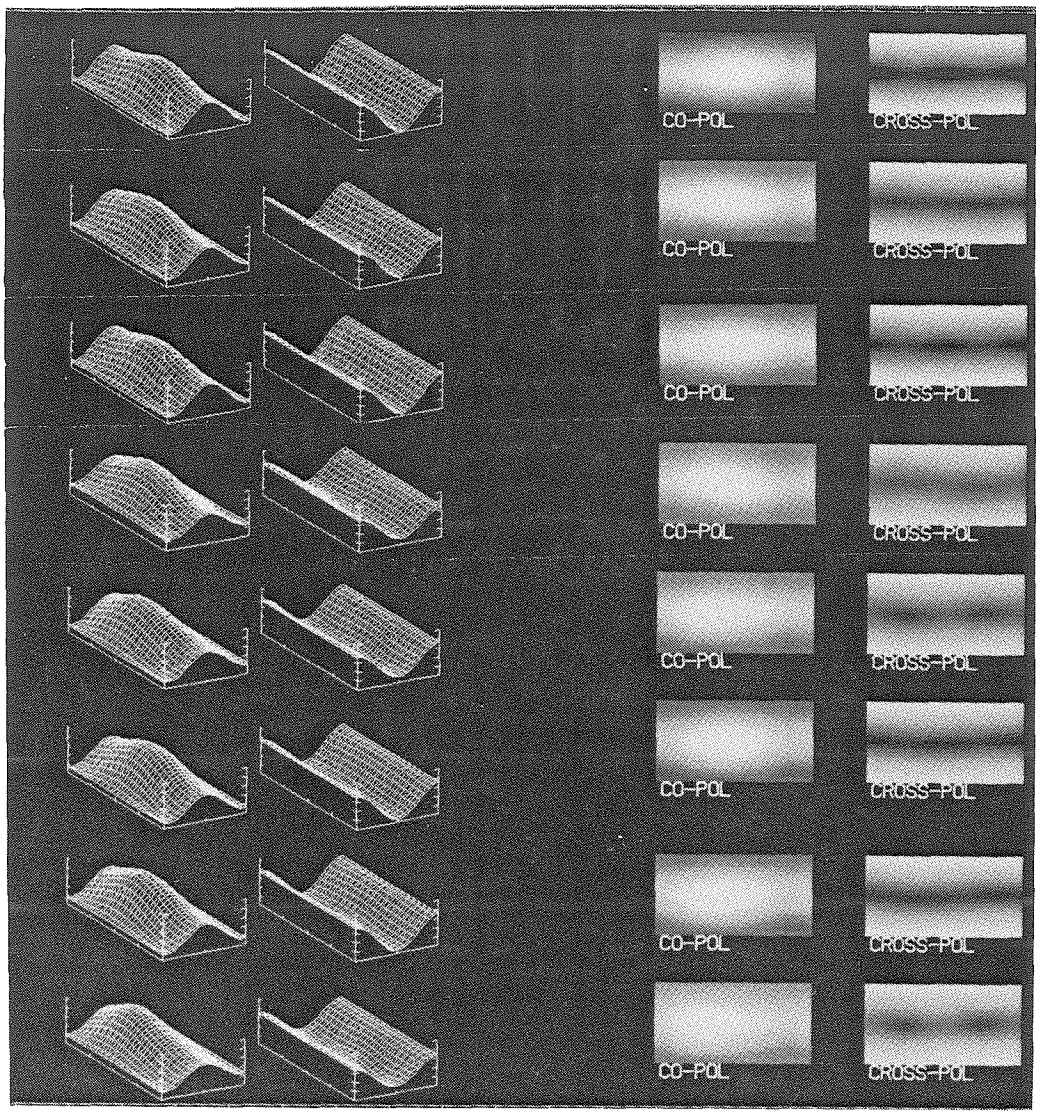

Figure 24: Polarization signatures for abandoned fields in the Manix Basin study area. The signatures are arranged from the most recently abandoned field at the top to the oldest abandoned field at the bottom. Note the strong leftward shift of the maximum co-polarization peak in some of the signatures. There seems to be a weak trend of increasing leftward shift with increasing time of abandonment.

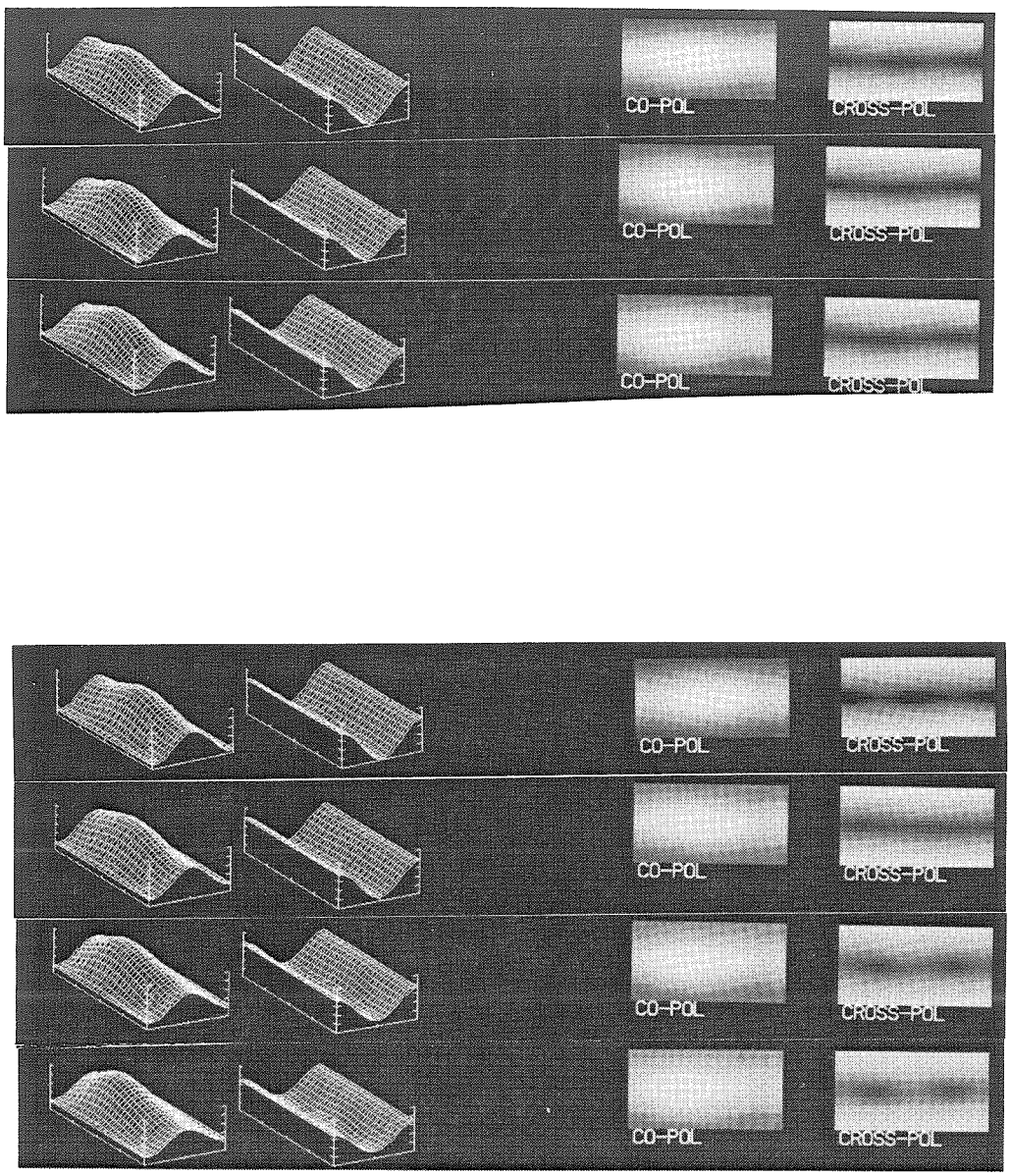

Figure 25: Polarization signatures for abandoned fields arranged in groups of fields with similar incidence angles. The fields are arranged from most recently abandoned at the top of each group to the longest abandoned at the bottom of each group. The top group is a set of 3 fields at 52° incidence (fields 3, 6, and 11), and the bottom group is a set of 4 fields at 57° incidence (fields 2, 4, 5, and 12). Note that there is a slight trend of increasing leftward shift with increasing length of time abandoned.

near the center of the polarization signature. The polarization signature from the alluvial fan has its maximum slightly to the right of VV (towards larger values of ψ)on the co-polarization signature, but the maximum is still quite close to VV. The polarization characteristics of the natural desert is therefore normal, which is not the case for the abandoned fields.

In figure 24, the L-band polarization signatures for several abandoned fields in the Manix Basin area are shown. The signatures are arranged from the most recently abandoned field at the top to the one abandoned for the greatest length of time at the bottom. The brightest spot in each signature shows the location of the maximum co-polarized backscatter. Notice that many of the fields have the bright peak of maximums shifted to the left in the co-polarization signatures. There is no definite trend with respect to increasing time of abandonment, but there is a hint of a trend of greater peak shift with increasing age for the abandoned fields.

The earlier experience with the pedestal height suggests that there may be a dependence on incidence angle for the peak location in the polarization signatures. Indeed, figure 23 showed a slight rightward shift in the polarization signature at 55°. In order to examine this possibility, in figure 25 the fields are grouped in sets at similar incidence angle. Here, there still seems to be weak trends of a leftward shift in the maximum co-polarized return as the length of time that the field was abandoned increases.

Close examination of the polarization signatures in figures 24 and 25 shows another intriguing feature. The co-polarized left-hand circular return is larger than the co-polarized right-hand circular return in those signatures showing the greatest amount of

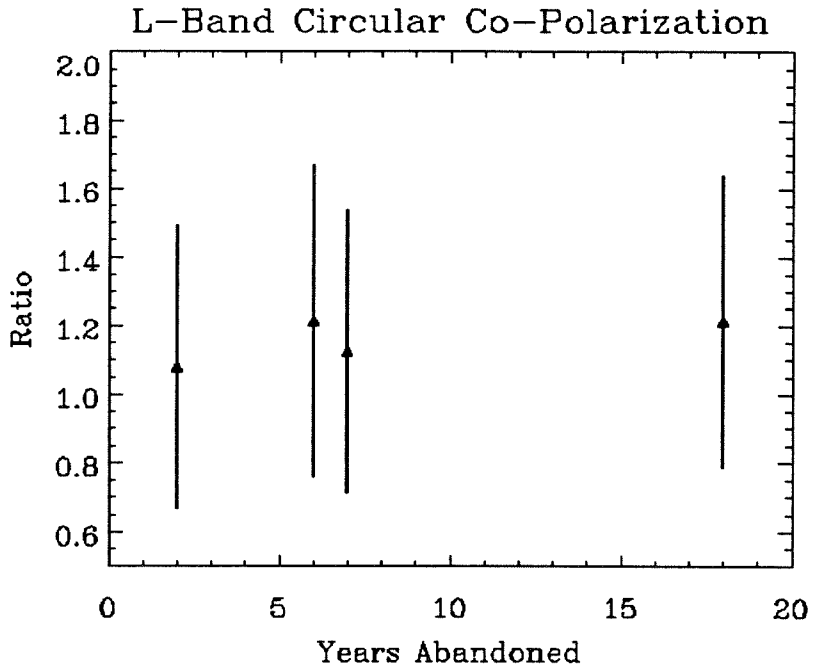

a)

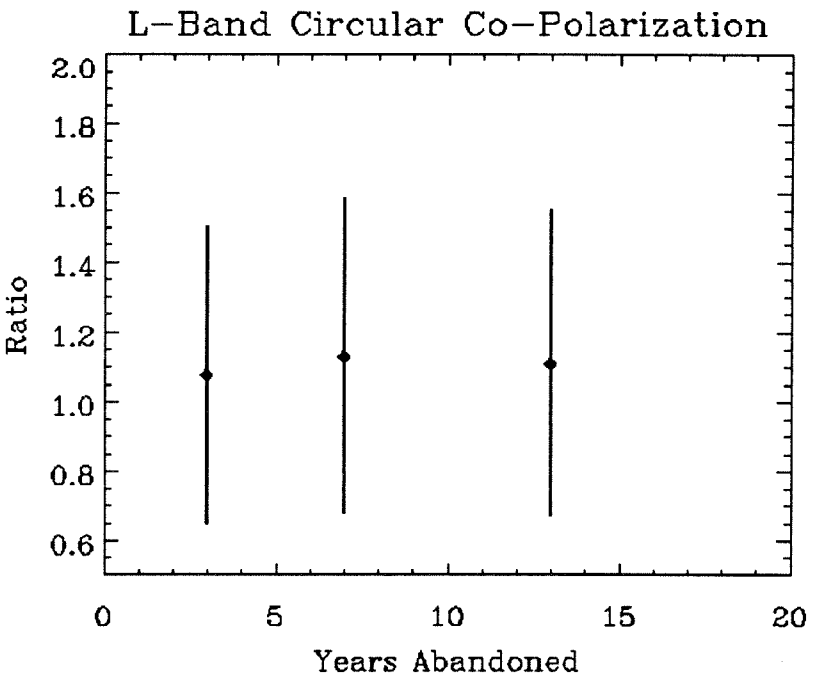

b)

Figure 26: Plots of the ratio of LL polarization to RR polarization as a function of length of time abandoned for fields grouped by incidence angle. Bars show 1σ variance. **a)** Fields at 57° incidence (fields 2, 4, 5, and 12). **b)** Fields at 52° (fields 3, 6, 11). Note the trend of an increase in this ratio as the number of years abandoned increases.

leftward shift in the location of the maximum return. Figure 52 is a plot of the ratio of co-polarized left-hand circular (LL) to co-polarized right-hand circular (RR) as a function of the number of years the field has been abandoned with the fields grouped with other fields at a similar incidence angle. There is a trend of an increase in this ratio as the number of years that the field has been abandoned.

Neither of these results is predicted by simple scattering models such as geometric optics, physical optics and the first-order small perturbation model. All of these simple models predict either equal return in all linear polarizations or a maximum return at VV polarization, and all of these models predict equal (and zero) values of the cross-polarized circular returns. Significantly, a common feature of these models is an assumption that the surface being modeled has an isotropic roughness where the same power spectrum gives a statistical representation of the roughness along any straight path taken from any point on the surface. This suggests that the surface required to produce such polarization signatures must exhibit anisotropic roughness. An alternative possibility is that all of the plant stems present on the surface are tipped at a certain angle or at least all to the same side. The co-polarized return for a short thin dielectric cylinder has its maximum at angle equal to the angle at which the cylinder is tilted in the plane perpendicular to the propagation direction of the radar. For a typical natural surface normally the dielectric cylinders (plant stems) are randomly oriented so that some tip to the right of vertical and some tip to the left. All of the cylinders have a vertical component and all of the horizontal components cancel, which results in a maximum return at VV polarization.

Part 4.2.3: *Wind Ripples*

The question of whether an anisotropically rough surface or a preferred orientation in the twigs and blades of grass is present on the fields showing the strong polarization shift can only be answered by in-situ investigations. Observations of plants in alpine tundra and other harsh environments with strong prevailing winds shows that plants in such environments will often hold twigs, branches, and stems pointing downwind. As discussed previously, the Manix Basin area does experience strong winds blowing from the west, so there might be some tendency for twigs and grass blades to point eastward rather than westward. If the resultant vector of the twigs and grass blades were a vector with an eastward component, the resulting co-polarization signature would tend to have the maximum shifted to the left as shown in the polarization signatures above.

An early survey of the area performed in November 1990 before completely processed data were available gave little evidence of a preferred orientation of plant twigs and grass blades. However, there was a considerable amount of evidence for wind erosion from several fields. The road passing between fields 8 and 9 was sufficiently drifted with sand to require the use of four-wheel drive on the field vehicle. Several residents pointed out other areas where sand had blown and drifted off of abandoned fields. Finally, the surfaces of several fields were observed to be covered by wind ripples.

Wind ripples clearly meet the requirement for anisotropic roughness discussed previously. A path orthogonal to the linear crests and furrows of the wind ripples will have a roughness described by a different power spectrum than the roughness seen along a path parallel to the crests and furrows. The action of wind blowing across a sandy surface

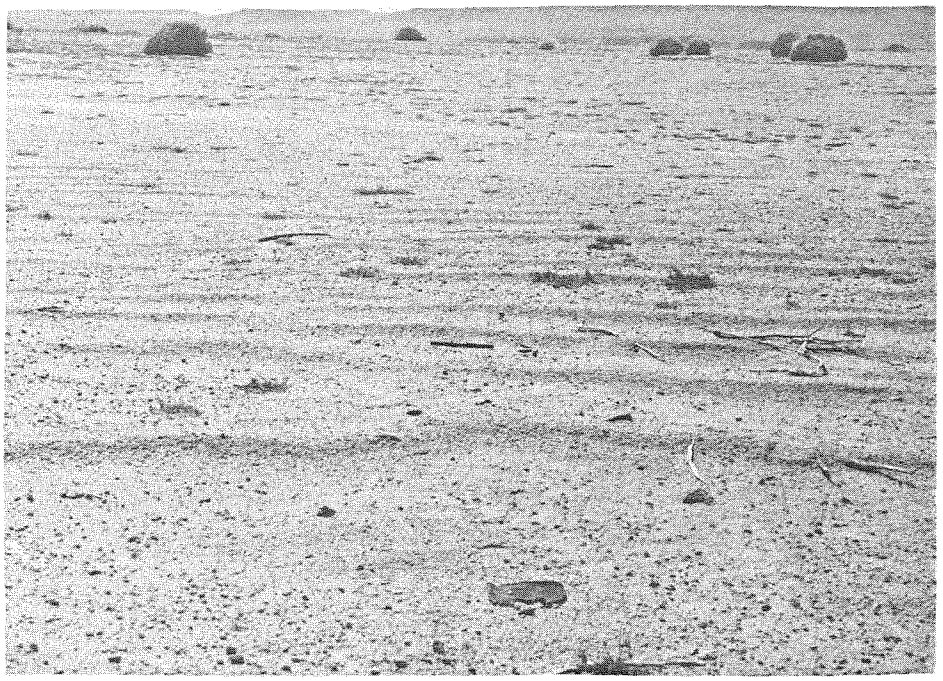

Figure 27: Photograph of field 12 showing a barren heavily wind-rippled surface.

Figure 28: Photograph of field 5 showing wind ripples and field geology hazard.

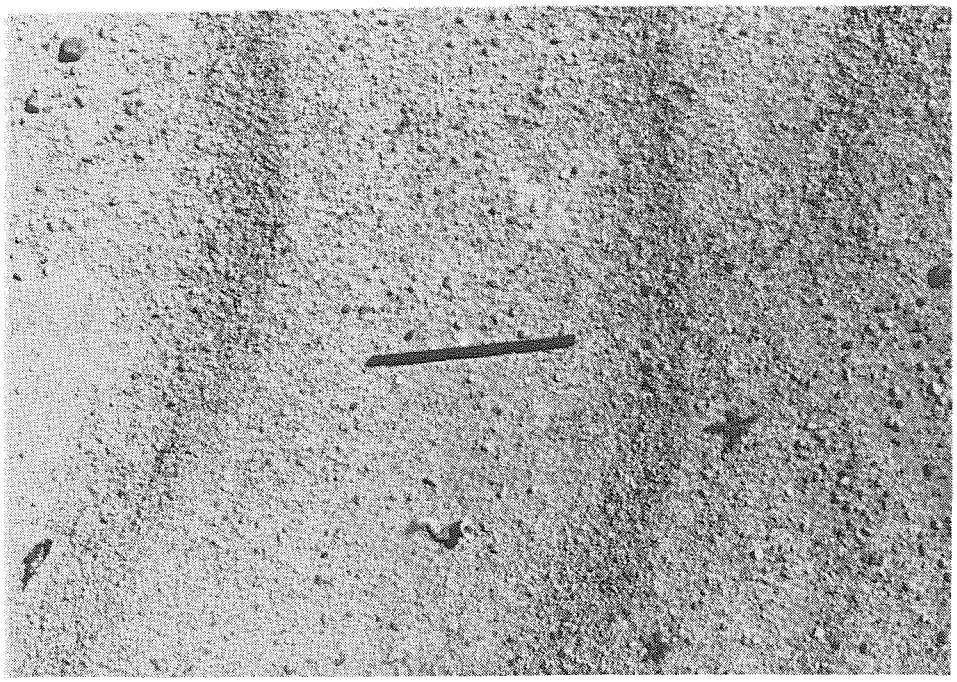

Figure 29: Close-up of the wind ripples on field 12. The dark bar is approximately 16.5 cm in length. Note the coarseness of the particles composing the ripples. Note that the wavelength of the ripples is close to 30 cm.

is known to produce a rippled surface either preceding the formation of larger dunes, or as the ultimate bedform where the windspeed is low and the supply of sand is limited (Sharp, 1963).

On April 13, 1991 a more detailed survey was carried out to characterize any ripples found on the fields. Of the fields observed (fields 8–10 were not observed), fields 5, 11, and 12 were all wind rippled. Field 12 was observed to be nearly barren and heavily covered with wind ripples (figure 27), and field 5 was also quite barren and largely covered with wind ripples (figure 28). Field 11 was less heavily covered with wind ripples, but significant ripples were observed on that field as well.

Figure 29 shows a close-up of the wind ripples on field 12. These ripples are composed of very coarse sand, and they are the type of ripples sometimes referred to as granule ripples or megaripples. The Manix Basin is the site of truly monstrous megaripples with Weir (1962) reporting ripples which were more than a meter in height on Coyote Dry Lake. These large ripples are obviously formed by strong, maintained winds (Sharp, 1963). The concentration of the particles which forms these ripples is likely due to deflation of the surface through the removal of the finer size fraction.

The ripples observed on fields in the study area are typically about 2.5–5 cm in height. The peak-to-peak wavelength is approximately 30 cm. The lengths of continuous ridges ranges from 3 to more than 6 m. The main class of particles forming the ridges are generally larger than 0.5 mm in diameter, with a large number of particles 1 mm and larger. It should be noted that particles larger than 1 mm in diameter are considered to be essentially non-erodible (Chepil, 1945; Woodruff and Siddoway, 1965; Holý, 1980). The ridges have a north azimuth of approximately 170°.

Part 4.2.4: *Modeling the Ripples*

With a potential culprit for producing the unusual polarization signatures observed in the AIRSAR data, the next matter to consider is the possibility that this is simply guilt by association. The mere fact that wind ripples are present on fields exhibiting the polarization shift and that the fields with the greatest shift have the heaviest coverage of wind ripples, does not prove by itself that the wind ripples are actually responsible for the

unusual polarization signatures. Likewise, the evidence does not allow uniquely identifying the presence of wind ripples solely from the odd polarization signatures. A numerical model connecting the polarization signatures to the rippled surface is required. Ideally, this model would predict the shift in the LL/RR ratio also found in the signatures with the shifted peak of maximums.

Most of the models used in the past to determine the return from rough surfaces are unsuitable to this task. The geometric optics and physical optics models predict no maximum in the co-polarized linear polarizations, let alone a maximum in the linear co-polarizations which is not at VV polarization. These two simple scattering models also predict that the LL and RR polarizations are both zero, so there is no way for these models to produce the observed results in the data. Likewise, the first-order small perturbation model is not capable of predicting the scattering from a rippled surface, since the first-order small perturbation model assumes that the surface roughness is isotropic.

However, there is nothing to prevent the extension of the small-perturbation models to higher order. Indeed a second-order small perturbation model was used by both van Zyl *et al.* (1987b) and Evans *et al.* (1988) to make predictions of features in observed polarization signatures not explainable with the first-order model. When the power series for the backscattered electric fields are expanded to the second-order terms in surface height variations, the following expressions, which have not been previously published, result (from unpublished notebooks by Jakob van Zyl):

$$\langle S_{HH}^{*} S_{HH} \rangle^{(2)} = \frac{1}{2} k_0^8 \cos^3\theta \left|\alpha_{HH}^{(2)}\right|^2 a^2 \sum_{k,l} \left|f_{HH}^{(2)}\right|^2 W(ak - k_0 \sin\theta, al) W(ak + k_0 \sin\theta, al)$$

$$\langle S_{VV}^{*} S_{VV} \rangle^{(2)} = \frac{1}{2} k_0^8 \cos^3\theta \left|\alpha_{VV}^{(2)}\right|^2 a^2 \sum_{k,l} \left|f_{VV}^{(2)}\right|^2 W(ak - k_0 \sin\theta, al) W(ak + k_0 \sin\theta, al)$$

$$\langle S_{HV}^{*} S_{HV} \rangle^{(2)} = \frac{1}{2} k_0^8 \cos^3\theta \left|\alpha_{HV}^{(2)}\right|^2 a^2 \sum_{k,l} \left|f_{HH}^{(2)}\right|^2 W(ak - k_0 \sin\theta, al) W(ak + k_0 \sin\theta, al)$$

$$\langle S_{HH}^{*} S_{VV} \rangle^{(2)} = \frac{1}{2} k_0^8 \cos^3\theta \left|\alpha_{HH}^{(2)}\right|^{*} \left|\alpha_{VV}^{(2)}\right| a^2 \sum_{k,l} \left|f_{HH}^{(2)}\right|^{*} \left|f_{VV}^{(2)}\right| W(ak - k_0 \sin\theta, al) W(ak + k_0 \sin\theta, al)$$

$$\langle S_{HH}^{*} S_{HV} \rangle^{(2)} = \frac{1}{2} k_0^8 \cos^3\theta \left|\alpha_{HH}^{(2)}\right|^{*} \left|\alpha_{HV}^{(2)}\right| a^2 \sum_{k,l} \left|f_{HH}^{(2)}\right|^{*} \left|f_{HV}^{(2)}\right| W(ak - k_0 \sin\theta, al) W(ak + k_0 \sin\theta, al)$$

$$\langle S_{HV}^{*} S_{VV} \rangle^{(2)} = \frac{1}{2} k_0^8 \cos^3\theta \left|\alpha_{HV}^{(2)}\right|^{*} \left|\alpha_{VV}^{(2)}\right| a^2 \sum_{k,l} \left|f_{HV}^{(2)}\right|^{*} \left|f_{VV}^{(2)}\right| W(ak - k_0 \sin\theta, al) W(ak + k_0 \sin\theta, al)$$

$$\alpha_{HH}^{(2)} = \frac{\varepsilon - 1}{\left(\cos\theta + \sqrt{\varepsilon - \sin^2\theta}\right)^2}$$

$$\alpha_{VV}^{(2)} = \frac{\varepsilon(\varepsilon - 1)}{\left(\varepsilon\cos\theta + \sqrt{\varepsilon - \sin^2\theta}\right)^2} \qquad (7)$$

$$\alpha_{HV}^{(2)} = \frac{(\varepsilon - 1)^2 \sqrt{\varepsilon - \sin^2\theta}}{\left(\cos\theta + \sqrt{\varepsilon - \sin^2\theta}\right)\left(\varepsilon\cos\theta + \sqrt{\varepsilon - \sin^2\theta}\right)}$$

$$f_{HH}^{(2)} = \frac{\sqrt{\varepsilon - \sin^2\theta}}{k_0} + \frac{(\varepsilon - 1)}{d(k,l)}\left(\frac{a^2 l^2}{D_{k,l}} - 1\right)$$

$$f_{VV}^{(2)} = \frac{\sqrt{\varepsilon - \sin^2\theta}}{k_0} + \frac{\varepsilon \sin^2\theta\, b(k,l)}{D_{k,l}} - \frac{\sin\theta\, c(k,l)}{k_0^2} + \frac{(\varepsilon - 1)(\varepsilon - \sin^2\theta)}{d(k,l)}\left(\frac{a^2 k^2}{D_{k,l}} - 1\right)$$

$$f_{HV}^{(2)} = \frac{a^2 kl}{d(k,l) D_{k,l}}$$

$$b(k,l) = \sqrt{k_0^2 - k^2 - l^2}; \quad c(k,l) = \sqrt{\varepsilon k_0^2 - k^2 - l^2}$$

$$d(k,l) = b(k,l) + c(k,l); \quad D_{k,l} = b(k,l) * c(k,l) + k^2 + l^2$$

Clearly, extending the small perturbation model to the second order produces a much more mathematically complex model. The preceding expressions are the second-order terms, and these terms are summed with the first-order terms presented in chapter 3,

part 3.4.2. This also means that considerably more computer time is needed to calculate the scattering for the second-order model.

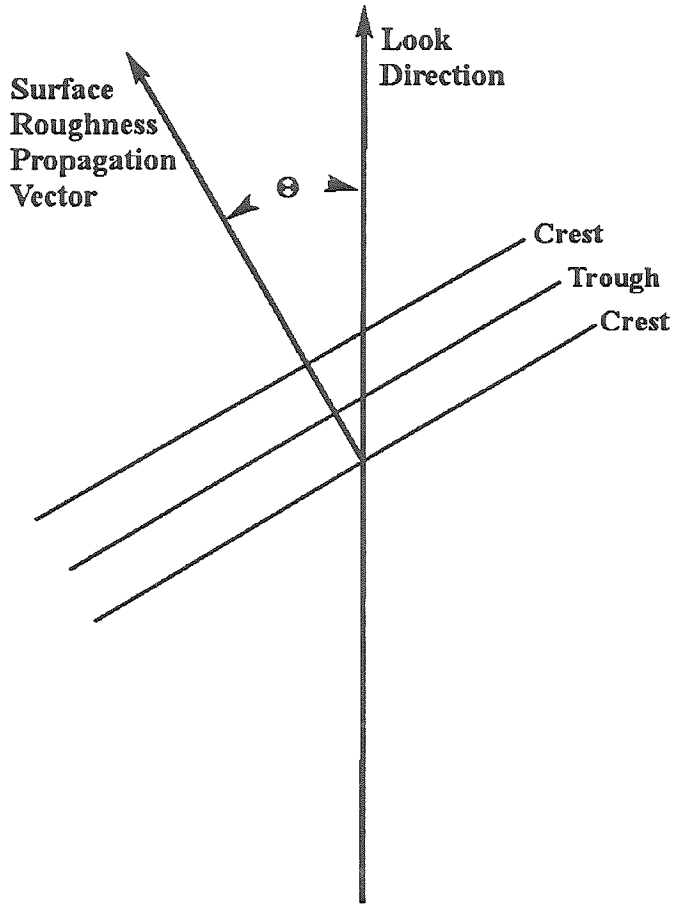

Figure 30: The geometry of the angle used to define the orientation of the wind ripples with respect to the radar look direction.

Figure 30 shows the geometry of the angle used to define the orientation of the primary component of the rippled surface. The angle used is that between the propagation direction of the primary component of the surface and the look direction. It is realized

that the rippled surface is not a pure sinusoid, so the surface is treated as nearly sinusoidal for this model. A pure sinusoid would have a power spectrum represented by two delta functions located at a distance equal to the wavenumber of the sinusoid. The nearly sinusoidal surface used produces two gaussian distributions with maxima located at the position where the delta functions for the pure sinusoid would be located. In effect, the surface is treated as a whole series of sinusoids of various phases all propagating along nearly the same vector. Some of these sinusoids have a slightly shorter wavelength than the primary and some have a slightly longer wavelength. Figure 31 shows the profile of such a surface along the line of the propagation vector of the dominant sinusoid.

The results of this model for a nearly sinusoidal surface with a wavelength of 30 cm and a dielectric constant of 2.0 are shown in figure 32. Figure 32a shows how the orientation angle of the maximum co-polarized response changes as the angle between the look direction and the propagation direction of the primary term in the sinusoid varies. Notice that the value of the orientation angle when the angle is between 0–90° is less than 90°, which would cause the co-polarization peak to shift to the left of center in the co-polarization signature. The values of the LL/RR polarization ratio as a function of the angle between the look direction and the direction of propagation of the primary term of

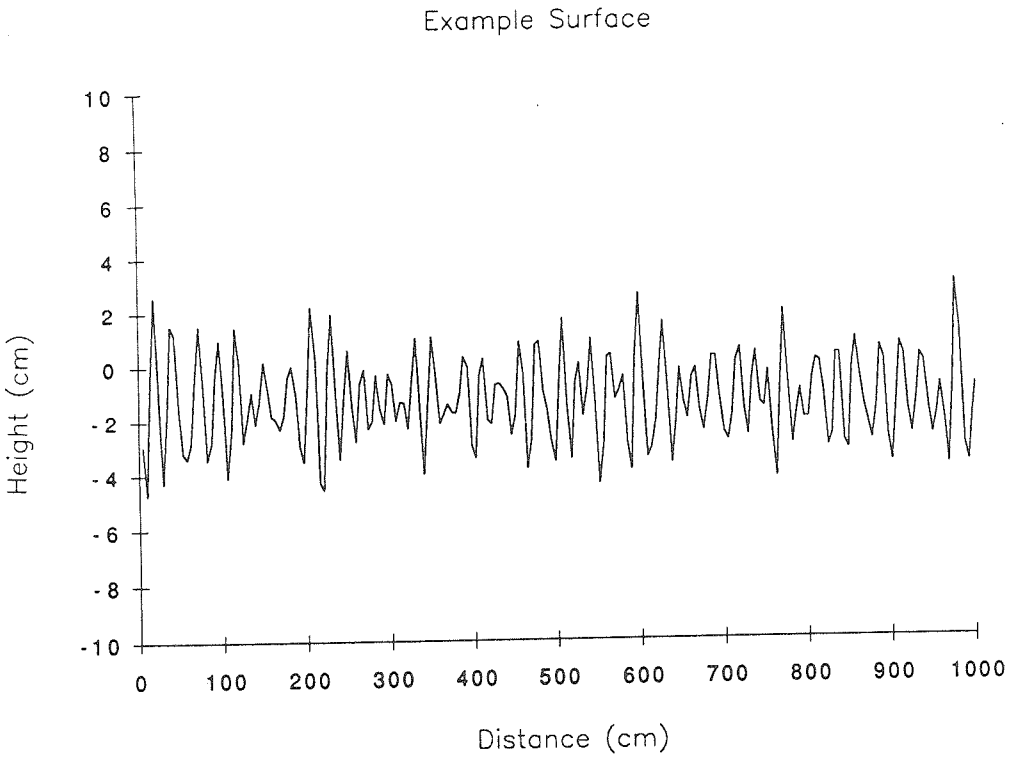

Figure 31: Profile of nearly sinusoidal surface used for the second-order small perturbation model of the wind-rippled surface. This profile is taken along the surface propagation vector as shown in figure 30.

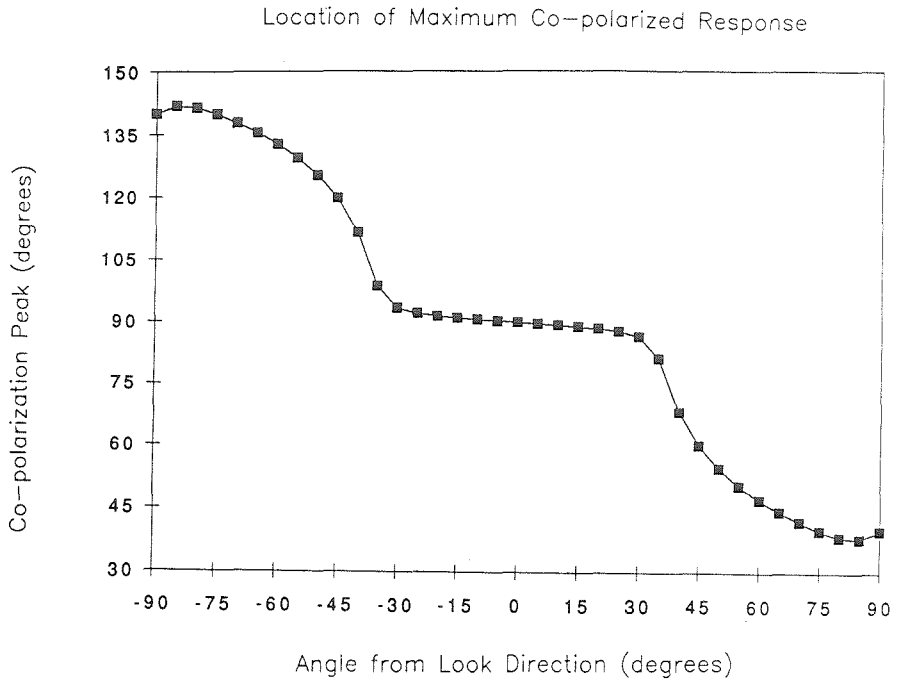

a)

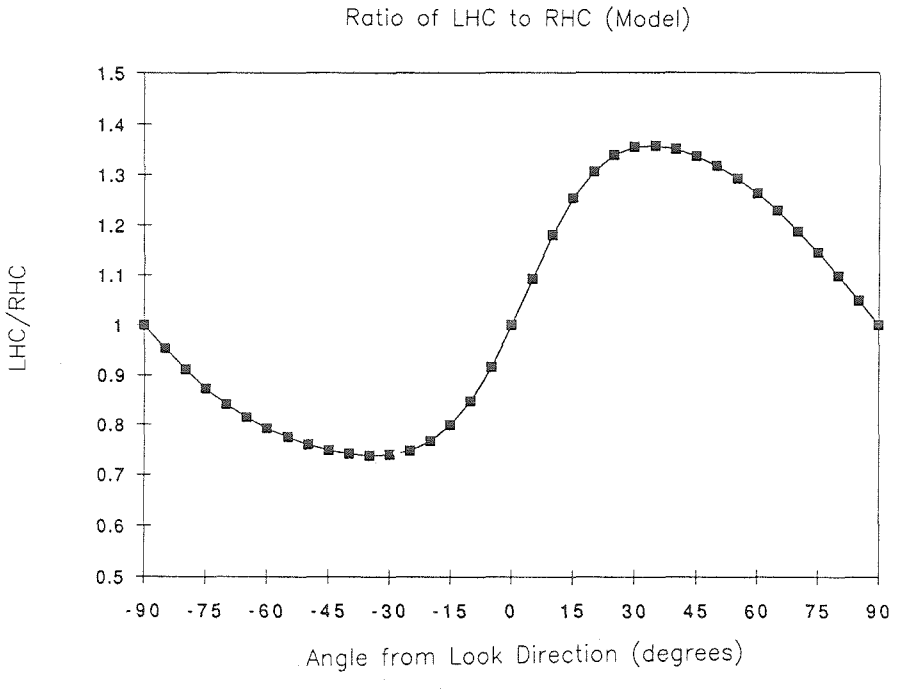

b)

Figure 32: Results of the second-order small perturbation model. The surface has a wavelength of 30 cm as compared to a wavelength of 24 cm for the radar, and the dielectric constant of the surface is 2.0, which is reasonable for dry sand. The rms. surface height variation is 2 cm. **a)** The orientation angle of the maximum co-polarization response as a function of the angle between the radar look direction and the propagation vector of the surface. **b)** The ratio of LL return to RR return as a function of the angle between the radar look direction and the propagation vector of the surface.

the surface undulations is plotted in figure 32b. Notice that the value of this ratio is greater than 1.0 for the same orientations of the surface that have leftward-shifted peaks in the co-polarization signature.

The results of this modeling appear to be consistent with the observations in the AIRSAR data of the Manix Basin discussed above. The polarization signature for a surface having several different scattering mechanism will be a combination of the polarization signatures for each scattering mechanism. A field without ripples is expected to have a polarization signature with a maximum at VV, and at large incidence angles all of the linear polarizations would have roughly equal power. A field thoroughly covered by wind ripples, would have a co-polarization signature like that shown in figure 33. A field partially covered by wind ripples would be some combination of these signatures.

Although this model seems to be consistent with the observations, there are several problems. The first problem is that the model predicts that the peak shift and the shift in the LL/RR ratio will get smaller with increasing incidence angles. This may not truly be a problem in these data, since the fields at the largest incidence angles also turn out to be the ones most pervasively covered by ripples. The polarization signature in figure 33 would tend to be flatter across the top with all linear polarizations being more equal in terms of backscatter. The tilt to the signature from left-hand circular to right-hand circular would become less pronounced, and the location of the peak would migrate towards VV polarization. However, neither of these features would disappear at the incidence angles covered by AIRSAR (25–62.5°).

The second problem is similar to that encountered with the first-order model when looking at the concentric furrows. The rms. height of the undulations used in the model was given as 2 cm, which is close to the most common observed height of 2.5 cm, and the second-order model is invalid when the rms. height of the surface exceeds one-tenth of the radar wavelength (24 cm). Additionally, the surface slopes which occur when the wavelength of the primary surface undulation is less than about twice the wavelength of the radar are outside the validity of the model, and the 30 cm wavelength observed on the surface clearly exceeds this limit. It should be recognized that, in the strictest sense, the small perturbation model is invalid for anything other than a nearly perfectly smooth surface (Kuga *et al.*, 1987; van Zyl *et al.*, 1987b; Zebker *et al.*, 1987b; Evans *et al.*, 1988). Thirdly, the characterization of the surface as nearly-sinusoidal is not completely correct, the surface more closely resembles a half-wave rectified sinusoid. The resulting surface power spectrum is appreciably different than for a full-wave sinusoid.

Future modeling of such periodic surfaces could be done using the conical diffraction model of Li *et al.* (1994), which does not suffer from the same limitations of allowable surface wavelength as does the small-perturbation model. Peak shifts as observed in these data have been observed in AIRSAR data over the oceans, but these are

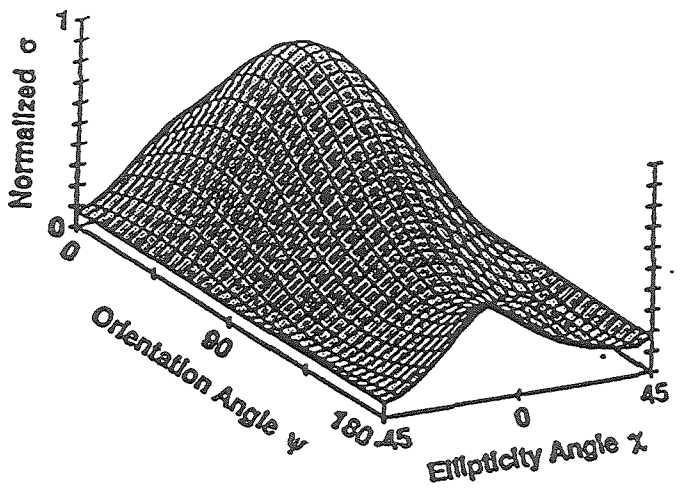

Figure 33: The co-polarization signature for a nearly-sinusoidal surface at 30° incidence and with the angle between the look direction and the propagation direction at 75°. The primary surface wavelength is 30 cm and the dielectric constant of the surface is 2.0. The rms. height variation of the surface is 2 cm. See figure 18 for an illustration of the features of polarization signatures.

mainly attributed to the tipping of a surface which would have the strongest co-polarization at VV if the surface were horizontal (Schuler and Lee, 1992). There has been no notice of peak shifts as shown in this study from a periodic surface in ocean applications, which may be due to the ripples on the ocean's surface not being truly static features.

Part 4.2.5: *Physical Meanings*

The limitations of the model used were discussed in the previous section. The model results are consistent with the observed data. However, it would be useful, and indeed, prudent, given the model limitations above, to make some assessment as to the reasonableness of the model results based on basic principles.

First, consider the shift in the location of the co-polarization peak. The co-polarization response for a conducting short, thin cylinder embedded in the plane perpendicular to the propagation direction of the incident radiation has its maximum at the linear polarization angle oriented parallel to the cylinder. A cylinder rotated out of the plane perpendicular to the propagation direction of the incident radiation would have a co-polarization maximum oriented parallel to the cylinders projection on the plane. If the ridges or the furrows on the surface are considered as a series of parallel wires, then rotating the surface would be expected to cause the co-polarization signature should vary in much the same way.

There is an inconsistency with this simple model of embedded wires. The small perturbation model predicts that the maximum co-polarized return when the angle between the look direction and the propagation direction of the primary surface component will be at VV polarization. The simple model of parallel conducting wires would predict a maximum co-polarized response at HH. Likewise, when the surface undulation propagation is perpendicular to the radar look direction, the small-perturbation

model predicts a maximum response closer to HH than to the VV polarization predicted by the simple wire model.

However, this model of parallel wires is clearly inconsistent with the undulating surface, since the undulating surface represents an undulating medium with a constant dielectric constant rather than a series of parallel conducting lines in a non-conducting medium. A better analogy for the surface might be a polaroid filter in visible light. Consider a sinusoidal surface where the propagation direction of the surface undulations is parallel the radar look direction. When a horizontally polarized radar wave strikes this surface, it senses a smooth surface, and the radiation passes into the underlying media with little backscattering (but significant forward scattering). A vertically-polarized wave is oscillating orthogonally to the ridges and furrows, and the wave is strongly scattered from the rough appearing surface. The polarization most strongly scattered by the surface would be the polarization perpendicular to the ridges and troughs, so the location of the maximum co-polarized return would clearly vary as the surface is rotated.

The more difficult question relates the LL/RR polarization ratio. It should be noted that the VH and HV returns in a monostatic radar case (where the transmitter and receiver are collocated) must be equal, but that the RR and LL polarizations are not necessarily equal, even though they are for most simple targets. The simplest example of this is the backscatter from a left-handed helix which has extremely strong backscatter in the LL polarization and no backscatter in the RR polarization. The HV and VH scattering amplitudes are both equal to i, and the VV and HH scattering amplitudes are -1 and 1,

respectively. The RR/LL imbalance can legitimately be produced in properly calibrated data.

In order to make the LL/RR depart from a value of 1.0, one of two conditions seem to be required. The first possibility is that the target has clock-face symmetry, which means that the roughness observed on a clockwise path about the target is somehow different that that observed on a counter-clockwise path. The difference between right- and left-handed helices is perhaps the most dramatic version of clock face symmetry. Producing the slight imbalance seen in the AIRSAR data does not require an extreme amount of clock face symmetry. The second possible way of enhancing one circular polarization compared to the other is to have a surface that encourages the H polarization to be retarded by 90° in phase compared to the V polarization (this produces R polarization) or vice versa (which produces L polarization).

It is difficult to see how either of these things occur on the wind rippled fields. One possible way in which the symmetry is broken is shown in figure 34. In 34a, the parallel lines formed by the ridges and troughs converge to the upper left and diverge to the lower right. When the surface is rotated in the opposite direction (figure 34b), the convergence is to the upper right and the divergence is to the lower left. This geometry may arise when the problem is formulated as near-field Fresnel diffraction.

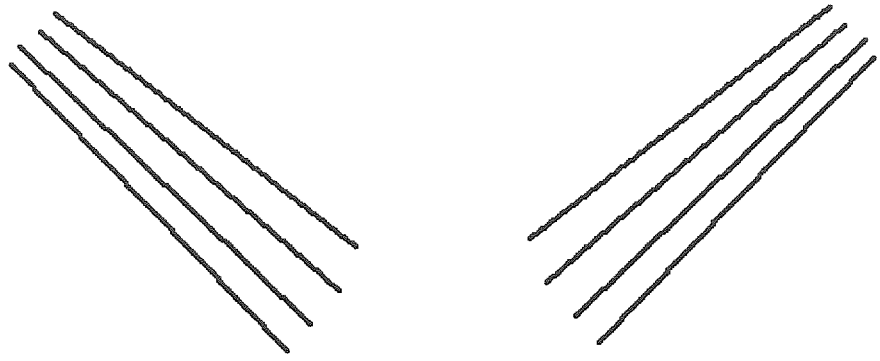

a) b)

Figure 34: Forced perspective view of a set of parallel lines. **a)** Rotated clockwise. **b)** Rotated counter-clockwise. Note how lines converge in the distance and diverge in the foreground.

Another matter to consider is the fact that the model discussed above is only concerned with the scattering from the surface. The low dielectric constant of the surface of dry sand and the dry sand substrate means that the radar energy will penetrate to an appreciable depth. This means that the polarization signatures observed in the AIRSAR data could be due to some subsurface structure. However, random digging on several of the abandoned fields to the depth of a single L-band wavelength revealed no remarkable structures. The weak return from the abandoned fields may indicate both a rough surface and that scattering within the dry sand is very low. The weak return also suggests that any subsurface structures reflect quite weakly.

One fortunate thing about the abandoned fields that are the most heavily wind rippled are also the most sparsely vegetated. Eliminating the vegetation roughness makes

the small perturbation model more likely to be valid with respect to the surface. The wind rippling of the surface is obviously a time-dependent process. As wind erosion proceeds on the surface the rippling will first occur on the areas most susceptible to wind erosion. As time passes, the surface becomes more homogeneously covered by the wind ripples. This, as discussed in the previous section, will cause the polarization signature to change from the polarization signature from an isotropically rough surface to the signature caused by the anisotropic roughness due to wind rippling.

The fields vary in terms of their protection from wind erosion. Fields 1, 3, 6, 7, 8–10, and 12 have no protection from wind erosion. Fields 2, 4, and 5 are surrounded by a shelter belt of trees, but field 5 does not have trees along its western edge where fields 2 and 5 join each other. Field 11 lies close to the foot of the Calico Mountains which may significantly alter the winds approaching the field over the mountains to the immediate west, and field 3 may share this feature to a lesser extent owing to its greater distance from the mountains.

The detection of the wind ripples on the abandoned fields in the Manix Basin area shows how the use of a great deal of information for a single pixel in an image may be used to infer features and processes acting on scales much smaller than the resolution of the remote sensing instruments. The wind ripples on the abandoned fields have a surface wavelength of approximately 30 cm, and the pixel resolution of the radar is 6–12 m, so the feature being detected is one or two orders of magnitude smaller than the pixel resolution. This is useful for monitoring, since larger pixel resolutions allow easier imaging of the Earth's surface with a good repeat cycle at reasonable spacecraft orbits.

Part 4.3: *The VIR View*

The previous sections have shown how having more information for each pixel can allow the extraction of information at the sub-pixel level. A polarimetric radar system such as AIRSAR provides all of the information which a given wavelength radar can collect by looking at a target at a given incidence angle. In the part of the spectrum covering visible light and the near-infrared, there are also advantages to having greater amounts of information in each pixel. The Landsat Multispectral Scanner with its four bands provided more information than was previously available using standard color photography. In 1983, the Landsat Thematic Mapper instrument increased the amount of information available in each pixel by collecting data in 6 bands (7 counting thermal infrared). However, this still represents little spectral information in each pixel.

Astronomers have used spectroscopy for many years to determine the composition of stars by examining their emission spectra. Many molecules in the atmospheres of planets absorb light at certain wavelengths, and those molecules can be identified by their absorption features. Reflectance spectra, which show the ratio of energy reflected from an object to the energy incident on the object as a function of wavelength, can also identify many materials based on their distinctive absorptions. Figure 35 shows the laboratory reflectance spectra for a common clay mineral (montmorillonite) and for calcite (from Grove *et al.*, 1992). In order to identify materials based on their reflectance spectra, a much higher degree of spectral resolution is required than is available from Landsat TM.

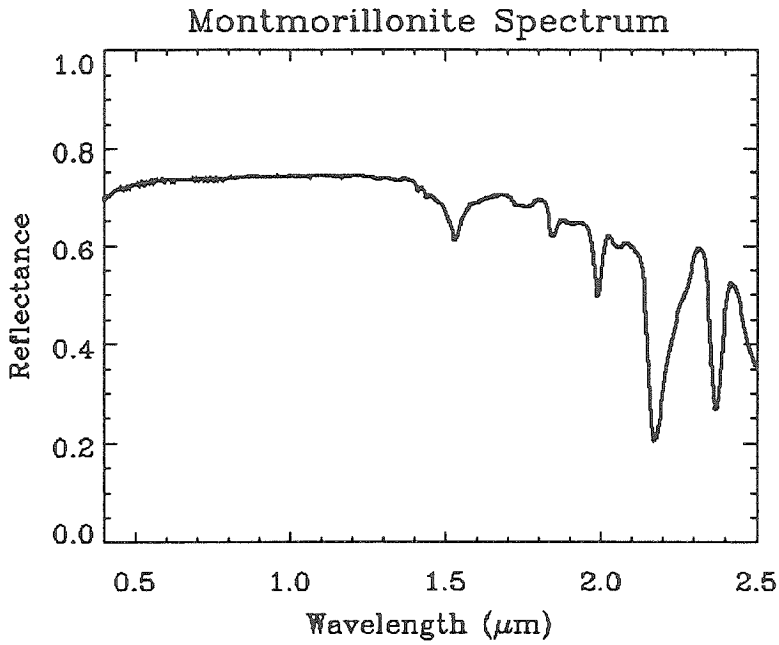

a)

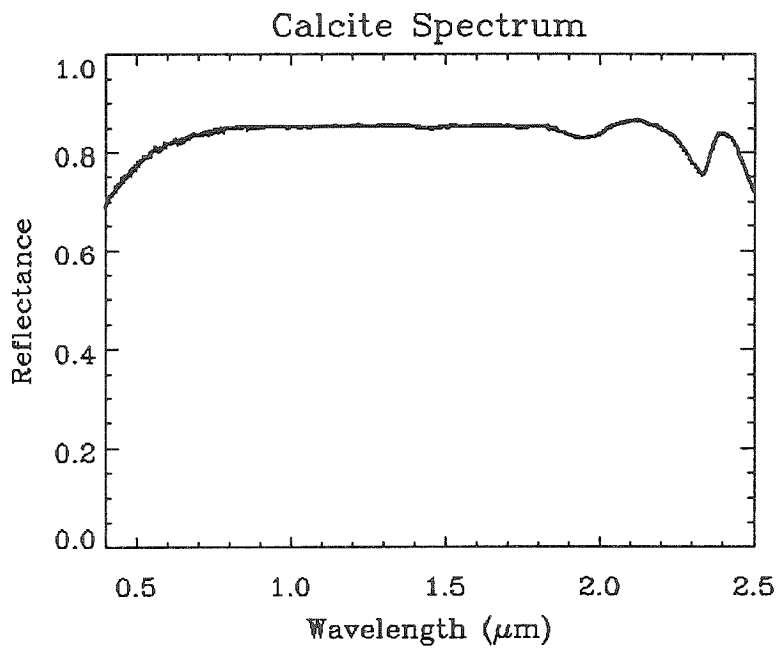

b)

Figure 35: Spectra of two common minerals. Data is from Grove *et al.* (1992). **a)** Montmorillonite (a clay mineral). **b)** Calcite. Note the differences between these spectra.

An imaging spectrometer is an instrument designed to collect data in many (tens to hundreds) narrow spectral bands for each pixel. The need to split the light coming into the instrument into the many spectral bands, and, if the individual bands are very narrow, a great deal of light is needed to ensure that enough photons fall in the narrow band to give an accurate measurement. This need for light requires either large optics or large dwell times (the instrument has to look at each point for a longer time), both of which negatively effect the pixel resolution. There are therefore tradeoffs between the spectral resolution of the instrument and its spatial resolution.

The SPOT instrument is a case in point. In the panchromatic mode, the SPOT instrument collects light in a single broad spectral band, which allows the SPOT instrument to achieve a spatial resolution of 10 m. When SPOT is operated in its multispectral mode, it collects data in three narrow spectral bands, but this comes at a price of the lower spatial resolution of 20 m.

The visible and near-infrared part of the spectrum is that part of the electromagnetic spectrum which begins with the shortest wavelength that is detected by the human eye (about 0.4 μm) and ends with the longest wavelength that can be photographed with infrared sensitive film (about 0.93 μm). The next longer region of the electromagnetic spectrum is often termed the mid-infrared which covers the spectral range 0.93–2.5 μm. The term near-infrared is sometimes used to include light up to the longest wavelength detectable by a silicon detector (about 1.1 μm), and, since neither infrared-sensitive film nor silicon detectors require cooling to operate, the visible/near-infrared spectral region can be considered to be light detectable with uncooled detectors.

Detectors composed of indium antimonide (InSb), which requires cooling, are usually used to detect wavelengths from 1.0 to 2.5 μm.

Part 4.3.1: *AVIRIS Overview*

The Airborne Visible/Infrared Imaging Spectrometer (AVIRIS) is operated by JPL and flies on NASA's ER-2 aircraft. The instrument characteristics are summarized in table 7. The AVIRIS instrument was flown over the study area on July 20, 1990. AVIRIS data are delivered in segments that are 614 samples by 512 lines (about 12.28 km by 10.240 km). In accordance with Murphy's Law of Imaging, the area of interest was split between two adjacent segments of the same flight line. This was remedied by using the Interactive Data Language (IDL) to essentially "glue" parts of the adjacent segments together to give a data "cube" the same size as a normal AVIRIS segment (614 samples × 512 lines × 224 bands × 2 bytes = 140,836,864 bytes of data). AVIRIS data are stored as integer data, requiring two bytes of storage per band per pixel. Strong water absorption features in the atmosphere and wavelength overlaps between the four spectrometers which comprise AVIRIS decrease the number of useful AVIRIS bands to 176.

Table 7: AVIRIS Characteristics	
Platform	Airplane (ER-2)
Operational Altitude	20 km
Spectral Coverage	0.4–2.5 μm 224 bands (176 useful) 0.010 mm Band spacing 0.005 μm FWHM
Swath Width	10.2 km
Ground Resolution	20 m
Quantization Level	10 bit
Image Building Strategy	Scanner

JPL performed a radiometric calibration and released the data to investigators as radiance data in units of watts/steradian/m^2. JPL's calibration of the data converted the digital counts registered in each band to radiance and corrected for the optical transfer function of the AVIRIS instrument. At the time these data were collected, the radiometric calibration had no worse than 10% absolute error, and that the variability of the radiometric characteristics of the instrument was no worse than 2% (Green *et al.*, 1991).

The calibration performed by JPL did not remove the effects of the solar spectrum or atmospheric absorption. The data used in this study were calibrated to apparent reflectance by using the empirical line technique (Conel *et al.*, 1987). In this technique, at least two field reflectance spectra are collected on the ground in the target area as close to the flight time as possible. The targets must be significantly different in overall albedo. A least squares fit is then performed to find the gain and offset to apply to each band in order

to force the spectra of the targets extracted from the AVIRIS data to most closely match the field reflectance spectra.

Figure 36: The PIDAS spectrometer in operation in the Manix Basin on July 21, 1990. This instrument was used to collect the calibration spectra for the 1990 AVIRIS data.

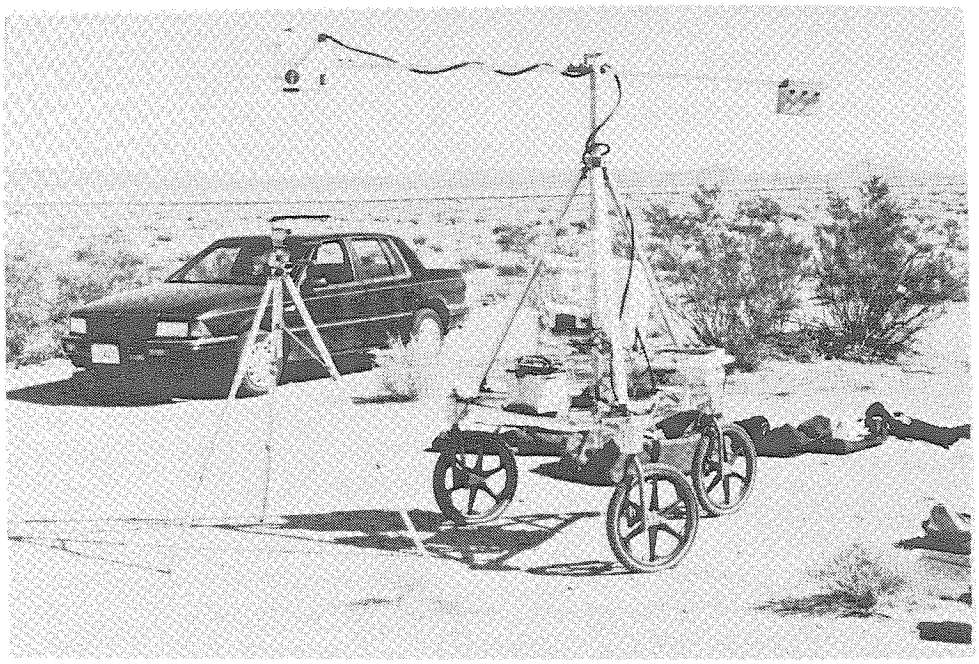

Figure 37: The GER spectrometer in operation in the Manix Basin on February 24, 1994. This instrument is now used by JPL to collect spectra for AVIRIS calibration.

The field spectra collected to calibrate these AVIRIS data were collected by Cathy Weitz and Veronique Carrere and on July 21, 1990. The instrument used was the PIDAS (Portable Instantaneous Data and Analysis System), which is pictured in figure 36 while collecting a field spectrum in the study area. PIDAS collected data in 880 spectral bands that were each 0.88 nm wide from 0.45–0.90 μm and 4.7 nm wide from 0.9–2.5 μm, and it covers the spectral range from 0.45 μm to 2.5 μm. PIDAS was retired shortly after these data were collected, and the instrument of choice for collecting field spectra for AVIRIS calculation was the GER spectrometer pictured in figure 37.

The gains and offsets for the two target calibration spectra are assumed to be valid for the entire image area. Once again, in accordance of Murphy's Law of Imaging, the

two reference targets did not fall on the same segment. Finding a large, smooth, low albedo target in the desert can be a significant challenge, as it was in this case. The low relief of the study area makes extreme differences in the atmospheric properties across the AVIRIS data unlikely, so the assumption of the same calibration applying across this data set is a reasonable approximation.

Plate 13 shows a spectacular, if not very informative, way of displaying AVIRIS data. This is a perspective view of the calibrated AVIRIS data covering the primary study area. The top of the image cube is a three-color composite of the AVIRIS data as it would have been seen using the MSS spectral bands. This illustrates how very high spectral resolution data can be used to simulate data from a sensor with lower spectral resolution. The sides of the cube show the color-coded spectra at each pixel along the edges of the data cube.

Plate 14 shows a synthetic Landsat Thematic Mapper image created from the AVIRIS data using the Landsat TM bandpasses from Markham and Barker (1985). The same band ratios are shown as those used in plates 8–10. Notice that several fields which appear red in plate 8b (taken July 28, 1985) are not red in plate 14, which indicates that those fields were inactive in July 1990. The difference between plate 8b and plate 14 once again show how human activities cause the most rapid changes in the Manix Basin Area.

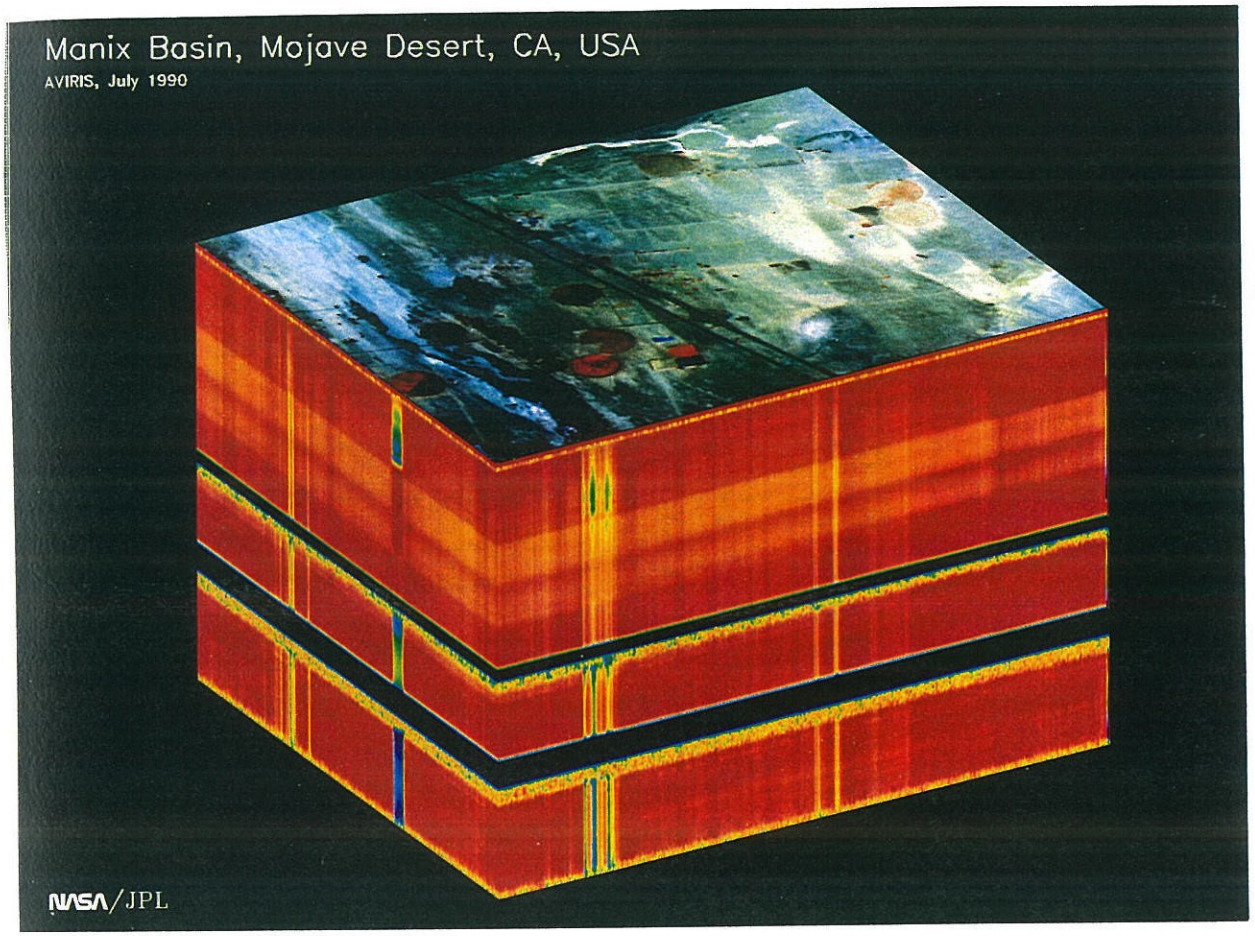

Plate 13: AVIRIS data cube. The top of the cube is a synthetic MSS image creating by resampling the AVIRIS data with the MSS bandpasses. Red is MSS band 7, green is MSS band 5, and blue is MSS band 4. The top image is rotated approximately 90° clockwise to all of the other plates. The vertical sides of the cube are the spectra of the pixels at the edges of the top image. These spectra have been color-coded so that blue represents low reflectivity and red represents high reflectivity. The two large blacked out areas in the spectra are the strong water absorption bands in the atmosphere near 1.4 and 1.9 μm. The MSS bandpasses were provided by Dr. Ron Blom of JPL.

Plate 14: Synthetic Landsat TM image created from AVIRIS data. Red is TM band 5/TM band 7, green is TM band 5/TM band 4, and blue is TM band 3/TM band 1. Compare this image to plates 8a and 8b,

Part 4.3.2: *The General Spectral Change*

The AVIRIS data provide high resolution spectra for each pixel in the image. As discussed earlier, these high resolution spectra may make it possible to identify materials present in the area of the ground covered by the pixel. The problem, of course, is the fact that most pixels of significant area (the AVIRIS pixels each cover an area of 400 m^2) on the Earth's surface are not covered by a single geological or biological material, but by a mixture of materials. Each pixel actually contains varying amounts of two or more materials, each having a distinctive spectrum. The spectrum for a given pixel is therefore a combination of the individual spectra of a number of materials.

In "Opticks," Newton, in 1704, used a color wheel to illustrate how differently colored light when mixed in various proportions would produce a color of light different than any of the colors that had been combined. Newton used the color wheel construction to predict what color would be produced by mixtures of individual colors. This construction could, in principle, be inverted to find what proportions of given colors would have to be combined to produce the color of interest. As is typical of inverse problems in science, the inverse solution clearly is not unique.

Newton's example is closely related to a concept known as linear spectral mixing (Adams *et al.*, 1989;. Boardman, 1989, 1990, 1991, 1994; Roberts *et al.*, 1993, 1994; Smith *et al.*, 1990). The fundamental idea of linear spectral mixing is that the spectrum observed in a given pixel is a linear combination of the spectra of the individual materials in the pixel. This model is generally considered to be valid when the different materials are mixed in a "checkerboard" pattern (Adams *et al.*, 1986;. Boardman, 1989, 1990, 1991,

1994; Roberts *et al.*, 1993, 1994; Smith *et al.*, 1990). In the "checkerboard" mixing condition, light reflecting from the surface interacts with one and only one target material before entering the remote sensing instrument. The mixing of the light occurs in the instrument as light from adjoining squares too small to be resolved is focused into a single pixel (Boardman, 1994).

This process of linear mixing in the human eye is taken advantage of in printing and computer graphics through "dithering," such as seen in black and white photographs in the newspaper. Only black pips can be printed in black and white printing, so the various shades of gray are produced by changing the proportion of black pips to white paper. When viewed from a distance, the appearance is that of many shades of gray. In much the same way, computer displays with limited selection of colors can display those colors in adjoining pixels in a proportion that tricks the distant viewer into seeing the desired undisplayable color.

Most workers with terrestrial remote sensing have used linear unmixing techniques where a least squares fitting technique is used to find the coefficients for each target material spectrum in the linear combination that will produce the observed spectrum, with the resulting coefficient taken to be the relative abundance of the given material (Adams *et al.*, 1986;. Boardman, 1989, 1990, 1991, 1994; Roberts *et al.*, 1993, 1994; Smith *et al.*, 1990). Workers at the University of Washington (Adams *et al.*, 1989;. Roberts *et al.*, 1993, 1994; Smith *et al.*, 1990), have typically constrained the unmixing so that the sum of the coefficients, and hence the total abundance of material in the pixel, is equal to 1.0. They take negative coefficients and coefficients greater than 1.0 to indicate either an

incorrect choice of endmembers or non-linear mixing. Other workers (e.g., Boardman *et al.*, 1989, 1991; Yuhas *et al.*, 1994) have constrained the coefficients to be non-negative, forbidding unphysical negative abundances in the pixel. It is also possible to constrain that the coefficients must be non-negative and that the sum of the abundances must not exceed 1.0, which restricts the abundances to physically realistic abundances of between 0.0 and 1.0. Unmixing can also be performed with no constraints on the coefficients.

One problem which arises in unmixing is the problem of choosing endmembers. The unmixing assumes that all endmembers being used in the unmixing have an equal right to be in the pixel. While the human analyst may readily understand that creosote bushes will not be on cultivated alfalfa fields, if creosote bush and alfalfa are selected endmembers, the mathematics of the unmixing will try to fit both endmembers to the pixels on the alfalfa field. In this way, a poorly selected endmember may be incorrectly identified in areas where it does not exist, but, more importantly, the poorly selected endmember will alter the relative abundance of the correctly selected endmember. Boardman (1993, 1994) has proposed an automatic technique of identifying the correct endmembers through the use of convex geometry. However, in the case of a dataset with a great deal of heterogeneity, no single set of endmembers will be suitable for unmixing the entire image. Spectral unmixing is sensitive to the target albedo.

Given the dependence of the results of linear unmixing an the correct selection of endmembers, and the interdependence of the resulting abundances, a technique that allows the identification of material in a pixel without recourse to unmixing would seem to be desirable. Such a technique has been developed by Boardman (1992), and it is called

Spectral Angle Mapping (SAM). This technique basically measures the similarity between the spectrum of the pixel, and user-supplied test spectra. The spectra are considered to be vectors in n-space, where n is the number of bands in both spectra. The angle between these spectra can now be found by taking their dot product and the results plotted as an image. When the vectors are parallel, the spectrum of the pixel is the same as the test spectrum, and the pixel could then be judged to be entirely covered by the material whose spectrum was being tested, and if the angle between the vectors is 90°, the conclusion that the pixel does not contain any of the tested material has a reasonable possibility of being true.

SAM does not provide any direct measurement of the abundance of materials within a pixel. All it basically can say is that the pixel looks more like the spectrum for material A than for material B. This may provide a qualitative measure of abundance, e.g., if the spectrum looks more like A than B, then A is more abundant than B in the pixel. SAM can be used as a technique of selecting likely endmembers for unmixing, or, if the results of a linear unmixing compare favorably with the results of SAM, this may enhance confidence in the unmixing result. SAM is insensitive to albedo differences.

The unmixing and spectral angle mapping presented in this thesis were performed using the Spectral Image Processing System (SIPS), which is a software package written in IDL by the Center for the Study of Earth from Space (CSES) at the University of Colorado at Boulder for the express purpose of analyzing data from imaging spectrometers such as AVIRIS. This software package has routines for linear unmixing with no constraints, abundances constrained to be greater than 0.0, and abundances

constrained to be greater than 0.0 with the sum of the abundances constrained to be 1.0 or less. SIPS comes with several libraries of laboratory spectra of geological minerals, along with green plant and dry grass spectra. Numerous attempts were made to use mineral and standard green plant and dry grass spectra for both linear unmixing and spectral angle mapping, but the results were very unsatisfactory. The active fields did show up as having a high abundance of green vegetation, but the results for other spectra was generally just noise.

Plate 15 shows the results of a highly successful linear unmixing using spectra extracted from the image. The endmembers used for this unmixing were the average spectrum of one of the most recently abandoned fields (field 1) and the average spectrum of the field abandoned for the greatest length of time (field 12). As might be expected, the active fields do not look very much like either of the abandoned fields. Notice that the

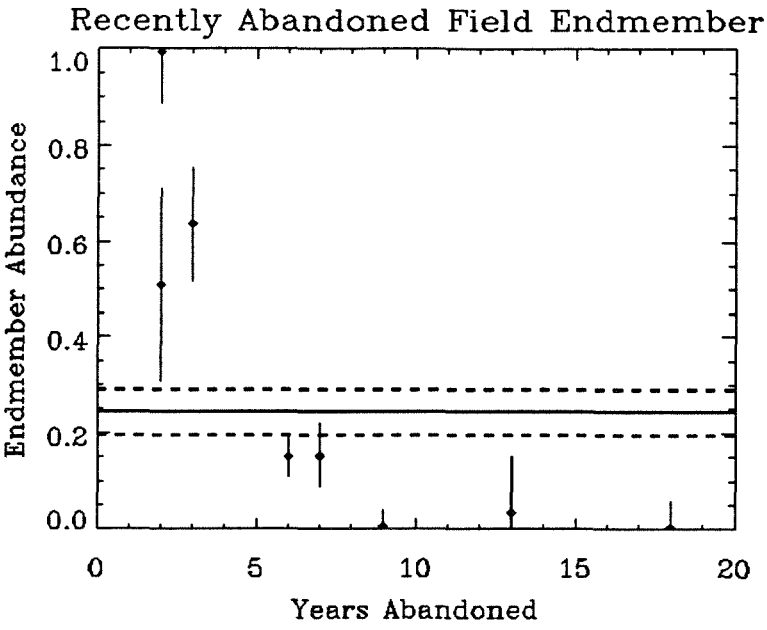

Figure 38: Plot of the abundance of recently abandoned field spectrum (the average spectrum of field 1, abandoned in 1988) as a function of number of years abandoned. Bars are 1σ variance. The solid line is the abundance of the spectral endmember for the undisturbed desert, and the dashed lines delineate the 1σ variance in the undisturbed desert. The higher the abundance of the recently abandoned field spectrum for the field, the greater the area of the field that looks like a recently abandoned field.

two endmember fields each have a very large abundance of their respective endmembers, and that the abundance of the active field spectrum tends to decrease with increasing length of time abandoned. Average values of the abundance of recently abandoned field spectrum for the abandoned fields as a function of the number of years abandoned in figure 38. There is a trend of decreasing recently abandoned field abundance as the number of years abandoned increases.

The total abundance for each field is very close to one, which indicates that the endmembers were a good choice for this unmixing. The most fully constrained unmixing available in the SIPS software requires that the total abundance be 1.0 or less, so a poor

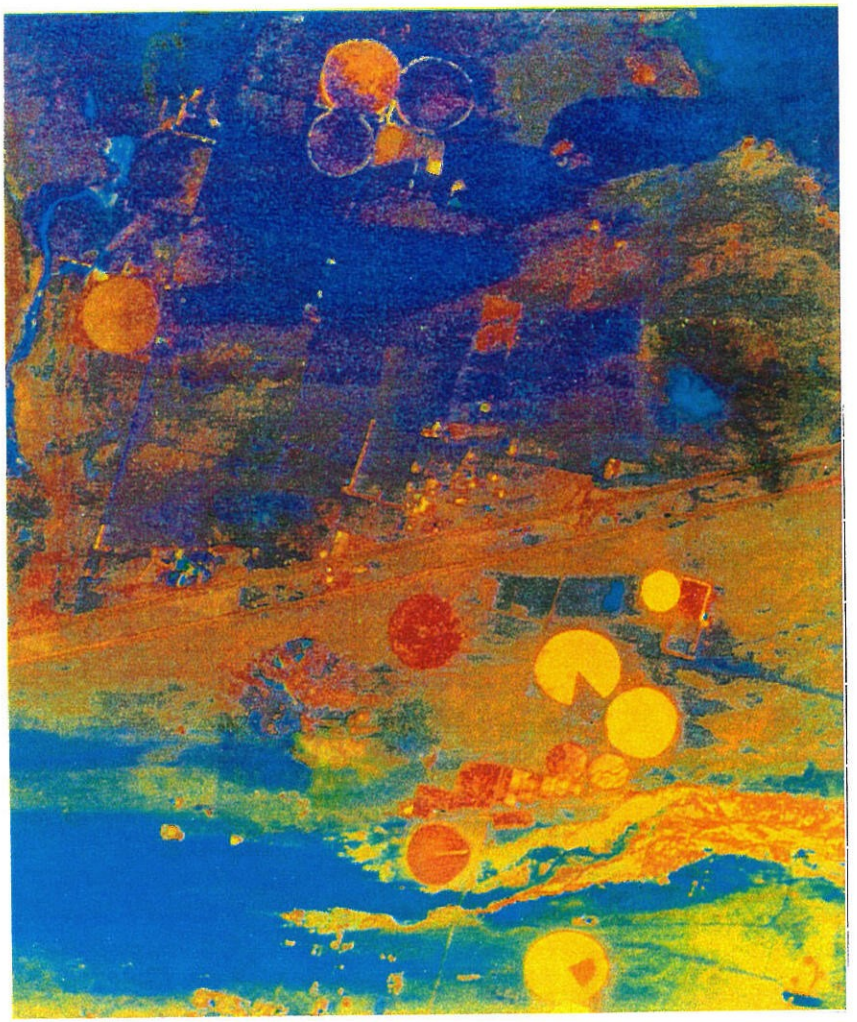

Plate 15: Image of a linear unmixing of abandoned field spectra for the study area. The red endmember is the average spectrum of field 1, abandoned in 1988, the blue endmember is the average spectrum of field 12, abandoned in 1972, excluding the spectrally distinct southwest quadrant.

Plate 16: Spectra Angle Map (SAM) image of study area. Red shows the similarity of the pixel to the average spectrum of field 1, and blue shows the similarity between the pixel spectrum and the average spectrum of field 12. The more intense the color (red or blue) the greater the spectral similarity. The green endmember is the error band from plate 15.

selection of endmembers would lead to a total abundance of significantly less than 1.0. Plate 16 is an image of the spectral angle mapping (SAM) with the same red and blue endmembers as in plate 15. The results are similar to those obtained in plate 15.

Figure 39 is a plot of the two spectral endmembers used for the recently active field and the oldest abandoned field. These spectra are quite similar to each other, with some slight possible differences between 0.4–0.7 μm, where variations in both vegetation cover and the iron oxide absorption in the soil will effect the spectrum. The most visible difference between the two spectra occurs at approximately 2.18 μm, which happens to be the location of a significant absorption feature for cellulose (Elvidge, 1990).

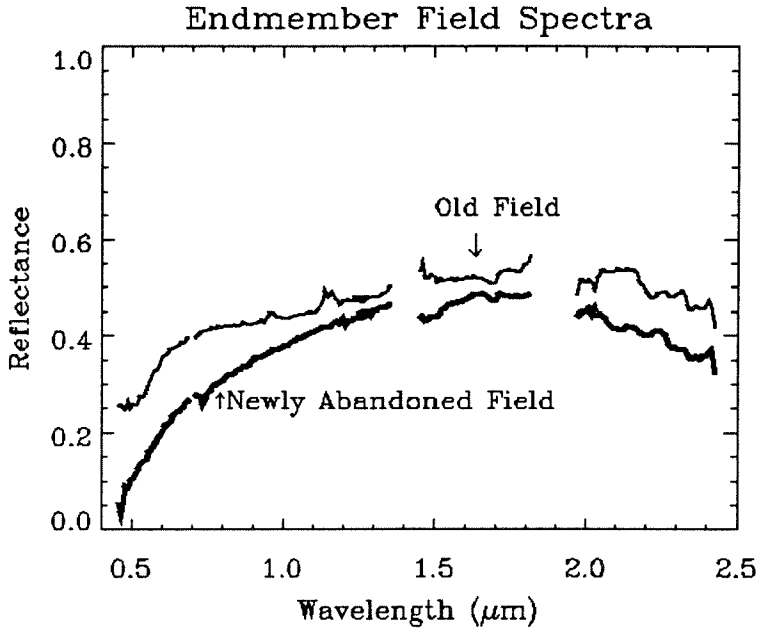

Figure 39: The two endmember field spectra used for the analysis shown in plates 14 and 15. Note the absorption feature in the recently abandoned field spectrum near 2.18 μm.

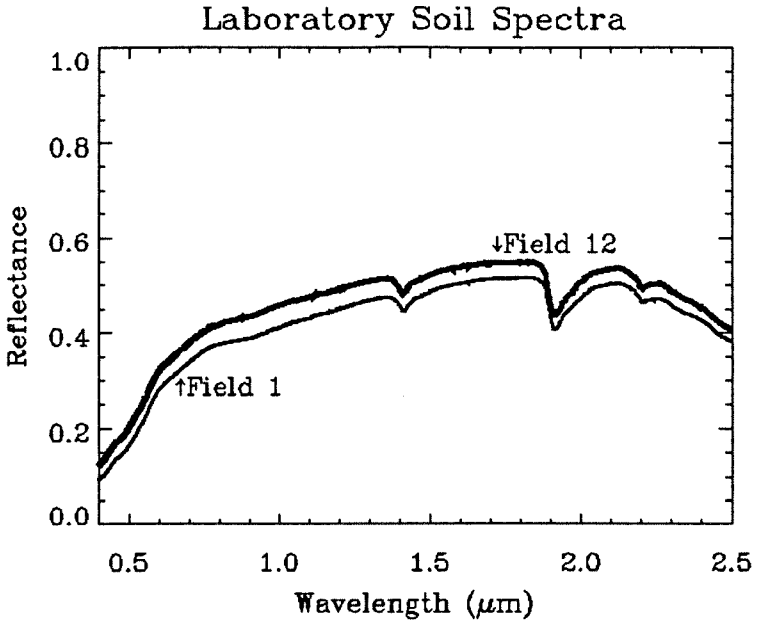

Figure 40: Laboratory spectra of soil samples from fields 1 and 12. Note the clay absorption features at about 1.4 μm, 1.9 μm, and 2.25 μm. There is an iron oxide absorption near 0.6 μm. Note the absence of an absorption feature at 2.18 μm.

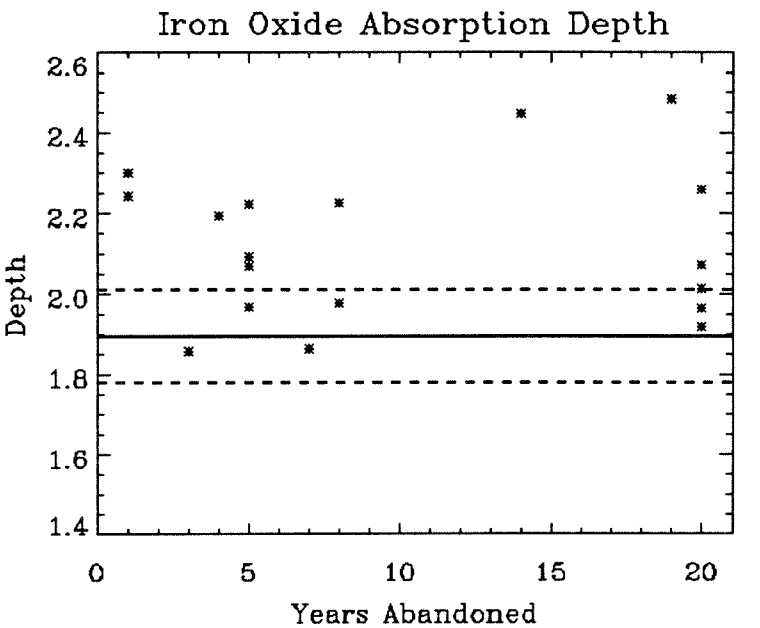

Figure 41: Plot of the depth of the iron oxide absorption feature near 0.6 μm as a function of number of years abandoned. Notice that there is no discernible trend. The solid line is the average value for undisturbed desert soil, with the dashed lines showing the 1σ variance.

Figure 40 show laboratory spectra for fields 1 and 12. Notice that although both laboratory spectra show significant absorption features caused by clay minerals at about 1.4 μm, 1.9 μm, and 2.25 μm, there are no significant absorptions near 2.18 μm, which indicates that there is no mineral in the soil causing the absorption feature. Figure 41 shows a plot of the depth of the iron oxide absorption band near 0.6 μm as a function of the number of years abandoned. There does not seem to be any consistent variation in the depth of this feature with respect to the number of years abandoned, so the presence of the cellulose feature is likely a significant fact in the spectral change observed with increasing time abandoned.

Looking back at figure 16, a picture of field 1 taken on April 13, 1993, a great deal of dead plant material is present, which can account for the strong cellulose absorption for the AVIRIS spectrum for that field. Figure 27, which shows field 12 on the same day, reveals that there is very little dead plant matter on this heavily wind-rippled field. A comparison of figures 16 and 27 also reveals a great deal of difference in live plant cover on these two fields, which may also influence the spectral change, and this effect will now be considered.

Part 4.3.3: *The Vegetation Cover*

Remote sensing vegetation indices are often used to estimate the vegetation cover over areas covered by digital imagery. The rationale behind vegetation indices is more thoroughly discussed in part 5.1. The most commonly used vegetation index is the

Normalized Difference Vegetation Index (NDVI). This can be simply calculated using the following equation:

$$NDVI = \frac{NIR - R}{NIR + R} \qquad (8)$$

where *NIR* is a band located in the near-infrared, and *R* is a band located in the red part of the visible spectrum. Plate 17 shows the NDVI image produced by using the Landsat Thematic Mapper bands synthesized from the AVIRIS data (plate 14). This image has been heavily stretched to show the relatively small differences between the background desert and the abandoned fields. The NDVI values for the active fields are very large, and a standard stretch produces very little contrast in the areas away from the active fields.

Notice that fields 1, 2, and 3 have significantly higher NDVI values than the surrounding desert. The NDVI values on fields 2 and 3 are somewhat heterogeneous, but the average value for the fields is higher than the surrounding desert. Most of the other abandoned fields have lower NDVI values than the surrounding desert. Figure 42 is a plot of the NDVI values, along with 1σ variance bars, against the number of years of abandonment. The NDVI value for the desert is plotted as a solid line, with the 2σ variance shown by dotted lines. This shows that the most recently abandoned fields do indeed have significantly higher NDVI values than the surrounding desert, and the oldest abandoned fields do have significantly lower values than the surrounding desert. It is interesting to note that the three fields abandoned in 1983 all have virtually identical NDVI values. In humid, highly vegetated regions, the NDVI value is directly proportional to the vegetation cover. We shall see, however, this is not the case in arid regions

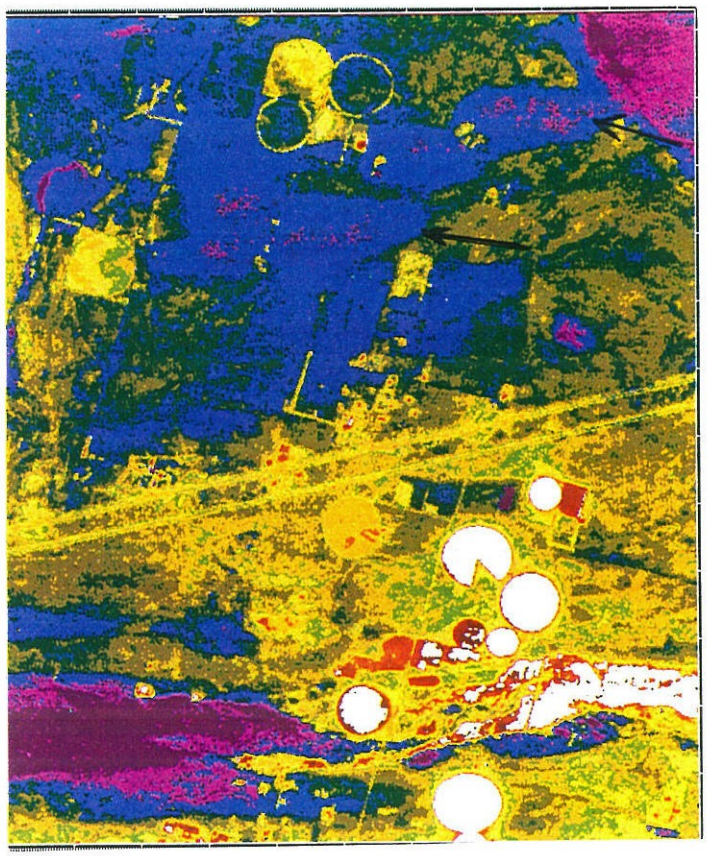

Plate 17: NDVI image from TM data synthesized using AVIRIS data (shown in plate 16). The near-infrared band used was TM 4 and the red band used was TM 3. Higher NDVI values are represented by colors in the red part of the spectrum and lower values by bluer colors. North is to the top of the image. Note the low NDVI areas extending ENE from abandoned fields (arrows).

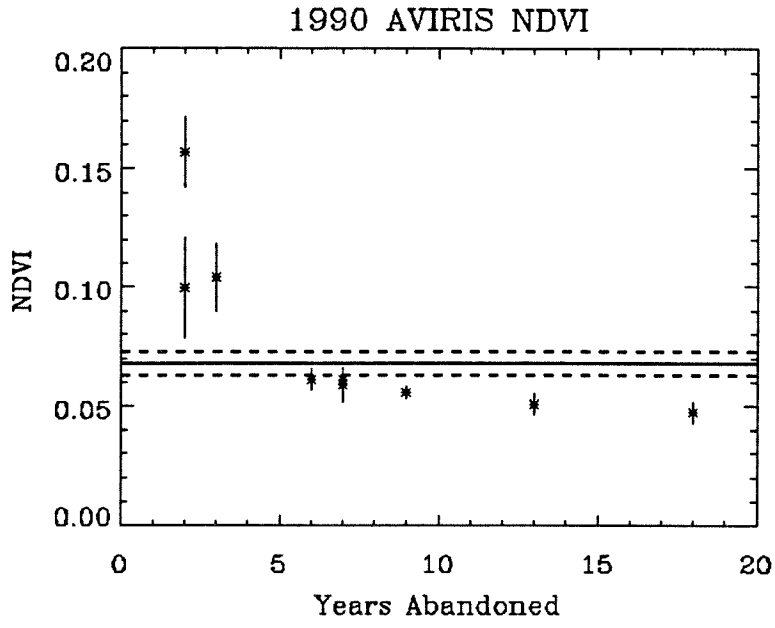

Figure 42: Plot of NDVI values from AVIRIS for abandoned fields as a function of the number of years the fields were abandoned prior to the acquisition of the image. The bars on the points are the 1σ variances. The value for the background desert is shown by the solid lines and the 1σ variance as the dotted lines.

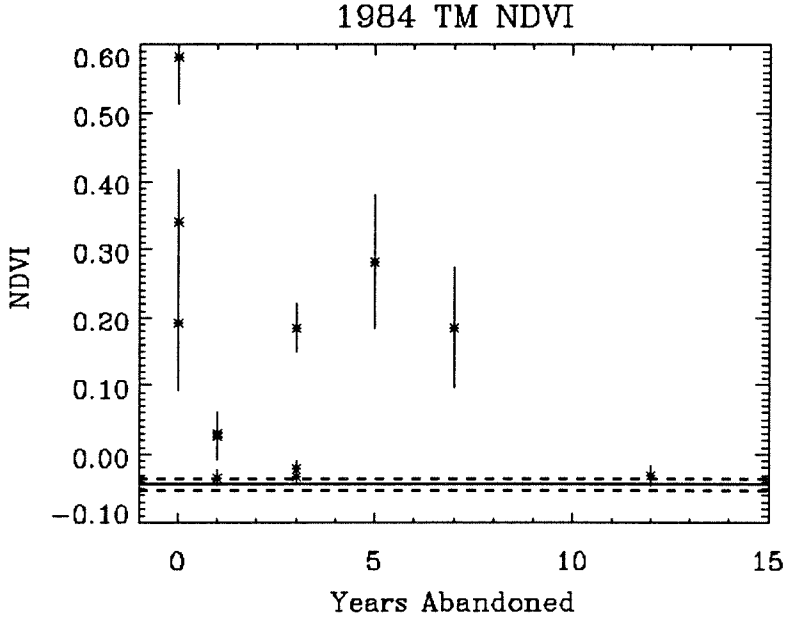

Figure 43: Plot of NDVI values from 1984 TM data for abandoned fields as a function of the number of years the fields were abandoned prior to the acquisition of the image. The bars on the points are the 1σ variances. The value for the background desert is shown by the solid lines and the 1σ variance as the dotted lines.

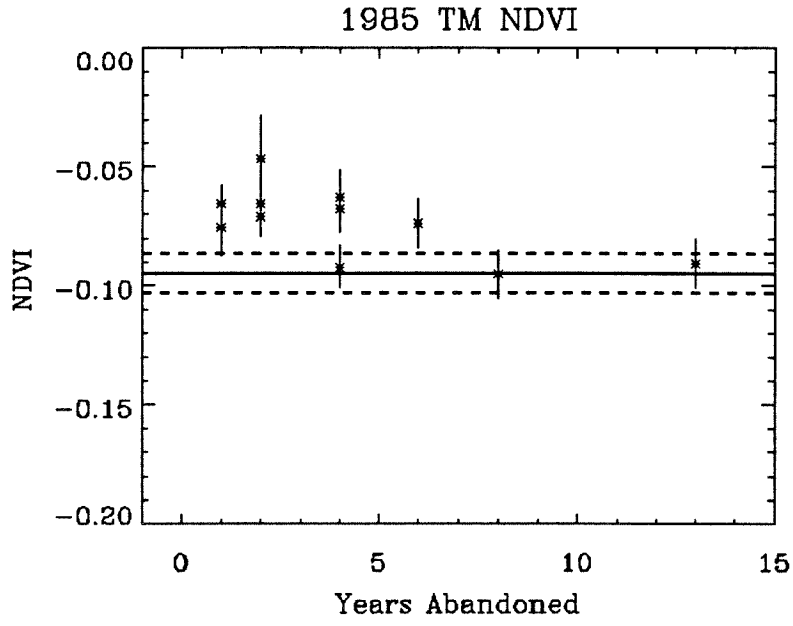

Figure 44: Plot of NDVI values from 1985 TM data for abandoned fields as a function of the number of years the fields were abandoned prior to the acquisition of the image. The bars on the points are the 1σ variances. The value for the background desert is shown by the solid lines and the 1σ variance as the dotted lines.

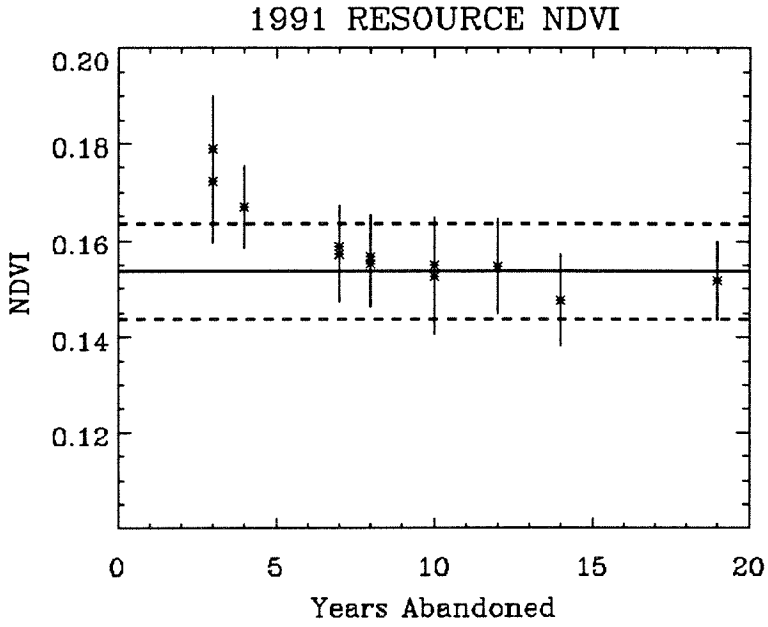

Figure 45: Plot of NDVI values from 1991 RESOURCE data for abandoned fields as a function of the number of years the fields were abandoned prior to the acquisition of the image. The bars on the points are the 1σ variances. The value for the background desert is shown by the solid lines and the 1σ variance as the dotted lines.

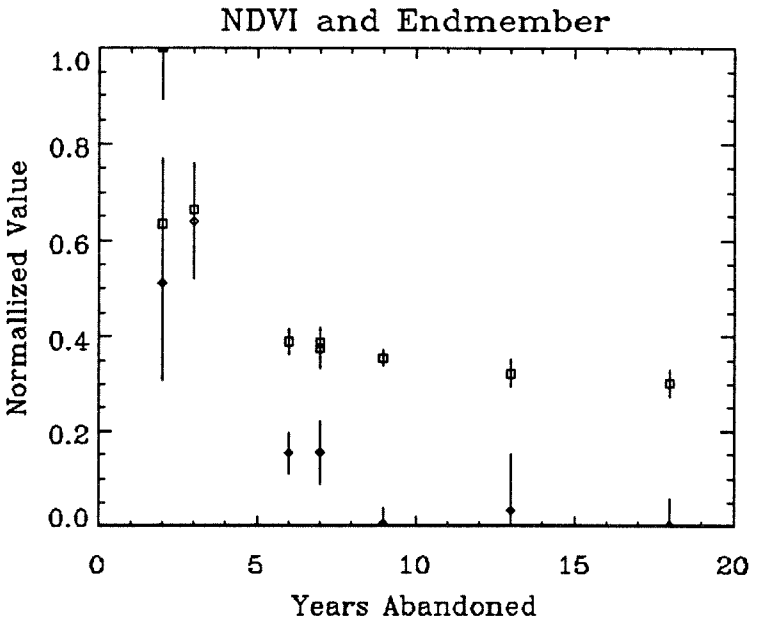

Figure 46: Plot of the recently abandoned field spectra abundance and NDVI values as a function of the number of years abandoned. The squares are the spectra abundance, and the diamonds are the NDVI values. Both sets of values have been plotted so that the NDVI value and the abundance on field 1 are at the same point. The bars show 1s of variance. Note that the NDVI change does not completely account for spectral change.

Figure 43 and 44 show similar NDVI values extracted from the 1984 and 1985 TM images shown in plate 8. The values are plotted as a function of the number of years that the field had been abandoned prior to the acquisition of the image. The same general trend as noted in figure 42 is seen in these figures. The variance on the fields is much higher in the TM data, although the variance in the background desert is much smaller. Figure 45 is a plot of the NDVI values calculated from the Russian RESOURCE data collected in January 1991 as a function of the number of years abandoned. Notice that the overall variance in this data is much higher than in either the TM or AVIRIS data. Even so, the same trend seen in figures 42–44 is still present.

In figure 45, the NDVI values and the abundances of the recently abandoned field spectra from the previous section are both plotted as a function of the number of years abandoned. The plot was performed so that the NDVI and abundance values for field 1 both plot at the same point. Notice that the changes in the spectral abundance are not entirely accounted for by the changes in NDVI. If the NDVI values are proportional to the vegetation cover, this indicates that the spectral changes is due to something more than the change in the amount of plant cover. This argues in favor of the cellulose absorption feature due to dead plant litter as a significant factor in the spectral change shown be the variation in the abundance of the recently abandoned field spectrum.

Part 4.3.4: *The Evidence for Blowing Sand*

In plate 17, there are "plumes" of low NDVI values extending downwind from many of the abandoned fields and from some of the active fields. As shown by table 4 in chapter 2, most of the erosive winds at Daggett Airport blow from directions nearly due west (WNW–WSW). The Soil Conservation Survey of the Mojave River Area of San Bernardino County (Tugel and Woodruff, 1986) lists that the soils in this area are generally very to extremely wind erodible, and hence unsuitable for many uses because of the hazard of soil blowing. In the second part of this chapter, it was shown how wind rippling of the fields explained many of the characteristics of AIRSAR data for the abandoned fields. As discussed in those sections, there was considerable evidence of blowing sand on the ground, with roads being drifted by blowing sand and complaints

from local residents about sand blowing. These considerations suggest that these areas of low NDVI are actually areas covered, or at least affected, by blowing sand.

Plate 18, is a three-color composite of synthesized MSS data, which served as the top of the AVIRIS cube in plate 13. Notice that the low NDVI areas indicated in plate 17 now appear as bright areas. Windblown sand has been recognized by several workers as having a higher albedo due to the loss of fine particles and the fact that dense mafic minerals tend to be more difficult to mobilize (Paisley *et al.*, 1991). A reasonable conclusion is that these areas are zones of wind blown sand. Notice that these areas appear as dark smudges in the synthetic TM band ratio image in plate 14.

Figure 47: Photograph of location A in plate 18. Note the lack of desert grass and of low-hanging limbs in the shrubs.

Plate 18: Landsat MSS image synthesized from AVIRIS data. Red is MSS band 7, green is MSS band 5, and blue is MSS band 4. Notice the bright areas extending east from several of the abandoned fields. The letter A indicates the location of figure 47.

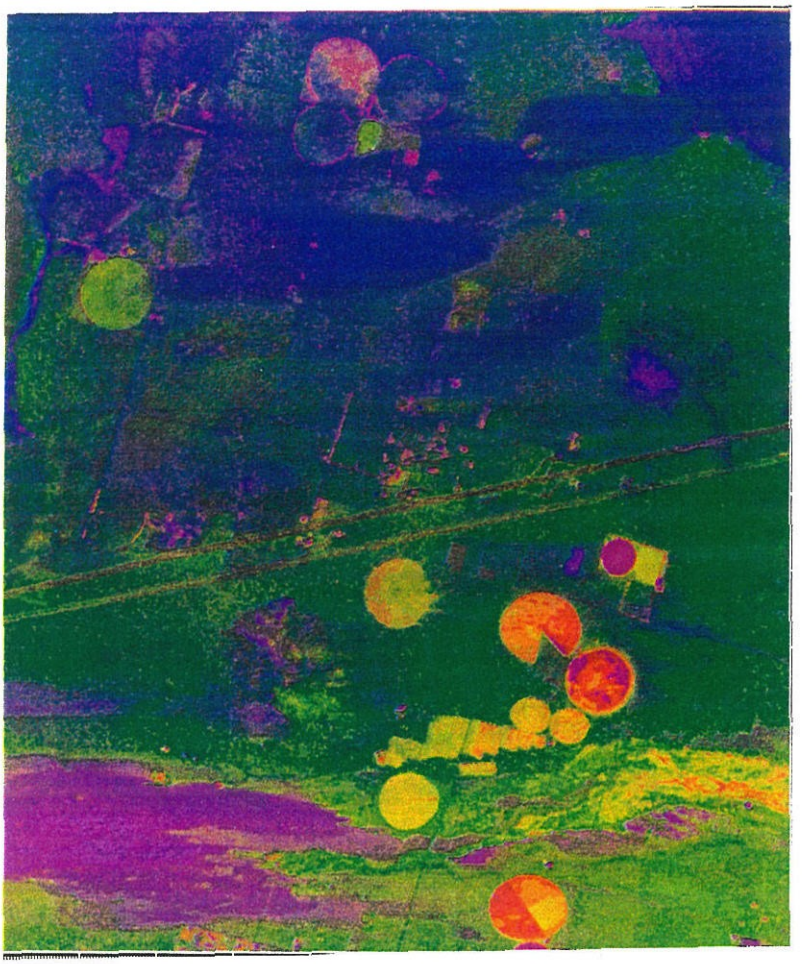

Plate 19: Linear unmixing using the spectrum from an area of undisturbed desert and from one of the areas of blown sand as endmember. The blown sand is shown in blue and the undisturbed desert as green. The red is the error to the fit.

Figure 47 is a ground photograph located at point A in plate 18. Notice the lack of small grass and of low limbs with leaves in the shrubs, and the presence of partially stabilized sand dunes. Wind ripples can be clearly seen in the foreground. The discussion of wind erosion in chapter 1 mentioned that one of the byproducts of wind erosion is damage to vegetation from the abrasive action of blowing sand and the burial of small plants that cannot outgrow the continuing deposition of sand. This lack of small vegetation and the apparent damage to parts of the shrubs within the saltation layer, provides further evidence of wind erosion.

Plate 19 shows the results of performing a linear unmixing using the area of blowing sand downwind of field 12 as the blown sand endmember (blue) and an area of undisturbed desert as the desert endmember (green). Naturally, the active alfalfa fields do not look much like either blown sand or undisturbed desert, so the error in the fit is large for those areas. Notice that all of the areas identified as a high abundance of blown sand, are the areas identified as blowing sand in plate 18 and as areas of low NDVI in plate 17.

The results of the linear unmixing depend on the albedo, so it is possible that all the linear unmixing is seeing is the effect of albedo. However, very similar results are shown by Spectral Angle Mapping (SAM), which only depends on the shape of the spectra. It should also be recognized that the same calculations for one member are completely separate from those for the other endmember, which is not the case in linear unmixing. The respective endmember spectra are plotted in figure 48. Notice that the blown sand does have a generally higher albedo than the undisturbed desert. The

separation between the two spectra in figure 48 gets smaller at wavelengths shorter than about 0.8 μm, and this is the only obvious difference in shape between these spectra.

A reasonable objection to the unmixing and SAM results above is to point out that the above results may only be saying, in essence, that all of the areas that look like blowing sand in plate 18 look alike. This is not truly news, as the human eye can see that these areas look alike in plate 18. Figure 49 shows two field spectra of in-situ soil samples from the Manix Basin field area. One is from the area of blown sand near field 12, and the other is from the undisturbed desert. Notice that the relationship between these two spectra is similar to that in the spectra shown in figure 48. Figure 50 shows a SAM image of the blown sand endmember based on the field spectrum, and the similarity between this and the blue component in plate 19. This provides a stronger argument for the validity of the unmixings in plate 19, and it also indicates that the spectral difference between the areas of blown sand and the undisturbed desert is not solely due to the lack of vegetation in areas of blown sand. The convergence of the two soil spectra in figure 49 is probably due to a difference in the iron oxide content of the blown sand compared to the undisturbed desert.

Figure 51 is a close-up of the blown sand endmember of the SAM image in figure 50 encompassing two active fields between I-15 and the Mojave River. Notice the double-pennant area identified as blown sand to the east of the larger complete circular field. This shows the effect of two factors controlling the amount of sand removed from a surface undergoing wind erosion. The amount of sand removed from an area by wind erosion is directly proportional to the length of the area from which sand can be mobilized

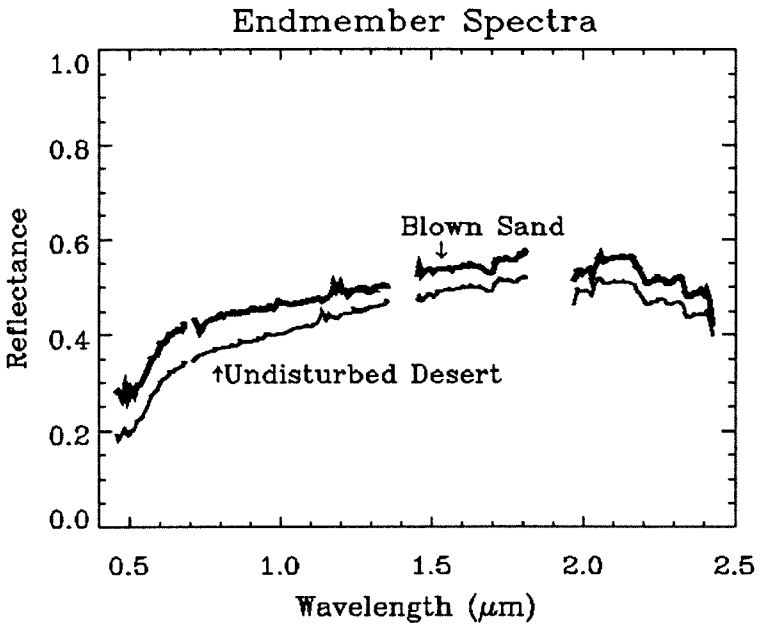

Figure 48: Plots of the two spectra used as endmembers in plate 19. The "undisturbed desert" spectrum is the green component of those plates, and the "blown sand" spectrum is the blue component.

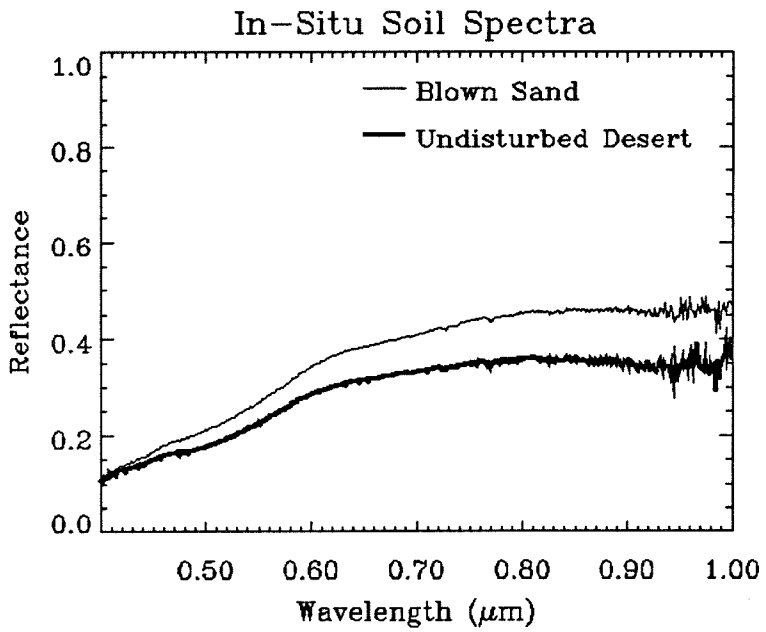

Figure 49: Plot of in-situ field reflectance spectra of blown sand and undisturbed desert soil. The blown sand spectrum above is the spectral endmember plotted in figure 50.

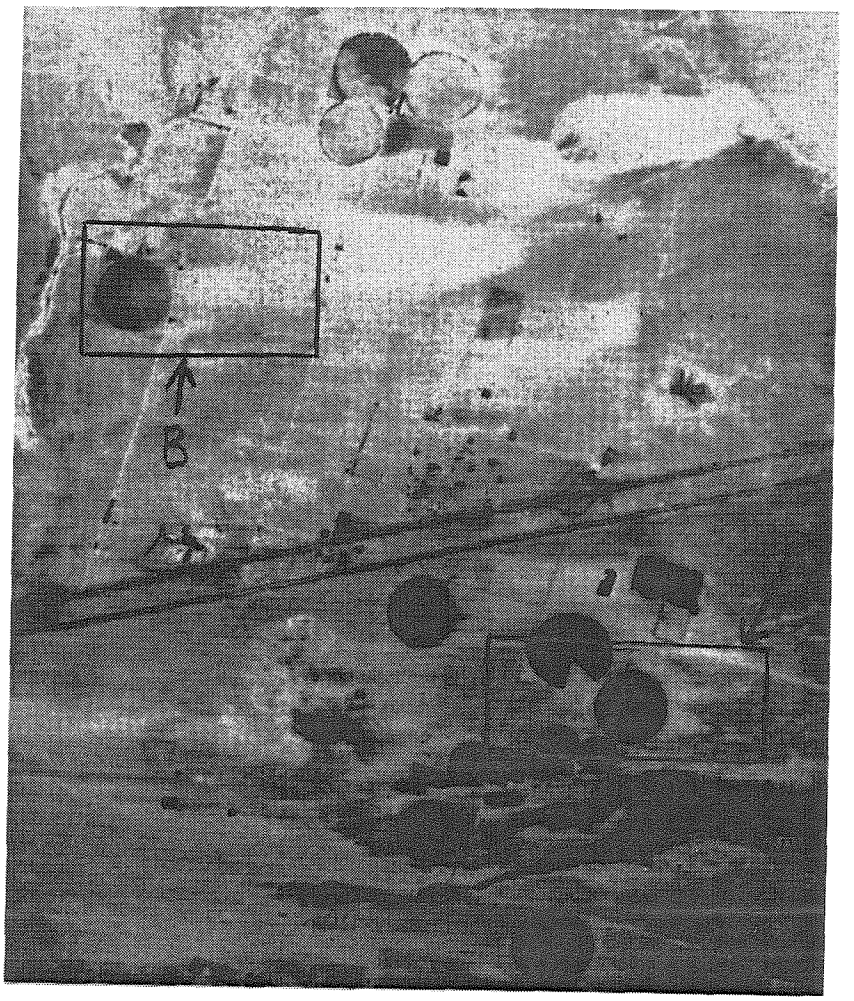

Figure 50: Spectral Angle Map (SAM) image of the blown sand endmember from figure 49. Brighter regions are regions most spectrally similar to the "blown sand" spectrum in figure 49. Note the similarity to the blue endmember in plate 19. Squares A and B are the areas shown as close-ups in figures 51 and 53 respectively.

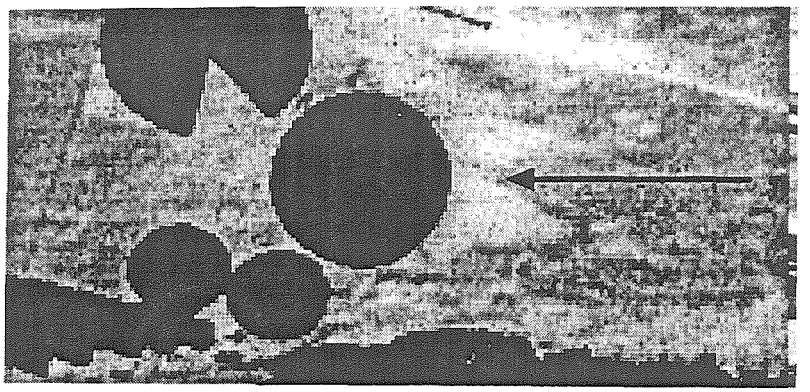

Figure 51: Close-up of box A in figure 50. Notice the odd double-pennant shape of the area of blown sand downwind of the active field (arrow).

a) b)

Figure 52: Circular fields experiencing wind erosion and the shapes of the resulting sand plumes. The prevailing winds blows from left to right in both cases. a) Bare field. The plume of blown sand narrows downwind since more sand can be removed along the field diameter than along the other chords. b) Field with concentric rows of cultivated crops. As the wind blows across the diameter of the field it constantly encounters rows of plants perpendicular to it's direction. This strongly retards erosion along the field diameter, leading to the double-pennant shape shown here and in figure 51.

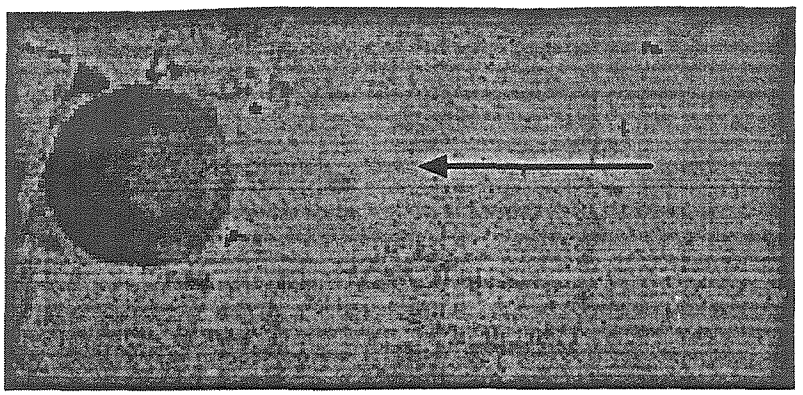

Figure 53: Close-up of box B in figure 50 showing a long, narrow patch of blown sand extending from abandoned field (arrow). There are valleys in the Calico Mountains just west of the field which approximately parallel the long axis of this patch of blown sand which would tend to channel airflow along that particular direction.

(Chepil, 1945; Woodruff and Siddoway, 1965; Holý, 1980). As show in figure 52a, this means that the most sand will be removed along the diameter of the field parallel to the wind direction, with much less removed along the edges. This explains why the patches of blown sand narrow in the downwind direction.

The presence of rows of actively growing vegetation is well known to decrease the amount of soil eroded by wind erosion, and that rows of vegetation oriented perpendicular to the wind are the most effective (Woodruff and Siddoway, 1965; Holý, 1980). Figure 52b shows that wind crossing the diameter of a field cultivated with concentric rows confronts perpendicular rows at every point across the field. This explains why the region of blown sand downwind of this active field gets shorter as the center of the field is approached. The advantage of circular cultivation is shown strongly here, not only does it provide equal protection from winds in all directions, it also provides the best protection along the part of a center-pivot field where the most sand would be removed.

Figure 53 shows a peculiar long, narrow strip of blowing sand extending downwind of one of the abandoned fields. This seems to be in conflict with the assertion of Holý (1980) that wind erosion does not affect the land in strips in the prevailing direction of the fluid flow. A focusing of wind along this particular line could explain this unusual feature. Looking back at figures plates 8–11, 16 and 20, a series of small valleys in the Calico Mountains just west of this abandoned field can be seen oriented in a direction very similar to that of this long sand strip, which may provide a channeling and focusing of wind. An examination of plates 16, 19 and 20 and figures 50 and 53 shows that this long string of sand originates on the field at the lowest point of the NDVI gradient on that field. This long strip of blown sand probably formed when strong winds funneled down the valleys in the Calico Mountains struck and area of very low vegetation on this abandoned field.

Looking back at plates 16, 20–22 and figure 50 we see the long regions of blowing sand extending from older abandoned fields. The very long region extending westward from the pair of adjoining fields 6 and 7 is due to the long area for mobilization provided by two adjoining abandoned fields. For fields 2, 4, and 5, the windbreak provided by the trees planted around the fields has clearly protected these fields from extensive soil loss. The trees along the downwind edge of the fields may slow the flow of wind along that edge of the field so that soil is not completely blown from the fields.

The sequence of abandoned fields in the Manix Basin Area provided the opportunity to observe fields in various stages of degradation each time a remote sensing instrument collects data over the area. Chapter 3 showed how scratching by humans on

the Earth's surface can be detected and characterized with a snapshot of data covering the area. This chapter showed how these snapshots of abandonment provide a view of land degradation showing that abandoned fields are experiencing continued land degradation, primarily due to wind erosion, even after human activity has been suspended. There is also evidence of land degradation in the form of wind erosion from active fields. These snapshots of degradation also showed the close tie between wind erosion and vegetation cover. In chapter 6, the time series of MSS imagery will be used to show the degradation over time, but first, the problem of measuring arid region vegetation needs to be considered in more detail.

Chapter 5: *Measuring Arid Region Vegetation*

It is essential to develop affordable techniques to monitor both where degradation has occurred and what areas are most at risk for further degradation due to erosion. The efficient and accurate measurement of arid region vegetation cover is the key to this problem. In addition, accurate knowledge of the vegetation cover in arid regions will allow hydrological fluxes in arid regions to be better constrained. Arid region plants are well-adapted to the hot, dry environment in which they live, and these adaptations, designed to conserve water and prevent overheating, have important consequences for visible and near-infrared reflectance sensing. These adaptations and dramatic variations over time, and between species, makes the standard vegetation indices useless for quantitative determinations. This chapter will demonstrate that the unique spectral features of arid vegetation necessitate higher spectral resolution data for monitoring arid regions, than for humid regions, and will identify specific parts of the spectrum to be emphasized in vegetation indices attuned to arid regions.

Part 5.1: *Vegetation Indices*

The following section discusses the basic spectral features of green vegetation and describes how the vegetation indices using broad-band remote sensing data have been developed. This section will also show that imaging spectroscopy, or at least remote sensing that uses narrow spectral bands, improves the measurement of vegetation cover. A further discussion of vegetation indices from a slightly different angle is provided in Appendix B.

Work on the spectral properties of plants began as early as 1913 when Willstätter and Stoll proved that light entering leaves is critically reflected internally at the cell walls where the refractive index changes from that of water (1.33) to that of air (1.00). This leads to highly efficient scattering of all wavelengths of light. Gates *et al.* (1965) performed some of the earliest work which treated the spectral properties of plants from the ultraviolet through the thermal infrared. Table 8 summarizes the absorptions features of some kay plant materials. Figure 54 shows the typical reflectance spectrum of green leaves in the spectral range of the visible and near- to mid-infrared (0.4 μm–2.5 μm). Plant pigments such as chlorophyll strongly absorb light in the visible, and the liquid water in plant leaves absorbs much of the light at wavelengths longer than 1.4 μm. This contrasts with strong reflectance in the near-infrared in the range from 0.75 μm through about 1.4 μm, wavelengths at which plant materials are relatively transparent.

Table 8: Absorption Features of Some Key Plant Materials (data from Gates, 1980 and Elvidge, 1990)	
Material	**Wavelength (μm)**
α-carotene	0.42–0.5
Arabinogalactan	0.99, 1.21, 1.45, 1.55, 1.74, 1.93, 2.10, 2.28, 2.32, 2.50
B-glucan (a hemicullulose)	1.45, 1.77, 1.93 2.09, 2.33, 2.50
Carnauba wax	0.93, 1.04, 1.21, 1.39, 1.41, 1.54, 1.73, 1.82, 1.93, 2.01, 2.05, 2.14, 2.31, 2.35, 2.39, 2.43
Cellulose	1.48, 1.93, 2.10, 2.28, 2.34, 2.48
Chlorophyll-a	0.38–0.45, 0.675
Chlorophyll-b	0.41–0.47, 0.61
D-ribulose 1,5-diphosphate carboxylase	1.50, 1.68, 1.74, 1.94, 2.05, 2.17, 2.29, 2.47
Humic Acid	0.4–0.7, 1.92, 2.30, 2.34
Lignin	1.45, 1.68, 1.93, 2.04–2.14, 2.27, 2.33, 2.38, 2.50
Lutein (a xanthophyll)	0.4–0.5
Pectin (apple)	1.44, 1.72, 1.92, 2.09, 2.24, 2.36, 2.48
Pectin (citrus)	0.98, 1.19, 1.44, 1.56, 1.68, 1.73, 1.78, 1.93, 2.08, 2.25, 2.32, 2.36, 2.48
Protochlorophyll	0.41–0.47,0.58
Starch	0.99, 1.22, 1.45, 1.56, 1.70, 1.77, 1.93, 2.10, 2.32, 2.48
Tannic Acid	0.99, 1.12, 1.46, 1.66, 1.93, 2.13, 2.26, 2.32, 2.50
Xylan (a hemicellulose)	1.21, 1.45, 1.72, 1.79, 1.93, 2.09, 2.26, 2.33, 2.50

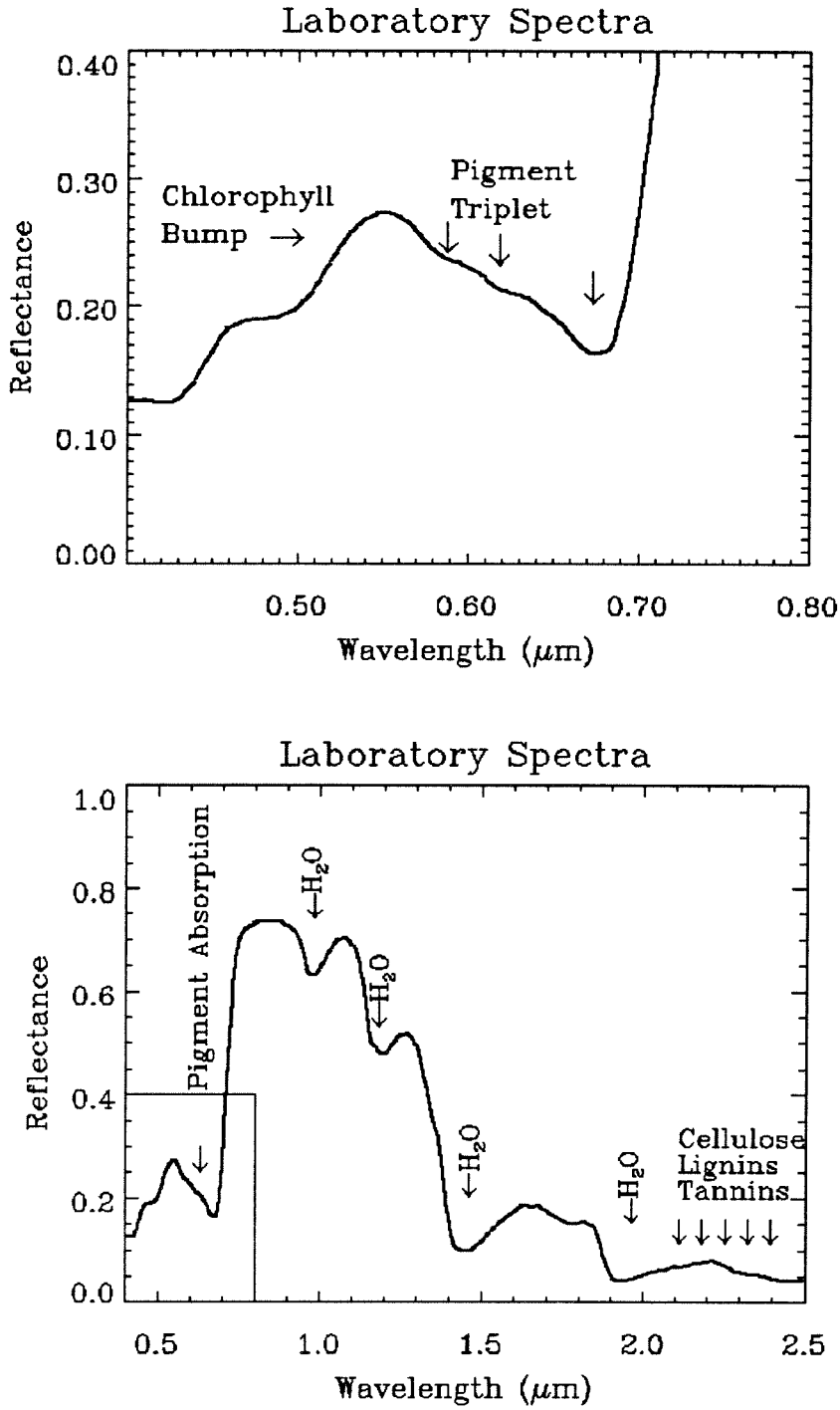

Figure 54: Typical green vegetation spectrum. Upper plot is an enlargement of the boxed region. Notice how the pigment absorption in the visible is actually caused by a triplet of pigment absorptions. The strong reflectance from 0.8–1.2 μm is caused by strong scattering from cell walls. Liquid water in the leaf is the most important absorber beyond 1.0 mm, but several plant materials have significant absorptions between 2.02.5 μm. Table 8 provides more information about the absorption locations of plant materials.

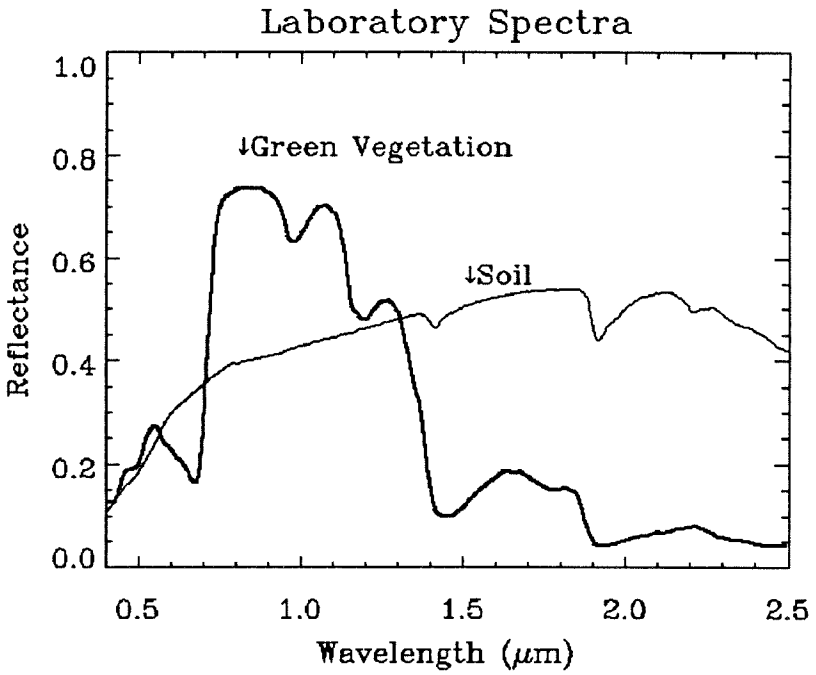

Figure 55: Green vegetation and soil spectra for the range 0.4–2.5 μm. Notice how the change in reflectance between the visible and the near-infrared is much smaller for the soil than for the green vegetation.

Much attention in the remote sensing of green vegetation is focused on the strong reflectance contrast between the visible and the near infrared (NIR) which forms a strong step in the spectrum of green vegetation which is often referred to as the "red edge." In figure 55 the spectrum of a soil is plotted for comparison with the green leaf spectrum. Notice that while there is some difference in the red and near-infrared reflectances of the soil (with the near-infrared being slightly higher) the difference is much smaller that that for plants.

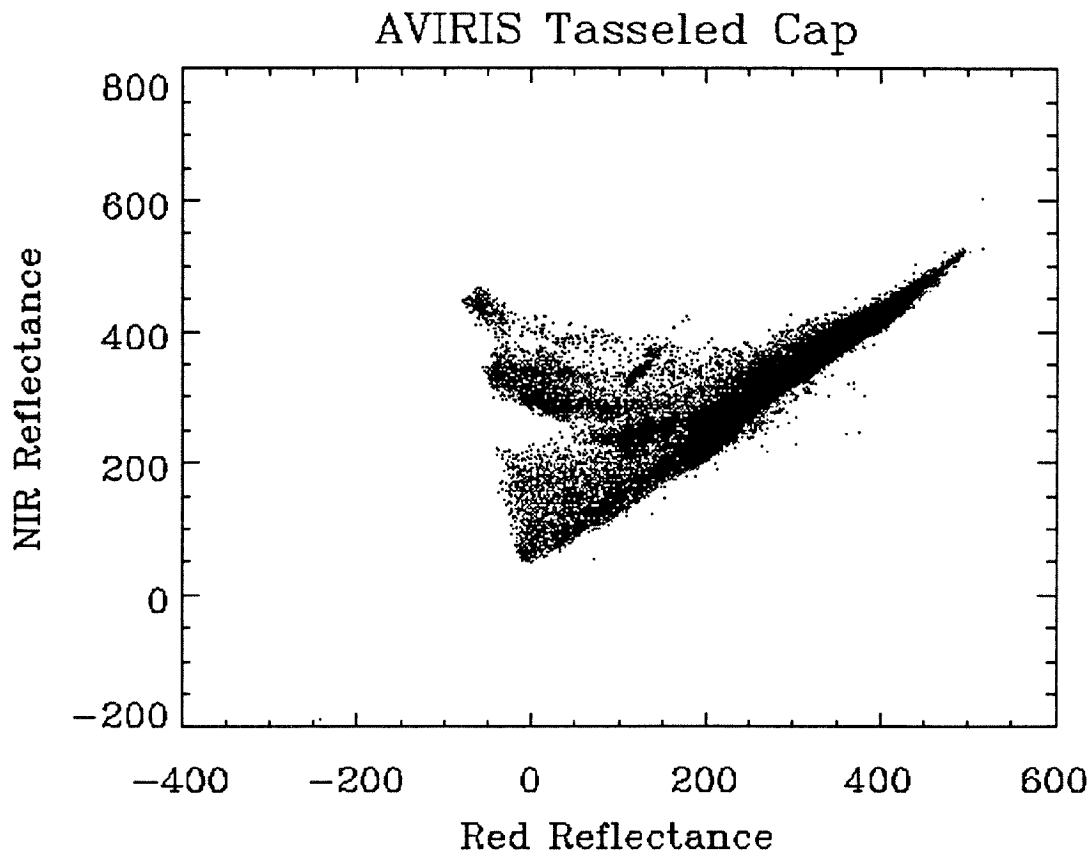

Figure 56: In this scatter diagram, NIR (0.755 μm) and red (0.674 μm) reflectances (normalized to 1000) are plotted for each pixel from an AVIRIS image. The lower right boundary of this sort of plot is taken to be formed by pixels containing only bare soil, and this boundary is referred to as the soil line. The "tip" opposite the soil line, which has high NIR reflectance and low red reflectance, is taken to be where pixels completely covered with vegetation plot on this diagram. All pixels covered by a mixture of bare soil and vegetation will plot between these two extremes. This sort of figure is sometimes called a tasseled-cap, because of its shape.

One consequence of the distinctive green vegetation spectrum is shown in figure 56. The lower right edge of the data point cloud forms a boundary which is generally identified as the soil line. There is also a tip to the graph opposite the soil line due to a strong NIR reflectance and a relatively weak red reflectance which is characteristic of green vegetation, and this point is defined as the green vegetation point. Points partly covered by green plants and partly covered by soil will plot between the bare soil line and the vegetation point. This figure was referred to by Kauth and Thomas (1976) as the "tasseled cap-agram" and is commonly known as the tasseled cap.

There have been two general approaches taken to develop indices for measuring green vegetation cover based on the characteristics of the tasseled cap. The first approach is to measure the distance between where the pixel plots in the tasseled cap plot from the soil line. The soil line is used because it is generally easier to find than the 100% vegetation point. The perpendicular vegetation index (PVI) of Richardson and Wiegand (1977) assumes that the perpendicular distance of the pixel from the soil line is linearly related to the vegetation cover. This index is calculated as follows:

$$PVI = \sin\alpha\,(NIR) - \cos\alpha\,(red) \qquad \textbf{(9)}$$

where NIR is the near-infrared reflectance, red is the red reflectance and α is the angle between the soil line and the near-infrared axis. This means that the isovegetation lines (lines of equal vegetation) would all be parallel to the soil line. A special case of this is the vegetation index (VI) mentioned by Lillesand and Kiefer (1987) which has more recently been christened the difference vegetation index (DVI) by Richardson and Everitt (1992):

$$VI = DVI = NIR - red. \qquad \textbf{(10)}$$

This case occurs when the soil line has a slope of 1.0.

The next possibility is to assume that the isovegetation lines all intersect at a single point. As the first approximation, Jordan (1969) developed the ratio vegetation index:

$$RVI = \frac{NIR}{red}. \tag{11}$$

RVI itself is no longer generally used in remote sensing. Instead a index known as the normalized difference vegetation index (NDVI) is used. This index is functionally identical to the RVI, and it can be written as:

$$NDVI = \frac{NIR - red}{NIR + red} = \frac{RVI - 1}{RVI + 1}. \tag{12}$$

Both RVI and NDVI basically measure the slope of the line between the origin of red-NIR space and the red-NIR value of the image pixel. The only difference between RVI and NDVI is the range of values that the two indices take one. The range from -1.0–1.0 for NDVI is easier to deal with than the infinite range of the RVI. NDVI can also be considered to be an improvement of DVI which eliminates effects of broad-band red-NIR albedo through the normalization. Crippen (1990) recognized that the red radiance subtraction in the numerator of NDVI was irrelevant, and he formulated the infrared percentage vegetation index (IPVI):

$$IPVI = \frac{NIR}{NIR + red} = \frac{1}{2}(NDVI + 1). \tag{13}$$

IPVI is functionally equivalent to NDVI and RVI, but it only ranges in value from 0.0–1.0. It also eliminates one mathematical operation per image pixel which is important for the rapid processing of large amounts of data.

Huete (1988) suggested a new vegetation index which was designed to minimize the effect of the soil background, which he called the soil-adjusted vegetation index (SAVI). This vegetation index takes the form:

$$SAVI = \frac{NIR - red}{NIR + red + L}(1 + L). \quad \textbf{(14)}$$

Huete showed evidence that the isovegetation lines do not converge at a single point, and he selected the L-factor in SAVI based where lines of a specified vegetation density intersect the soil line. The net result is an NDVI with an origin not at the point of zero red and near-infrared reflectances. For high vegetation cover, the value of L is 0.0, and L is 1.0 for low vegetation cover. For intermediate vegetation cover L=0.5, and that is the values which is most widely used. The appearance of L in the multiplier causes SAVI to have a range identical to the of NDVI (-1.0 – 1.0). Huete (1988) suggested that SAVI takes on both the aspects of NDVI and PVI.

Qi *et al.* (1994a) developed a vegetation index which is basically a version of SAVI where the L-factor is dynamically adjusted using the image data. They referred to this index as the Modified Soil Adjusted Vegetation Index or MSAVI. The factor L is given by the following expression:

$$L = 1 - 2 \times slope \times NDVI \times WDVI \quad \textbf{(15)}$$

where WDVI is the Weighted Difference Vegetation of Clevers (1988) which is functionally equivalent to PVI and calculated as follows:

$$WDVI = NIR - slope \times red.$$

The *slope* used in both of the preceding equations is the slope of the soil line which is determined as described above. Qi *et al.* (1994a) also created an iterated version of this vegetation which is called MSAVI2:

$$MSAVI2 = \frac{1}{2}\left(2(NIR+1) - \sqrt{(2\times NIR+1)^2 - 8(NIR-red)}\right). \qquad \textbf{(16)}$$

This was developed by substituting 1-MSAVI(n-1) as the L factor in MSAVI(n), and then inductively solving MSAVI(n)=MSAVI(n-1). Note that all of these kinds of vegetative indices use only two filter passbands — red and near-infrared.

One important difficulty which has been encountered in using the vegetation indices which attempt to minimize the effect of a changing soil background is an increase in the sensitivity to variations in the atmosphere (Leprieur *et al.*, 1994; Qi *et al.*, 1994b). There have been several approaches in the development of vegetation indices which are less sensitive to the atmosphere, such as the Atmospherically Resistant Vegetation Index (ARVI) of Kaufman and Tanré (1992) and the Global Environmental Monitoring Index (GEMI) of Pinty and Verstraete (1991). Chehbouni (1994, personal communication) has data demonstrating that GEMI is highly sensitive to soil noise. Qi *et al.* (1994b) demonstrated that soil noise caused GEMI to violently break down at low vegetation covers, and that all of the vegetation indices designed to minimize the effect of the atmosphere have increased sensitivity to the soil, which makes these indices completely unsuitable for arid regions.

There are still specialists trying to develop vegetation indices using two band combinations other than the NIR-red. Pickup *et al.* (1993) proposed an index similar to PVI which made use of MSS bands 4 and 5. Although Pickup *et al.* (1993) claimed that it

was highly effective at detecting both dry and green vegetation, this band combination would be sensitive to the iron oxide absorption feature present in many soils. The detection of dry and green vegetation with this index, which is called PD54, is probably due to the fact that vegetation cover would obscure this feature, but this feature can also be highly variable in many soils.

Jackson (1983) showed how a set of *n* bands could be used to construct a perpendicular vegetation index. The basic procedure is to pick two or more soil points to define a soil line in *n*-space and then to use Gram-Schmidt orthogonalization to find the "greenness" line which passes through the 100% vegetation cover point and is perpendicular to the soil line. Two of the indices, both known as the Green Vegetation Index, have seen considerable use. A four-band GVI, for use with MSS data, was developed by Kauth and Thomas (1976), and a six-band version was developed for TM data by Crist and Cicone (1984).

An extremely important point to realize about the soil line used in many of these vegetation indices is that the soil line will be different for different areas, and the soil line will vary for different NIR and red bandpasses. Table 9 gives the slope and intercept for the soil line calculated from AVIRIS data for different bandpasses. The clear implication is that the only truly valid way of making use of a vegetation index which uses a soil line is to compute the soil line for each image. If a good calibration is available, calculating the soil line for each target for each instrument once might suffice. Of course, even the assumption that all of the bare soil spectra in a single image form a line may also be inaccurate, and this possibility will be examined later in this chapter.

Table 9: Red-NIR Soil Line Parameters for AVIRIS Data Sampled at Different Bandpasses

Instrument Simulated	Red Bandpass μm	NIR Bandpass μm	Slope	Intercept
MSS	0.6–0.7	0.8–1.1	0.9034	52.95
TM	0.63–0.68	0.8–0.9	0.7939	71.39
AVIRIS	0.674	0.755	0.8863	55.00

Elvidge and Chen (1995) found that SAVI and PVI consistently provided better estimates of LAI and percent green cover than did NDVI or RVI. They also found that there was a steady improvement in all of these vegetation indices as narrower and narrower bands were used for the near-infrared and red reflectances, with SAVI being the best index at the very narrowest bandwidth. The advantage of narrow bands for use with vegetation indices provides additional arguments for the use of high spectral resolution remote sensing as discussed in chapter 4.

The advent of imaging spectroscopy in remote sensing opens up the possibility of using the entire spectrum of the target pixel to measure vegetation cover. Elvidge and Mouat (1988) and Elvidge and Chen (1993) showed that trace quantities of green vegetation could be detected in data acquired by the JPL AVIRIS instrument. The red edge was found to be a persistent feature down to less than 5% green cover. However, these detections were made in areas with a relatively uniform soil background (Elvidge and Chen, 1993).

Elvidge and Chen (1995) investigated the feasibility of a vegetation index based on high spectral resolution data. The first of these indices used the first derivative of the spectra. The first derivative vegetation index (1st DGVI) was calculated by integrating the first derivative of the spectra from 0.626 μm to 0.795 μm as shown in figure 57. The next vegetation index tested by Elvidge and Chen (1995) used the integral of the absolute value of the second derivation of the target spectrum over the same range as used for the 1st DGVI. This second derivative green vegetation index 2nd DGVI was found to be superior to SAVI and PVI at estimating LAI and percent green cover, while the 1st DGVI was inferior to SAVI and PVI. They found that they could produce a vegetation index superior to 2nd DGVI by integrating the departures in the first derivative spectrum from a baseline given by the first derivative of the reflectance at 0.625 μm. This local baseline 1st DGVI had the most linear relationship with LAI and percent green cover of any of the vegetation indices tested. They found that there was no gain in using a local baseline for the 2nd DGVI. The local baseline correction to the 1st DGVI seems to eliminate the overall slope observed in the spectrum of nearly all materials from the ultraviolet to the near-infrared, and since this would cause a DC shift in the first derivative, it should be absent in the second derivative.

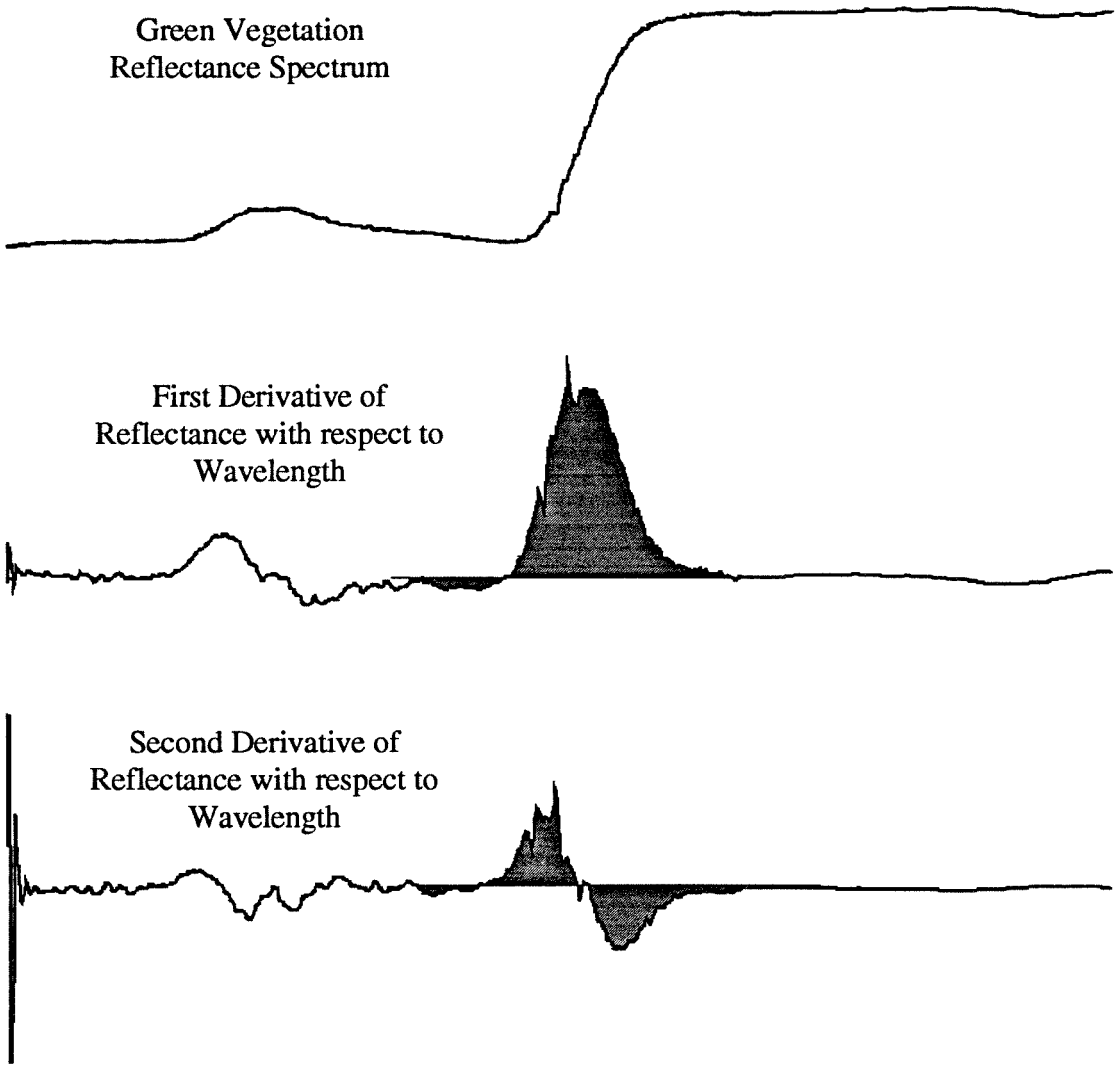

Figure 57: The spectrum of a green leaf (top) and its first and second derivatives (middle and bottom). The shaded regions on the first and second derivative spectra is the area used for the derivative-based vegetation indices of Elvidge and Chen (1995).

It should be noted that all of these vegetation indices are fundamentally based on empirical measurements and correlation between the vegetation index and vegetation cover found with on-site investigation. The adjustment performed to produce SAVI was justified by Heute (1988) by using basic radiative transfer, but it was initially constructed from experimental data. There has been no success at relating vegetation index values to plant cover on the basis of actual soil and plant spectra included in a rigorous radiative scattering model. Results like those of Elvidge and Chen (1995) show that different soil backgrounds give different vegetation index values for the same cover of a given plant type. It is likely that different plant types may also give different vegetation index values for the same plant cover.

All of these vegetation indices are dependent on the presence of the red edge feature. The red edge is due to the distinctive spectral properties of green leaves which contain pigments which strongly absorb visible wavelengths while remaining highly transparent in the near-infrared, and also due to strong scattering from leaf cell walls as photons try to travel from the water-rich cells into the air-filled intercellular spaces. Clearly, the ideal target plant for these indices is one with large leaves with high water content and high pigmentation, and little soil or stem structure visible in the overhead view.

Part 5.2: *Differences Between Arid and Humid Vegetation*

> *A number of forms are to be found in every desert, having structural features which give them a distinct aspect, and it is to these that reference is usually made in the characterization of the flora of any arid region. Such plants have many physiological capacities definitely suitable for activity during the drier seasons, and may in fact remain inactive in the periods furnishing conditions suitable for the activity of mesophilous forms. It is the origination of the qualities and characters which distinguish these species that invites attention in the present connection.* (Spalding, 1909)

Plants native to the arid regions of the Earth have evolved adaptations to allow them to survive under conditions of low water availability. Plants which exist in the Mojave Desert, and in many of the world's other arid regions which are being pressed into agricultural service, must additionally have adaptations for survival under conditions of high temperatures. It is important to consider how these adaptations will affect the different types of vegetation indices discussed in the previous section.

Although desert succulents such as cacti or yucca are usually thought of when deserts are mentioned, these plants are generally not the most important species in arid regions. Solbrig (1977) points out that the most abundant life form in deserts are usually small xerophytic shrubs. As an example of this, consider the three species of *Larrea*, — *L. tridentata, L. divaricata, L. cuneifolia* — which dominate much of the arid and semiarid landscapes of North and South America in terms of both numbers and biomass (Mabry *et al.*, 1977).

Although Cody (1989) reports on the variety of "growth forms" in the world's deserts, much of this diversity occurs in the form of the below-ground root structure,

which is not generally visible to remote sensing. Much of this also counts the succulents, which account for very little of the canopy cover, and ephemeral species. The focus in this section is on the xerophytic shrub class of vegetation and annual grasses. Succulents and minor plants are also considered in appendix C. Finally, we will briefly consider the changes that are typically observed during times of significant precipitation. This will show how arid vegetation provides many unique problems and opportunities for remote sensing, and it will also point toward the surface data required to monitor arid regions effectively with satellite remote sensing.

Part 5.2.1: *Initial Observations*

As discussed in chapter 2, the principal vegetation types seen in the Manix Basin are the creosote bush (Larrea *tridentata*), white bursage (*Ambrosia dumosa*), Russian Thistle or tumbleweed (*Salsola kali*), and a small desert grass which is probably fluffgrass. These plants are not usually closely spaced in the undisturbed areas of the desert both in order to efficiently use water (Fonteyn and Mahall, 1978; Fowler, 1986) and also because of allelopathic (anti-plant) substances produced by some plants such as the creosote bush (Mahall and Callaway, 1991). When a vegetated desert landscape is observed, except after a recent rain, one is struck by the lack of green in the landscape (plate 1). The small leaves of some plants, such as the creosote bush, are green (plate 2) , but other plants, such as bursage, tend to be more of a gray-green then the green that we usually associate with plants (plate 3). The small desert grass appears yellowish during most of the year (plate 4). Tumbleweed, which is most common in the most recently

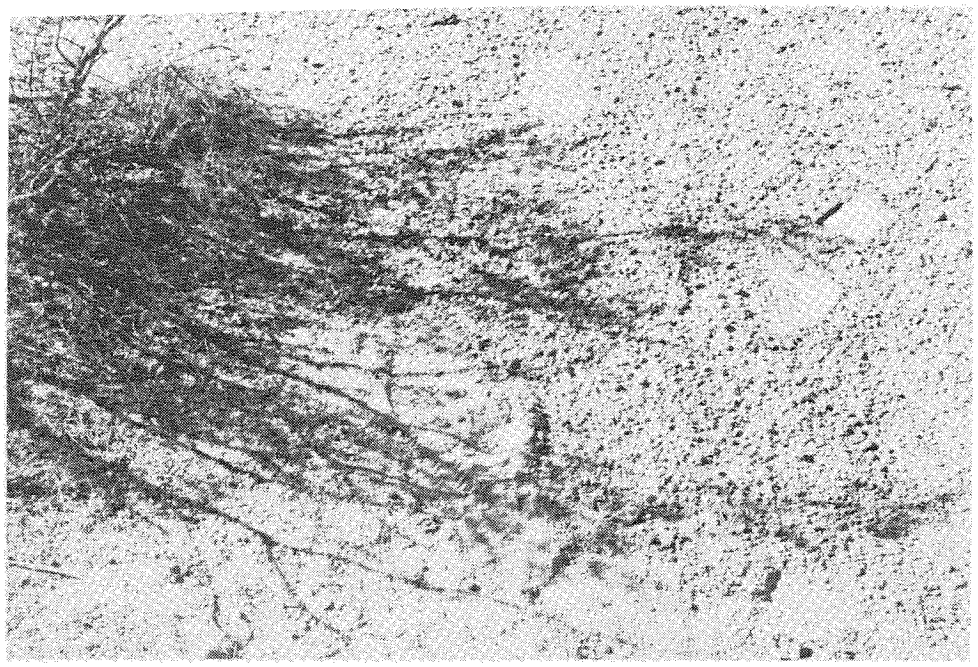

a)

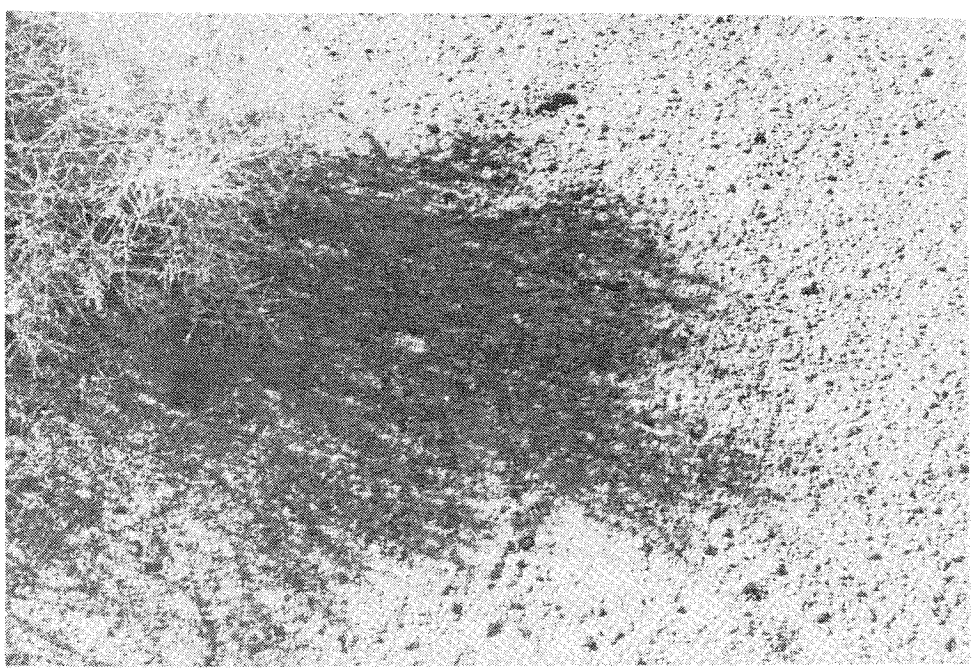

b)

Figure 58: Photographs of the shade cast by **a)** creosote bush and **b)** bursage. Note that the bursage shadow is much more solid than that of the creosote bush.

disturbed areas is quite green during its brief growing season (plate 5)., but it soon dries up forming a brownish ball which is driven across the landscape by the wind.

A closer examination of the creosote bush reveals that the green is due to the small paired green leaves with a distinctive greasy appearance. Another immediately apparent feature is the fact that the canopy of the creosote bush is very open allowing the underlying soil or grass to be easily seen through the creosote bush. An obvious consequence of this is that any observation of creosote bushes using either remote sensing or field instruments inevitably will include direct observations of the soil beneath the shrub. In addition to this, different parts of the canopy cast shadows which fall on the soil, the underlying vegetation and other parts of the canopy. This further complicates the observation of these plants since we will not only see the shrub's leaves and twigs, but we will also see the underlying soil and vegetation along with leaves, twigs, soil, and vegetation that are in partial shadow.

A closer examination of the white bursage shrubs often reveals a plant which appear nearly leafless. There are usually numerous small buds that look somewhat like coarse sand, as well as some fully developed leaves with complex shapes which have a silvery appearance. The bursage canopy consists of a dense thicket of twigs, buds, and leaves through which the underlying soil and vegetation is seldom seen. Instead, observation results in a view of the twigs and leaves illuminated by direct sunlight underlain by shadowed twigs and leaves until only dark shadows can be discerned from within the deeper parts of the plant's canopy. The shadow cast by the main part of a

typical bursage shrub is more nearly solid than that cast by a typical creosote bush (figure 58).

Part 5.2.2: *Surviving the Lack of Water*

Water accounts for 70–90% of the weight of most fresh non-woody plants, with the contents of plant cells being 85–90% water (Fitter and Hay, 1987). One of the most important functions of water in plants is to enable photosynthesis. In order to acquire the carbon dioxide needed for photosynthesis, the plants have small openings (stomata) in the surface of the leaves to allow gases to exchange with the leaf tissue. The natural state of most leaves is for the air spaces to be completely saturated with water vapor (Fitter and Hay, 1987), and since the air is typically not saturated with water vapor, there is a tendency for water vapor to exit the leaves and enter the atmosphere when the stomata are open.

The loss of water through the stomata is referred to as transpiration, and it is important to the plant for several reasons. Transpiration produces a water gradient which enables the roots to pull water from the soil and the water to be pumped to the leaves. This flow of water from the roots to the leaves helps drive the flow of photosynthesized sugar from the leaves of the plant to the actively growing roots. Finally, the evaporation of water from the leaves during transpiration helps to maintain the leaf temperature (Henderson, 1913; Gates *et al.*, 1967).

When all of these vital activities of water are taken into account, it is clear that plants living in arid and semiarid regions must have special adaptations to accommodate the scarcity of water. Adaptations are necessary to improve the plant's acquisition of the scarce water resource, to increase the efficient use of water, or to enable the plant to store water (MacDougal, 1908; Fitter and Hay, 1987). Roots provide the primary moisture-gathering ability of most plants. The root system of the creosote bush is one that both branches widely near the surface and also penetrates deeply into the soil (Spalding, 1909). This allows the creosote bush to tap deep water during the periods when there is no water near the surface. Yet, it can also efficiently draw water from the near surface soil in the periods when rains deposit water on the desert surface and help the creosote bush react rapidly to rainfall, as will be illustrated later in this chapter.

The extensive root systems of arid and semiarid plants increases the ratio of absorbing root length to the area of transpiring leaf. This ratio can be further increased by reducing the plant's leaf area. This represents a problem since smaller leaves cannot intercept as much solar radiation which decreases the possible rate of photosynthesis and lower potential production (Fitter and Hay, 1987). This is counterbalanced in some desert plants by thicker leaves which can provide more photosynthetic mesophyll to transpiring leaf area (Fitter and Hay, 1987).

Perversely, simply making the leaves smaller can actually make the problem of transpirational water loss worse. Smaller leaves have thinner boundary layers, which reduces the resistance to water loss. Smaller leaves often have more stomata per unit area than do larger leaves (Fitter and Hay, 1987). This thinning of the boundary layer and

increase in stomatal density reduces the leaf's resistance to water loss. The thickening of the leaves mentioned above can help increase the leaf's resistance to water loss, but the rather equivocal impact of decreasing leaf size may indicate that smaller leaves are an adaptation for dealing with temperature stress (Gates, 1980; Fitter and Hay, 1987) as discussed below.

Even with the stomata closed, leaves continue to lose water through the leaf cuticle. Most humid species have a cuticular resistance to water loss much smaller than that of arid species (Cowan and Milthorpe, 1968). These high resistances are achieved by thick layers of cutin and thick coatings of wax on the leaves (Martin and Juniper, 1970). The greasy look of the leaves of the creosote bush (*Larrea*) is an example of this adaptation for combating water loss. The presence of leaf hairs tends to increase the boundary layer thickness which in turn increases the resistance to transpirational water loss (Gates, 1980; Fitter and Hay, 1987). Also, these hairs are often found to be specifically clustered around the stomata (Fitter and Hay, 1987) which tends to restrict the gas exchange through the stomata.

Another path for conserving water is to adjust the properties of the leaf canopy. Plants can reduce water loss from one leaf surface by rolling the leaves. Some plants such as *Encelia farinosa* grow hairy leaves during the dry part of the year and less hairy leaves during the rainy season (Fitter and Hay, 1987). A more extreme way of altering the plant canopy characteristics is represented by the drought-deciduous plants, i.e., plants that lose their leaves during the drier part of the year. Many plants in desert regions will drop their leaves on a non-seasonal basis during dry periods of the year. An example of this from the

Mojave Desert is white bursage (*Ambrosia dumosa*) which drops its leaves during the dry periods of the year. Even the creosote bush, which is typically an evergreen shrub, will shed its leaves during extreme drought, and the creosote bush will go so far as shed twigs and entire branches during the worst droughts (Mabry *et al.*, 1977). Orshan (1963) found that the chamæphytes of the Mediterranean and the Middle Eastern deserts would not only shed their leaves on a periodic basis but that they grew different types of leaves during the summer and winter, and these leaves would drop off during different seasons. Perhaps the most extreme example of altering the leaf canopy is represented by the various types of desert plants such as Crucifixion Thorn (*Canotia holacantha*) and Mormon Tea (*Ephedra* spp.) which have no leaves at all for most of the year and depend instead on photosynthetic tissue in their stems.

Part 5.2.3: *The Temperature Problem*

When the temperature of a plant leaf climbs too high, many vital metabolic processes such as photosynthesis, respiration, enzyme activity, and protoplasmic streaming begin to break down (Gates *et al.*, 1967; Gates, 1980; Fitter and Hay, 1987). Even though photosynthetic activity in many species can take place at temperatures in the range of 45–50 °C, nearly all plants experience decreased photosynthesis when these temperatures are attained.

Plant leaves absorb energy from intercepted sunlight. As this light is scattered in the internal structures of the leaf, most of the visible light is absorbed by the various

pigments within the leaf (chlorophyll, xanthophyll, etc.), and light in the mid-infrared is absorbed by water in the leaf. This energy absorbed from the light as well as any absorbed or metabolically produced energy must be balanced by energy exiting the leaves.

There are three ways for energy to be removed from the leaves, radiation, transpiration and convection (Gates *et al.*, 1967; Gates; 1980; Fitter and Hay, 1987). Radiation is a temperature-related process where the temperature of the leaf will increase to a level sufficient to achieve a balance between energy entering the leaf and energy exiting the leaf. Thus, it is not an effective way of regulating the temperature of the plant. Plant temperatures exceeding 40 °C nearly always occur during periods of high water stress that has led to the cessation of transpiration by stomatal closure (Fitter and Hay, 1987). The need to conserve water prevents most arid region plants from utilizing transpiration in order to regulate their leaf temperatures.

Taking the above into consideration, we might expect that plants living in hot arid regions to have metabolic adaptations in order to withstand high temperatures in their tissues, and some plants do seem to have adapted metabolic functions which can operate at these higher temperatures (Fitter and Hay, 1987). However, most desert shrubs, such as *Larrea* (creosote bush), and grasses, which typically constitute the predominant plant cover (in terms of ground area covered), tend to be unable to sustain photosynthesis at temperatures exceeding 50 °C (Fitter and Hay, 1987). Gates *et al.* (1967) noticed that desert shrubs and grasses tended to have a leaf temperature within 3 °C of the air temperature. They concluded that the leaves are effectively regulating temperature without significant transpiration.

Gates *et al.* (1967) showed that there were three ways in which plant leaves eliminated the heat resulting from absorbed light energy: radiation, transpiration, and the removal of heat by wind (which he called convection). The modeling they performed showed that as long as the leaf area was less than 1 cm^2 that the leaf temperature would climb no higher than 3 °C above the air temperature even under conditions of no transpiration. By contrast, leaves with area exceeding 100 cm^2 would reach temperatures much higher than the surrounding air as the transpiration rate decreases. This led Gates *et al.* (1967) to conclude that there might be a physiological advantage for plants in arid and semiarid regions to have small leaves allowing heat removal by convection to be the dominant mechanism for thermal regulation. Open canopies with non-overlapping leaves helps to enhance the convective cooling process as well, by minimizing the leaf boundary layer resistance (Fitter and Hay, 1987).

The most straightforward way for plants to ease the problem of eliminating thermal energy absorbed from intercepted light is to keep the interception of solar energy at the minimum required for the physiological operations of the plant. It has already been shown that the need to minimize the ratio of transpiring leaf area to root length and to allow convection to be the dominant temperature regulatory process leads to small leaf size for arid plants, and an additional advantage to small leaves is the fact that they intercept less solar radiation than larger leaves. Many plants living in arid and semiarid areas have additional ways of avoiding excessive absorption of solar energy. Many desert species such as *Larrea* (creosote bush) and *Prosopis glandulosa* (mesquite), which have small leaves, tend to hold their leaves vertically during midday (Gates, 1980). The active

movement and cupping of leaves in order to avoid the sun used by many arid region plants is referred to as paraheliotropic sun tracking (Ehleringer and Forseth, 1980). Leaf hairs, such as those on bursage, increase the albedo of the plant leaves especially in the part of the spectrum absorbed by chlorophyll. Other plants such as *Atriplex hymenelytra* secrete salt on the surfaces of the leaves in order to increase their reflectance.

Part 5.2.4: *Consequences for Remote Sensing*

Clearly the various adaptations of arid region plants will impact laboratory, field and satellite measurements differently. Some of the adaptations will change the reflectance of the leaf directly and this strongly impacts both field and laboratory measurements, while many of the morphological adaptations will tend to quite significantly influence the spectra of whole plants as observed with field spectrometers or airborne and satellite instruments. This section will examine these consequences and predict what will be seen in the field and laboratory spectra later in this chapter.

A lack of chlorophyll and other absorptive pigments will naturally lead to larger reflectance in the visible part of the spectrum. There will also be no markedly enhanced reflectance in the green region of the spectrum. A secretion of salt on the leaves will tend to reflect more light across the entire spectrum before the light actually enters the plant leaves. Less light entering the leaf will strongly increase the visible reflectance since there will be no opportunity for the chlorophyll and other absorptive pigments to interact with the light. High leaf pubescence increases the total reflectance in the 0.75–1.0 μm range

and decreases the reflectance in the 1.0–2.5 μm range, but it has very little effect on the reflectance of light in the range 0.5–0.75 μm (Gates, 1980). The effect of pubescence is to flatten the spectrum in much the same way as done by the salt secretions, but the flattening will not be quite as great in the visible with the leaf hairs as with the salt.

As discussed in an earlier section, Willstätter and Stoll (1918) showed that there would be efficient reflections at each cell wall, and this, coupled with the low absorptance of plant tissue in the near infrared, leads to the strong near-infrared reflectance usually observed in plants. The amount of water within the leaf tissue of the plants strongly controls the near-infrared reflectance of plant leaves. However, most arid and semiarid shrubs and grasses have very little tissue water because water stress is the normal situation. This means that, in addition to the adaptations of the leaf surface to prevent light from entering the leaf, the near-infrared reflectance of these leaves will be further suppressed by their low water content. This also has significant consequences for microwave remote sensing, since the low water content will lead to a significantly reduced dielectric constant in these plants which will lead to much less radar reflection from these arid plants compared to humid vegetation.

In summary, it is expected that the leaves of plants which are adapted to prevent light entering the leaf will have stronger reflectance in the visible compared with humid region plants. The typical green bump caused by the relatively weak green light absorption of chlorophyll would also be less apparent. Considering the design of conventional vegetation indices, this suppression of the red edge will lead to an inherently low estimate of the abundance for arid plants.

Next we must consider how the adaptations to arid and semiarid environments will influence the whole plant spectra as observed by field spectrometers. The previous discussion has shown how small leaves and open canopies are favored in arid and semiarid environments by of the need to both conserve water and to promote leaf cooling. Because the leaves are small, less leaf area is seen looking into the canopy than would be seen if the leaves were larger. The open canopy means that we easily see past the outer boundary of the canopy into the underlying twigs and perhaps leaves. With some arid region plants such as the Creosote bush (*Larrea*) this means that it is common to see the soil beneath the shrub and also the shadow cast by the shrub onto the soil below. This means that the substrate of the shrub is inevitably included in any acquisition of a whole-plant spectrum. This has several consequences, beginning with the fact that bright soils have been shown to yield lower values of ratio-based vegetation indices such as NDVI (Huete *et al.*, 1985; Elvidge and Lyon, 1985), but this is not universally true as will be shown later. Elvidge and Lyon (1985) also showed that variations in the slope from red to near-infrared reflectance in the substrate can produce significant variations in the vegetation index.

Another effect of viewing the substrate of shrubs in whole-plant spectra is related to the non-linear mixing of the plant spectra with the soil spectrum. Note that the imcoming light which has interacted with plant leaves will tend to be depressed in the intensity of visible light and enhanced in the intensity of near-infrared light. If this once-reflected light then subsequently strikes a bright soil surface much of it will be once again reflected, and that reflected light will look more like a green plant than a high-albedo soil (Roberts *et al.*, 1993; Huete *et al.*, 1985). This could tend to counter the depression of

the vegetation index due to bright substrates mentioned previously (Elvidge and Chen, 1995). However, arid shrubs and succulents tend to have very low transmittances (Gates *et al.*, 1965), so this effect would tend to be observed in arid regions only when the incoming light was bright enough that light multiply reflected or scattered from the leaves and then on to the soil would still have a significant influence on the spectrum of the light reflected by the soil. The open, small-leafed canopy would tend to minimize these multiple leaf scatterings as well. It is also noted that a high-albedo soil might also provide an additional source of light to interact with the plant leaves. This multiple scattering of light between the plant canopy and the soil can lead to significant non-linear spectral mixing.

White bursage (*Ambrosia dumosa*) presents the observer with a dense underlying thicket of branches with lots of internal shadows, providing a dark background of shadows with little to no soil visible. The observed spectrum should be essentially a mixture of the reflectance spectra of the plant materials and the shadows within the canopy, leading to a lower overall brightness for the shrub. This will also be observed to an extent when shadowed soil can be seen through the canopy. The contribution to the spectrum of the plant from shadowed leaves and twigs would be generally lower in albedo than their non-shadowed counterparts, and this would once again tend to diminish the overall albedo of the whole-plant spectrum. This means that in many cases areas covered with arid vegetation will often be darker than bare soil in both the visible and the near-infrared, as compared to areas covered by humid vegetation which are nearly always brighter than bare soil in the near-infrared.

In addition to the effects of the adaptations on the laboratory spectra of the leaves and on the whole-plant spectra, the adaptations have another important impact on data sensed from high overhead. The previous section showed that plants in arid and semiarid regions tend to control the orientation of their leaves to minimize their exposure to the sun. This is done throughout the day by active means, and nearly all plants in these areas use a vertical orientation of their photosynthetic surfaces to avoid the intense midday sun. Usually satellite remote sensing systems are designed to minimize the shadows in the image, and, in the case of multispectral remote sensing, very bright illumination is necessary to achieve the needed spectral resolution with any sort of reasonable spatial resolution. These two factors lead to most visible light and non-thermal infrared remote sensing systems doing nadir-looking data acquisition near midday. Arid region plants are specifically adapted to not intercept sunlight during precisely the brightest (and hottest) period of the day which is when most visible and non-thermal infrared remote sensing is done. Even if these instruments avoided this time of the day, the fact that they do look nearly vertically down means that they always observe the edges of the leaves. Looking nearly straight down on dry-adapted plants is probably the worst way of sensing the true leaf area in arid and semiarid regions.

The next issue relates to the sparseness of vegetation in arid and semiarid regions. The fact that remote sensing instruments incorporate light reflected from significant areas of the ground into each pixel means that in an area with sparse vegetation the main contribution in any pixel will be the soil or rock substrate. Consequently, the variations in

vegetation index that are seen across a remotely sensed image of an arid or semiarid region can be partly due to variations in the spectrum of the soil.

Part 5.2.5: *The Wet Times*

The conditions under which the plants of the desert grow change radically when rain falls. Many annual species will take advantage of the brief period of high moisture in order to complete as much of their life cycle as possible before the excess of water is depleted. In order to achieve this, the plants must photosynthesize as rapidly as possible. Many annual plants will exhibit diaheliotropic sun tracking and use leaf motion and rolling in order to maximize the amount of intercepted solar radiation (Ehleringer and Forseth, 1980).

When water is plentiful, there is nothing to prevent adequate temperature maintenance through transpiration, and no reason for the leaves of the plants to be small. The perennial plants may also alter their leaf orientation and reflectivity in order to take as much advantage as possible of the plentiful water (Fitter and Hay, 1987). This ability to take advantage of the ephemerally abundant water is further enhanced by the transpiration increasing effects of small leaves discussed in section 5.2.2. As one particular example, *Encelia farinosa* has greener, less-pubescent leaves during the cooler, wetter months of the year, and the greenness of the leaves decreases and the pubescence of the leaves increases as the temperature increases and the environment becomes dryer during the

summer (Fitter and Hay, 1987). Also, some plants may have significant amounts of protochlorophyll in their leaves which can be rapidly converted into chlorophyll.

These considerations mean that arid regions will always appear much greener during wet periods. However, it is clear that this is not just due to an increased production of plant biomass. The plant biomass, which was there all the time, also changes its character to better intercept and absorb the solar radiation which leads to an enhancement of the visible light absorption and the near-infrared reflectance. Finally, both the previously present biomass and the newly produced biomass re-orient to achieve the maximum interception of sunlight, even at midday. The important thing to bear in mind is that the plant cover which is normally hard to see through remote sensing will give the appearance of vastly increased plant cover, even excluding the ephemerals which were triggered by the increased moisture.

Part 5.3: *Field and Laboratory Spectra*

In the previous section the adaptations of plants to arid regions were discussed, and some predictions were made regarding how these adaptations would affect the reflectance spectra of these plants. The differences between the reflectance spectra of xerophytic plants and the mesophytic plants which the vegetation indices used in remote sensing have been based on will have important consequences for the accuracy and utility of these vegetation indices in arid and semiarid regions. In this section, the predictions

made in part 5.2 will be put to the test through the use of field and laboratory spectra collected in the Manix Basin area.

The field measurements were taken in four field experiments between July 1993 and March 1994. As has been described previously, the dominant plant types seen in the Manix Basin area are creosote bush (*Larrea tridentata*) and white bursage (*Ambrosia dumosa*). A type of *Graminae* (grass), probably fluffgrass, is very common, and the aggressive invader species *Salsola kali* (Russian thistle or tumbleweed) is common in disturbed areas. The primary foci of data collection were the two dominant long-lived shrubs (creosote bush and white bursage), the grass, and the annual tumbleweed. Most of these data were collected in the areas indicated in figure 59.

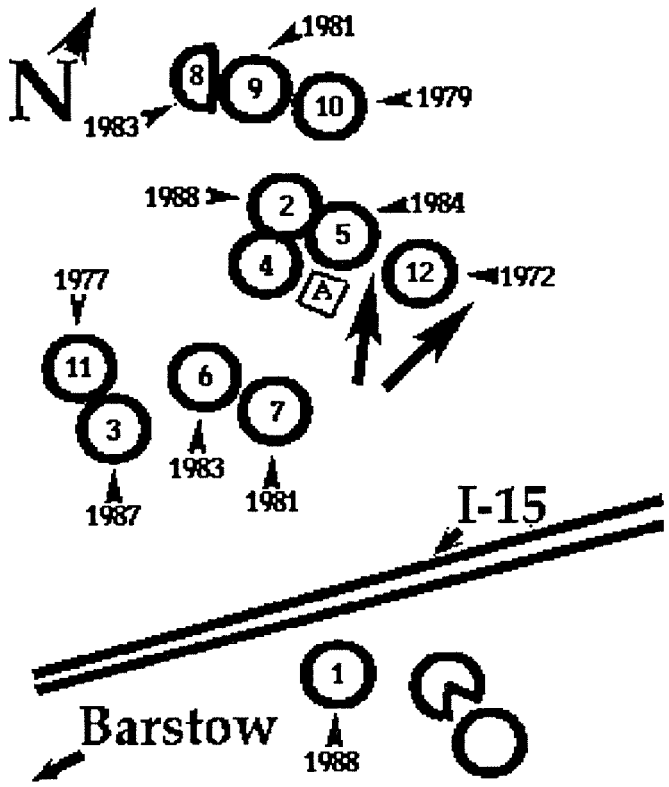

Figure 59: Sketch map showing primary areas where field spectra were collected (arrows).

Data were collected using two field spectrometers. The first spectrometer used was an Analytic Spectral Devices Personal Spectrometer 2 (PS2) that has specifications as listed in table 10. The instrument is quite small and portable (figure 60), and its main limitation lies in the small amount of memory available in the pocket PC which controls the instrument and records the data. The silicon detector used in this spectrometer tends to be quite noisy as one exceeds about 0.975 μm, and the data collected at wavelengths longer than 1.0 μm are usually too noisy to be useful, although this can be to some degree compensated for by averaging large numbers of spectra.

Table 10: Specifications of Analytic Spectral Devices PS2

Detector Type	Silicon
Spectral Range	338 nm – 1064 nm
Number of Bands	512
Sampling Interval	1.4 nm
Integration Time	variable (56 ms – 5 s)
Field of View	25° (foreoptics can give 5° 10° 15°)
Reference Target	Spectralon panel

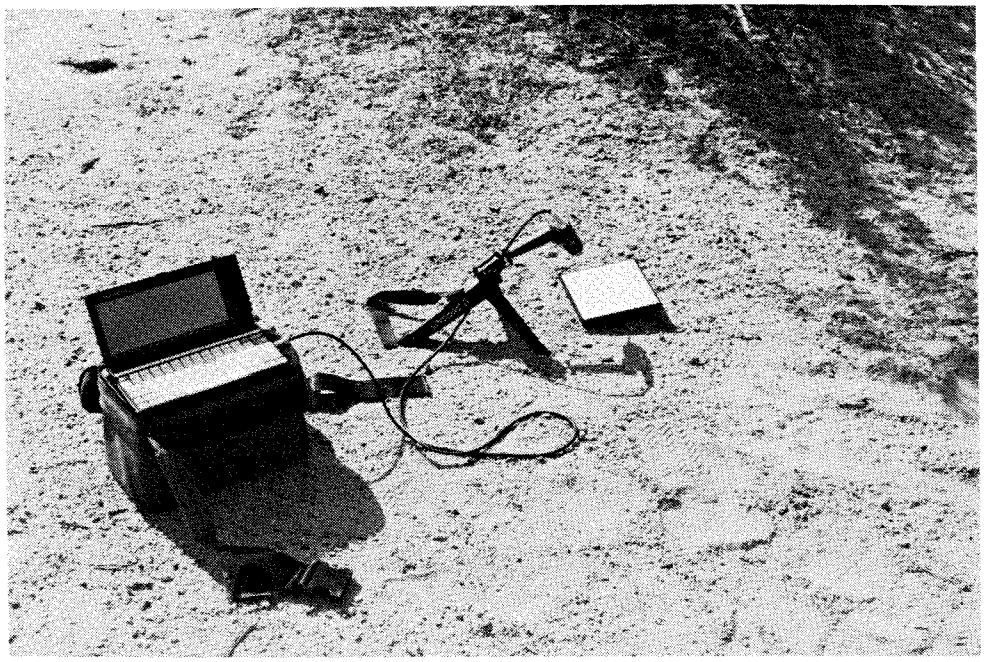

Figure 60: Photograph of Analytic Spectral Devices Personal Spectrometer 2 in operation in the Manix Basin.

Spectra were collected using this instrument on July 24 and 25, 1993; October 10 and 11, 1993; and February 8 and 9, 1994. Table 11 lists the target types and the number of spectra collected for each target type. In the case of many of the creosote bushes, one of the white bursage shrubs, all of the tumbleweeds and several of the minor plant spectra, the spectrum of the plant was collected with a "dark target" covering the soil background in addition to a spectrum collected with the soil background exposed. The "dark target" consisted of several pieces of heavy posterboard thickly coated with Krylon Ultra-Flat Black spraypaint. Figure 61 shows the reflectance spectrum of the dark target. In general, the white bursage shrubs had a sufficient thicket of branches to hide the soil from direct observation. The use of the dark target is complicated by the fact that the creosote bush often grows in the form of a "fairy ring" produced by buried branches and runners sending up stems centered around a primary plant (Mabry *et al.*, 1977).

Three creosote bushes and three bursage bushes were located and identified for repeat acquisitions. Each of these targets were measured in during each field experiment. This was undertaken in order to identify any seasonal changes which might occur. This also provided spectra from two instruments for each of these targets.

The JPL GER (Geophysical Exploration and Research) spectrometer was utilized in the field area on February 24, 1994. This instrument is much larger and bulkier than the ASD PS2 as shown in figure 37. The advantage of this instrument is that it collects field spectral data covering the entire range of the AVIRIS instrument (0.4–2.5 μm). These data are collected in 826 spectral bands, with data at shorter than 1.0 μm collected in narrower

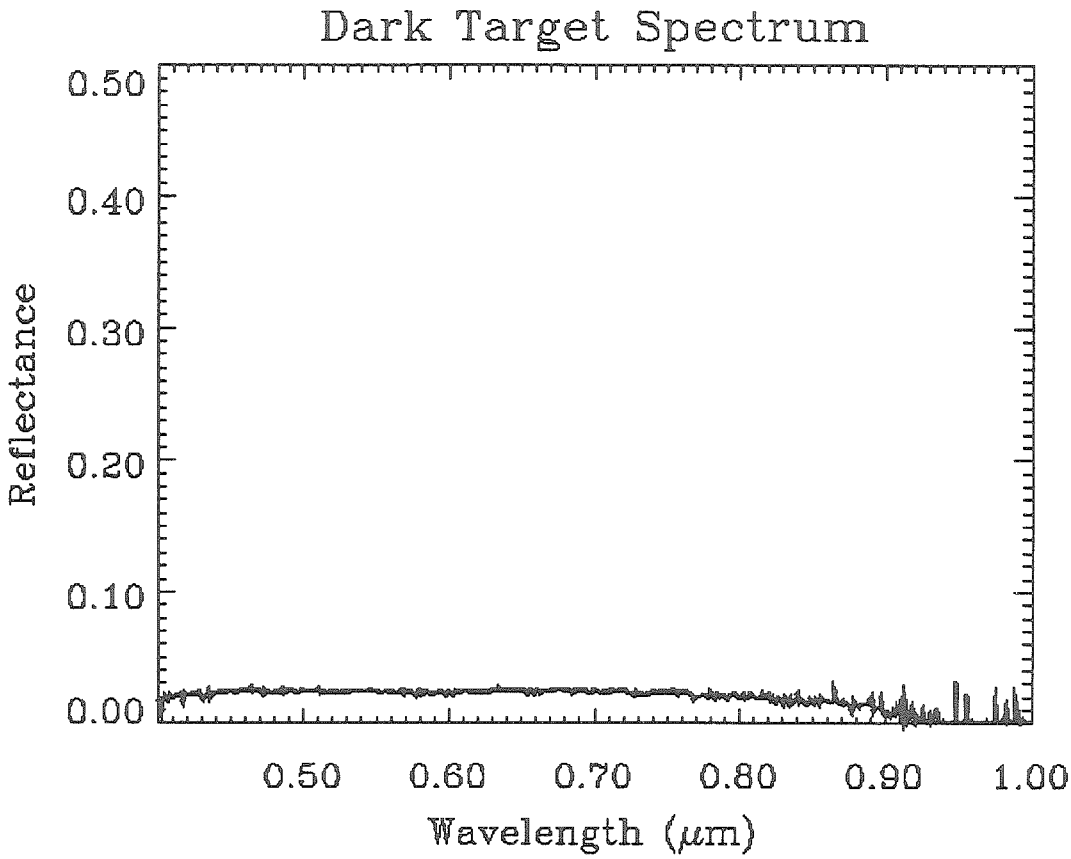

Figure 61: Dark Target Spectra collected by PS2.

Table 11: Enumeration of Spectra Collected with PS2	
Target Type	Number of Spectra Collected*
Alfalfa (*Medicago savati*)	4 (1 corrupt)
Basalt (unweathered)	4
Basalt (weathered)	2
Bursage (*Ambrosia dumosa*) (dark target)	1
Bursage (*Ambrosia dumosa*) (soil)	25
Bursage (*Ambrosia dumosa*) (leaves only)	1
Bursage (*Ambrosia dumosa*) (twigs only)	1
Bursage (*Ambrosia dumosa*) (shadow on soil)	1
Bursage (*Ambrosia dumosa*) (shadow on self)	2
Bursage (*Ambrosia dumosa*) (shadow on reference)	1
Cactus	1
Chinchweed (*Pectis papposa)* (dark target)	1
Chinchweed (*Pectis papposa)* (soil)	1
Creosote Bush (*Larrea tridentata*) (dark target)	14
Creosote Bush (*Larrea tridentata*) (soil)	29
Creosote Bush (*Larrea tridentata*) (leaves only)	1
Creosote Bush (*Larrea tridentata*) (twigs only)	1
Creosote Bush (*Larrea tridentata*) (shadow on soil)	2
Creosote Bush (*Larrea tridentata*) (shadow on self)	2
Creosote Bush (*Larrea tridentata*) (shadow on reference)	1
Dead Wood	2
Desert Velvet (*Psathyrotes ramoisissima*) (dark target)	1
Desert Velvet (*Psathyrotes ramoisissima*) (soil)	1
Dirt Road	1
Grass (*Graminae*)	20
Soil	28
Solid Shadow on soil	1
Solid Shadow on reference	1
Tumbleweed (*Salsola kali*) (dark target)	4
Tumbleweed (*Salsola kali*) (soil)	4
Wooly Daisy (*Eryiophyllum wallacei*) (dark target)	1
Wooly Daisy (*Eryiophyllum wallacei*) (soil)	1

bands than the longer wavelengths as shown in table 12. The instrument collects three spectra of the reference target and averages those spectra to produce the reference radiance spectrum. Three spectra of the target are then collected and averaged, giving the radiance spectrum of the target. The target reflectance spectrum is then computed by dividing the radiance spectrum of the target by the reference spectrum. The entire process for collecting a single GER spectrum takes about 6 minutes, so it is very important that the sky be free of cirrus clouds which could cause variance during the spectral acquisition.

Table 12: Specifications of the JPL GER Spectrometer

Detector Type	Silicon (visible), PbS (NIR)
Spectral Range	0.4 μm – 2.5 μm
Number of Bands	826
Sampling Interval	2.5 nm (visible), 3.0 nm (NIR)
Integration Time	60 s
Field of View	25°
Reference Target	Spectralon panel

The length of time required to set up the instrument, coupled with its relative lack of portability and the length of time required to collect each spectrum, limited the number of spectra which could be collected. Data collection focused on the marked shrubs with spectra also collected for two patches of grass and two areas of bare soil. Table 13 lists the spectra which were collected using the GER spectrometer. Unlike the PS2, the GER

provides no real-time spectral display which would probably have revealed that one bursage spectrum was corrupt in the field and allowed a reacquisition.

Table 13: Enumeration of Spectra Collected with the GER	
Bursage (*Ambrosia dumosa*) (soil)	3 (1 corrupt)
Bursage (*Ambrosia dumosa*) (leaves)	1
Bursage (*Ambrosia dumosa*) (twigs)	1
Creosote bush (*Larrea tridentata*) (dark target)	3
Creosote bush (*Larrea tridentata*) (soil)	3
Creosote bush (*Larrea tridentata*) (leaves)	1
Creosote bush (*Larrea tridentata*) (twigs)	1
Soil	3
Grass (*Graminæ*)	3
White Reference Target in Solid Shade	1

Strong absorption by atmospheric water near 1.4 μm and 1.9 μm makes 84 instrument bands useless, which leaves 706 useful bands.

An important feature in remote sensing images is shadow. Shadow is not an infinitely dark target, and it is also not a spectrally flat target. Figure 62 shows the spectrum of the reference targets for the PS2 and GER spectrometers in solid shade (shade without holes). In this case, no direct sunlight is striking the reference target. There is strong reflectance in the blue part of the visible spectrum with an exponential drop in reflectance towards longer wavelengths, and this pattern is clearly caused by the Rayleigh scattering in the atmosphere that makes the sky look blue. A very important consequence of this is the fact that light scattered from the atmosphere, which is what is

being seen in figure 62, is not entirely accounted for by the use of the reference target. There is still some component due to atmospherically scattered light which complicates all of the reflectance spectra collected by the field spectrometers. However, since the white reference target is being defined as a perfectly reflecting target, these reflectance spectra of shadow can be used as weighting functions to simulate how a shadowed target would appear to the field spectrometer.

Laboratory spectra of plant leaves and twigs brought back from the field were collected on October 4, 1994 using two instruments at JPL, the modified Beckman UV5240 spectraphotometer and a PIMA spectrometer. Branches were cut from two creosote bushes and two bursage shrubs. One creosote bush and one bursage were located on abandoned field 12, and the other ones of each were located to the west of the abandoned field. A branch was also cut from a Mormon Tea (*Ephedra* spp.) shrub and sprigs of alfalfa were cut from an irrigated field. The specimens were placed in plastic bags and stored on ice for transport from the field area to JPL. The samples were prepared and measured during the afternoon of the same day that the plant material was cut.

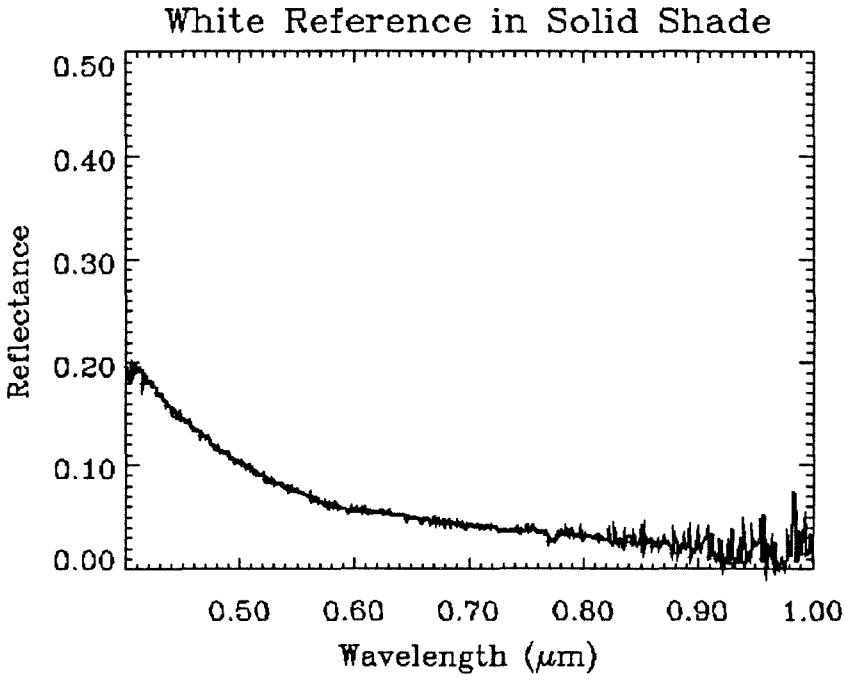

a)

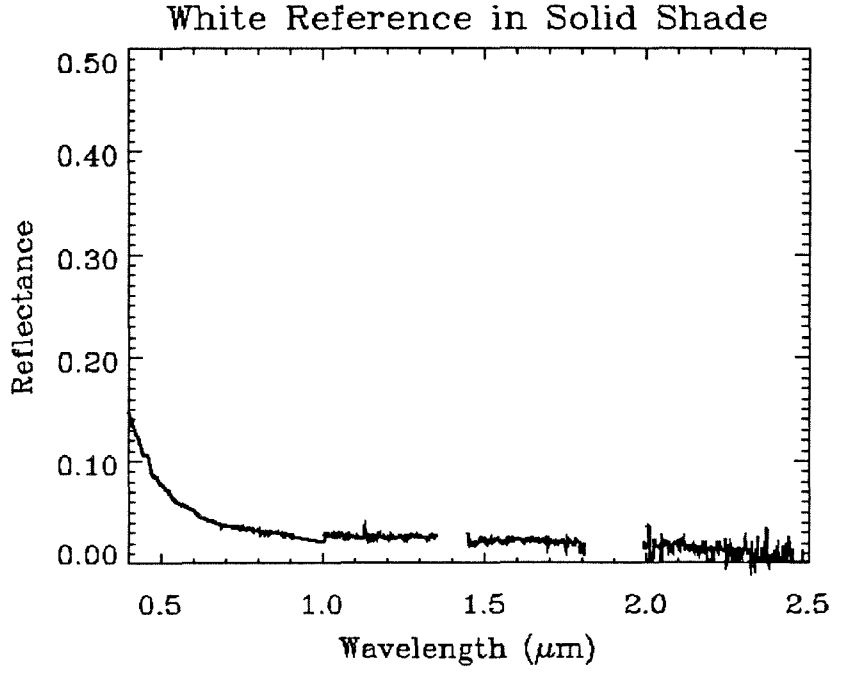

b)

Figure 62: Reflectance spectra of white reference target in solid shade showing Rayleigh scattering component from diffuse atmospheric scattering. **a)** PS2 **b)** GER

The Beckman spectrophotometer collects data across the spectral range from 0.4 μm through 2.5 μm in 826 spectral bands. The modification made to the instrument was a 90° rotation of the integrating sphere which allows the material to remain in a horizontal position in the sample holder, preventing loose materials such as soil and small leaves from falling out (Grove *et al.*, 1992). The characteristics of the Beckman UV5240 spectrophotometer are summarized in table 14.

The PIMA spectrometer is a portable spectrometer which contains its own light source, and, like the Beckman, the sample is contained in a cup which is placed in contact with the instrument aperture. It collects data in 601 spectral bands covering the range from 1.3 μm to 2.5 μm. The characteristics of the PIMA spectrometer are summarized in table 15.

Table 14: Specifications of the Beckman UV5240 Spectrophotometer	
Detector Type	Silicon (Visible); PbS (NIR)
Spectral Range	0.4 μm – 2.5 μm
Number of Bands	826
Sampling Interval	1 nm (Visible); 4 nm (NIR)
Integration Time	825 s
Field of View	3.2 cm diameter circle
Reference Target	Halon Standard

Table 15: Specifications of the PIMA Spectrometer	
Detector Type	PbS
Spectral Range	1.30 μm – 2.5 μm
Number of Bands	601
Sampling Interval	2 nm
Integration Time	20–30 s
Field of View	3.2 cm diameter circle
Reference Target	Halon Standard

Part 5.2 elucidated the many adaptations of plants to arid environments which should have significant impacts on remote sensing. Some of these adaptations should affect the laboratory spectra of the leaves of the plant, while others should become apparent when the spectrum of entire plants in natural surroundings are observed. In the remainder of this section, the spectra of these plants will be examined in some detail, and these observations will be related to the adaptations discussed previously.

Part 5.3.1: *Alfalfa*

The alfalfa present on the irrigated fields in the study area provides an excellent example of a normal green plant, and therefore an excellent basis to compare with the desert plants. Alfalfa is rich in chlorophyll, which is one of the reasons for its cultivation, it has relatively large leaves and forms a very thick canopy. This makes alfalfa virtually the type class of the remote sensing "green plant."

Figure 63 shows an alfalfa spectrum collected using the Beckman spectrophotometer. This plot clearly shows the strong absorption in the visible caused by the pigments in the alfalfa leaves. There is a significant chlorophyll bump in the visible near 0.55 μm, and the pigment triplet discussed earlier can also be seen between 0.6–0.7 μm. There are several subtle absorption features between 2.0 μm and 2.5 μm which may be due to various plant materials listed in table 7.

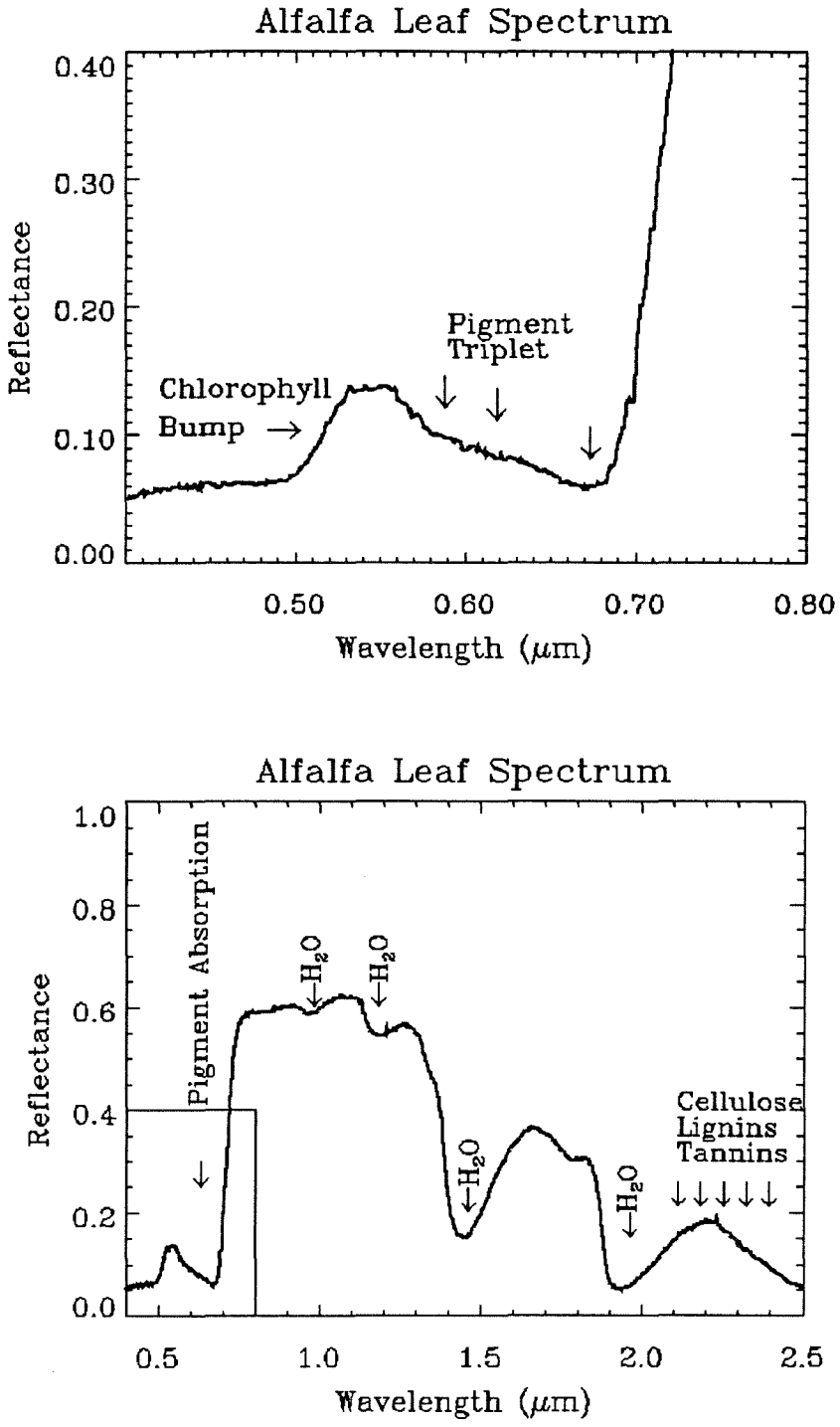

Figure 63: Beckman spectrum of alfalfa. The upper plot is an enlargement of the boxed area. The pigment features between 0.5–0.7 mm are clearly visible, as are water absorption features. There are several subtle absorption features due to cellulose, hemicellulose, lignins, and tannins as shown in table 7 and figure 92.

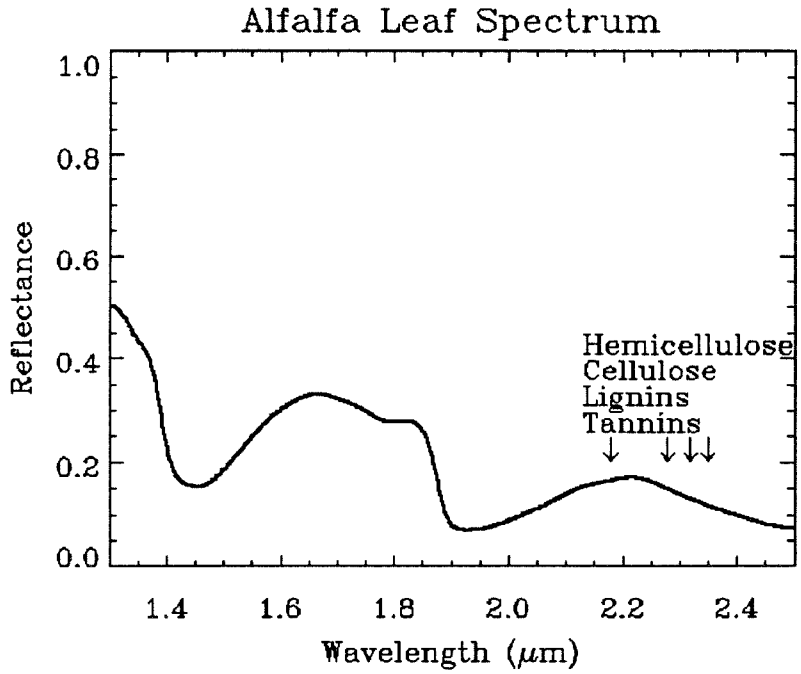

Figure 64: PIMA spectrum of alfalfa.

Figure 64 shows the PIMA spectrum of the same sample of alfalfa. Notice the smoother appearance of this spectrum, which suggests that the PIMA is a less noisy instrument. Close examination of the region between 2.0 μm and 2.5 μm shows a waviness to the line which is suggestive of subtle absorption features. Slight absorptions can be seen at 2.18, 2.32, and 2.35 μm. All of these features are so subtle that seeing them in satellite or airborne data seems improbable.

A field spectrum of alfalfa is shown in figure 65. Again, the strong absorption in the visible and the high reflectivity in the NIR are both clearly apparent. The chlorophyll bump at 0.55 μm and the pigment triplet are also clearly visible. One might expect some of the subtle absorptions between 2.0 and 2.5 μm to also be visible, but due to the low portability of the GER spectrometer no alfalfa spectra were collected with that instrument.

Figure 66 shows two spectra of alfalfa collected using the PS2. In contrast to the spectrum in figure 65, these spectra were collected with the instrument detector further away from the plants which makes these more representative of the spectra of an alfalfa field than of a single alfalfa plant. Figure 66a was taken with the 5° field-of-view foreoptic, and the chlorophyll bump and the NIR reflectance are both suppressed in comparison to figure 65. The pigment triplet between 0.6–0.7 μm is still visible. In figure 117b the 25° field-of-view of the PS2 with no foreoptic is used. The NIR reflectance is further suppressed, but the chlorophyll bump at 0.55 μm is approximately the same reflectance as

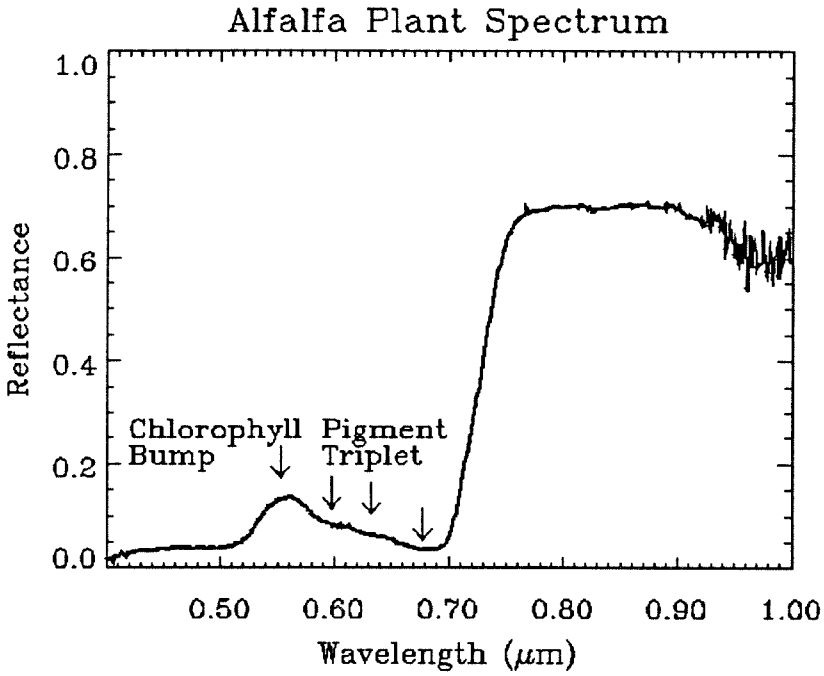

Figure 65: PS2 spectrum of alfalfa plant. Notice the similarity between this and the enlargement of the visible and very near infrared (VNIR). The pigment features can be clearly distinguished.

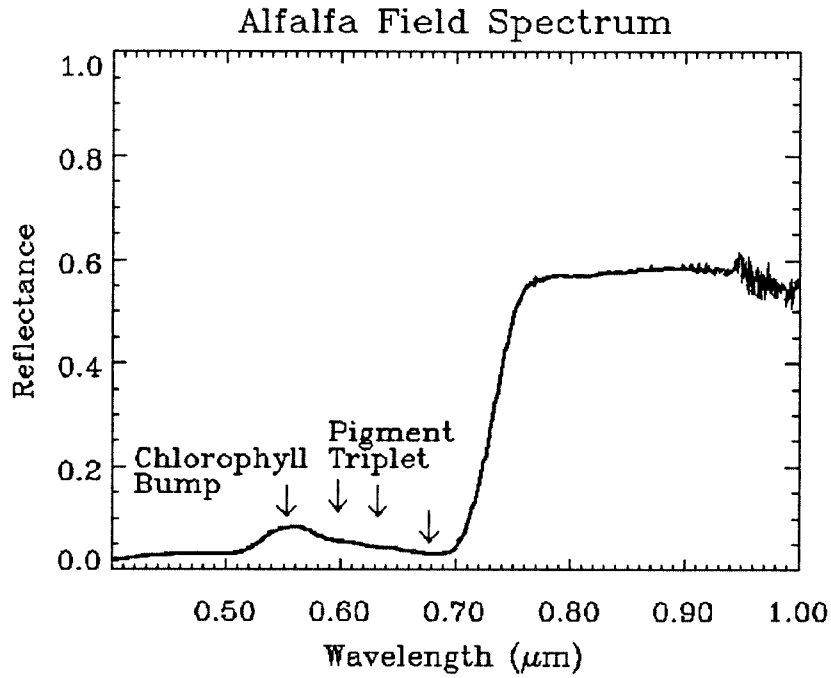

a)

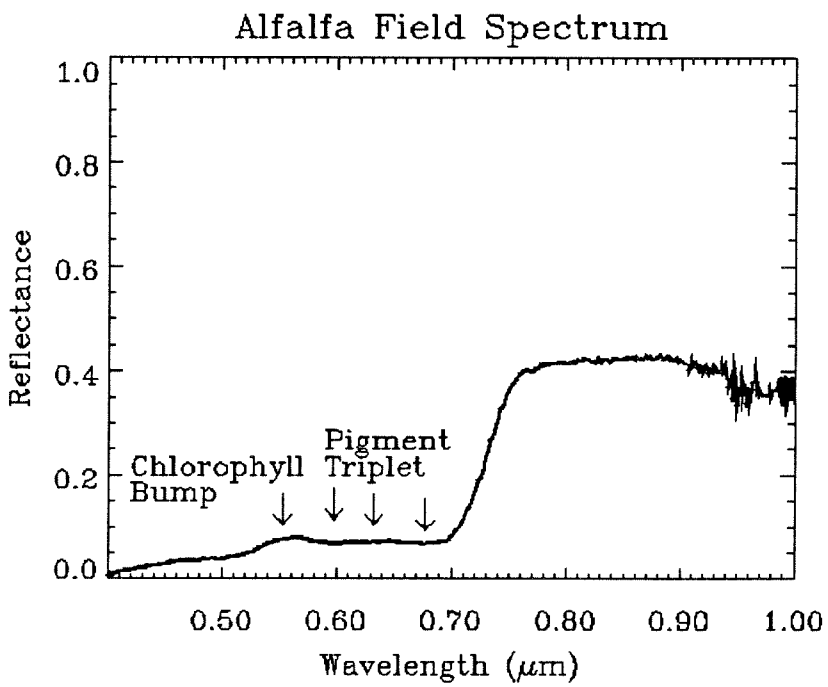

b)

Figure 66: PS2 spectra of alfalfa field. **a)** 5° FOV foreoptic. **b)** 25° FOV Notice how the pigment features flatten as the increased field of view admits more photons which have not interacted with the alfalfa.

that in figure 66a. Given the broad FOV of the instrument (25°) in figure 117b and the angle at which it was held (about 60° incidence), it is likely that there are contributions due to the landscape and sky in figure 66b, so this should perhaps be looked at in the same manner as a mixed pixel in remotely-sensed data.

Part 5.3.2: *Creosote Bush*

Figure 67 shows the Beckman laboratory spectrum of creosote bush leaves taken from a creosote bush on abandoned field 12. In general terms this spectrum is quite similar to figure 64. However, the pigment features are all generally suppressed compared to those for alfalfa. Additionally, the region around 2.2 μm has stronger absorption features caused by a combination of cellulose, hemicellulose, lignin, and tannins. The absorptions near 2.2 mm can be more clearly seen in the PIMA spectrum of this sample (figure 68). There is an absorption near 1.72 mm visible in the PIMA spectrum, which may be due to a wax similar to carnauba wax.

Mabry *et al.* (1977) reported the broad range of chemicals produced by the creosote bush. Of particular note, given the spectral feature which is similar to that of carnauba wax, is a complex wax which represents some 0.1% of the plants dry weight which reportedly is physically and chemically similar to carnauba wax in many respects. Looking back at table 7, it can be seen that a wax with similar absorption characteristics to carnauba wax would also have absorptions near 2.31, 2.35, 2.39, and 2.43 μm, which is consistent with figure 68.

Mabry *et al.* (1977) and Rhoades (1977) discuss the important lignan catechol nordihydroguaiaretic acid or NDGA which represents between 3.82–12.58% of the dry weight of *Larrea tridentata* leaves (Rhoades, 1977). Mabry *et al.* (1977) list four other lignans present in the resin coating creosote bush leaves which are related to NDGA. It is understood that lignins are complex phenylpropanoid polymers while lignans are phenylpropanoid dimers, but it does not seem completely unreasonable to believe that the lignans are similar to lignins in terms of their spectral characteristics. This means that the resin should strongly contribute to absorption at many of the same places as would a carnauba-like wax. However, the absorption between 2.10 and 2.17 μm could be produced by lignin and not by the wax, while the absorption near 1.72 μm could be due to the wax and not due to lignin. The 1.73 μm carnauba wax absorption is very strong (Elvidge, 1990).

These significant absorptions in the creosote bush leaf spectrum seem, therefore, to be tied to the sticky resin on the leaves. This resin serves to seal the leaf cuticle to prevent water loss (Fitter and Hay, 1987) and it also appears to be a deterrent to herbivory (Rhoades, 1977). The sticky resin also complicates the preparation of creosote bush leaf samples because the resin causes the leaves to stick to each other and to the instruments used to handle the leaves.

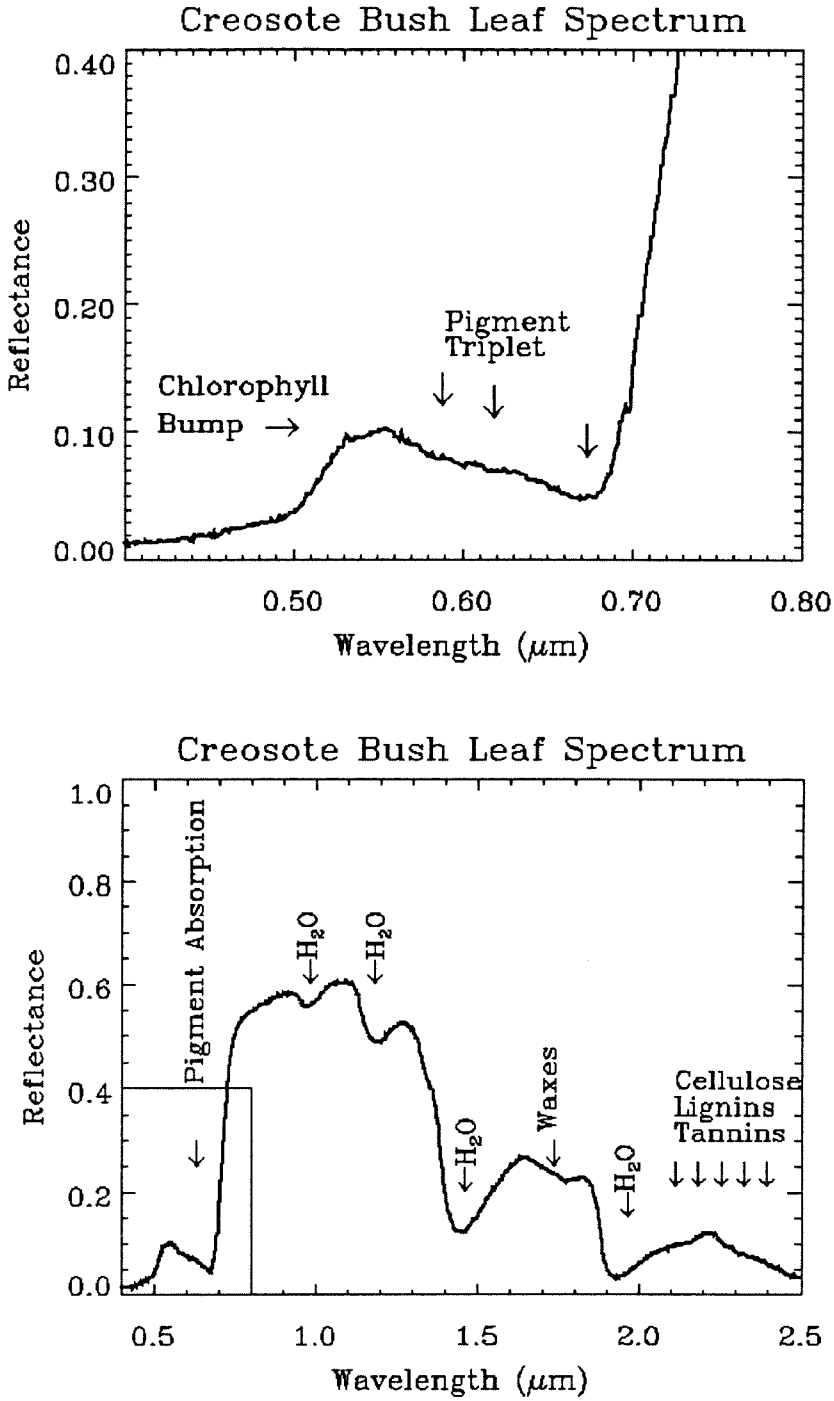

Figure 67: Beckman laboratory spectrum of creosote bush leaves from a bush on abandoned field 12. The upper plot is an enlargement of the boxed area. Notice that the pigment features are not as pronounced as those for alfalfa in figure 63. However, the cellulose, lignin, and tannin features on either side of 2.2 μm are stronger for creosote bush than for alfalfa. Notice the absorption due to waxes near 1.7 μm.

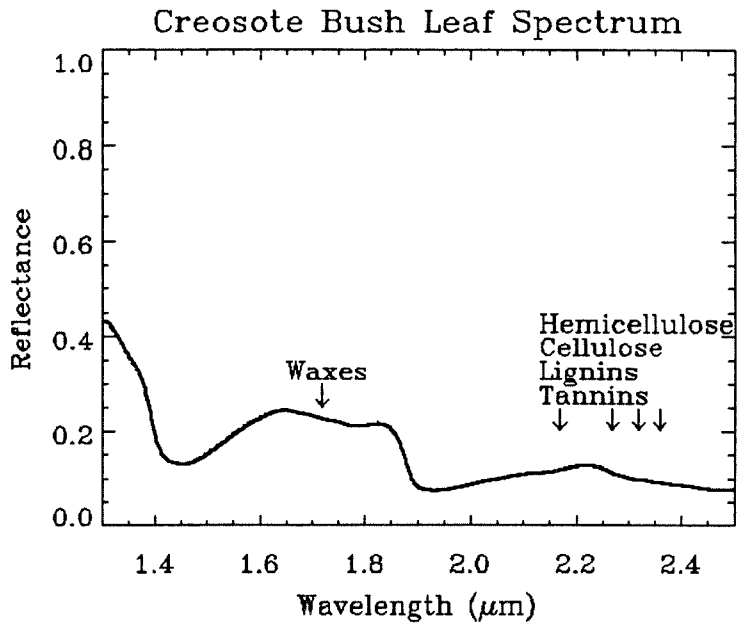

Figure 68: PIMA laboratory spectrum of the same sample as figure 67. The cellulose, lignin, tannin, and hemicellulose absorptions about 2.2 μm are clearly present, and the "bump" at 2.2 μm is suppressed compared to alfalfa (figure 64). The wax absorption near 1.7 μm is also visible in this figure.

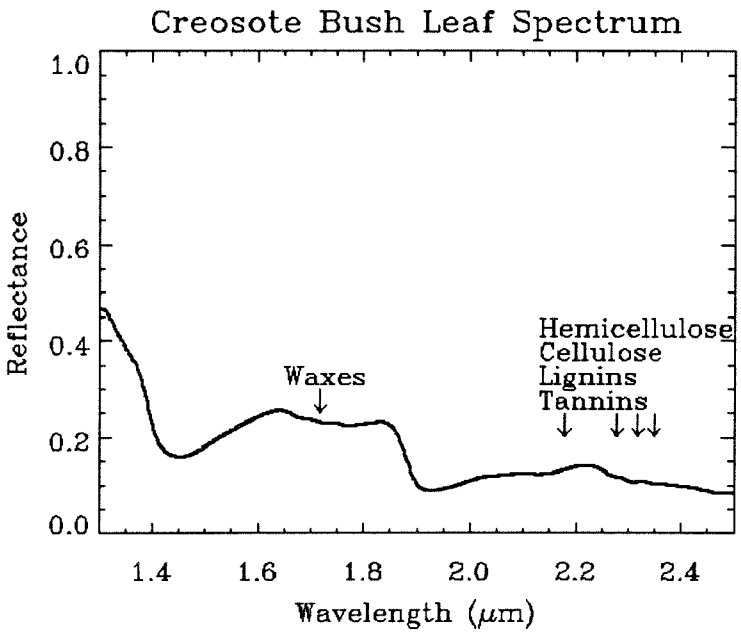

Figure 69: PIMA laboratory spectrum of creosote bush leaves from a bush on the undisturbed desert. The hemicellulose, cellulose, lignin, and tannin absorptions are stronger for this sample than for the abandoned field sample in figure 68.

Figure 69 shows the PIMA spectrum for leaves from a creosote bush in the undisturbed desert. This spectrum is very similar to the spectrum in figure 68, but there are stronger absorptions to either side of the 2.2 μm bump. This suggests that there may be more resin on the leaves of the plant in the undisturbed desert. Rhoades (1977) reports that young creosote bush leaves have more resin than old creosote bush leaves. This seems to conflict with the expectation that creosote bushes in the abandoned field would be younger than that in the undisturbed desert. However, the abandoned field was abandoned no later than 1972, so the creosote bush on the field could be older than a randomly-selected creosote bush in the undisturbed desert. Also, there is no reason to believe that all leaves on an older creosote bush are older than the leaves on a younger

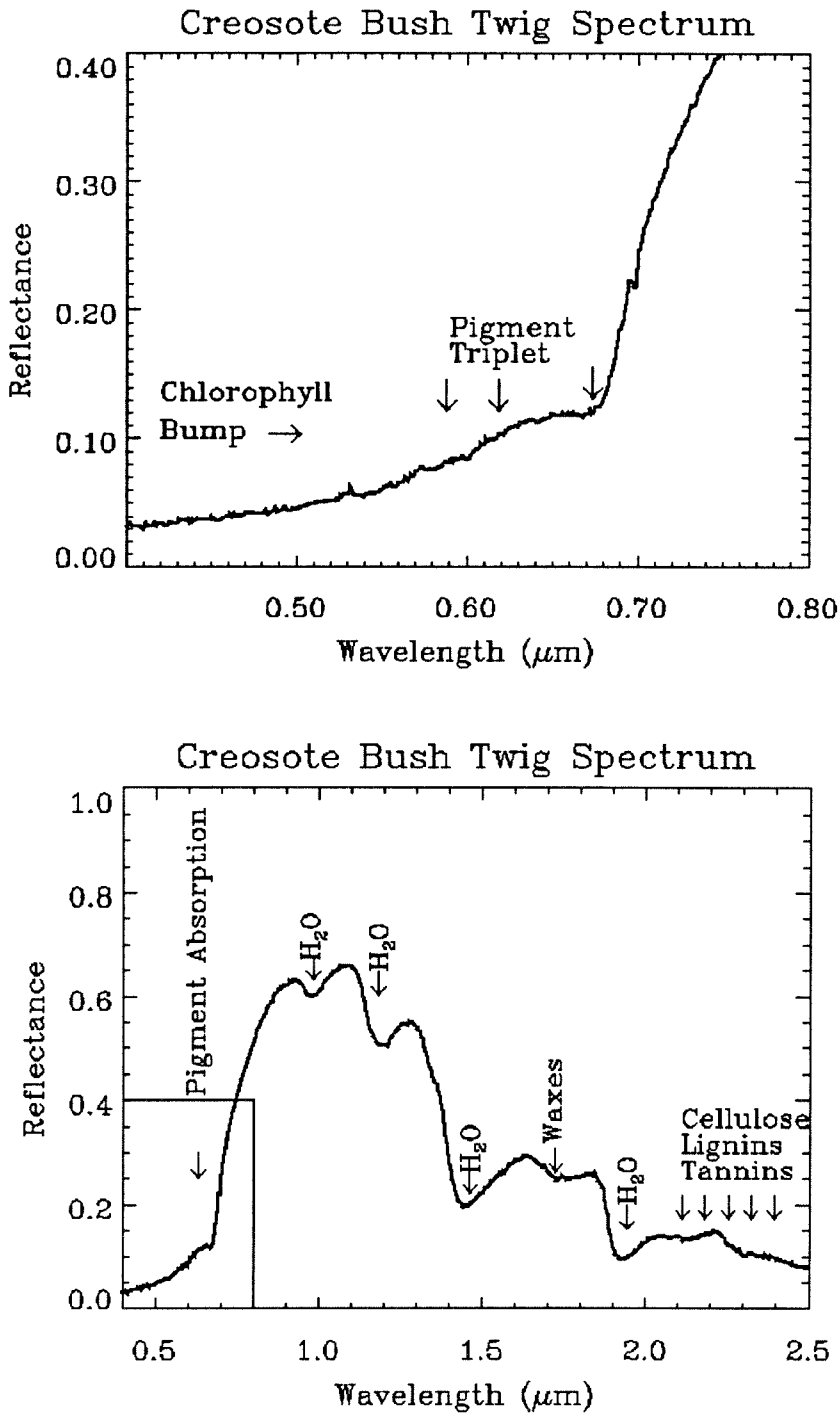

Figure 70: Beckman spectrum of creosote bush twigs from a bush on abandoned field 12. Notice that most of the distinctive pigment features are missing. Note that the wax absorption and the cellulose, hemicellulose, lignin, and tannin absorptions around 2.2 μm are quite strong.

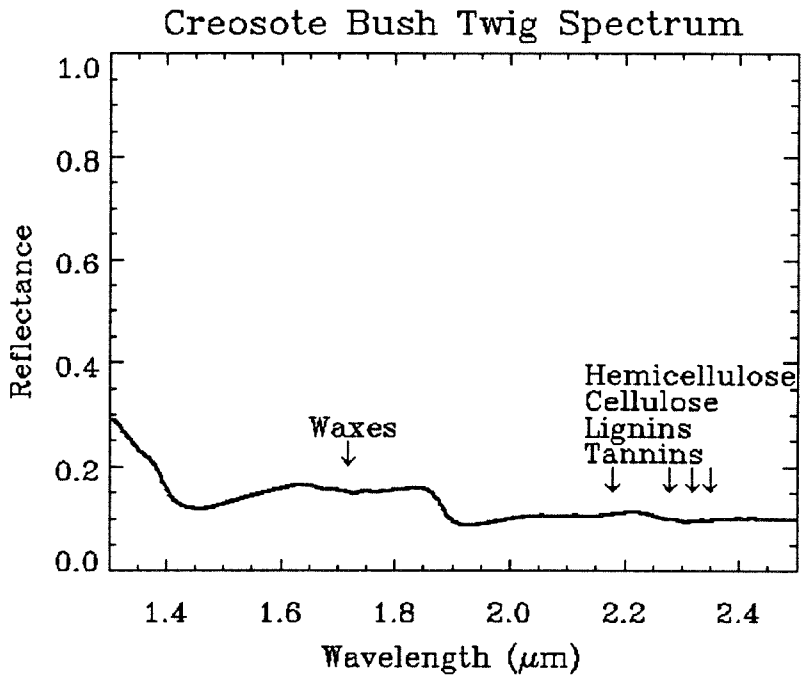

Figure 71: PIMA spectrum of creosote bush twigs. Notice the extreme flattening of the "bump" at 2.2 μm caused by the surrounding cellulose, hemicellulose, lignin, and tannin absorptions.

bush. Finally, the water absorption features in figure 70 are smaller than those in figure 69, so that the apparently enhanced resin absorptions may be more due to less water absorption than to more resin.

As discussed previously, the open canopy of the creosote bush causes the twigs and branches of the shrub to be visible, so it is important to consider the spectra of the twigs. Figure 70 shows the Beckman spectrum of twigs from the creosote bush on the abandoned field. Notice that the twigs are still strongly absorptive in the visible wavelengths. However, there is really no evidence of the chlorophyll and protochlorophyll in the spectrum. Elvidge (1990) does show that lignins and tannins have strong visible absorption, and the twigs should be largely composed of lignin. The twigs have a resinous coating which may be similar to the leaf resin. The bump near 2.2 μm has a similar appearance to the same portion of the spectrum for the leaves, and a 1.72 μm wax absorption is also apparent. The twigs from the bush on the undisturbed desert were generally darker, but the shape of the spectrum is virtually identical. Figure 71 shows the PIMA spectrum for the abandoned field creosote bush twigs, which shows the absorptions more clearly. Although the spectral shape is similar to that for the leaves, the water absorption features are much weaker than those in the leaves.

Figure 72 is a field spectrum of a creosote bush taken with the natural soil background. The chlorophyll bump is clearly present at 0.55 μm and the triplet of pigment absorptions can be seen between 0.6–0.7 μm. Comparison of figure 72 and

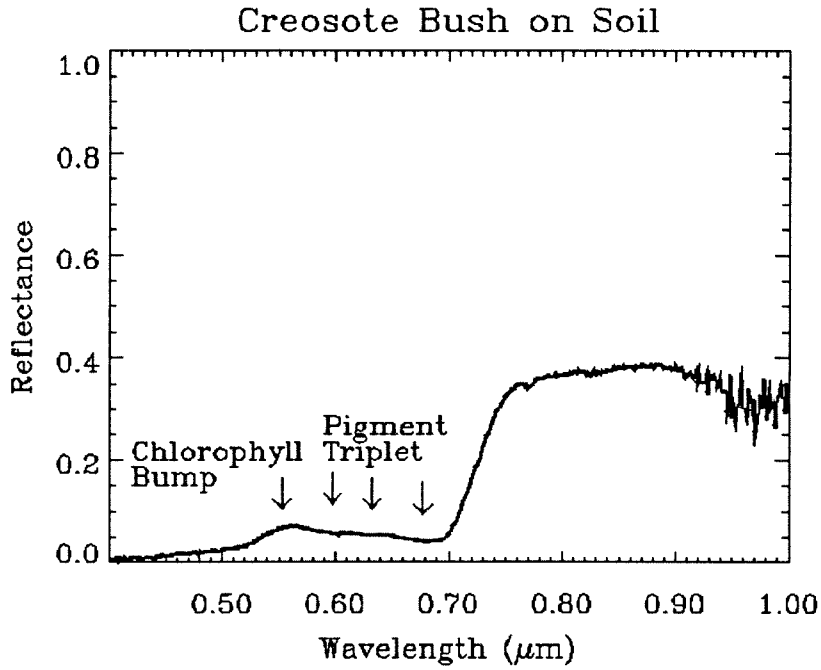

Figure 72: PS2 field spectrum of a creosote bush with the natural soil background. Notice that this is significantly darker than either figures 70 or 71. This is largely due to the small leaf area of creosote bushes. Pigment features are still clearly visible.

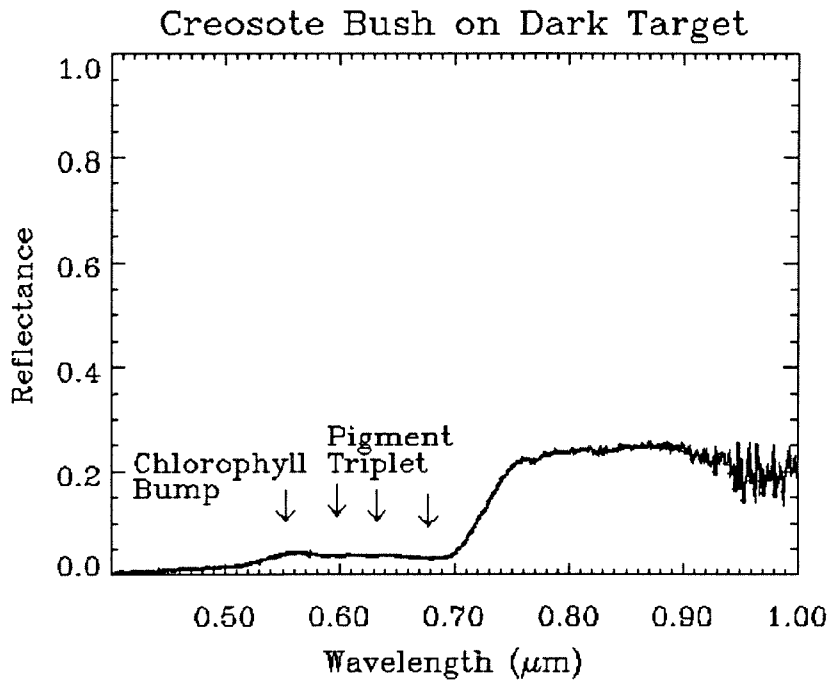

Figure 73: A PS2 field spectrum of the same bush in figure 72 with the soil covered by the dark target. Notice how the elimination of the soil background suppresses all of the spectrum, including the pigment features.

figure 65 shows that the reflectance for the creosote bush in the NIR is significantly less than the NIR reflectance of the alfalfa. A comparison of figures 67 and 63 shows that the laboratory spectra of the leaves predict very similar reflectances for both plants. The most straightforward explanation of this is the fact that the visible leaf area is much smaller for the creosote bush.

In figure 73, the soil background has been covered by the dark target. The overall reflectance is suppressed compared to that in figure 72. A close examination shows that the deepest point of the chlorophyll absorption (0.675 μm) and the top of the NIR plateau are much closer together in the dark target spectrum than the spectrum against the bare soil, which should lead to lower vegetation index values.

This suggests that the soil background may be slightly enhancing the NDVI value. It should be pointed out that across the entire set of creosote bushes this is not always the case. Sometimes there is very little difference between the dark background and the soil background in some cases, and in other cases the removal of the dark target suppresses the NDVI value. The earlier discussion about soil noise listed two mutually opposing effects of soil brightness on vegetation index values. Linear mixing with a bright background tends to suppress vegetation index values, while non-linear mixing will enhance it.

Figure 74 compares the three spectra of one of the creosote bushes over the 8-month period for which data were collected. There is a clear decrease in NIR reflectance from summer to autumn, but little change in the pigment features. From autumn to winter the NIR reflectance does not significantly change, but the pigment features get much

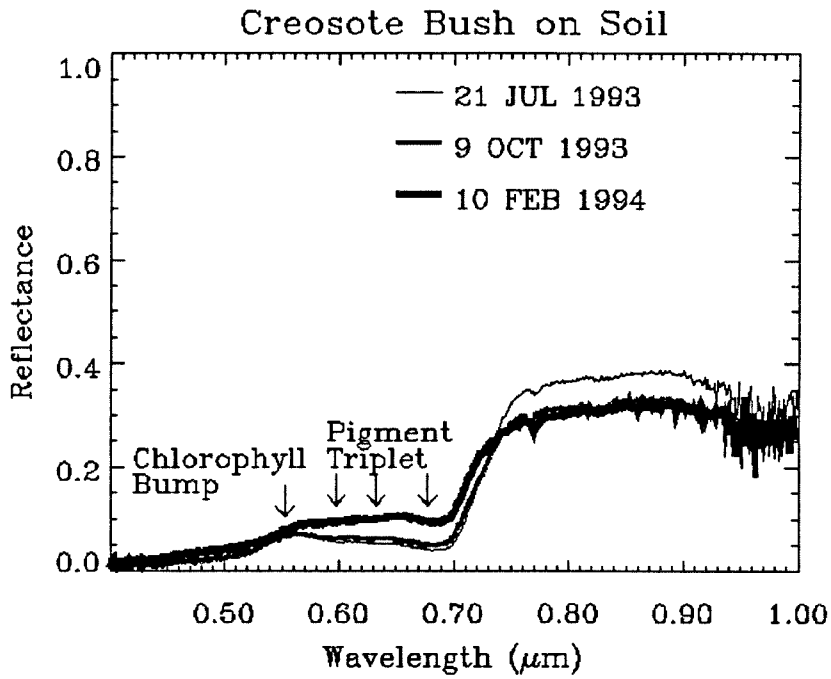

Figure 74: Comparison of PS2 field spectra of a single creosote bush against the soil background collected over 8 months. Notice how the overall spectrum flattens. The pigment features weaken significantly from the summer to the winter. The NIR reflectance decreases from summer to autumn with little change in the pigment features, but there is little change in NIR reflectance from autumn to winter.

weaker. This sequence is replicated by all three creosote bushes observed across these dates, and the spectra against the dark target which were collected in July and January. This argues against this difference being due to either soil variation or the fact that creosote bush canopies are heterogeneous and the instrument was probably not pointed precisely at the same part of the canopy in each observation.

A GER spectrum of a creosote bush against the dark target acquired on February 24, 1994 is shown in figure 75. Although the chlorophyll bump at 0.55 μm is somewhat flattened, the pigment triplet is clearly visible. The is more similar to the October 10, 1993 spectra than to the February 10, 1994 spectra. Rain had occurred in the field area just

prior to February 10, and the differences between the two dates may be due to pigment production triggered by the rain over the intervening 14 days. This quick reaction to rain is consistent with the creosote bush root systems ability to quickly acquire near-surface water discussed earlier.

Figure 76 shows the same creosote bush with the dark target removed. The entire spectrum is somewhat brighter, but a close examination reveals that the NIR reflectance has been enhanced much more strongly than the visible reflectance which increases the "step" from red to NIR measured by vegetation indices. For the three creosote bushes measured with the GER spectrometer, #1 showed this enhancement, #2 showed a much weaker enhancement, and #3 showed a disenhancement. Significantly,

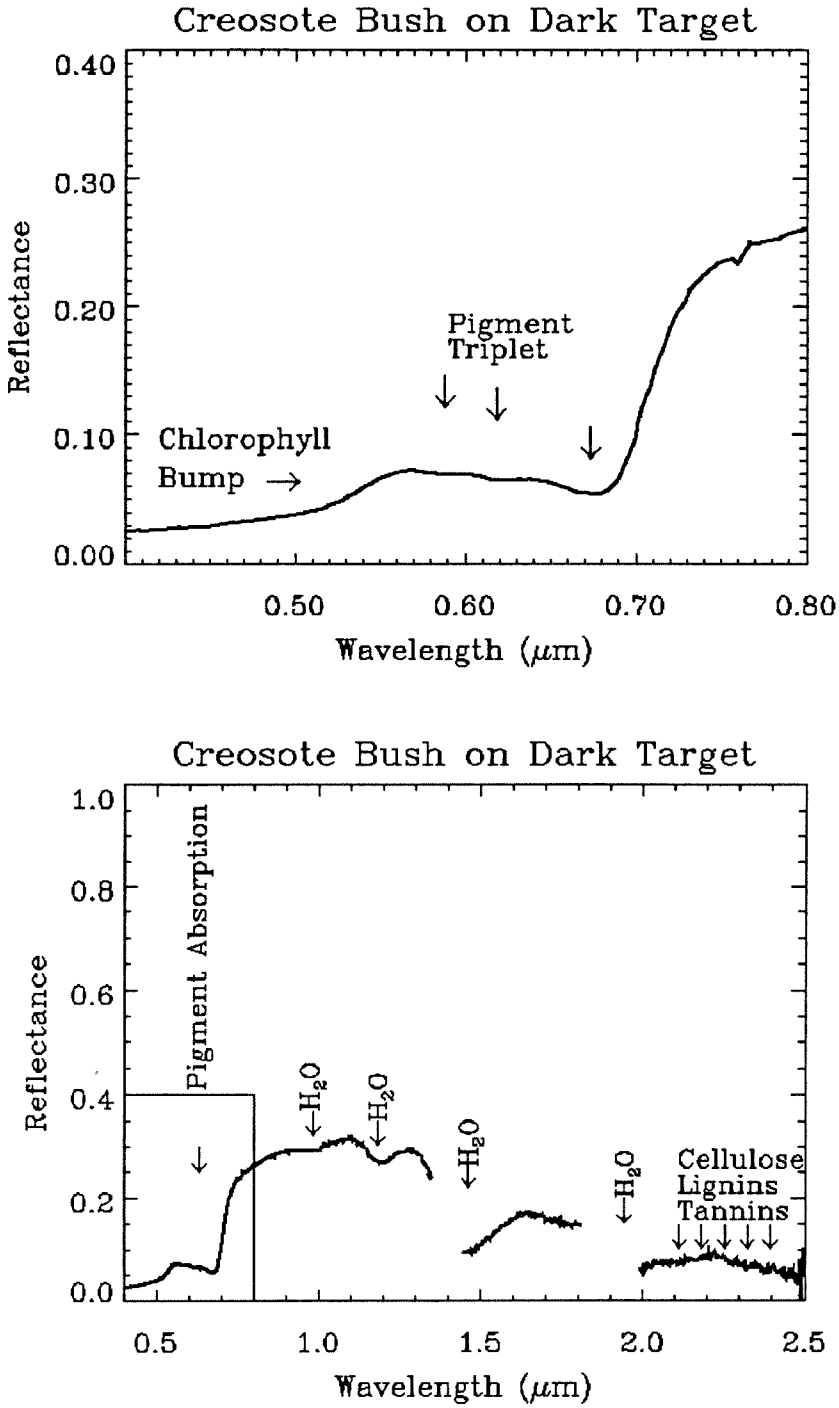

Figure 75: GER spectrum of creosote bush against dark target. Spectrum was collected February 24, 1994. Notice the strengthening of the pigment features compared to the February 10, 1994 spectrum in figure 74. The noise near 2.2 μm obscures the absorption features due to cellulose, lignin, and tannin. Rain had occured on February 9, 1994, and these changes are likely due to the creosote bush's reaction to the precipitation.

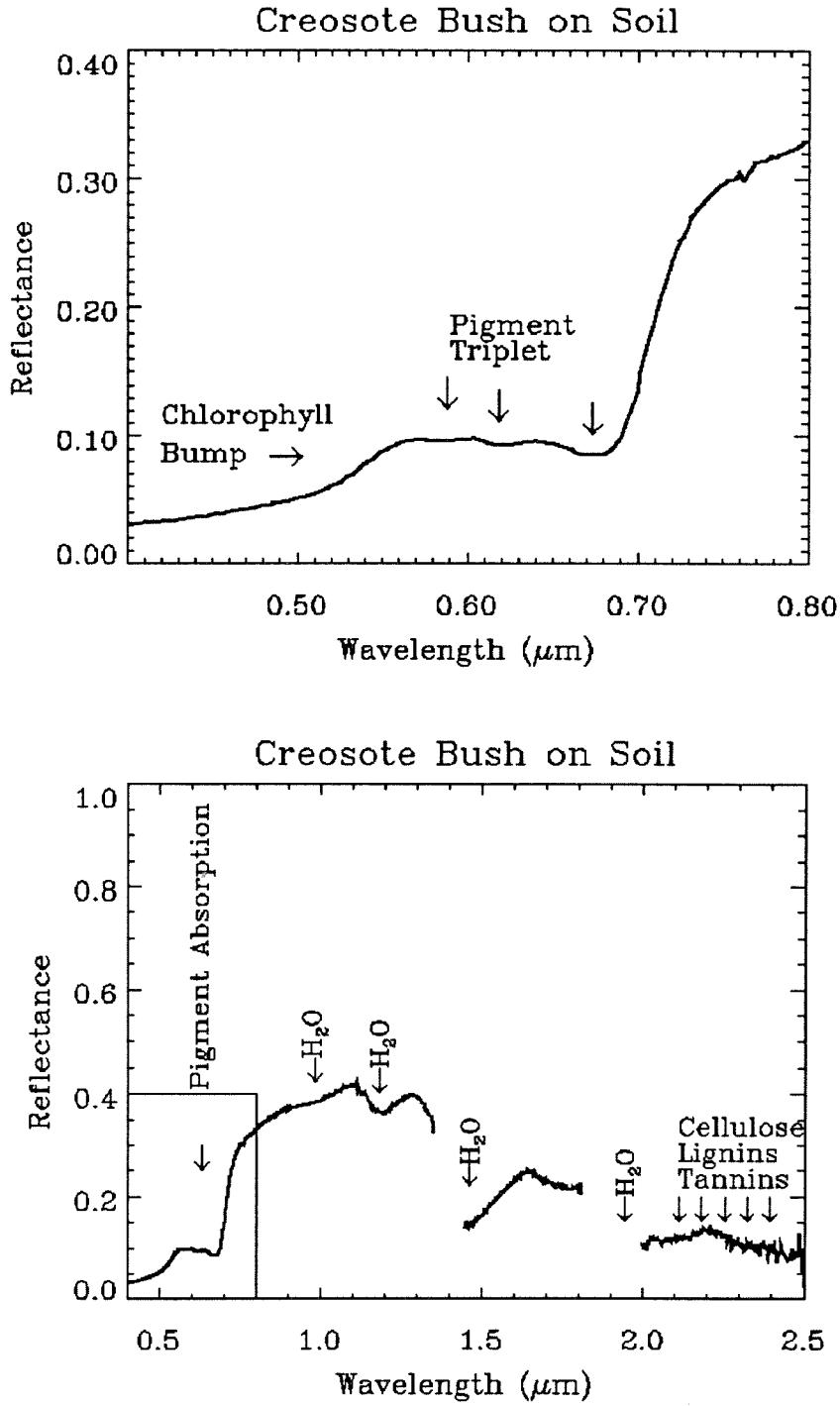

Figure 76: GER spectrum of same creosote bush as in figure 75 but with the dark target removed. Notice the enhancement of the red edge compared to figure 75.

this exactly agrees with the February 10 PS2 measurements which gave the same results for each shrub (#1 enhanced, #2 less enhanced, #3 disenhanced).

Creosote bush leaves look similar to those of humid plants like alfalfa, but with weaker pigment features and stronger features due to other plant materials. The whole plant spectrum of the creosote bush shows the effect of small leaves in the weakening of the pigment absorption and NIR reflectance as compared to the leaf spectrum. The seasonal cycle of drying initially decreases the NIR reflectance through water loss and then weakens the pigment features as chlorophyll is diminished to decrease the photosynthetic demands on water. The pigment features strengthen quickly after rainfall because of the extensive near-surface roots of the creosote bush.

Part 5.3.3: *Bursage*

The next important shrub in the Manix Basin area is bursage. Figure 77 shows the Beckman laboratory reflectance spectrum for bursage leaves from a shrub on the undisturbed desert. These leaves were almost entirely small, tightly-rolled leaves with a sand-like appearance. Figure 78 shows the Beckman laboratory reflectance spectrum for bursage leaves from a shrub on abandoned field 12, and this sample differs from that shown in figure 77 in having many unrolled leaves covered by silvery hairs. The differences seen between figures 77 and 78 are most likely due to the leaves being unrolled in figure 78. The presence of unrolled leaves on the shrub in the abandoned field indicates that it was growing more actively than the bursage in the undisturbed desert.

The first obvious difference is the higher reflectance in the visible in figure 77 as compared to figure 78. There is a suggestion of the pigment triplet in both spectra, but the only truly definite feature in either case is the chlorophyll minimum at 0.675 μm. The NIR reflectance is similar for both spectra, although the water absorptions at 1.2, 1.4, and 1.9 μm are all weaker in figure 77 than in figure 78. Figure 79 shows the PIMA spectrum of the unrolled leaves and figure 80 shows the rolled leaf spectrum. All of the cellulose, hemicellulose, lignin, and tannin absorption features are significantly weaker for the unrolled leaves. This suggests that the rolled and unrolled leaves are chemically similar, with the main differences being due to the lower water content of the rolled leaves as shown by the weaker water absorption features.

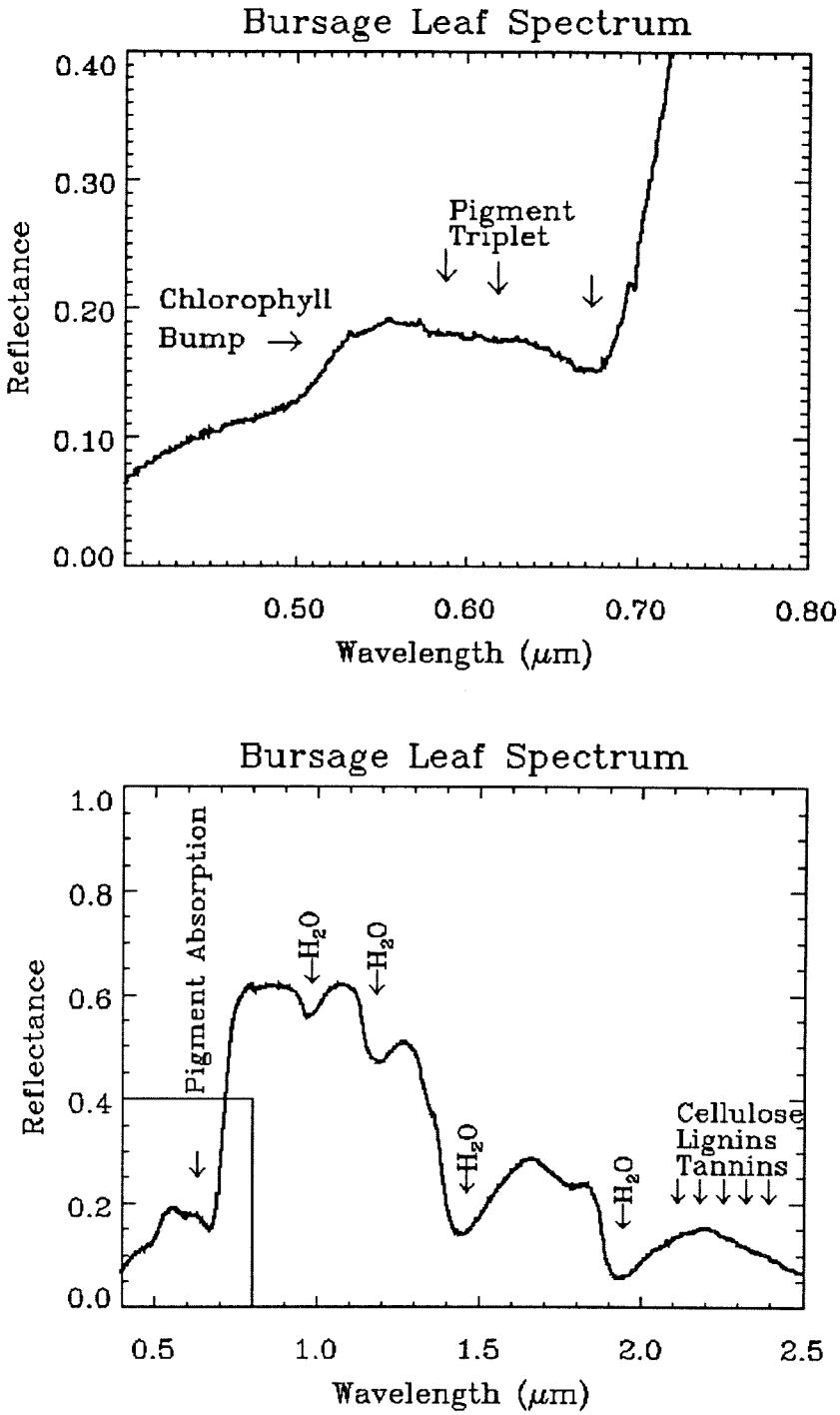

Figure 77: Beckman spectrum of bursage leaves from bush on undisturbed desert. All of these leaves were tightly rolled. The upper plot is an enlargement of the boxed area. Note the weak and indistinct nature of the pigment triplet and the lack of distinct absorptions around 2.2 μm.

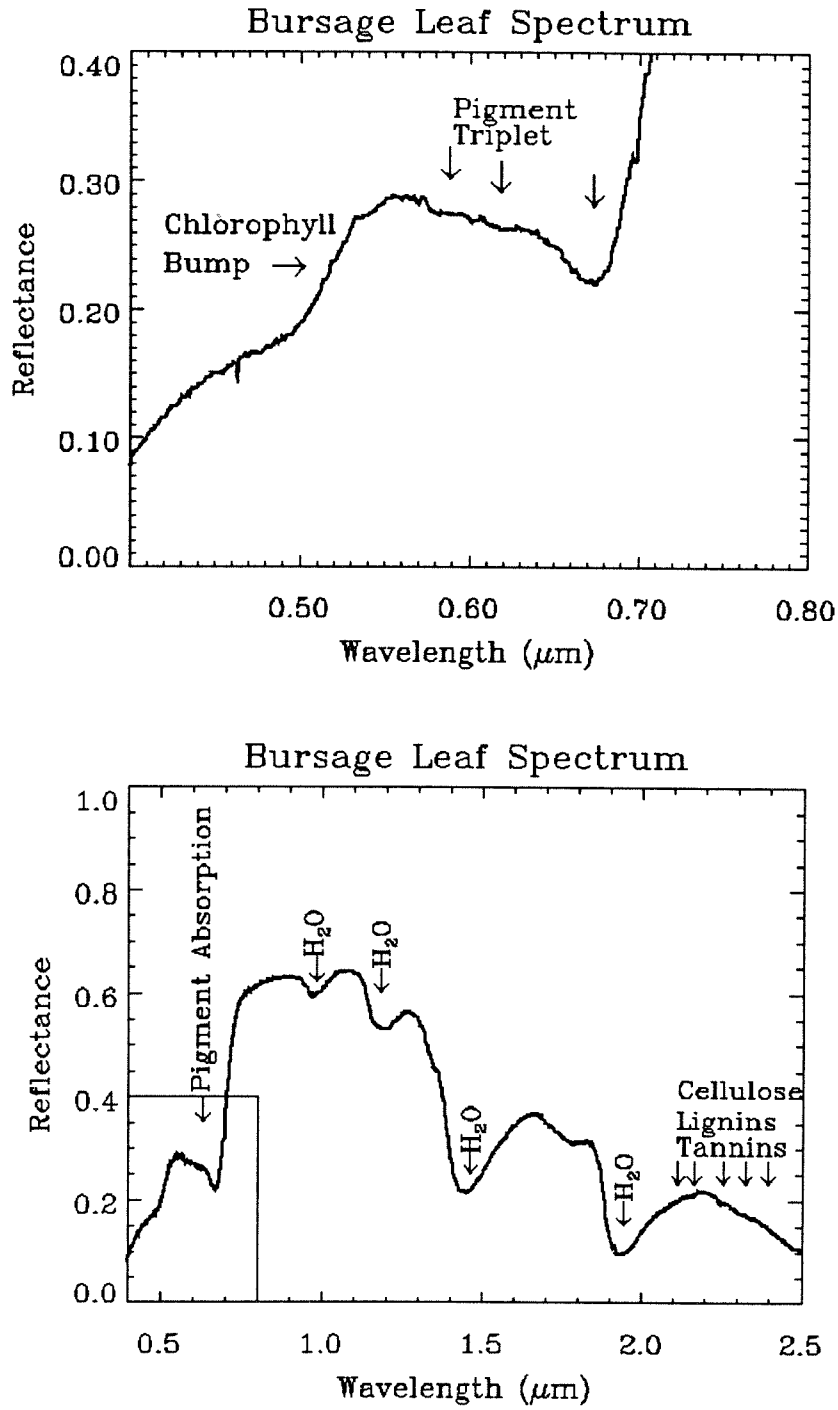

Figure 78: Beckman spectrum of bursage leaves from bush on abandoned field #12. Most of these leaves were unrolled and hairy. Note that the visible reflectance is significantly higher than in figure 77. Also note the indisctinctness of the chlorophyll-b and protochlorophyll absorptions (the left and middle arrows of the pigment triplet). There are no distinct absorptions around 2.2 μm.

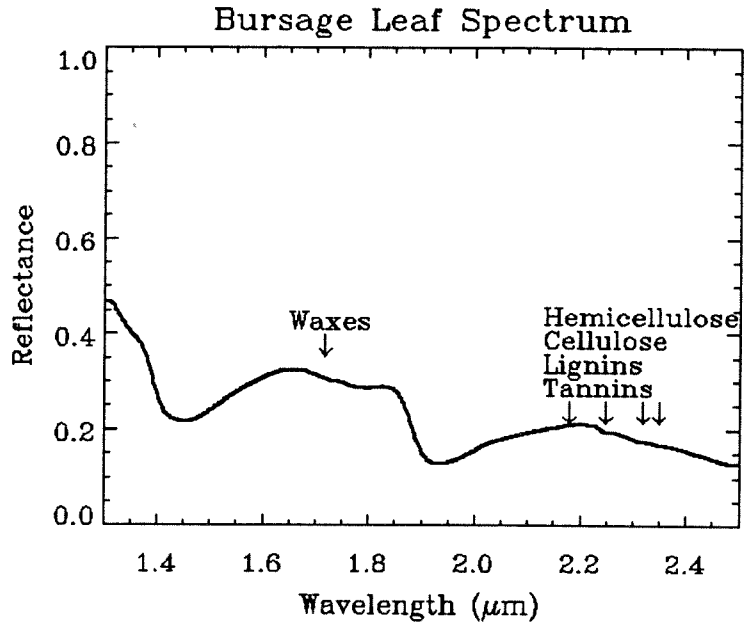

Figure 79: PIMA spectrum of bursage leaves from bush on undisturbed desert. This is the same sample as that for figure 77. All of these leaves were tightly rolled. Note the subtle absorptions around 2.2 μm due to cellulose, hemicellulose, lignin, and tannin, and also note the absorption near 1.7 μm which may be due to waxes.

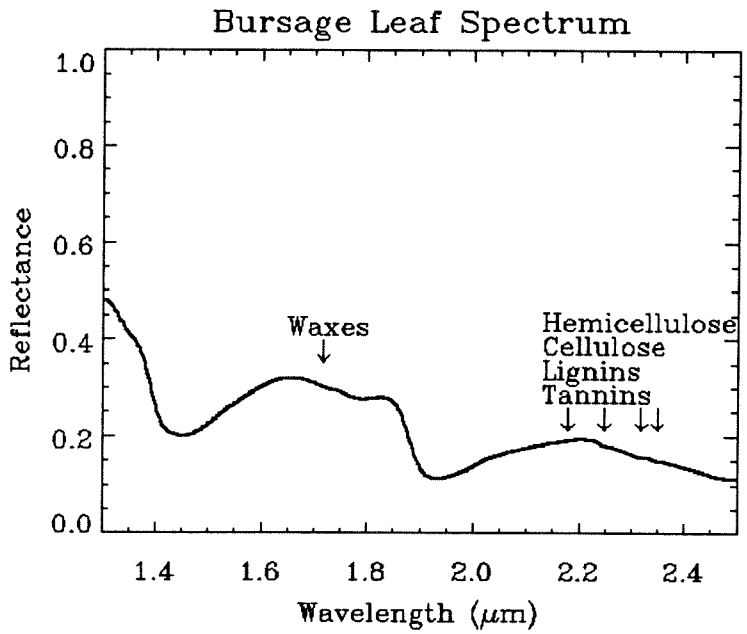

Figure 80: PIMA spectrum of bursage leaves from bush on abandoned field #12. This is the same sample as that for figure 78. Most of these leaves were unrolled and hairy. Notice that the wax absorption and the hemicellulose, cellulose, lignin and tannin absorptions are weaker than those in figure 79.

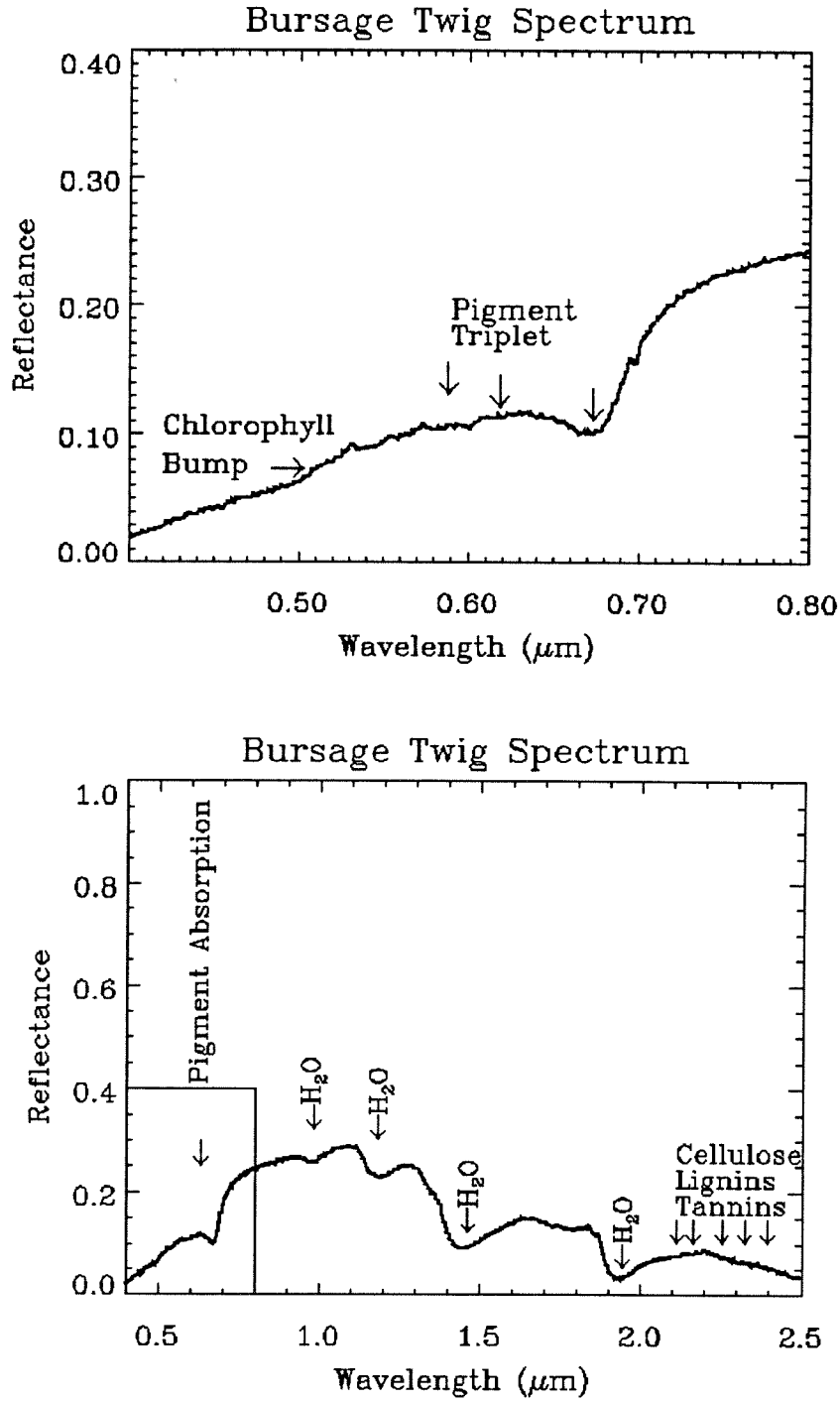

Figure 81: Beckman spectrum of bursage twigs from bush on abandoned field #12. The upper plot is an enlargement of the boxed area. Note the lack of pigment features except for the chlorophyll-a feature at about 0.675 μm. Subtle absorptions around 2.2 μm are also present.

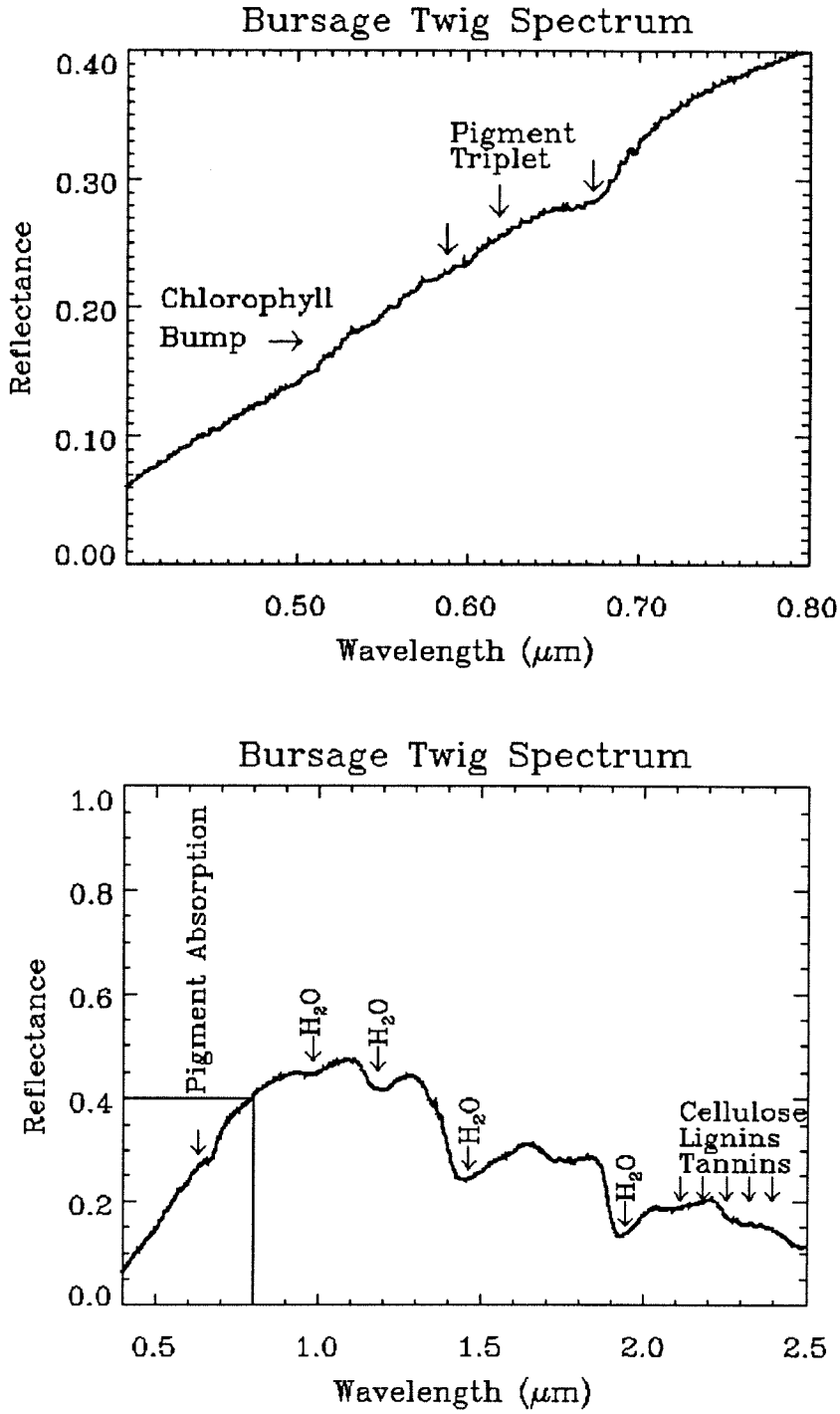

Figure 82: Beckman spectrum of bursage twigs from bush on undisturbed desert. The upper plot is an enlargement of the boxed area. As in figure 81, the only definite pigment feature is the chlorophyll-a absorption. The cellulose, hemicellulose, lignin and tannin features around 2.2 μm are more definite here than in figure 81.

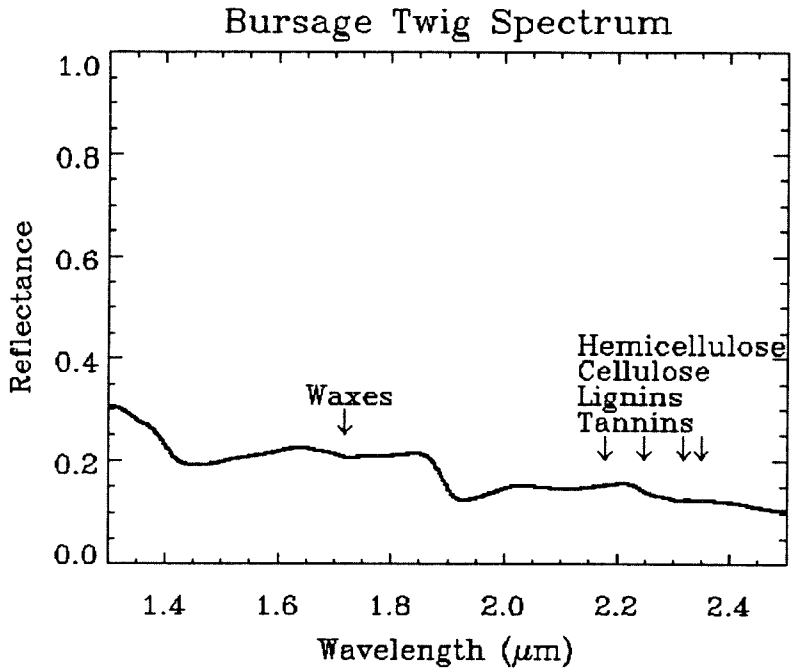

Figure 83: PIMA spectrum of bursage twigs from bush on undisturbed desert. This is the same sample as for figure 82. Note the clear absorptions due to cellulose, hemicellulose, lignin and tannin.

Figures 81 and 82 are the reflectance spectra of twigs from bursage shrubs on the abandoned field and in the undisturbed desert respectively. One reason for the significantly darker spectrum in figure 81 is the fact that the sample cup was not completely full. Comparisons of the absolute value of the reflectances is probably inappropriate, but differences in shape may still be significant. The twigs still strongly absorb in the visible, but the only chlorophyll absorption is near 0.675 μm. This absorption is more pronounced in the abandoned field twigs, and this probably indicates a higher vascular activity in the shrub on the abandoned field which is necessary to support the actively photosynthesizing unrolled leaves. Figure 83 shows the PIMA spectrum for

the bursage twigs from the undisturbed desert, which shows the broad absorptions to either side of 2.2 μm.

Figure 84 shows a PS2 spectra of a bursage shrub against the dark target, and figure 85 shows the same shrub without the dark target. The first item of interest is the fact that there is virtually no difference between these spectra. In the earlier discussion it was indicated that the bursage canopy was composed of a thick tangle of twigs which completely obscured the soil from direct view. In essence, the ever-deepening shadows seen in the bursage canopy means that the natural background for the shrub is basically a dark target. Recall from figure 6 that the bursage is more grayish than green, so the fact that the long-wave visible reflectance is rather flat is not surprising. The relatively weak reflectance in the NIR is once again due to the very limited leaf area presented by the rolled leaves of the bush.

In general, the bursage shrubs in the study area are observed to be mainly covered with small, rolled leaves with relatively few unrolled leaves. Figure 86 shows the PS2 spectrum of the shrub pictured in figure 87 at the time the picture was taken. Notice that the NIR reflectance is very strong, and in fact stronger than that observed for any of the leaf laboratory spectra for any species. The reasonable conclusion is that the unrolled leaves were still quite hairy and that much of the high reflectance is due to the hairs and not the underlying leaf material. These open leaves are reflecting away more than one-third of the radiation available for photosynthesis even during the cool morning.

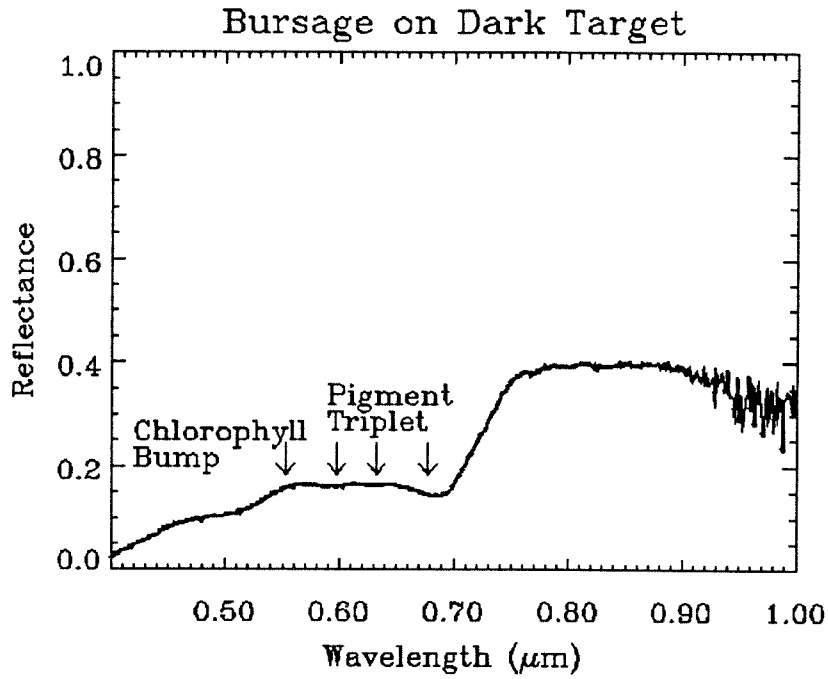

Figure 84: PS2 spectrum of bursage shrub against dark target. Notice how flat the spectrum is across the pigment triplet as opposed to the same feature in the alfalfa or creosote bush.

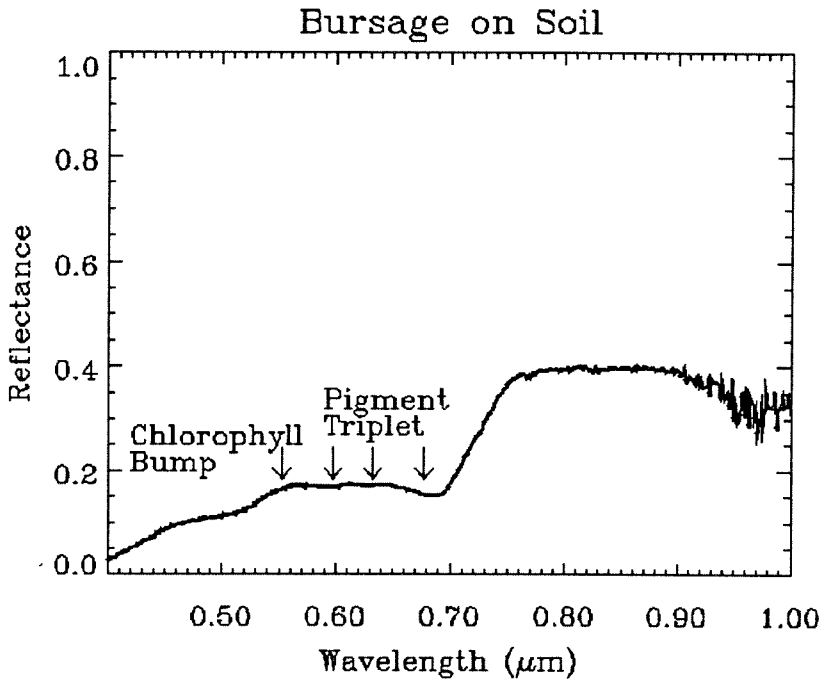

Figure 85: PS2 spectrum of same bursage as in figure 84 but with the dark target removed. Note how similar figures 84 and 85 are to each other.

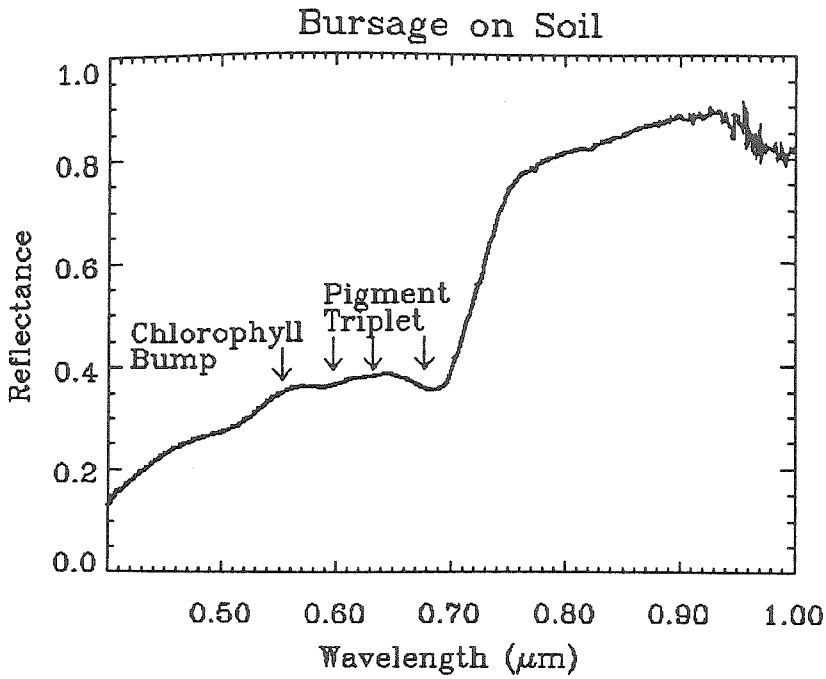

Figure 86: PS2 spectrum of bursage pictured in figure 87. Note the very strong NIR reflectance, and the strong and relatively flat reflectance across the pigment triplet.

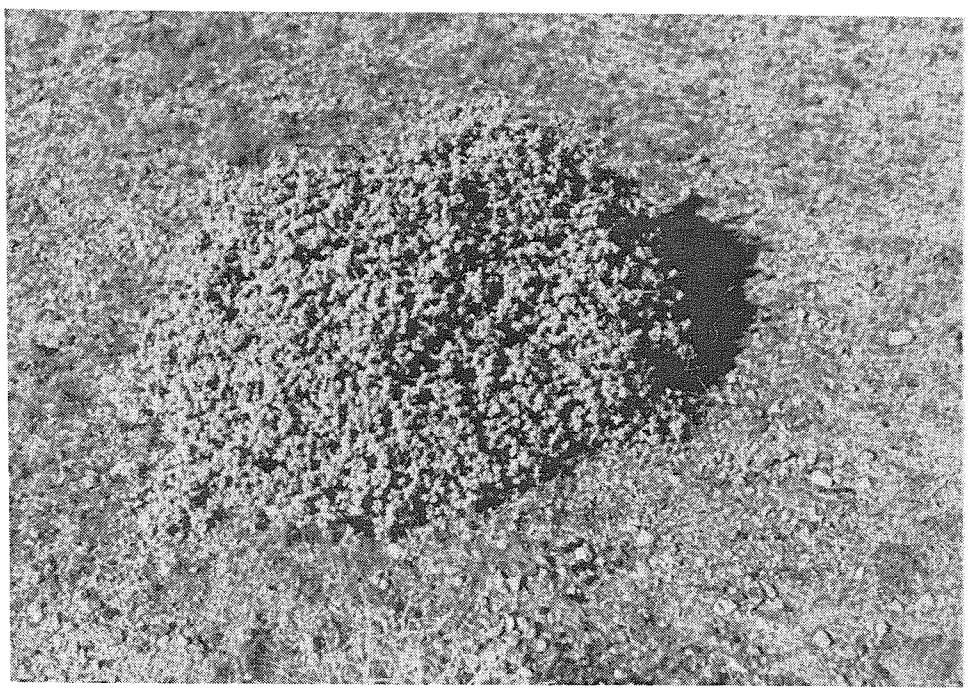

Figure 87: Photograph of bursage with unrolled leaves in the early morning. The spectrum in figure 86 was acquired from this shrub at the time this picture was taken.

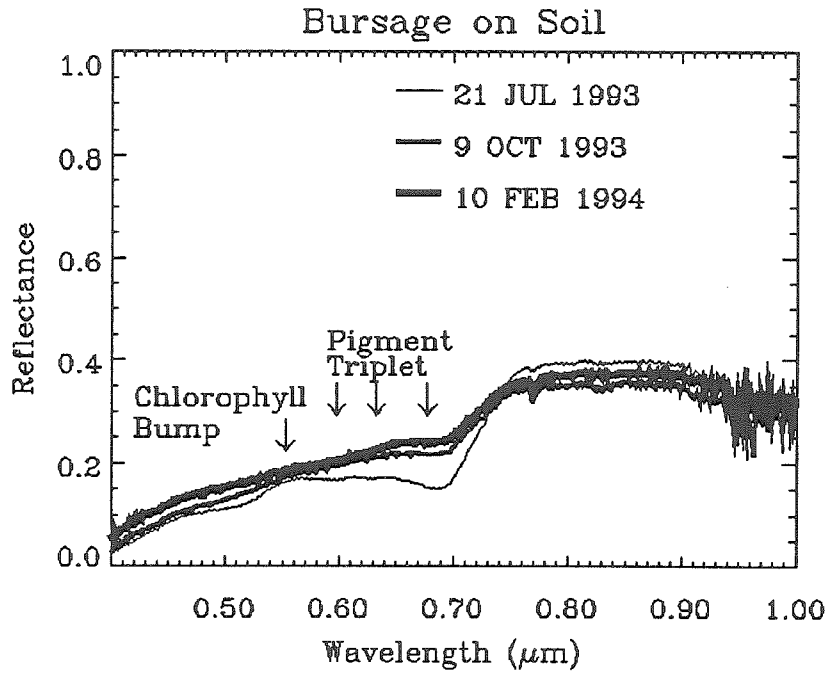

Figure 88: Comparison of PS2 field spectra of a single bursage against the soil background collected over 8 months. Note how the NIR reflectance is suppressed from July to February and how the pigment features are eliminated over the same time.

Figure 87 shows a bursage at about 10 AM PST with nearly all of its leaves unrolled. It should be noted that these unrolled leaves were all positioned so as to efficiently intercept the early morning sunlight.

Figure 88 shows three spectra collected of the same bursage shrub over the 8-month period covered by the data collection. Notice the similarity to figure 71 for the creosote bush. From July to February there is a clear weakening of the pigment features in the visible coupled with a slight decrease in NIR reflectance. All three of the bursage shrubs observed on all three dates showed the same pattern. Clearly both the creosote bush and the bursage decrease their capability to photosynthesize and grow during the dry autumn and cold early winter.

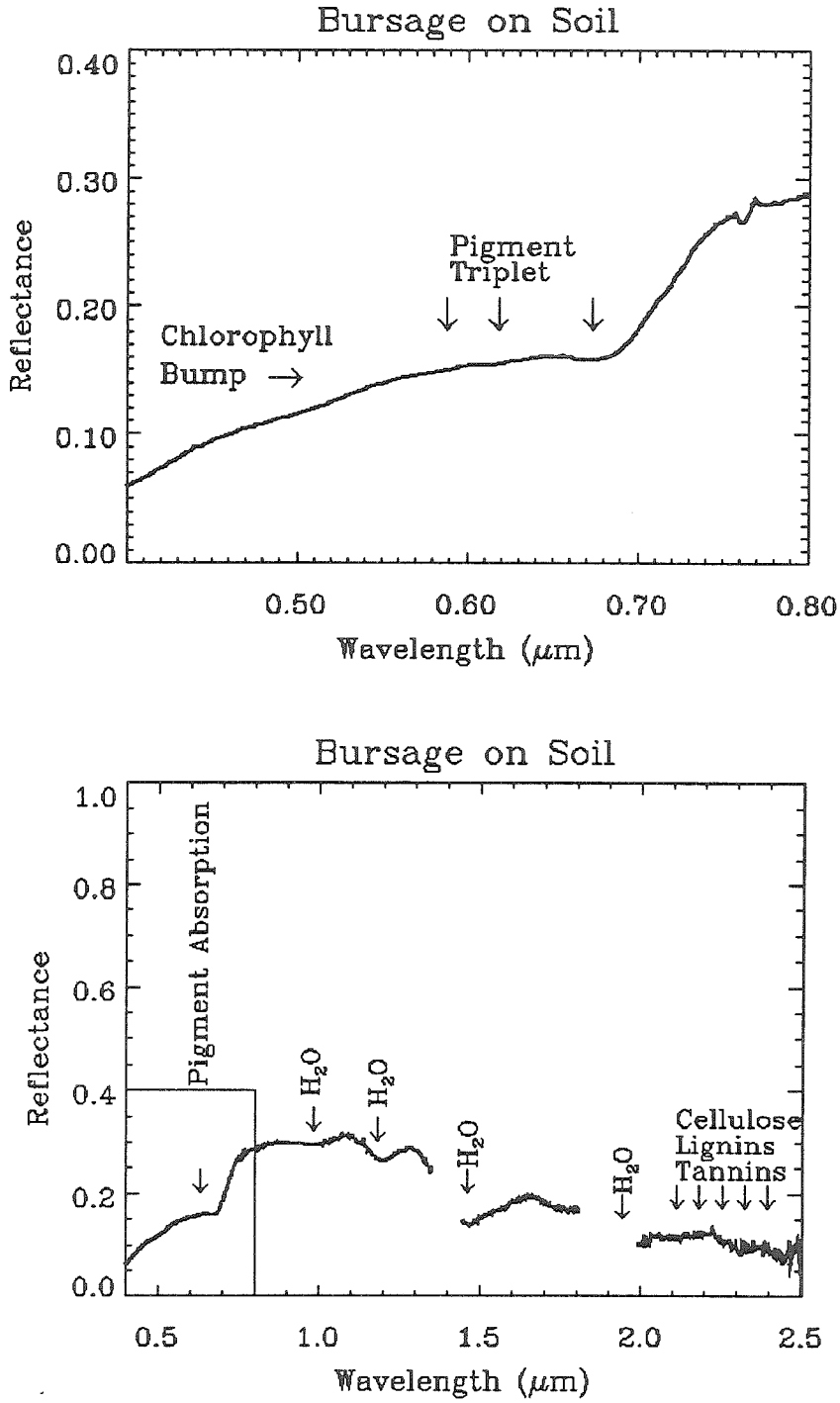

Figure 89: GER spectrum of bursage. The upper plot is an enlargement of the boxed area. This spectrum was collected February 24, 1994 from the same bursage as in figure 88. Note that, unlike creosote bush, the pigment features have not changed over the two weeks since the precipitation. There appear to be cellulose, hemicellulose, lignin, and tannin absorptions around 2.2 μm.

A GER spectrum of a bursage shrub collected on February 24, 1994 is shown in figure 89. The pigment features in the visible are just as weak as that shown in figure 88 for February 10, 1994. This can be compared to the previous results for the creosote bushes which showed that all three creosote bushes had stronger pigment features during late February as compared to early February which suggested that there was an increase in chlorophyll pigments due to the rain in early February. The fact that this does not appear to happen for bursage suggests that there is a longer time lag between increased water availability and pigment generation in bursage than there is for creosote bush.

In general, a comparison between the spectra of creosote bush and of bursage shows that the bursage generally has weaker pigment features than does creosote bush. The bursage is generally more reflective than the creosote bush in the visible and less reflective in the NIR. Both types of plants clearly show absorption features due to plant materials such as cellulose, hemicellulose, and lignin. Additionally, the creosote bush laboratory spectra clearly show a NIR absorption which is related to waxes present in creosote bush leaves. Bursage will tend to look less like green vegetation than creosote bush under all conditions, and it will react more slowly to rainfall than creosote bush. The differences in the shape of the pigment features between these two shrubs may enable their discrimination in future remote sensing.

Part 5.3.4: *Desert Grass*

The third important plant present in the study area is a short, usually yellow grass. This grass covers many of the areas between shrubs in the undisturbed desert and it is very prolific on some of the recently abandoned fields. Figure 90 shows PS2 spectrum of a clump of the yellow grass. The grass is highly absorbing in the short wavelength visible and there is a smooth rise to moderate NIR reflectivity. This spectrum is very similar to the lignin spectra in Elvidge (1990), except that this spectrum is less reflective overall.

In figure 91, the yellow grass spectrum is plotted along with a spectrum of bare soil in the field area. Notice that the grass is generally darker that the soil, and that the slope of the spectrum in the visible wavelength is higher than that for the soil spectrum. Although the yellow grass spectrum is very similar to the soil spectrum in shape, there is a definite iron oxide absorption in the visible for the soil which is not present in the yellow grass.

A GER spectrum of the yellow grass is shown in figure 92. The visible spectrum is quite similar to that shown in the PS2 spectrum. Near 2.2 μm there are significant absorption features. The first feature is centered at 2.1 μm and is probably a combination of lignin and cellulose absorptions, and another broad absorption near 2.3 μm is most likely due to the same plant constituents. There is also a small absorption right at 2.2 μm which is probably related to the phyllosilicate absorption seen in the laboratory soil spectra. Generally, this grass looks like bare lignin and cellulose, which is reasonable given the visible lack of pigment, combined with small amounts of soil.

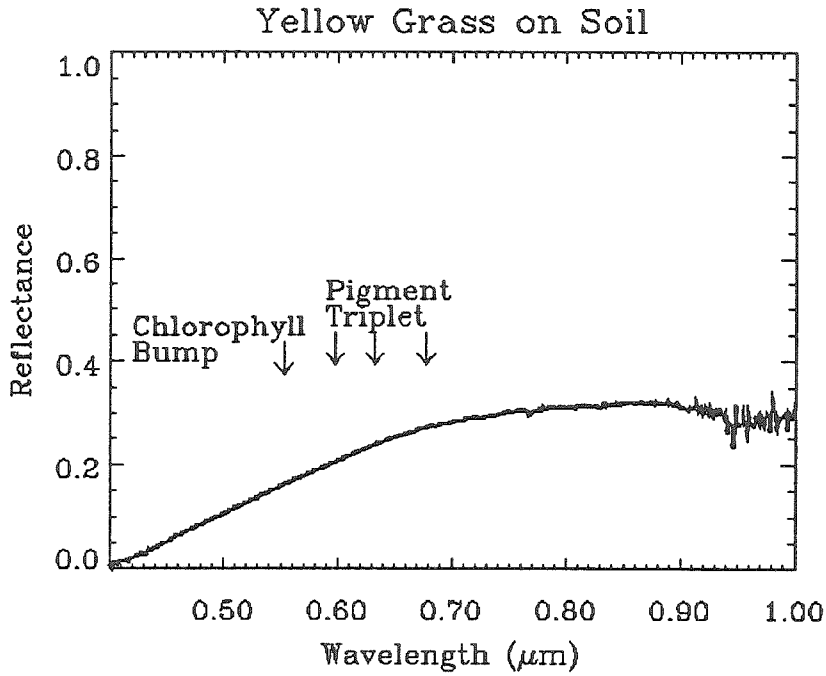

Figure 90: PS2 spectrum of a clump of yellow desert grass. Note the complete lack of pigment absorption features.

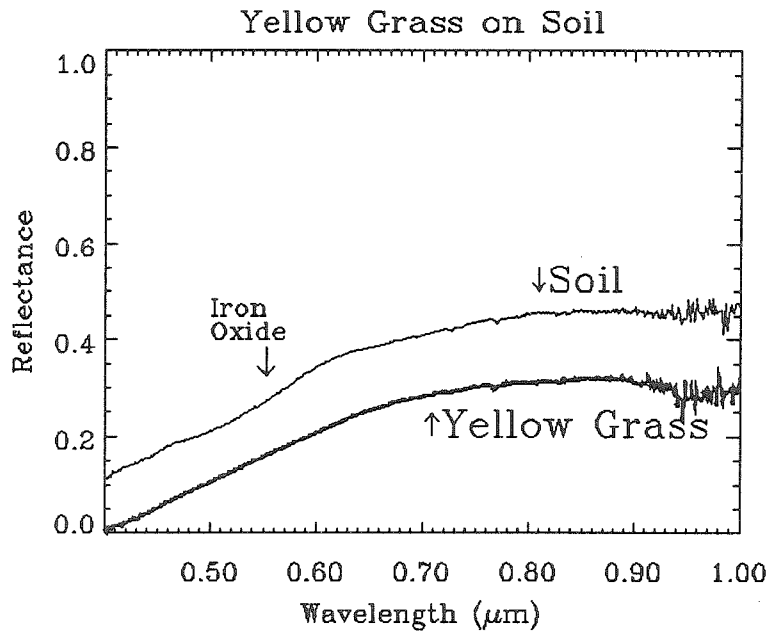

Figure 91: PS2 spectra of bare soil and the yellow grass in figure 90. Note that the grass spectrum is darker overall than the soil spectrum. Notice the lack of an iron oxide absorption feature in the grass spectrum.

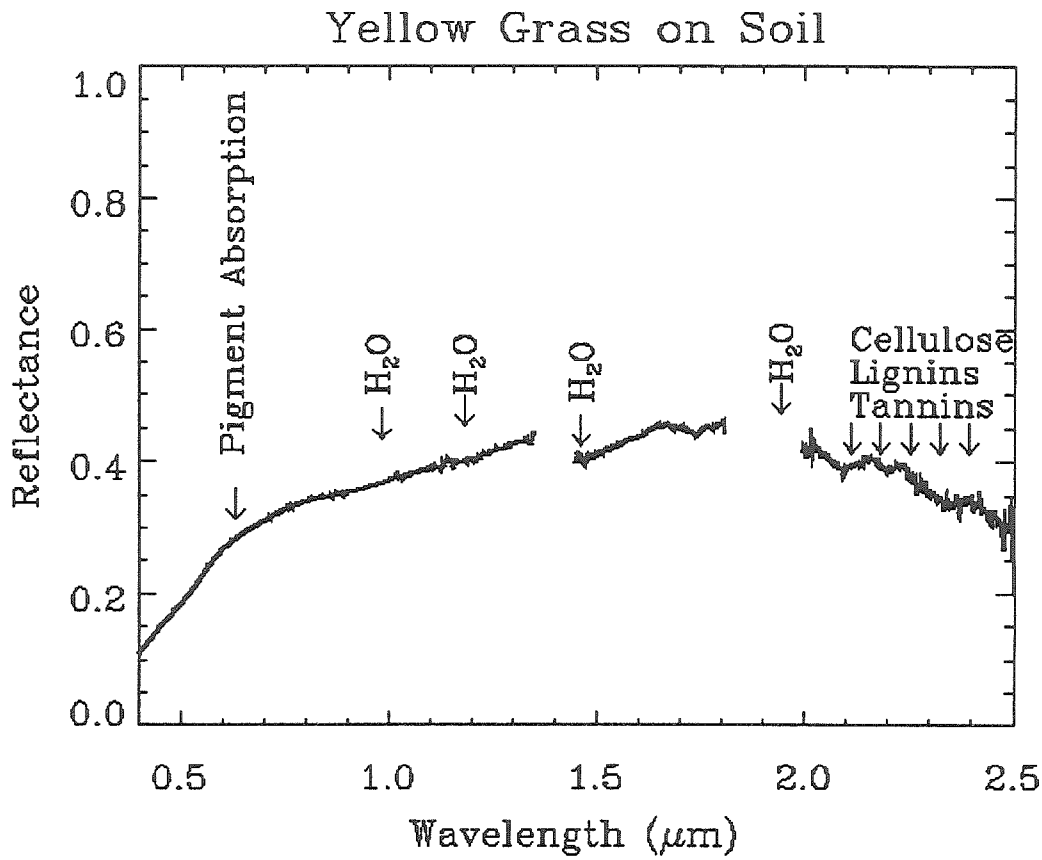

Figure 92: GER spectrum of yellow desert grass. Note the presence of cellulose, hemicellulose, lignin, and tannin features around 2.2 μm.

Part 5.3.5: *Tumbleweed*

The final major plant in the field area is the Eurasian invader *Salsola kali* or Russian Thistle. More commonly known a tumbleweed, figure 93 shows a PS2 spectrum of an example of the plant against the dark target. Figure 94 shows the same plant with the natural soil as the background. The removal of the dark target led to a slight enhancement of the red to NIR step in the spectrum for both tumbleweeds observed in this manner.

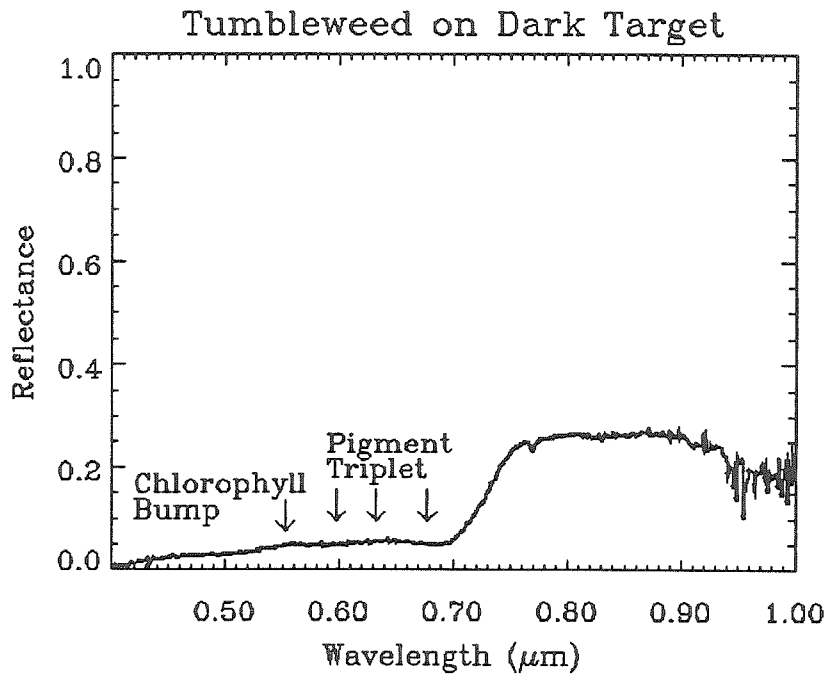

Figure 93: PS2 spectrum of tumbleweed against the dark target. Note the lack of a chlorophyll-b feature (middle arrow of the pigment triplet).

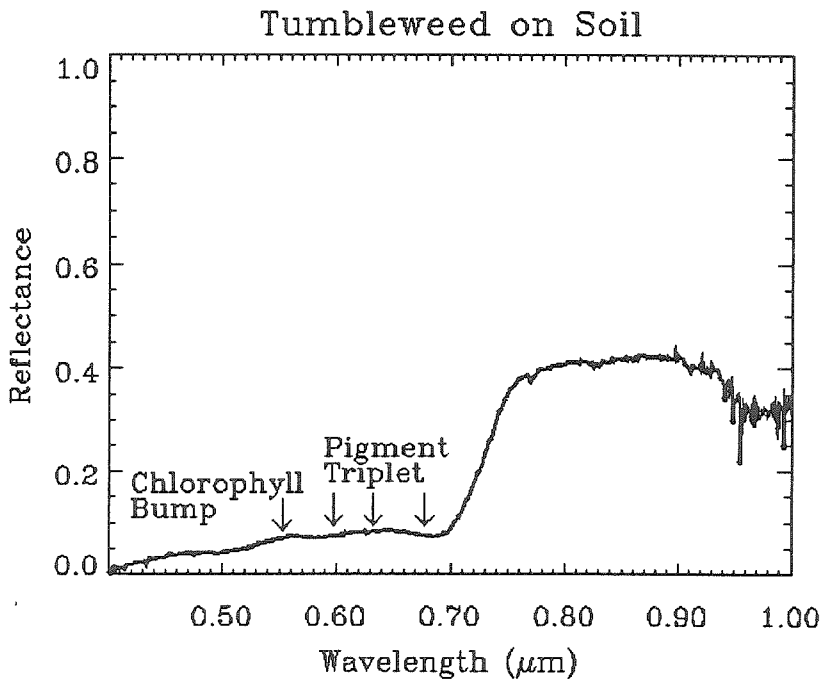

Figure 94: PS2 spectrum of tumbleweed for figure 93, but with a soil background. Note the enhancement of the visible-NIR step.

Part 5.3.6: *Shadows*

Earlier discussion of the desert shrubs indicated that partially shadowed soil and vegetation would always be seen through the directly lit canopy, so it is important to look at the spectral characteristics of these shadows to understand how this will affect measurements of this vegetation.. As shown in part 5.5, non-linear mixing depends on the interaction of light with multiple targets, and light passing through the canopy to the underlying soil or to other parts of the canopy is an important factor in such mixing. In figure 62, the reflectance spectrum of the white reference target in solid shadow is shown for both the PS2 and GER spectrometers. The white reference target is defined to have a reflectance of unity and that definition allows reflectivity values to be assigned to the target. Figures 95 and 96 are the reflectance spectra for the reference target in the shade of a creosote bush and in the shade of a bursage shrub respectively. The reflectance for the creosote bush shade is brighter than that for bursage across the entire spectrum, and the bursage is in turn brighter across the entire spectrum than the spectrum of solid shade shown in figure 62. This indicates that more direct sunlight reaches the soil through the creosote bush canopy than through the bursage canopy, which means that the soil background should have little influence on the spectral characteristics of bursage as observed by either field spectrometers or airborne and satellite remote sensing instruments. The greater amount of light reaching the soil through the creosote bush canopy makes the soil a much more important factor in measurements of creosote bush.

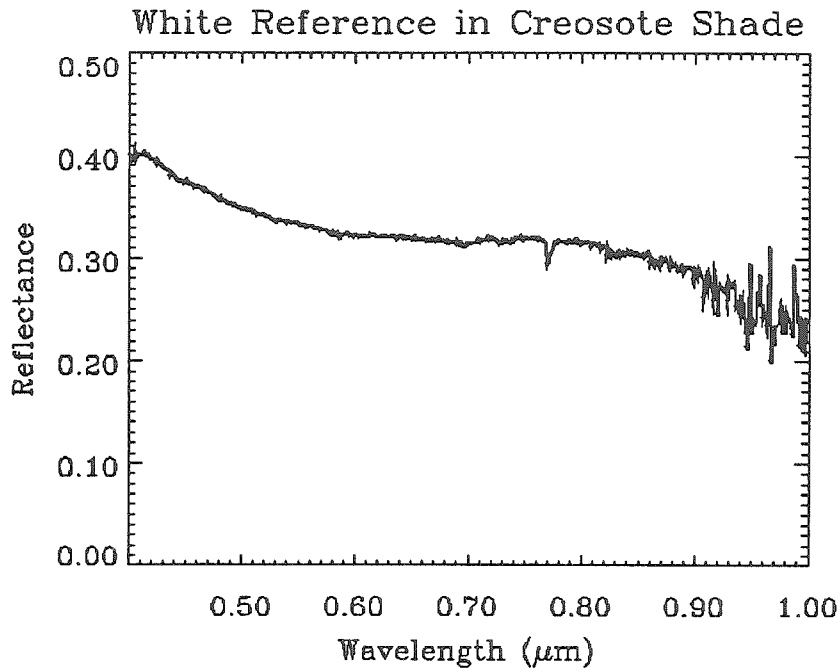

Figure 95: Reflectance spectrum of the white reference target in the shade of a creosote bush.

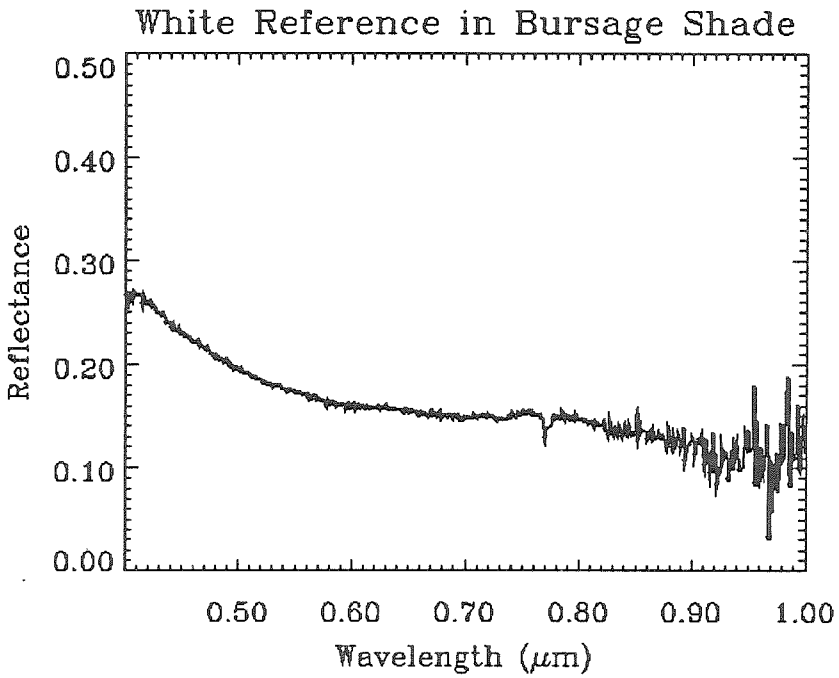

Figure 96: Reflectance spectrum of the white reference target in the shade of a bursage.

The broad bump seen in figures 95 and 96 between 0.7–0.9 μm suggests that the light passing through the canopy into the shadow of the plant has been distorted by the reflectance of the plant, since that is the spectral region where the reflectance of vegetation dramatically changes. Gates (1980) has shown that creosote bush leaves transmit very little light, and the leaves of the bursage are also fairly thick and they should not transmit much light. The significantly brighter creosote bush shade is due to the fact that more direct sunlight is clearly seen in the shade as bright sunlight patches (figure 58).

Figures 97 and 98 are PS2 spectra of self-shaded creosote bush and bursage respectively. In each of the cases, a part of the shrub is being measured that lies in the shadow cast by another part of the shrub. The pigment zone from 0.5–0.7 μm is very flat in both cases, but the creosote bush is much flatter and less reflective in the visible. In figure 158, the protochlorophyll and chlorophyll-a absorptions for the bursage can still be seen. The enhanced NIR reflectance is still clearly present in both spectra. Note vegetation indices which depend on ratios will give large values for both of these spectra since the reflectance in the red is very small in each case. For example, the standard NDVI value for a typical creosote bush spectrum is about 0.68, while the NDVI value for the spectrum in figure 97 is about 0.90 (exact NDVI values depend on instrument bandpasses).

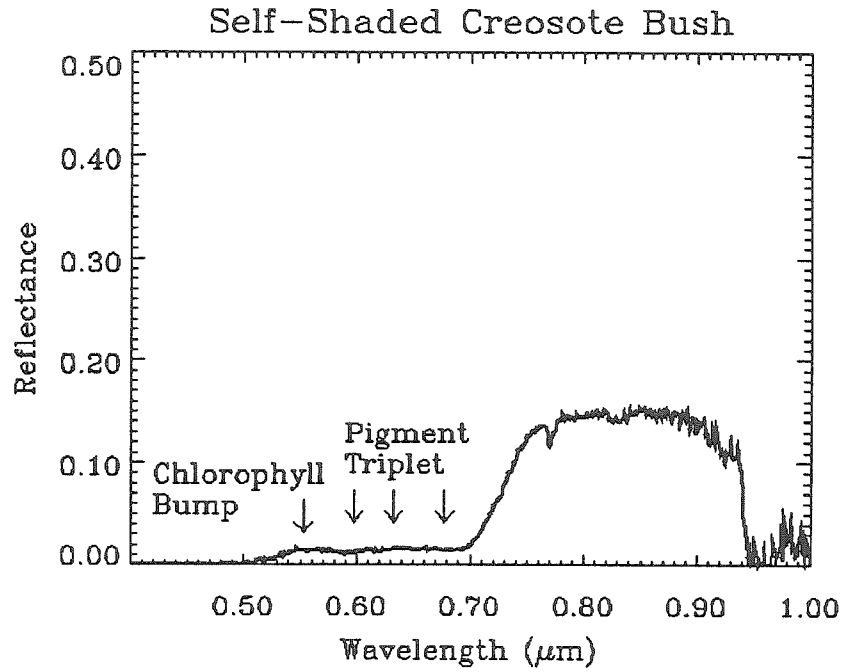

Figure 97: PS2 spectrum of creosote bush in its own shade. Note the very flat pigment zone.

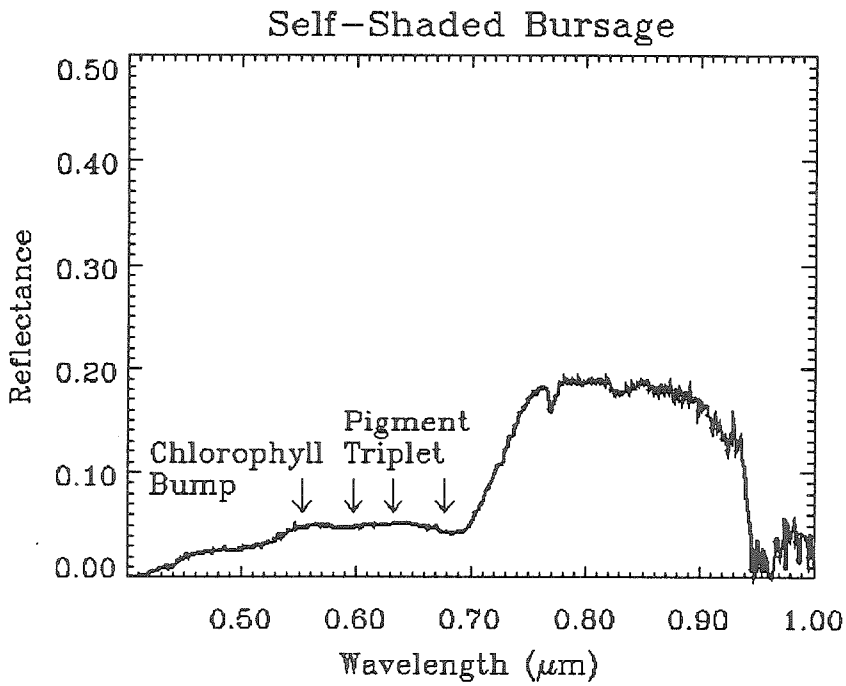

Figure 98: PS2 spectrum of bursage in its own shade.

Part 5.3.7: *Summary*

Several things are clear from the spectra or arid plants discussed above. First, the desert shrubs like creosote bush and bursage share many spectral characteristics with more typical green plants such as alfalfa. Second, the leaves of the desert shrubs have comparable NIR reflectances to alfalfa. Third, the gray-green leaves of the bursage do appear flatter in the pigment zone (0.5–0.7 μm) than the greener alfalfa or creosote bush leaves. Fourth, the spectra of arid plant leaves tend to have significant NIR absorptions related to lignin, cellulose, and hemicellulose, while these features are not seen in plants from less arid conditions such as alfalfa. Fifth, the overall lower reflectance of whole shrub spectra is largely due to the small leaf area of the arid shrubs. Sixth, bursage tends to have a smaller red–NIR step than creosote bush, which in turn has a smaller step than alfalfa. Seventh, both creosote bush and bursage appear to lose chlorophyll pigments during the dry autumn and cold winter, and this results in a smaller red–NIR step than observed during the summer months. Eighth, the dry yellow desert grass resembles a combination of lignin and cellulose in spectral characteristics, and differs from the soil in the visible primarily in the lack of an iron oxide absorption. Ninth, the shaded parts of creosote bush and bursage give higher values for ratio-based vegetation indices than do the parts experiencing direct sunlight. Tenth, the light in the shade of creosote bush and bursage have been altered by reflectance in the canopy.

The different shapes of the pigment features in creosote bush and bursage may provide an opportunity for discriminating between the two shrub types. The evidence of fast changes in the pigment features for creosote bush after rainfall and the substantive

changes in the spectra of creosote bush and bursage during dry periods indicates that a good knowledge of the meteorology in the area will be required for effective monitoring. Finally, the significant smaller red edge step in bursage as compared to creosote bush casts severe doubts on the ability of standard vegetation indices to provide accurate information.

Part 5.4: *Application of Standard Vegetation Indices.*

The previous two sections have shown that arid region plants exhibit important spectral differences from plants typical of humid regions. These adaptations significantly alter the visible-NIR part of the spectrum which all of the standard techniques of determining vegetation use. There is also significant variability in these features between plant types. Before moving on to more complicated schemes better suited to arid vegetation, the capability of the standard vegetation indices to deal with arid vegetation should be examined.

The dependence of many vegetation indices on the idea of a "soil line" suggests that consideration be given to the validity of the concept of a soil line. Figure 99 shows that the spectral region in red-NIR space mapped out by linear mixtures of the soil spectra from the Manix Basin field area is more of a cloud than a line. Note the similarity between the lower edge of this plot and that of figure 56. The practical result of this is that many pixels with low vegetation cover will fall within this region filled by bare soil mixtures,

making them indistinguishable from soil on the basis of red-NIR combinations. Since red-NIR combinations are the bases of all commonly used vegetation indices, this makes their use in arid regions rather suspect.

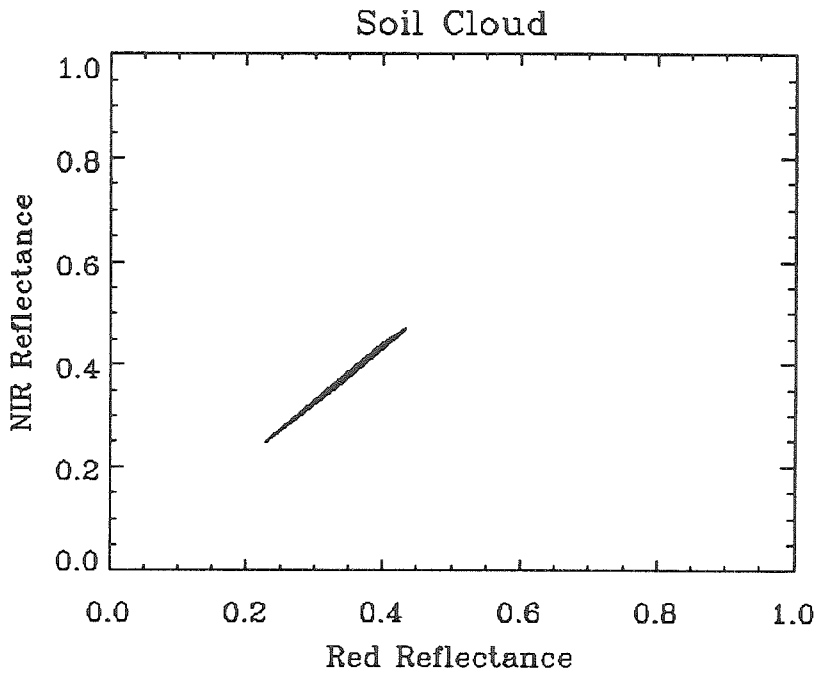

Figure 99: The soil "cloud" in red-NIR space. The red band is at 0.675 μm and the NIR band is at 0.755 μm. Although the cloud is quite narrow, many points of low vegetation cover will still fall into it.

Figure 100 and 101 show the red-NIR plots for creosote bush and bursage respectively. The tendency of creosote bush to be darker than the soil in both the visible and the NIR is shown clearly in figure 100. This is in conflict with the common view that NIR reflectance increases with increasing vegetation cover. The bursage in figure 101 shows a greater variability in the location of the 100% vegetation point than seen in the creosote bush case. The point that plots at very high NIR reflectance is for a

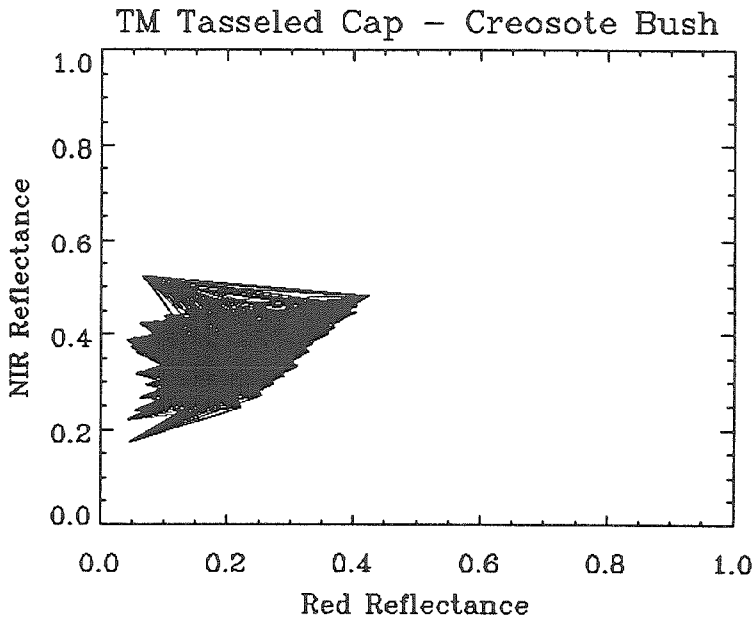

Figure 100: Red-NIR plot for creosote bush using Landsat TM bands. All pixels partially covered by creosote bush should fall within this plot. Note how the points opposite the lower right edge seem to form a line with a different slope than the soil edge. This would be the "line" of 100% creosote bush cover.

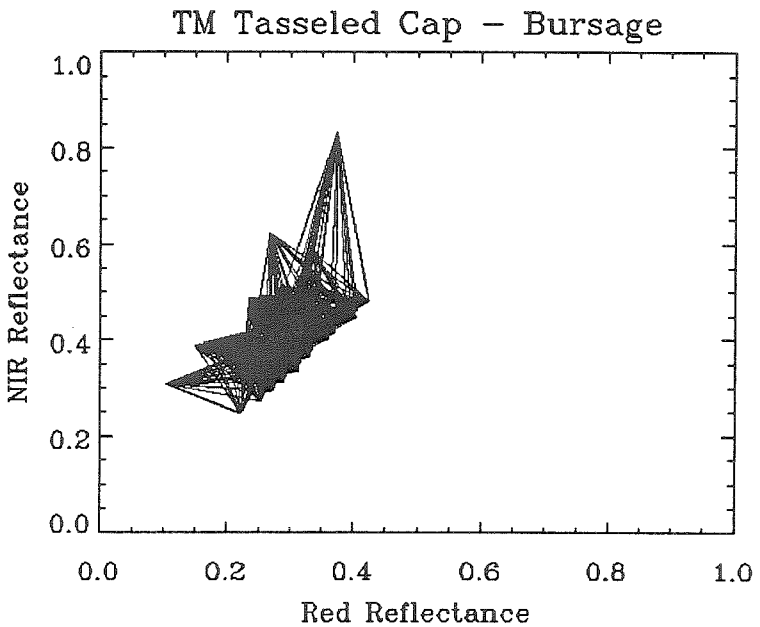

Figure 101: Red-NIR plot for bursage using Landsat TM bands. All pixels partially covered by bursage should fall within this plot. Note how the points opposite the lower right edge form a line approximately parallel to the lower right edge. This line would represent 100% bursage cover.

bursage with leaves unrolled, which may occur on a daily basis and certainly will occur during wet periods. Many of the high bursage cover values plot at brighter NIR reflectance than any of the creosote bush cover values; however, the low vegetation cover pixels for both species tend to fall in the same region on the plot, making them indistinguishable by using red-NIR combinations alone.

Examining figures 100 and 101 show that the idea of isovegetation lines parallel to the soil line fits the bursage quite well, since the 100% vegetation points seem to form a line nearly parallel to the soil line. On the other hand, the creosote bush plot seems to be more compatible with the idea of isovegetation lines converging at the origin of red-NIR space. This means that an NDVI-type index should be more suitable for creosote bush while a PVI-type index would be better suited for bursage. Picking a single point for each species as the 100% vegetation point would be very difficult.

Figures 102 and 103 further illustrate the difficulty of using standard vegetation indices to measure the cover of arid region shrubs. Both figures show that the bare soil has NDVI values ranging from 0.22–0.28. The considerable variance of creosote bush and bursage within the species is shown by 100% creosote bush NDVI values ranging from 0.51–0.84. The NDVI range for 100% bursage ranges from 0.36–0.62. Although most of the NDVI values for high covers of creosote bush are greater than the values for similar covers of bursage, by the time 20% and less cover is reached there is no appreciable difference between the NDVI values for the two species.

Low-level oblique airphotos taken over the study area in March 1994, analyzed by Caltech undergraduate Cailin Henderson, indicated that about 12% shrub cover was the

most common level in undisturbed areas. The values of about 12% cover for the undisturbed desert agrees well with the average of three 5 m plant traverses which were performed by the author in one of the undisturbed desert areas covered by the photography. The maximum cover estimated from the aerial photographs was 50%. This means that cover values higher than 50% are really irrelevant to the vegetation index problem, and that much lower percentages are important.

In figure 104, an average of the bursage spectra and an average of the creosote bush spectra have been linearly mixed with an average soil spectrum. For each of the four vegetation indices, the bursage line is consistently at lower vegetation index values for a given percent cover than the creosote bush. Table 16 shows the creosote bush cover having an equal vegetation index value to a pixel 50% covered by creosote bush for each of these four vegetation indices.

Table 16: Equivalent Bursage and Creosote Bush Cover for Four Vegetation Indices

Vegetation Index	Bursage Cover	Creosote Bush Cover
NDVI	50%	31%
PVI	50%	36%
SAVI	50%	34%
MSAVI	50%	37%

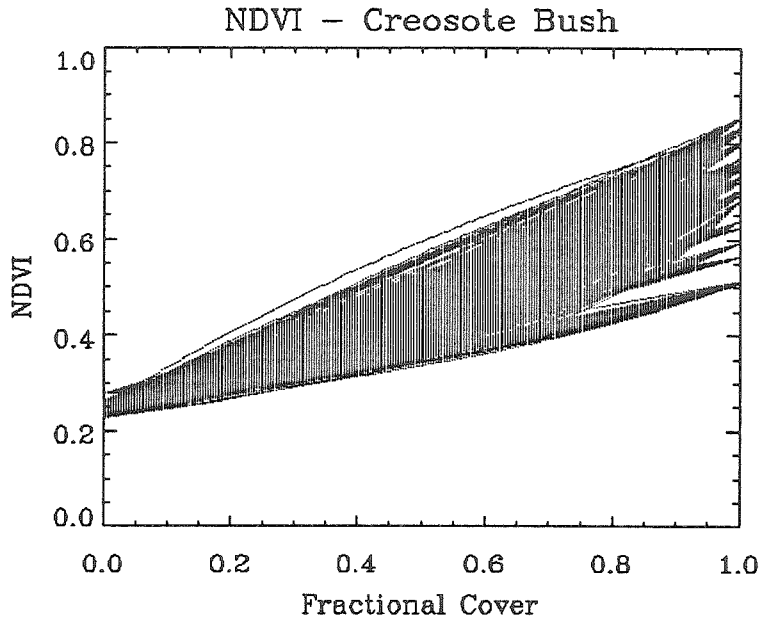

Figure 102: NDVI values for creosote bush. Each of the 29 creosote bush on soil spectra are used as 100% vegetation points and linearly mixed with each of the 28 bare soil spectra. Note how the highly variable soil background coupled with spectral variability among shrubs causes these points to overlap with those in figure 103.

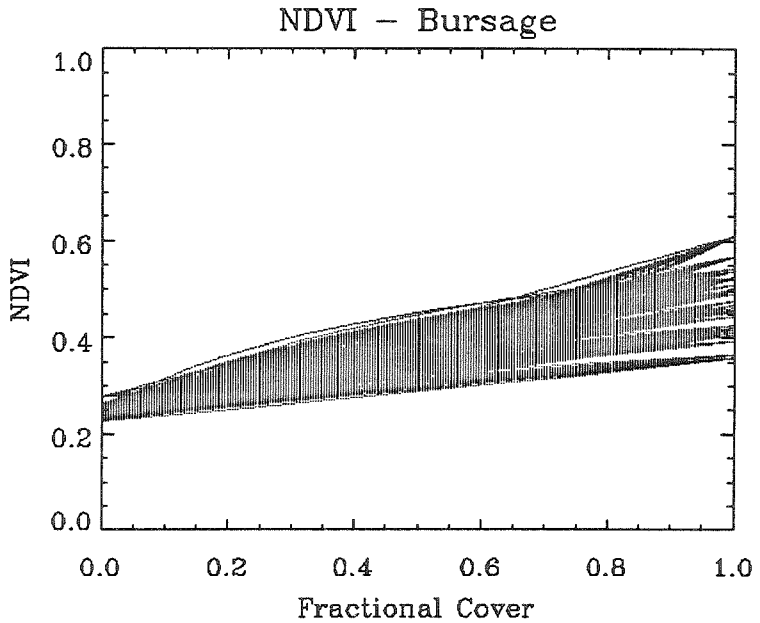

Figure 103: NDVI values for bursage. Each of the 24 bursage spectra are used as 100% vegetation points and linearly mixed with each of the 28 bare soil spectra. Notice the overlap at low fractional cover with figure 102.

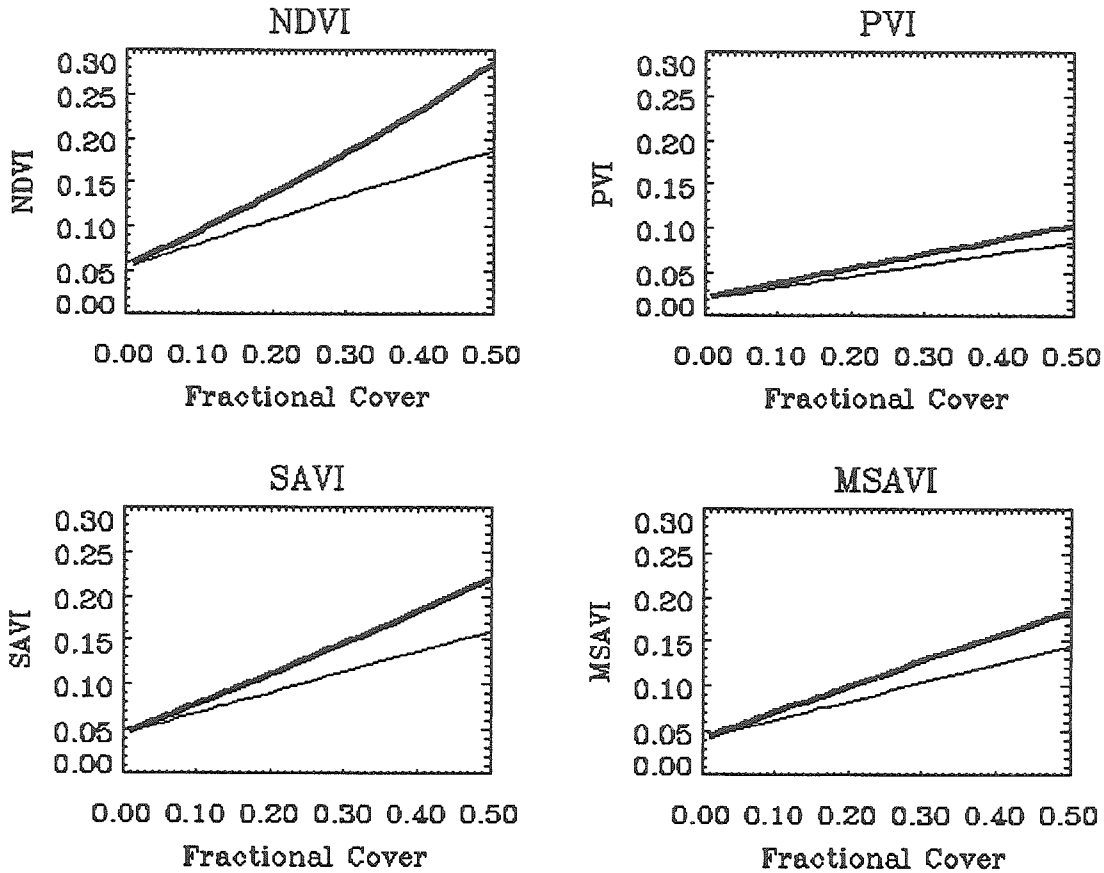

Figure 104: Plots of vegetation index values for creosote bush (thick line) and bursage (thin line). NDVI has the most divergent results for creosote bush and bursage. PVI brings the lines closer together, but this achieved with a large sacrifice of dynamic range. SAVI is intermediate between NDVI and PVI in terms of the similarity of the lines and in dynamic range. MSAVI brings the lines nearly as close together as PVI, but MSAVI keeps a larger dynamic range than PVI.

Based on these results, MSAVI seems to be the best vegetation index for use with TM or MSS data that have been calibrated for atmospheric effects. The use of the vegetation indices like ARVI and GEMI, which are designed to perform an automatic and simple atmospheric correction to eliminate variability caused by the atmosphere, seems unwise, given their extreme sensitivity to soil noise discussed previously. Figures 100–104 all show significant variability in the soil, so the use of a vegetation index intended to

minimize soil variability seems to be the best solution. The derivative-based indices of Elvidge and Chen (1995) were not significantly better than MSAVI at diminishing soil variability or the differences between bursage and creosote bush vegetation index values for the same plant cover, and the added complexity of computation makes them less desirable than MSAVI. However, the principle of using narrow bands for improved vegetation indices should apply equally to MSAVI.

The quantitative values given by even the best broad-band index (MSAVI) are probably inadequate for the accurate quantitative measurements required for assessments of land degradation. The extreme difficulty of discriminating between bursage and creosote bush at less than 20% cover using red-NIR combinations is also serious since a shift from creosote bush to bursage could indicate land degradation. However, the differences in the shape of the pigment features between creosote bush and bursage may allow the discrimination between the two shrub types, which would greatly improve the utility of these indices.

Part 5.5: *Non-Linear Spectral Mixing in Desert Vegetation*

Linear spectral unmixing was used in chapter 4 to discriminate between areas of undisturbed desert and those covered by blown sand. The results of linear unmixing are abundances for each endmember spectrum which are presumed to be directly related to the percentage of the pixel covered by the endmember substance. It seems reasonable to use such a technique with the field spectra of the plants. This has been attempted, with

mixed results. Some areas of high bursage cover are properly identified, but the creosote endmember is most commonly associated with the edges of the actively irrigated fields.

However, the spectra can also mix in a non-linear manner (Adams *et al.*, 1986, 1989;. Boardman, 1989, 1990, 1991, 1994; Hapke, 1981; Johnson *et al.*, 1983; Nash and Conel, 1974; Roberts *et al.*, 1993, 1994; Singer, 1981; Smith *et al.*, 1990, 1994). This generally occurs when the mean free path for photons is larger than the distance between the mixed materials (Adams *et al.*, 1986), and this type of mixing is often termed as intimate mixing. This was probably first seen in mixtures of finely-powered minerals (Nash and Conel, 1974; Singer, 1981). Hapke (1981) and Johnson *et al.* (1983) have used radiative transfer to model the spectral mixing involving intimate mixtures, and both authors showed that single-scattering albedos would mix linearly for intimate mixtures.

Non-linear mixing basically occurs when light reflecting from the target interacts with multiple materials. The light that interacts with multiple materials will be altered by the reflectivity of each material, and, in cases where some of the target materials transmit light, by the transmissivity of the materials. The resulting light entering the instrument does not look like light reflected by any of the target materials, but rather as some complex, multiplicative function of the reflectance (and possibly transmittance) spectra of the target materials.

Different pigments of paint are an example of non-linear mixing. Even when viewed at a very fine scale, most paints do not break down into a checkerboard pattern of different colors. The compounds creating the paint's color are so finely mixed that light striking the paint must interact with all of the color-producing compounds. This non-

linear mixing is why it is extremely difficult to produce certain pigment colors on computer displays or by three-color printing (which are inherently linear mixing techniques). Boardman (1994) aptly pointed out that techniques that linearize the non-linear component of spectral mixing made the linear mixing component non-linear, and that linear and non-linear mixing should be treated as separate problems. Boardman (1994) maintained that the problems should be separable, since non-linear mixing is a function of the target, and linear mixing is a function of the instrument.

The phenomenon of non-linear mixing between soil and vegetation spectra has been observed by numerous authors (e.g., Roberts *et al.*, 1993; Smith *et al.*, 1990; Huete *et al.*, 1985). Usually these observations have involved attributing the residual between linear mixing results and the original spectrum being unmixed to non-linear mixing. Boardman (1994) has suggested that these mismatches may be due to an incorrect choice of endmembers, while Smith *et al.* (1994) is of the opinion that this may be due to a "fuzziness" in the endmembers. This indicates that these residuals may be more due to an inadequacy in the linear model than due to non-linear mixing caused by light interacting with multiple endmembers. This phenomenon of non-linear mixing can be observed in the field spectra of arid region plants, and there is clear evidence that it is due to interactions between the soil and the vegetation. Such non-linear mixing can magnify the apparent vegetation cover in remotely sensed data.

The light detected by a spectrometer observing a plant can take many paths from the light source (usually the sun) to the instrument. The four most basic paths the light can take are: 1) Source⇒plant⇒instrument, 2) Source⇒background⇒instrument, 3)

Source⇒plant⇒background⇒instrument, 4) Source⇒background⇒plant⇒instrument. Let us begin by assuming that both the plant and the soil reflect light isotropically. We define the reflectivity of the plant to be R_p which includes all the multiple reflections of light which occur between the various leaves and twig which comprise the canopy as well as light directly scattered by the leaves and twigs. The reflectivity of the background is R_b. We can now define the effective reflectivity seen be light interacting with both the background and the plant to be $R_p \times R_b$. The reflectivity observed by the instrument is now given by:

$$R = \alpha R_p + \beta R_b + \gamma R_p R_b \tag{1}$$

where α, β, and γ are weighting coefficients. Linear mixing assumes that the cross product is small or unimportant for the endmembers being considered. This simple cross product is itself a dramatic oversimplification, and the actual non-linear component will involve many scatterings between leaves, twigs, and soil.

Consider the case when the spectrum of a plant has been acquired with two different backgrounds. If we take the difference between these two spectra we get:

$$R_d = R' - R = \alpha R_p - \alpha R_p + \beta R_b' - \beta R_b + \gamma R_b' R_p - \gamma R_b R_p \tag{2}$$

$$R_d = \beta \left(R_b' - R_b \right) + \gamma \left(R_b' R_p - R_b R_p \right) \tag{3}$$

where we have eliminated the direct contribution of the plant. If linear mixing is assumed and we ignore the cross terms, we expect the difference spectrum R_d to be equal to some multiple of the difference between the two background spectra.

Figure 105 shows the spectrum of a single creosote bush against the dark target and against the soil background. In figure 106, we see the difference between the creosote bush against the soil background and the same creosote bush against the dark background, R_d. The difference between the soil spectrum and the dark target spectrum, R_{bd}, is plotted on the same scale. Clearly these spectra are not multiples of each other, which is reinforced by figure 107, which shows the results of dividing R_d by R_{bd}. Spectra of other creosote bushes and Russian thistle (tumbleweed) give similar results. Most spectra of white bursage show very little difference between the different backgrounds, probably because the bursage canopies have much denser tangles of twigs than do creosote bush or tumbleweed.

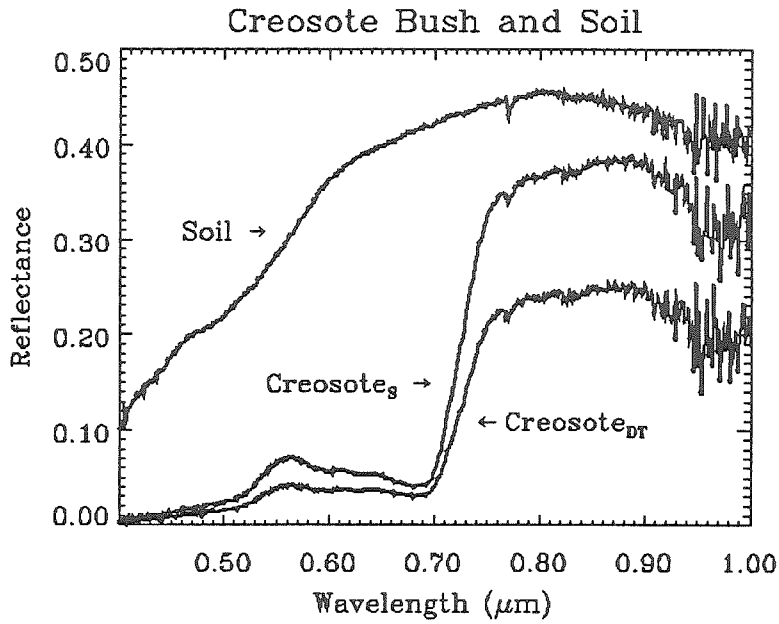

Figure 105: Plot showing the reflectance spectra of soil, a creosote bush against the soil background (Creosote$_S$), and the same creosote bush against a dark non-reflective target (Creosote$_{DT}$). Note the strongly enhanced red edge and pigment features for Creosote$_S$ as compared to Creosote$_{DT}$.

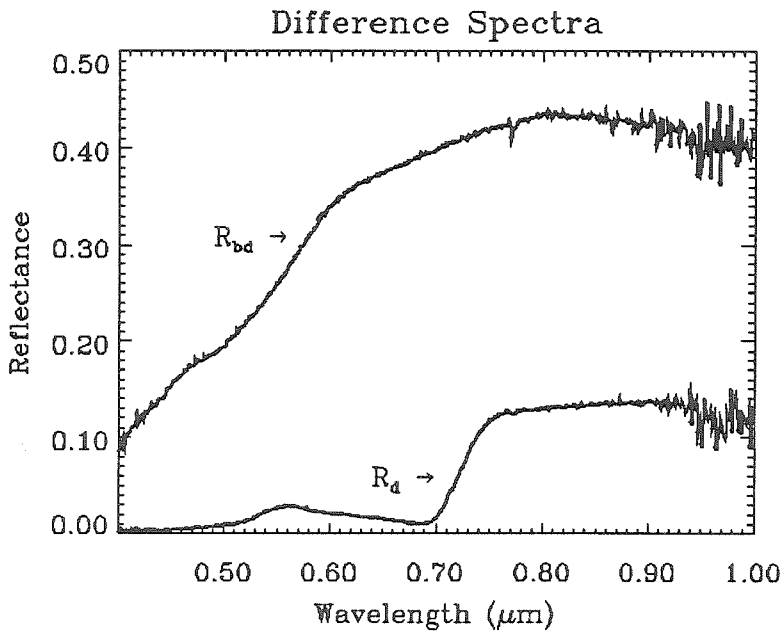

Figure 106: Plot of the difference between the soil spectrum and the dark target spectrum (R_{bd}) and of the difference between the spectrum of the creosote bush against the soil and the creosote bush against the dark target (R_d). Clearly these two spectra are not multiples of each other.

This result strongly indicates that non-linear mixing is occurring because the only thing that changed between the acquisition of the two creosote bush spectra was the background. This inference can be tested in a crude way by attempting to unmix the difference spectrum using the bare soil and the product of the soil and plant reflectance spectra. The creosote bush against the dark target can be taken as the "true" creosote bush reflectance, although it is probably slightly darker than the true plant reflectance because there is some spectral mixing with the dark target. This is our best option short of a radiative transfer model of the plant with multiple scatterings from leaves and twigs. This would require a proper statistical model of the number and orientation of leaves and twigs in the creosote bush (and creosote bushes in general). However, as shown in figure 108, the spectrum produced by the mixing model is very similar to the difference spectrum that we were trying to match. The mixing model suggests that the difference between the creosote bush spectrum against the soil and the creosote bush against the dark target is 4.3% bare soil and 95.6% soil-plant interaction.

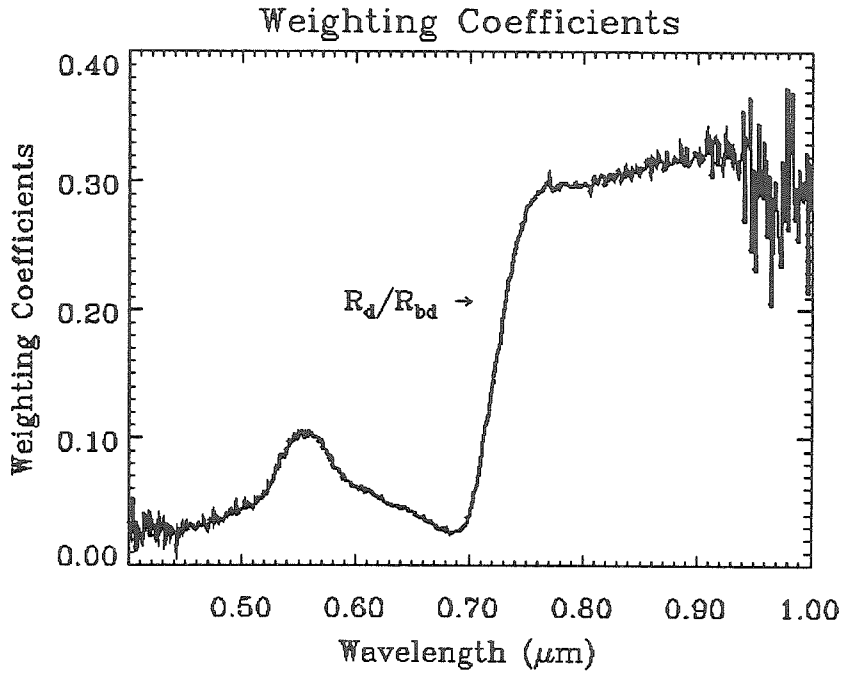

Figure 107: Plot of R_d/R_{bd}. These weighting coefficients are what each wavelength of R_{bd} would need to be multiplied by to get R_d. If linear mixing were occurring, all of these weighting coefficients would be equal.

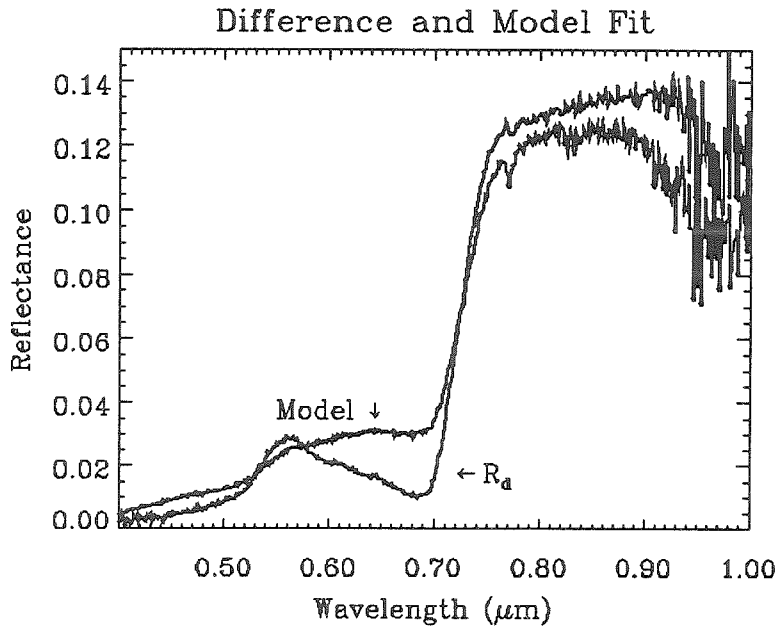

Figure 108: Comparison of the difference between the spectrum of creosote bush against soil and creosote bush against the dark target (R_d) with the model fit of 4.3% bare soil and 95.6% plant-soil interaction. Notice that the model predicts too much red reflectance and slightly too little near-infrared reflectance. The model is only valid in the range 0.4-0.9 μm.

Returning to the original spectrum of creosote bush against the soil background, a linear unmixing using the creosote bush against the dark target and the composite cross-product plus soil spectrum as the other endmember results in 22.5% creosote bush, 3.3% bare soil, and 74.1% plant-soil interaction. This compares to 79.6% creosote bush and 20.3% bare soil predicted by a conventional linear mixing between creosote bush against the dark target and bare soil. Table 17 summarizes the results of the unmixing models.

Table 17: Results of Spectral Mixing Models for Creosote Bush

Model Type	Endmember Abundances		
	Creosote Bush	Bare Soil	Plant-Soil Interaction
Model 1: Conventional Linear (Plant and Soil)	79.6%	20.3%	---------
Model 2: Plant-Soil Interaction (relative abundances)	22.5%	3.3%	74.1%
Model 2: Plant-Soil Interaction (absolute abundances)	53.6%	8.0%	176.8%
Model 3: Plant Only (absolute abundances)	155.3%	--------	---------

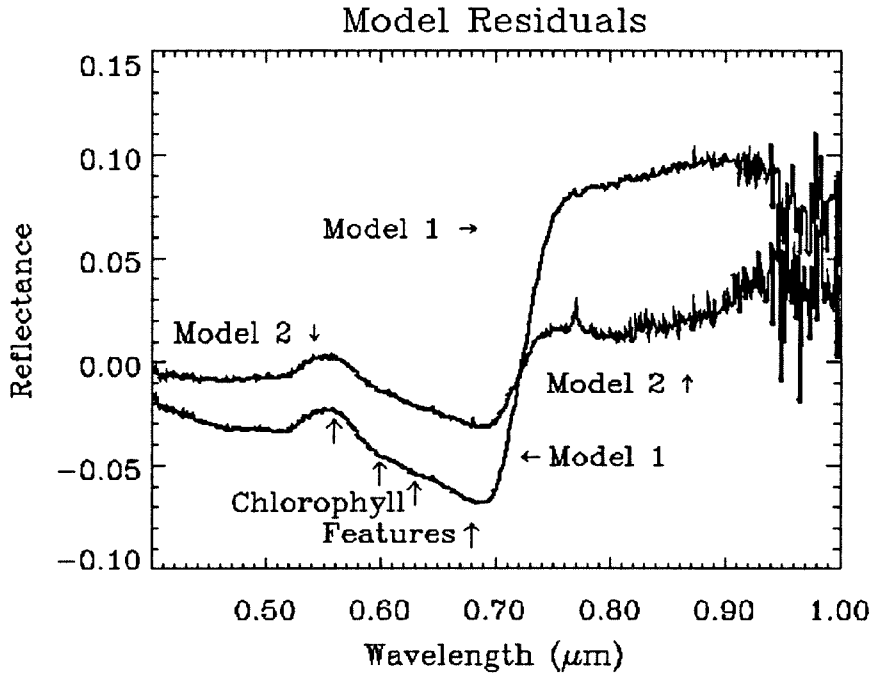

Figure 109: Residuals for two mixing models. Model 1 was a conventional linear mixing model using creosote bush against the dark target and bare soil as endmembers. Model 2 used creosote bush against the dark target and the model fit from figure 4 as endmembers. Both models overestimate visible reflectance and underestimate near-infrared reflectance, but model 2 has smaller residuals. Notice that the model 1 residuals have significant chlorophyll features indicating that the residual light contains some element of interaction with photosynthetic vegetation.

Figure 109 shows the errors in fit for each of the two unmixing models used above. Clearly the mixing model using the creosote bush against the dark background and the plant-soil cross term as endmembers has a much smaller error than the creosote bush against dark target and bare soil model. The creosote bush-soil model produces a much higher visible reflectance and much lower near-infrared reflectance than is observed. The mixing model that includes the non-linear interaction between the soil and the plant does a significantly better job in both the visible and near-infrared. It is noteworthy that a slightly better fit than that using the soil-plant interaction can be arrived at by simply multiplying

the creosote bush against dark target spectrum by 1.553 which represents a 50% inflation in the apparent amount of vegetation. This shows that the general result of the non-linear mixing is to increase the apparent amount of vegetation.

While the residuals for the mixing between the creosote bush and the plant-soil interaction are encouragingly small, we must nevertheless still consider how well this corresponds to reality. The creosote percentages listed above were the percentage of the total abundance, and if we take the weights directly as the abundances we get 53.6% creosote bush against dark target, 8.0% bare soil, and 176.8% soil-plant interaction. It should be pointed out that since 100% creosote bush against dark target was used to find the difference spectra, abundances greater than 100% are permissible in this case. An abundance exceeding 100% is also not unreasonable for the cross-product term since it is composed of two reversible paths. This is close to the 10% coverage by directly lit soil seen in pictures of creosote bushes, and 50% cover by directly lit creosote bush does not seem unreasonable based on photographs. The rest of the area is covered by shadows and dimly lit creosote bush that is probably reflecting light reflected from the soil beneath the plant. The plant-soil interaction spectrum is less than half as bright in the visible as are fully lit leaves, which supports this conclusion. Therefore, non-linear spectral mixing between plant and soil can be the dominant factor in the remotely sensed spectra of desert regions, and can significantly alter the apparent abundance of vegetation inferred from remotely sensed data.

There are several sources of error in the approach used here. First, our assumption that the plant and the soil reflect isotropically is not correct, from the simple

fact that the plant will not be reflecting as much light on its shadowed side as its sunlit side. Also, it has been noted that the upper and lower surfaces of the leaves of many plants have different reflectivities (Gates *et al.*, 1965). The leaves of some plants have significant transmissivities, but the leaves of the creosote bush tend to be have very low transmissivities (Gates *et al.*, 1965). The spectrum of the creosote bush against the dark target is almost certainly darker than the hypothetical true reflectance of the creosote bush not having any background, and since the reflectance of the dark target decreases in the near-infrared wavelengths, there is a slight suppression in the near-infrared reflectance. An examination of figure 167 shows stronger visible-wavelength chlorophyll features which may be indicative of an enhancement in multiple scattering inside the canopy due to more light being reflected from the soil into the canopy. The results from part 5.3.7 which showed that the parts of arid shrubs in the shadow of other parts of the same shrub tend to have higher NDVI values than are found for the parts in direct sunlight. This is another enhancement of the NIR reflectance relative to the red reflectance which is also a contribution of non-linear mixing.

This illustration shows that non-linear mixing is important in the observation of plants in arid environments. This example also shows that the error observed in the simple linear mixing model can be accounted for by the interaction of light with multiple endmember materials, which demonstrates that "non-linear" mixing does not just mean the error in a linear mixing model. The enhancement in apparent vegetation through this non-linear mixing is a double-edged sword in that it makes vegetation more detectable, which is useful, but it also makes accurate quantitative assessments of vegetation cover more

difficult. Finally, since the strength of the plant-soil interaction can vary from vegetation type to vegetation type, non-linear mixing effects may confound conclusions about the relative abundances of different plant types in communities observed by remote sensing.

The preceding shows how an additional endmember can be added to a linear unmixing in an arbitrary attempt to deal with the non-linearities. Roberts *et al.* (1993) used a canopy shade endmember to help account for some non-linearities. However, this idea of simply manipulating the linear endmembers to deal with the non-linearities in the spectral mixing seems to simply be avoiding the inevitable. Clearly, if the non-linear component of the spectral mixing is due to a single interaction between the plant and the soil, the non-linear component is itself a function of the vegetation cover. Simply adding a linear endmember is not a sufficient solution to this problem. The large potential impact of non-linear spectral mixing in arid vegetation makes linear unmixing an inadequate solution for measuring arid vegetation cover.

This means that work must be done to assemble good architectural models of the arid shrubs typical of the area being monitored. Such models can be used along with spectra of plant components to construct radiative transfer models of the shrub canopies. This must then be coupled with the non-shrub soil to generate a model of the shrub canopy and the underlying soil. Unlike the work of Huete (1985) the sparse placement of the shrub canopies will require that the model of a single pixel include a large bare soil component.

Part 5.6: *Towards A Useful Arid Vegetation Index*

The preceding has shown that the adaptations of arid region plants has important consequences for remote sensing. Arid vegetation is inherently harder to see with remote sensing due to its tendency towards smaller leaves and leaves oriented to avoid the overhead sunlight. These plants also have leaves which are spectrally different from the leaves of plants from humid regions, which further complicates their detection. The plants can rapidly change characteristics in response to rainfall in ways which can radically alter their spectral characteristics. Finally, the sparseness of arid vegetation causes variability in the soil to become an extremely important factor in vegetation cover measurements.

Present remote sensing vegetation indices are inadequate to the task of giving more than qualitative assessments of vegetation cover. The development of vegetation indices for measuring the vegetation in arid regions will require careful attention to the plant communities in the monitoring region. For the Mojave Desert, the dominance of bursage over creosote bush in areas subjected to past human disturbance has been well-documented (Vasek *et al.*, 1975a; Vasek *et al.*, 1975b; Vasek *et al.*, 1979/80; Carpenter *et al.*, 1986). The preceding has shown that bursage tends to give lower vegetation index values than areas with an equal cover of creosote bush, which makes lower vegetation index values a qualitative sign of degradation either through decreased vegetation cover or changes in the vegetation community. A narrow-band index designed to deal with soil noise in a sophisticated manner is probably the best choice for arid monitoring.

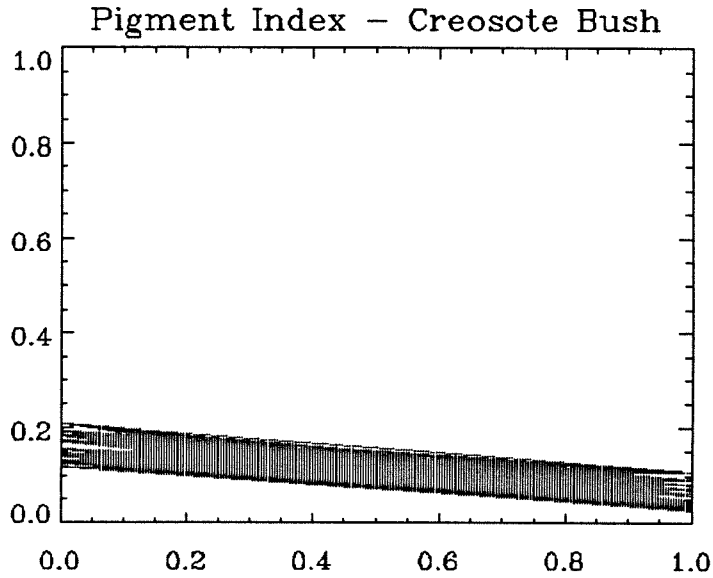

Figure 110: Plot of the difference between TM band 3 and TM band 1 for creosote bush. Note that these values are generally smaller for creosote bush than the bursage shown in figure 111. These two bands focus on pigment absorptions on either side of the 0.55 μm chlorophyll bump.

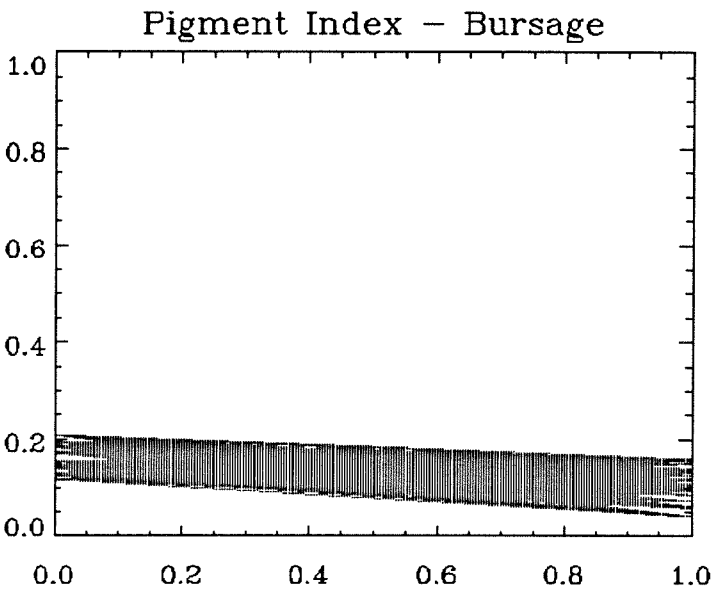

Figure 111: Plot of the difference between TM band 3 and TM band 1 for bursage. Note that these values are generally smaller for bursage than the creosote bush shown in figure 110. These two bands focus on pigment absorptions on either side of the 0.55 μm chlorophyll bump.

It may be possible to use an index focused on the chlorophyll features near 0.55 μm to discriminate between bursage and creosote bush under conditions of heavy cover. As a crude example, the difference between TM band 3 and TM band 1 is shown for creosote bush in figure 110 and for bursage in figure 111. The creosote bush tends to have lower values of this parameter for a given vegetation cover, which is exactly what would be expected based on the spectra earlier in this chapter. This particular parameter calculated with narrow bands could be combined with an MSAVI-like index. Such a combination would tend to suppress the difference between creosote bush and bursage for the MSAVI index since bursage, which has the lower MSAVI value has the larger value of this pigment index. Monitoring observations of an area can potentially allow the use of the more rapid after-rain greening of creosote bush as compared to bursage. In order to use the rapid greening of creosote bush as a factor in monitoring requires linking rainfall monitoring to satellite remote sensing observations. Such knowledge of the rainfall will also help improve the accuracy of plant cover monitoring by helping compensate for the dramatic changes brought about in desert flora by precipitation which, as discussed earlier in this chapter, cause an apparent enhancement in vegetation cover not completely related to changes in vegetation biomass.

The class of techniques based on linear spectral mixing must be approached with care because of the measurable non-linear spectral mixing which can be observed in arid region plants. Accurate detection of arid region vegetation will require an instrument which produces data that can be calibrated to within 5% absolute reflectance. This accuracy is necessary to detect and characterize arid vegetation. Dense stands of creosote

bush and bursage can potentially be discriminated from each other by using differences in the shape of the chlorophyll bump for 0.45–0.68 μm.

Chapter 6: *The Time Factor*

Part 6.1: *Introduction to Temporal Remote Sensing*

The third part of chapter 1 discussed the importance of long-term monitoring in order to make any effective conclusions about desertification. Warren and Agnew (1988) stated that one of the main problems in our understanding of land degradation was "the ignorance in establishing trends and speeds, because trends and speeds require sequential surveys." These sequential surveys will have to be continued over long periods of time as indicated by the statement of Dregne and Tucker (1988) that 30 to 40 years of observation by satellites and ground studies will be required to determine if any permanent changes in the boundaries of the Sahel are shifting.

The need for long term and continual monitoring by satellite remote sensing systems leads to the problem of adding the time dimension to remote sensing data. The first logical step to take in examining the problems of temporal remote sensing is to assemble data for a known study area extending into the past. By assembling and analyzing such a dataset, many of the problems and requirements for effective temporal monitoring systems. Additionally, analyzing a temporal dataset extending into the past can help in the preparation of the baselines required for monitoring of the area in the future (Nelson, 1988; Rodenberg, 1991; Murray, *et al.*, 1994). Finally, in the absence of

temporal data extending into the future, temporal data extending into the past provide the only way to use remote sensing data to study the land degradation processes over time.

In this chapter, the value of temporal remote sensing data will be demonstrated. The temporally discontinuous nature of land degradation due to wind erosion will be clearly illustrated, as will the temporal impact of wind erosion on vegetation cover. Factors such as rainfall and wind strongly influence degradation by wind erosion, and this chapter demonstrates that regionally averaged meteorlogical data is not useful for predicting local land degradation.

In 1967, the United States Department of the Interior and NASA began a conceptual study of the feasibility of a series of Earth Resources Technology Satellites (ERTS). The first of a planned sequence of six satellites was launched by a Thor-Delta rocket on July 23, 1972 (Lillesand and Kiefer, 1987). The program was re-christened as Landsat in January of 1975, just before the launch of the second satellite in the series. All of the five satellites in the series which have been successfully launched carried an instrument known as the Multispectral Scanner (MSS). The characteristics of this instrument are summarized in table 18. The nearly continuous operation of this single instrument since late 1972, provides the longest term temporal satellite dataset of multispectral images

.

Table 18: Landsat Multispectral Scanner (MSS) Characteristics		
Platform	Satellite	
Operational Altitude	Pre-1982: 900 km Post-1982: 705 km	
Repeat Cycle	16 days	
Spectral Coverage	Band	Range (μm)
	Band 4 (1)	0.5–0.6
	Band 5 (2)	0.6–0.7
	Band 6 (3)	0.7–0.8
	Band 7 (4)	0.8–1.1
Swath Width	185 km	
Ground Resolution	Instrument IFOV	82 m
	Processed Pixel Pre-1978	57 m × 79 m
	Processed Pixel Post-1979	57 m
Quantization Level	4 bit	
Instrument Type	Whiskbroom Scanner	

Another important advantage of the MSS data is the fact that all MSS data acquired by the instrument more than two years ago are available for the cost of reproduction ($200/image). This compares to the cost of Landsat Thematic Mapper (TM) data from EOSAT, which is currently $4400 per image. TM data acquired more than ten years ago are also available for the cost of reproduction ($190/image), but since TM has only been in active service since late 1983, this means that only a very limited amount of time is covered by affordable Landsat data.

Table 19 lists the 16 MSS images which are used in this study. These images were selected using the Global Land Information System (GLIS) which is an on-line service developed by the USGS EROS Data Center which allows a user either over the internet or a dial-up modem to interactively search the database of available Landsat data. As it happens, the EOSAT Corporation, which controls the commercial rights to Landsat data, uses this system to process requests for listings of available Landsat data. GLIS provides information on the acquisition date, the quality of the data in each band, the amount of cloud cover and the formats (hardcopy and digital) in which the data are available.

Table 19: Dates of Acquisition for MSS Images
June 29, 1973
June 24, 1974
June 18, 1975
June 3, 1978
July 22, 1979
July 25, 1980
July 20, 1981
May 13, 1982
July 15, 1983
June 23, 1984
July 28, 1985
June 13, 1986
July 18, 1987
July 20, 1988

The AVIRIS data used in this study were collected on July 20, 1990, and, in order to minimize the potential effects of different seasons, MSS data collected at dates as near to July 20 as possible were selected for comparison. In many cases, the presence of cloud cover, poor data quality, and missing bands forced images on earlier of later dates to be used. For the years prior to 1978, there was often only a single image in digital form available, which naturally restricted the selection drastically. The 1975 image was collected on the next orbit east of the orbit for which all of the other images were collected, and it only covers part of the study area. The 1974 image has considerable

cloud cover, but it was the only image available in digital format for that year. The 1982 image was collected in May, but no images later in the year were of adequate quality and many were missing at least one band.

No MSS images were available that cover the field area during the period 1988–1992. Conveniently, the AVIRIS airborne system and the Russian satellite instrument RESOURCE (nominal resolution of 30 m and bands as shown in table 20) data used in this study were collected during this time gap. This circumstance provides an opportunity to examine how holes in a monitoring dataset may be filled by data from either higher spectral and spatial resolution system or systems with similar spectral bands and of equal to better spatial resolution. Additionally, the analysis here illustrates how data from more targeted remote sensing systems with higher spatial resolution may be used to increase the temporal coverage of satellite monitoring data.

Table 20: Characteristics of RESOURCE Bands

Band	Spectral Range (μm)	Digitization Level (bits)
1	0.5–0.6	7
2	0.6–0.7	7
3	0.8–0.9 0.8–1.0	8

The two values given for the band 3 range are two conflicting reports from the Institute for Space Devices Engineering. The back of the band 3 hardcopy image is stamped 0.8–0.9 μm, while an advertisement poster put out by the institute list the band as 0.8–1.0 μm.

This study will also show the importance of ancillary data such as rainfall and other meteorological data to the analysis of temporal remote sensing data. The fluctuating nature of land degradation will be seen, and the relationship of drought to the disclosure of land degradation will also be illustrated. However, before the temporal data can be analyzed, there are several important chores which must be performed.

Part 6.2: *Co-registration and Calibration*

The first hurdle which must be cleared is to place all of the data on a common spatial basis. This will make it possible to compare selected areas in the various images directly and also to display temporal information as images or maps. This process is very common in the use of geographic information systems, and it is commonly known as co-registration. The basic requirement for co-registration is the presence of a series of tiepoints, which are features that can be recognized and accurately located on the images being co-registered. The 1988 MSS image served as the base image to which all of the other images were registered.

If the images being co-registered have different spatial resolutions, the first step is to convert all of the images to the same resolution. For these data, all of the images were resampled to the 57 m $\times$ 57 m pixel resolution of the 1988 MSS data. The four oldest MSS images were originally at 79 m $\times$ 79 m pixel resolution, which required "splitting" these pixels and interpolating the values onto the new grid. For the AVIRIS data with 20 m $\times$ 20 m pixels and RESOURCE with 30 m $\times$ 30 m pixels, adjacent pixels were

averaged together to produce pixels covering the larger area. The AVIRIS and RESOURCE images were also interpolated, since the MSS pixel size is not some integer multiple of the AVIRIS and RESOURCE pixel size. The interpolation caused during this resampling is the first example of a transformation that distorts the image. In this study, the actual resampling of the images was done using the IDL CONGRID routine. (IDL is the Interactive Data Language which is a commercial software package produced by Research Systems Inc. of Boulder, Colorado.)

Only on extremely rare occasions will a satellite have a repeat orbit with exactly the same ground track. The first-order co-registration correction is simply a shifting of one image so that a tiepoint near the center of the image being co-registered aligns with the corresponding point on the base image. This transformation does not distort the images since it simply involves shifting the image a certain number of pixels in the required direction.

At this point, it is possible to go directly on to the final step of co-registration, which is known as rubber-sheeting. In this procedure, tiepoints are selected on each image. The basic principle in selecting tiepoints is that there be as many of them as possible, and that some are found in all parts of the image. Once the locations of the tiepoints in the image being registered and the base image are known, each tiepoint in the image being registered is forced to align with its location on the base image. This results in the areas between the tiepoints being warped (stretched and compressed). The term rubber-sheeting comes from the visual analogy of the image being registered as being printed on a rubber sheet and the tiepoints on the rubber sheet being pinned to the

corresponding points on the base. The area outside the outer boundary of the tiepoints is warped by mathematically extrapolating the warping to the edges of the image. This image warping, as indicated by the name, is a distorting transformation, and it is produces the strongest distortion of all the co-registration transforms. Unlike the other distorting transforms, rubber sheeting distorts different parts of the image in different ways, and it is capable of altering the relationships between objects in the image. In this study, the rubber-sheeting was performed using the IDL WARP_TRI routine, and more than 20 tiepoints were used in each image.

Sometimes, when two images are aligned by the shifting of the images discussed above, a rotation between the two images is observed. Image rotation is typically caused by slight differences in the yaw attitude of the satellite between the two image acquisitions. In Landsat data, this is most often noted when images from different satellites in the series are being co-registered. While this rotation can be eliminated by rubber sheeting, n intermediate step may be applied to reduce some of the severe distortions caused by rubber sheeting. This intermediate transform involves a solid rotation of one image relative to another about the tiepoint. This distorts the image because the rotated set of pixels will not align with the non-rotated set, so interpolation of the image values may be required. However, as in spatial resampling, the same type of distortion is occurring across the entire image, which is not the case for rubber sheeting. Image rotation was only performed on the AVIRIS and RESOURCE data, which were the last images added to the series.

The registration of one image to another is an iterative process. The steps of spatial resampling and image translation are very straightforward, and they can typically be done in a single operation. The solid rotation of the image may require iteration in order to find the correct angle for rotation. The final rubber sheeting may require many interations as areas of undesirable distortion are evident and additional tiepoints need to be selected to correct those distortions. Software which can rapidly display alternating images, such as the FLIP routine in IDL, is very useful in helping to spot areas of poor registration. Scanning systems produce a variable instrument footprint along the scan line which introduces distortions which make it impossible to achieve a perfect co-registration.

In this study, all of the images were directly registered to the 1988 image. Alternatively, it might be preferable in some other cases to perform the registration as an iterative series of steps. For example, the 1973 image would be registered to the 1974 image. Second, the 1974 image would be registered to the 1975 image. The transformation that was applied to the 1974 image would be applied to the images registered to the 1974 image (the 1973 image), which would mean that the 1973 and 1974 images would both now be registered to the 1975 image. The process would be repeated, registering each image, and all images already registered to the image being registered, to the next image in the time series. This process would make it easier to locate tiepoints common to both images, and would result in a smoother, more photogenic sequence of images (see part 6.3), but the added distorting transformations may alter the data in undesirable manner.

The second common basis required for temporal remote sensing involves the spectral bands. The characteristics of the atmosphere and the calibration of the Landsat MSS instruments varied among the images used in this study. Remember that Landsat is a series of satellites, and that the data in this study span the entire series. Also the Russian RESOURCE instrument is not an exact copy of any of the MSS instruments. In order to eliminate these differences, the images must be co-calibrated. This was done by picking certain alluvial fans as spectrally "invariant" targets. Low-level aerial observation of these alluvial fans showed them to be nearly devoid of vegetation. In addition, they are of low relief and, unlike playas, they do not suffer large-scale episodic resurfacing with evaporites and clays. Thus, the alluvial fans were considered to be "unchanging" reflection targets. The fans were divided into areas 5×5 pixels in size. A modification of the Crippen (1987) regression-intersection method was used to determine the relative gains and offsets to apply to each MSS image and to the RESOURCE image to eliminate variations in atmospheric and instrument characteristics between each of the images and the 1988 MSS image. This was done by plotting the values extracted from each of the subdivisions of the alluvial fans in each MSS band from the 1988 image with the corresponding band from the image being calibrated to the 1988 image. If the reflectance properties of the target had not changed and the atmospheric and instruments conditions were the same in both images, the scatterplot of points would form a line with a slope of 1.0 which passes through the origin. The deviations in slope and intercept from the expected line were then used as the gains and offsets to perform the relative calibration of one image to the other.

This process was not performed on the AVIRIS synthetic MSS data so that the AVIRIS data could be used to independently check the final MSS calibration.

Instead, the AVIRIS data were calibrated to apparent reflectance using the empirical line technique of Conel *et al.*, (1987) with field spectra collected the day after the AVIRIS flight by Cathy Weitz and Veronique Carrere. A modified empirical line technique (Roberts, 1991; Gamon *et al.*, 1993) was used to calibrate the 1988 MSS data. The standard empirical line technique uses spectra collected from specific targets that can be identified in the image and a least squares fit is performed to find the set of gains and offsets to convert from radiance to apparent reflectance. The modified empirical line technique requires that the user select areas of known surface type such as green vegetation, bare soil, and basalt. The spectra of these targets collected from the image are then compared with a library of spectra of that type of target. The gains and offsets are computed from the sets of spectra that best meet the criteria specified by the users.

Because all of the MSS data and the RESOURCE data were co-calibrated to the 1988 MSS image, these values can be used to determine the apparent reflectances for all the images. These results were compared to the AVIRIS data calibrated with the standard empirical line calibration using an alluvial fan as an unchanging target. The results of this comparison showed there to be a relative error between the MSS calibration and the AVIRIS calibration of 15–20% of the expected (AVIRIS) apparent reflectance and an absolute error of 5–7% apparent reflectance. The absolute error is at the level of the error in AVIRIS calibration (Green *et al.*, 1993) indicating that the calibration of the MSS data to apparent reflectance is acceptable.

Part 6.3: *Data Visualization*

One of the major recommendations of the Caltech/WRI joint study (Murray *et al.*, 1994) was that the results of analyses should be disseminated in a format that provides the most effective visualization of the information. One way of observing temporal changes using the data set of this thesis is to display it as a temporal sequence in a "movie." This can be done using any of a number of software packages that provide the ability to display a sequence of images on the computer monitor. It is also possible to transfer the image to video tape, although this leads to an appreciable loss of image resolution and color fidelity. Both of these techniques provide a compact and intuitively clear way of observing qualitative temporal changes in either the original image data or a derived data set such as vegetation index images.

A multitemporal data set of this kind can be easily manipulated using software designed for looking at multiband image data. Since most of the inter-image biases have been removed through the co-calibration described above, it is possible to do quantitative comparisons of this series of images. The distortions introduced during the co-registration process discussed above does add some uncertainty to the quantitative results, but this is outweighed by the increased ease of analyzing temporal changes in areas of the co-registered images. However, the uncertainties and distortions produced in the co-registration process makes attempts to pick a single pixel and track its changes over time ill-advised. The uncertainties can be minimized if analyses are restricted to areas of many

pixels which do not lie close to significant edges, like the edges of active and abandoned fields.

The explosion of multimedia for entertainment and education purposes suggests its use in communicating scientific results. This may be done either through the creation of a videotape or through the use of various types of software for preparing multimedia presentations. The temporal series of images may be enhanced through the use of narration, additional plots, still photographs, and other remote sensing images of the study area. A presentation of this sort can be used to enhance poster papers at meetings and some types of oral seminars (e.g., Ray *et al.*, 1994b). It provides a way of distributing important results which is more engaging and less formidable than a printed paper. Although preparing cogent and timed narration for a multimedia presentation is time consuming, producing the narration is no more involved than the production of a brief paper. Many of the principal results of this paper are summarized and displayed in JPL video #AVC-95-075, which is available through the Public Information Office at JPL and included in this thesis. This video was produced with the assisstance from Eric M. De Jong, Shigeru Suzuki, and Jeffrey R. Hall using the facilities of the JPL Digital Image Animation Laboratory (DIAL).

Part 6.4: *Human Activities*

The study area has been extensively used for growing irrigated crops since the mid-1960's. The principal crop grown in this area has been alfalfa with some small production of other field crops and of pistachios. Most of this agriculture has been performed using sprinkler irrigation, with center-pivot systems being used on most fields since 1978 as shown in table 21. The peak level of cultivation and the peak number of center-pivot systems occurs in 1985. Little surface water exists in this area; consequently, these irrigation systems are groundwater fed through pumping.

The Landsat data set of this thesis shows a series of 16 center-pivot fields located in this area that have been abandoned during the past 22 years as illustrated in table 22. According to the residents of the area, these fields were abandoned for economic reasons. Many of the farmers have found that the cost of electricity needed to pump the groundwater for irrigation made growing alfalfa unprofitable. The general trend was for the fields located the greatest distance north of the Mojave River to be abandoned first and those nearest the river abandoned last. Note that the rate of abandonment increased rapidly in the 1980's. The peak rate of abandonment occurred in 1984 which, paradoxically, was the year preceding the peak level of center-pivot cultivation in the Manix Basin.

Table 21: Irrigated Acreage and Number of Center Pivot Fields		
Year	Hectares in Cultivation	Number of Active Center-Pivot Systems
1973	1113	0
1974†	964	0
1975‡	3103	0
1978	1477	9
1979	1532	11
1980	1622	11
1981	1918	15
1982	1884	18
1983	2548	25
1984	2417	21
1985	3062	37
1986	2886	37
1987	2995	36
1988	2748	37
1990‡	1007	13
1991†	2131	30

Years marked with † in the table may have slightly underestimated values due to either cloud cover or lack of areal coverage in the image. Years marked with ‡ in the table may be significantly underestimated due to lack of areal coverage in the image.

Table 22: Number of Center-pivot Fields Abandoned During Various Years

Year	Number of Center-Pivot Fields Abandoned
before 1974	1
1974–1978	2
1981	2
1982	2
1984	5
1986	1
1989	1
1992	2

Land degradation is initiated by human activity, so the number of years the field was under cultivation should provide a measurement of the degree to which the field has been degraded. This degradation is then revealed either by drought, as discussed by Mainguet (1994), or by the removal of the irrigation which has previously hidden its effects. Enhanced wind erosion produced by the removal of shrub cover to begin agriculture followed by the loss of the irrigated vegetation with abandonment is an important example of land degradation occurring after human activity has ended. Futhermore, the degree to which the land was degraded by human activity during the time of active cultivation may affect how degradation proceeds after abandonment. Table 23 lists each of the twelve abandoned fields from figure 37 and gives the number of years that each is observed to be active in the MSS data. There is no evidence of activity on fields 11 and 12. Conversations with local residents indicate that field 11 was used in 1975–

1977, which is not covered by the MSS data, and field 12 was abandoned in 1972, before the MSS sequence begins.

Table 23: Number of Years Each Field Abandoned Prior to 1990 is Observed to be Active in MSS Data

Field Number	Number of Years Active
1	4
2	8
3	6
4	6
5	6
6	5
7	5
8	3
9	4
10	3
11	0
12	0

Part 6.5: *Vegetation Changes*

Figure 112 shows the IPVI (Crippen, 1990) for two abandoned center-pivot fields. Figure 112 shows a strong drop in IPVI levels when a field is abandoned. It is also seen that the fields remain at slightly higher IPVI values than the background desert for the first 5 years of abandonment. After that time, the IPVI values are seen to dip below those of the surrounding desert. It is important to note that field 7, which is downwind of field 6, has lower IPVI values from 1985 through 1991 than field 6. We might expect this if field 6 was acting as a source of blowing sand. A similar pattern is seen in figure 113, which shows normalized IPVI values for fields 8–10.

These analyses must consider the problems with vegetation indices discussed in chapter 5. The analysis of chapter 5 showed that the different types of desert vegetation which dominate during different stages of the process of biological succession tend to give distinctly different results for any vegetation index. However, chapter 5 did suggest that qualitative comparisons related to the degree of degradation and disturbance can still be made using broad-band vegetation indices such as IPVI. In these cases, lower values of the vegetation index are associated with degraded areas with either less vegetation or plant communities which are more representative of disturbed areas than of the climax creosote-bush dominated community.

As shown in chapter 5, desert vegetation is darker than the desert soil in this area across the entire spectral range of 0.5–1.1 μm covered by Landsat MSS. Consequently, areas in this dataset that appear brighter tend to have lower vegetation cover. Abandoned

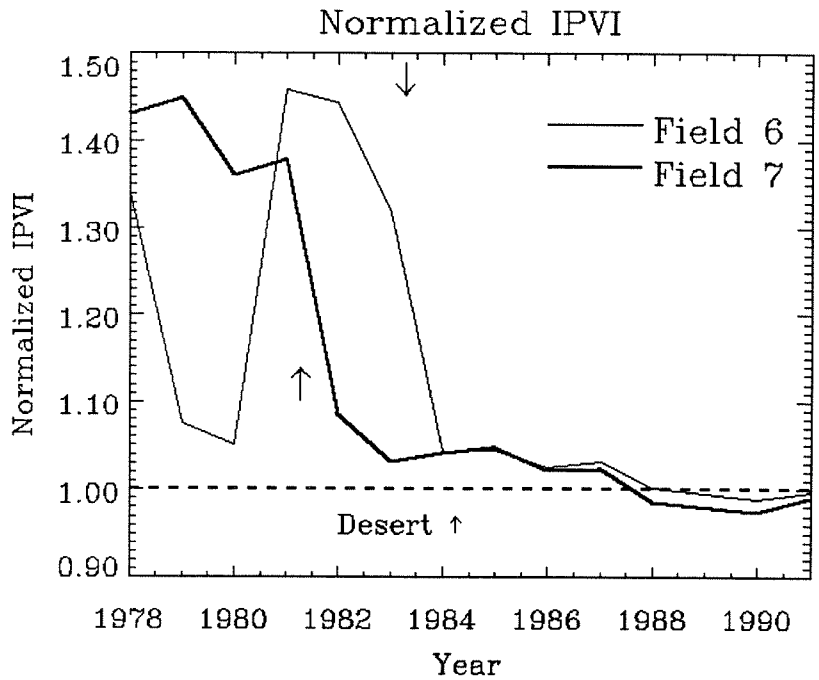

Figure 112: Normalized IPVI values for fields 6 and 7. The values have been normallized so that the average value of the background desert is 1.0 (the dotted line). This normalization was performed to eliminate global changes in vegetation cover. Note how the vegetation cover drops dramatically after the fields are abandoned. Note the tendency of the downwind field (field 7) to have lower IPVI values than the upwind field.

fields tend to remain darker than their desert surroundings for the first few years after abandonment. The darkness of the fields should indicate the level of vegetation cover, and to a degree this will remain true even if the vegetation type changes.

The AVIRIS data discussed in chapter 4 showed a very similar result of initial high levels of vegetation followed by a rapid collapse to levels at or below those of the surrounding desert (figure 42), as did the TM data from 1984 and 1985 (figures 43 & 44). This may reflect the presence of residual fertilizer coupled with the fact that the deep roots of the alfalfa plants may still be providing some resistance to wind erosion. After the residual fertilizer is consumed and the alfalfa root systems decay, much of the invading

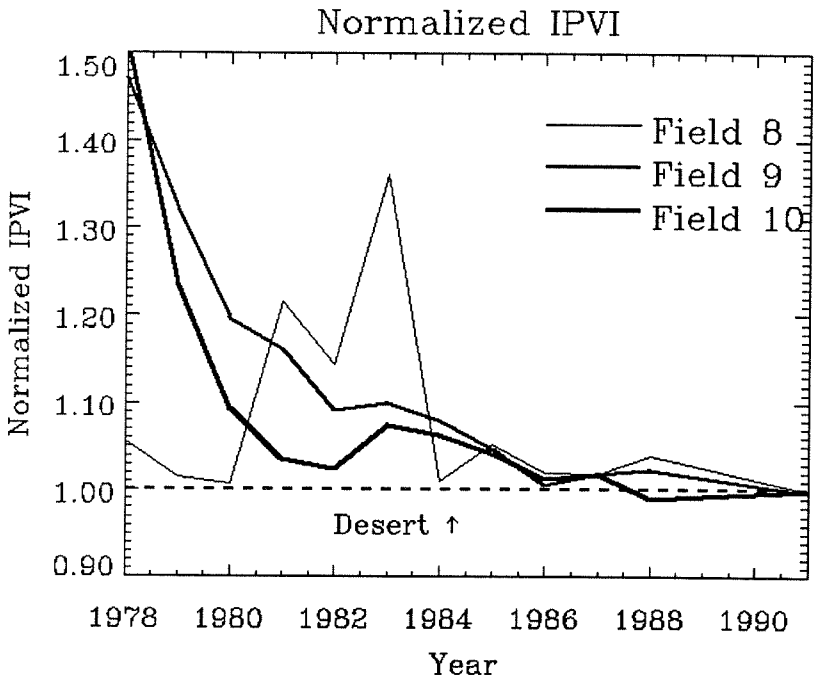

Figure 113: Normalized IPVI values for fields 8, 9 and 10. The values have been normallized so that the average value of the background desert is 1.0 (the dotted line). This normalization was performed to eliminate global changes in vegetation cover. Note how the vegetation cover drops dramatically after the fields are abandoned. Note the tendency of the downwind field (field 10) to have lower IPVI values than the upwind field (field 8), while the middle field (field 9) has intermediate values.

desert grasses die off and wind erosion begins. Additionally, the higher than 90% mortality rate of young desert shrubs like the creosote bush (Mabry *et al.*, 1977) indicates that few of the small number of shrubs that sprout on the abandoned fields will survive more than a few years. On-site observations and low-level aerial observations confirm that recently abandoned fields tend to support higher levels of vegetation cover than the surrounding desert, and that old abandoned fields tend towards less vegetation cover than the surrounding desert.

Part 6.6: *Blowing Sand*

As shown in chapter 4, the high albedo regions in the synthetic MSS image produced from AVIRIS data (plate 20) can be identified as windblown sand both by spectral analysis of the AVIRIS data and by on-site corroboration. Many of these areas appear to extend from abandoned (and sometimes active) fields. Areas of windblown sand can also be seen in the real MSS data, and the time series allows the observation of how they evolved over time.

Figure 114 shows how the temporal data may be used to observe the fluctuating process of degradation. Figure 114 shows the changes in several areas of blowing sand over the period from 1984 through early 1991. Figure 114a shows a few small areas of blowing sand that disappear by the time of the 1985 image (figure 114b). The areas of blowing sand seen in 1984 seem to be inactive in 1985, 1986, and 1987. Between the MSS image taken in the summer of 1987 and the MSS image taken during the summer of 1988 (figure 114c), significant areas of blown sand appear. These areas persist and spread over the period from 1988 through 1990 and shrink very slightly by the early part of 1991 as shown in figure 114d. Figure 114 shows why it is important to observe areas multiple times. From comparing figures 114a and 114b, we would conclude that the area has recovered, but the addition of figures 114c and 114d conversely suggests that the area is being further degraded.

The areas of blown sand appear during some years and are not apparent in others. Many times a formerly high albedo area that returned to the same appearance as the undisturbed desert for a few years will become bright again. When these areas become bright again, they often cover a larger area than they were seen to cover during their

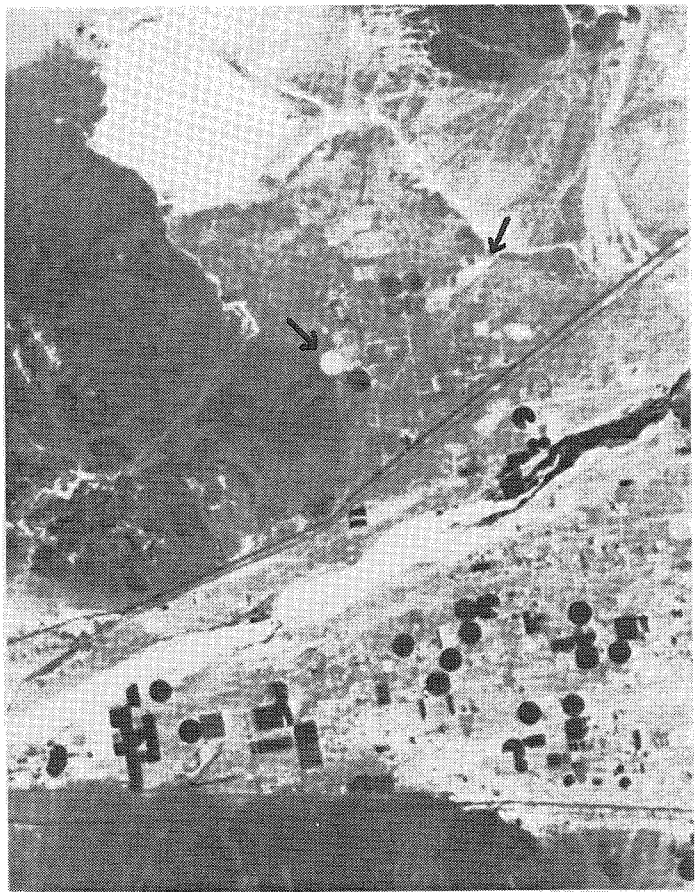

a)

Figure 114: A series of remote sensing images of the Manix Basin area of the Mojave Desert taken by multispectral satellite systems. A, B and C were taken by the Landsat Multispectral Scanner (MSS) instrument, and D was taken by the ex-Soviet RESOURCE instrument. All images cover the spectral range of 0.6–0.7μm (MSS Band 5, RESOURCE Band 2). North is to the top. The double dark lines crossing diagonally from lower left to upper right is Interstate-15, and Interstate 40 can be seen as a pair of dark lines near the bottom of the images. Daggett Airport can be seen as a small 'V', which opens towards the upper right, located just above Interstate-40 in the lower left part of each image. The bright area in the upper left of each image is a playa called Coyote Dry Lake. The dark circles and squares are irrigated fields, and between the playa and the interstate are other circular patches (some slightly darker than the surrounding area and some brighter) which are abandoned fields. a) MSS band 5 obtained on June 23, 1984. A bright region of sand blowing off a field is indicated by arrow at upper right. A very bright abandoned field is indicated by an arrow at center. (JPL P43868A)

b)

Figure 114: b) MSS band 5 obtained on July 28, 1985. The bright areas pointed out in figure 114a have disappeared, suggesting that some vegetation has grown on them. (JPL P43868B)

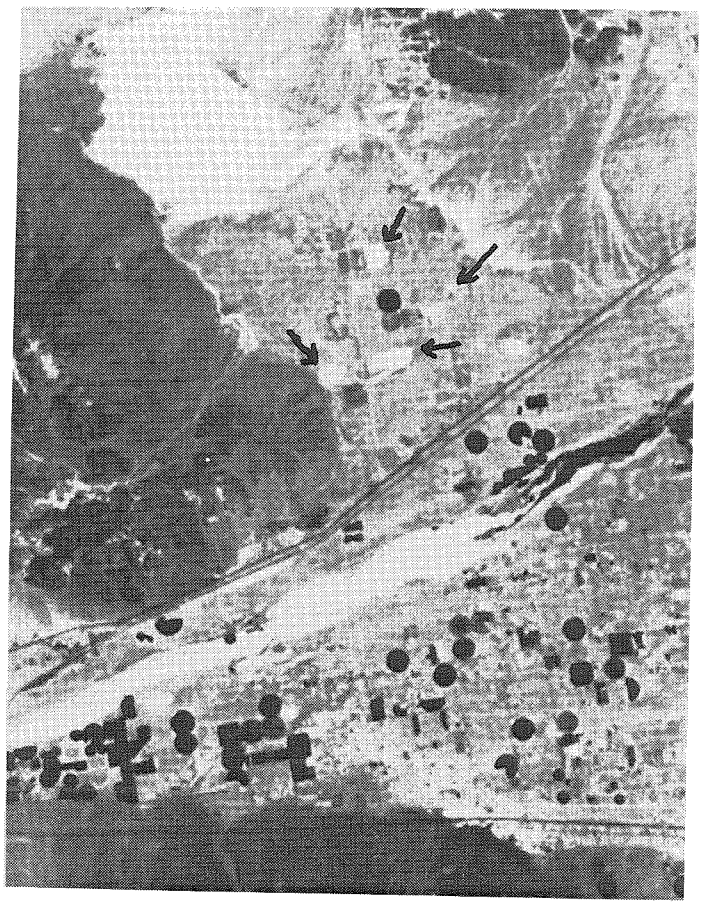

c)

Figure 114: c) MSS band 5 obtained on June 20, 1988. Two new bright patches of blowing sand are marked by arrows at upper center and center. The field that was bright in 1984 (figure 114a) is bright again, which means that it has lost its vegetation. (JPL P 43689B)

d)

Figure 114: d) RESOURCE band 2 obtained January 23, 1991. The three bright patches of blowing sand have grown substantially. At this point they cover as much area as the fields that produced them. Notice that the patch of blowing sand indicated in 114a has reappeared (arrow at upper right) (JPL P 43689A).

previous period of high albedo. Table 24 shows how the size of various features near abandoned fields identified as blowing sand has changed over time. As discussed in chapter 4, the identification of several of these areas as blowing sand has been confirmed by on-site investigations which have revealed sand drifting onto roads, heavily wind-rippled surfaces and small dunes, as well as by the AIRSAR results.

Table 24: Area (in hectares) of Blowing Sand Associated with Abandoned Fields Measured from Remote Sensing Data

Year	Field 3	Fields 6&7	Field 11	Field 12	Fields 8–10	Field #A
1979	0.0	0.0	0.0	2.6	0.0	16.6
1980	0.0	0.0	0.0	0.0	0.0	16.9
1981	0.0	8.8	17.5	13.0	6.5	18.2
1982	0.0	0.0	0.0	9.4	13.3	23.1
1983	0.0	12.3	0.0	0.0	0.0	0.0
1984	0.0	0.0	0.0	28.3	0.0	15.9
1988	18.5	61.1	0.0	0.0	48.7	0.0
1990	32.1	122.2	0.0	90.6	------	41.6
1991	32.1	137.1	0.0	98.1	79.9	44.8

The ability of windblown sand to adversely affect plant life leads to a further problem. It is well recognized that vegetative cover is an important factor in controlling wind erosion (Bagnold, 1942; Woodruff and Siddoway, 1965). Less vegetation cover leads to a greater potential for wind erosion, and wind erosion in one area can lead to less vegetation cover in the area immediately downwind. This process may then cause the

downwind area to become a new source of wind-driven sand. The positive feedback suggests that successful remote monitoring of arid regions requires techniques to identify and measure both of these properties of arid lands. Figure 112 shows how this synergism works in the case of fields 6 and 7. The downwind field of the pair has lower vegetation values than its upwind counterpart, and, as shown in table 6.4, this pair of fields produces a much larger area of blowing sand than the single fields. The set of fields 8–10 shows a very similar pattern, although the resulting area covered by windblown sand is considerably smaller than that from field 12 or the field 6&7 pair.

The large temporal changes revealed in figure 114 should be explainable in terms of the factors that control the rates and amounts of wind erosion. The two most important factors to consider are rainfall and the wind regime. Vegetation cover, which is in part controlled by rainfall, and the particle size distribution and roughness of the surface, which can be modified by the wind erosion itself, also impact the rate and amount of wind erosion. Meteorological data covering the time of the remote sensing series are available from the National Climatic Data Center (NCDC). Monthly and daily rainfall data for Daggett Airport, Barstow Fire Station and Goldstone Echo 2 were extracted from volumes 75–95 of **Climatological Data: California**, covering the years 1972–1991 (NCDC, 1972-1991). Monthly rainfall, temperature, and Palmer Hydrological Drought Severity Index (PHDI) data averaged over each climatological division in the contiguous United States were acquired from the NCDC in digital form (NCDC, 1990a). The National Renewable Energy Laboratory (NREL) has archived hourly meteorological and solar radiation data from numerous National Weather Service (NWS) stations as part of

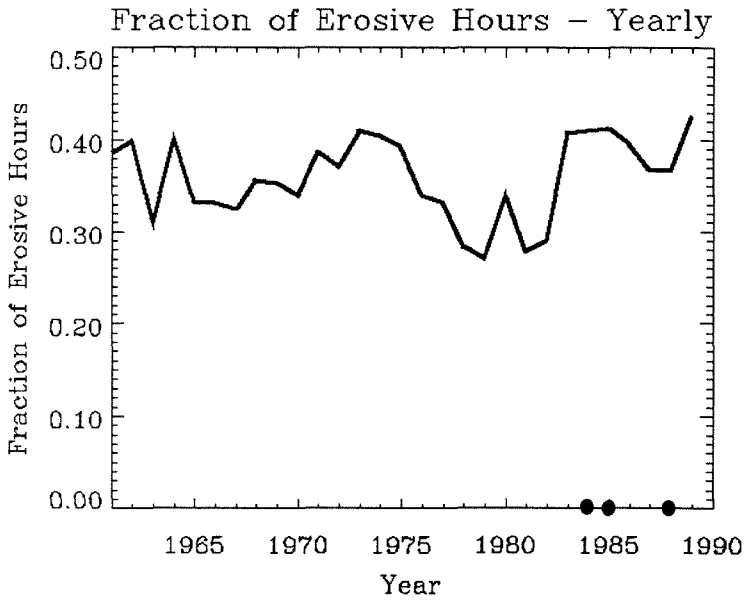

a)

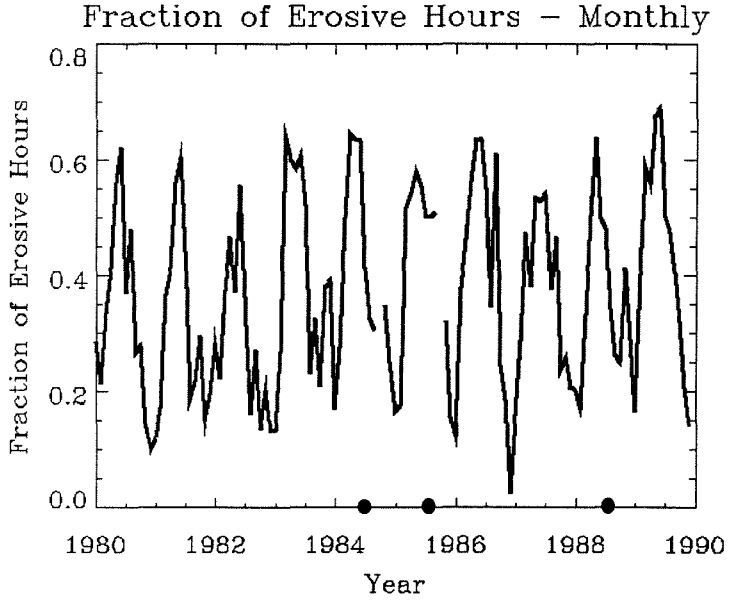

b)

Figure 115: Plots of the fraction of observed hours that the windspeed exceeded 5.56 m/s, which is the wind erosion threshhold. The three dots show years when MSS images in figure 114 were acquired. **a)** The annual fraction of erosive hours. The period 1983–1985 is seen to be a period of high levels of erosive winds, and an increase in the fraction of erosive winds can be seen in 1989. **b)** The fraction of erosive winds on a monthly basis for 1980–1990. This shows that the most erosive winds occur during the months of May and June, and the years 1983–1990 had more erosive winds during the first half of the year than the years 1980–1982.

the National Solar Radiation Data Base (NSRDB) in digital format (NREL, 1991a; NREL, 1991b). One of the NSRDB stations is the Daggett Airport for which wind speed and direction data are available for the period 1961–1990. Unfortunately, no rainfall data from Daggett were included in the database.

Figure 115 shows the fraction of the observing hours where the wind speed data extracted from the NSRDB (NREL, 1991b) exceeded the mobilization threshold for sand. The threshold speed was defined as 5.56 m/s based on the standard of 12 mi/hr reported by Tugel and Woodruff (1986). On the basis of these data we might expect significant sand movement throughout the period from 1983–1985 and 1989–1990. This agrees in part with table 3 which shows significant sand mobilization in 1981, 1984, and 1988, but there are inconsistencies which indicate additional controlling factors. No mobilization is observed in 1983 or 1985, and the wind conditions do not appear to be particularly conducive to wind erosion in 1981 and 1988.

Digital rainfall and PHDI data from NCDC (1990a) for the Southeastern California Desert Basins Climatological Division are displayed in figure 116. The monthly total precipitation data shown in figure 116a reveals that the last half of 1980 was extremely dry

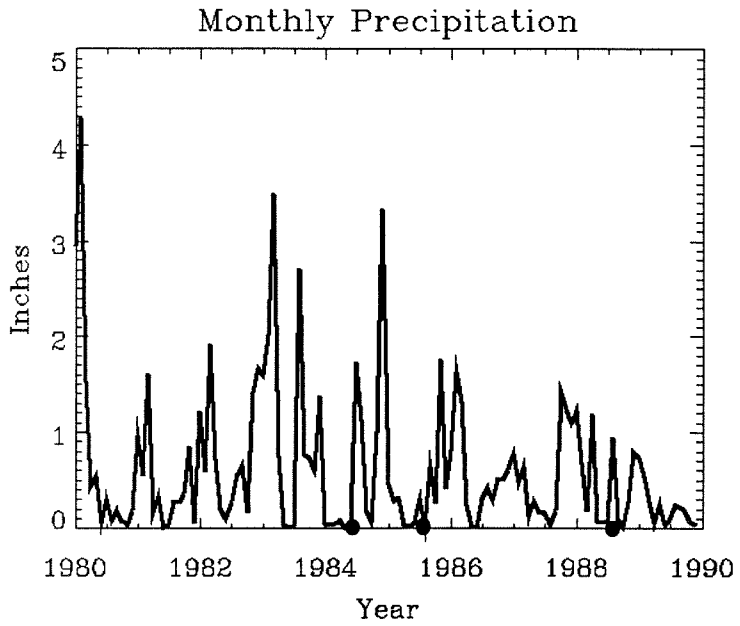

a)

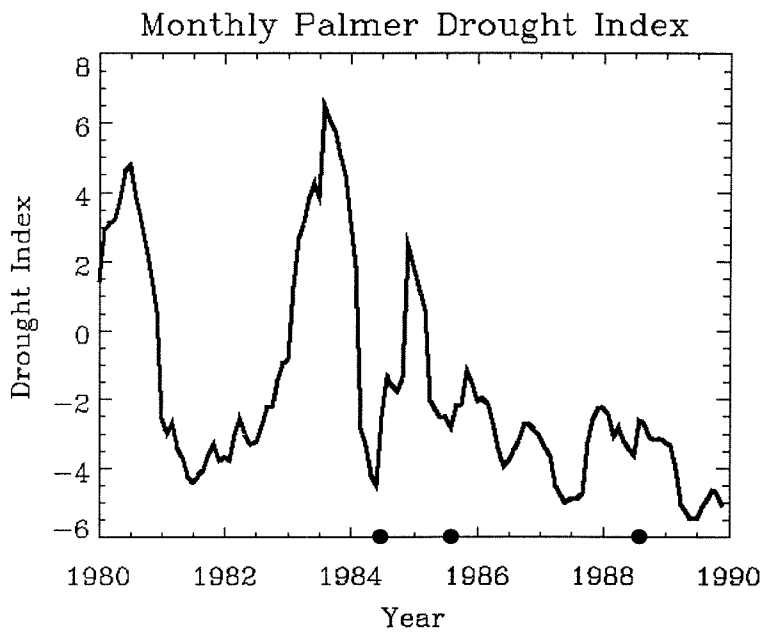

b)

Figure 116: Climatological data for the Southeast California Desert Basins Climatic Region. The three dots show years when MSS images in figure 114 were acquired. **a)** Plot of monthly rainfall data. **b)** Plot of Palmer Hydrological Drought Index data. Values from 1.5 to -1.5 are considered normal, values from 1.5 to 3.0 are considered moderately wet, values greater than 3.0 are considered extremely wet, values from -1.5 to -3.0 are considered moderately dry, values from -3.0 to -4.0 are considered severely dry, and values lower than -4.0 indicate conditions of extreme drought.

and that 1981 and 1982 were fairly dry years. A large amount of rain fell in 1983, especially during the first half of the year, which counterbalances the high windspeeds observed in 1983 at Daggett Airport. However, 1988, a year in which significant mobilization is observed, does not seem to have been a year significantly drier than 1986 or 1987 when no mobilization is observed. The 1989 and 1990 rainfall data do support the vast expansion of the areas of blowing sand observed between 1988 and 1990, particularly when coupled with the increasing fraction of erosive winds observed in figure 115.

Figure 116b shows the monthly PHDI values for the climatological division. The year 1981 was a period of severe to extreme drought severity. During 1982, the hydrological regime returned to normal, which was followed by the very wet year of 1983. In the first part of 1984 there was a sudden return to extreme drought conditions followed by the moderately wet period from late 1984 through early 1985. The fact that late 1984 and early 1985 were wet periods explains the absence of blowing sand in the 1985 image, since ephemeral plants and the relatively drought-intolerant grasses would be growing in profusion at that time. From late 1985 through 1989 the area experienced moderate to extreme drought with late 1987 and 1989 as the periods of most extreme drought. Again, these data still fail to indicate why 1988 is a prime period for mobilization as compared to 1986 and 1987. It is also important to note that PHDI is based on long term averages for the climatological division in question (Palmer, 1965; Alley, 1984); hence, an abnormally wet period is only wet as compared to the normal arid conditions, and extreme drought indicates very severe conditions of aridity.

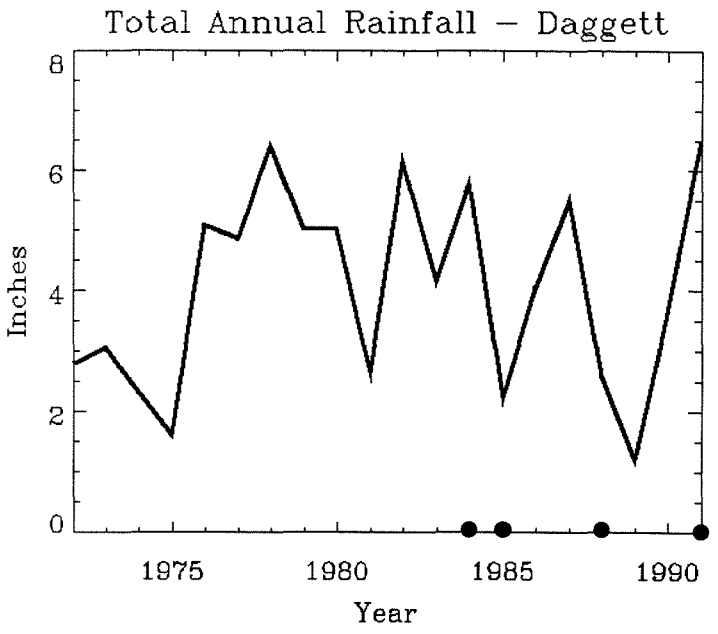

a)

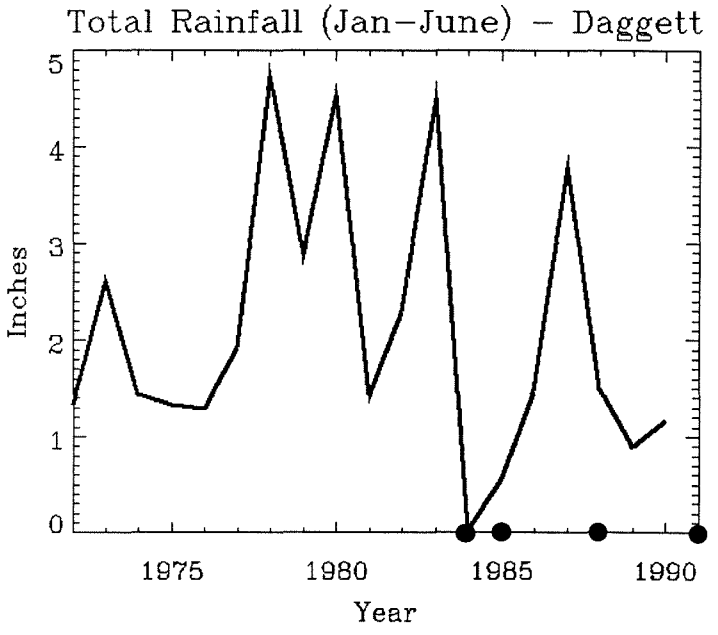

b)

Figure 117: Rainfall data from Daggett FAA Airport, 1972–1991. The four dots show years when MSS images in figure 114 were acquired. **a)** Total annual precipitation. **b)** Total precipitation during the first six months of the year. Note the absence of precipitation during the first six months of 1984.

One important failing of the data shown in figure 116 is the fact that it is an average over a climatological region which stretches from Calexico at the U.S.-Mexico border in the south, to Lee Vining near Mono Lake in the north. Therefore, those data may not well represent the conditions in the Manix Basin. Examination of the non-digital NCDC (1972-1991) data reveals three data stations near the Manix Basin: Daggett FAA Airport, Barstow Fire Station, and Goldstone Echo 2. Of the three, Daggett FAA Airport is the nearest, and it is also the most complete data set of the three. Figure 117 shows rainfall data for Daggett Airport. In figure 117a, the annual rainfall data shows that 1981 was a dry year, which accounts for the mobilization seen at that time, but 1982 appears to be a very wet year, which is contrary to the mobile sand observed at that time. The years 1983 and 1985 were drier than 1984, which conflicts with the fact that wind erosion is observed in 1984 but not in 1983 or 1985. The data show that 1988 was a significantly drier year than 1987, which explains the absence of mobilized sand in the 1987 MSS data. Although we have now explained the 1981 and 1988 mobilizations with the Daggett rainfall data, it seems that the 1984 mobilization is inconsistent with the data.

Figure 117b reveals the solution to this problem. In this figure the amount of the rain which fell in the first six months of the year is displayed. It is immediately obvious that all of the rain observed in 1983 fell during the first six months of the year, while all of the rain observed in 1984 fell during the last half of the year. The 1983 image was acquired on July 15, and the 1984 image was acquired of June 23. The 1983 image was preceded by six months of heavy rain, while the 1984 image was preceded by nearly 12 months with no measurable precipitation. The last six months of 1984 were very wet,

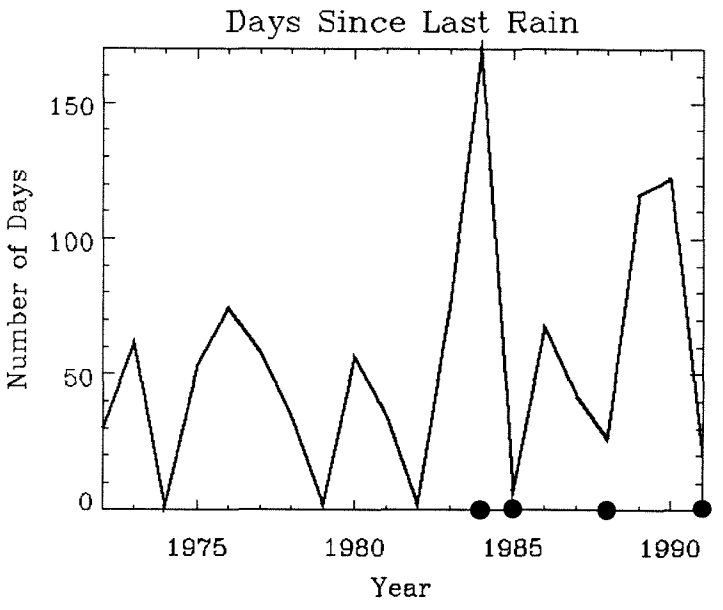

Figure 118: Plot showing the number of days between the acquisition of each year's MSS image (AVIRIS image in 1990; RESOURCE image in 1991) and the most recent previous measureable rainfall. For years when no image is available (1976, 1977, 1989) the number of days between July 20 and the nearest preceeding measureable rainfall is plotted. The four dots show years when MSS images in figure 114 were acquired.

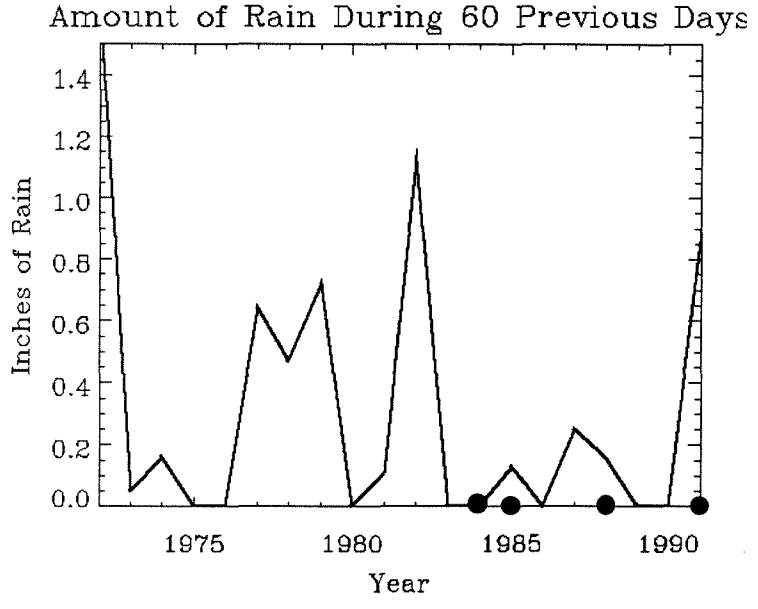

Figure 119: Inches of rain in the 60 days prior to the collection of each year's image. For the three years with no remote sensing data (1976, 1977, 1989) the rainfall during the 50 days prior to July 20 is plotted. The four dots show years when MSS images in figure 114 were acquired.

which accounts for the lack of mobilized sand in 1985. The lack of mobilization during 1986–1987 is further supported by the fact that the annual fraction of erosive winds was decreasing over that time.

Figure 118 shows the number of days since the last measurable rain for each image. The 1974 MSS image was actually acquired on a day of measurable rain, and the 1979 MSS image was acquired less than a week after the last measurable precipitation. The long dry period prior to the 1984 MSS image is another outstanding feature. The minimum amount of precipitation required to be considered "measurable" is 0.25 mm (0.01 inches), and, if the last rain was only the minimum measurable level, this might not have a dramatic impact on the hydrologic conditions in the area. In figure 119, the rainfall for the 60 days prior to the acquisition of the MSS image is shown for Daggett Airport. The wettest period is in 1972 where nearly 3.18 cm (1.25 inches) fell in the 60 days prior to July 20. The next wettest period happens to be the 60 days prior to July 20, 1990 when the AVIRIS data were collected. The fact that there were significant rains during the 60 days prior to image acquisition is 1978–80, 1987, 1990, 1991 means that some caution may be required in comparing these data to images acquired in years where less rain fell just prior to image acquisition. On the other hand, the 1990 and 1991 images which were immediately preceded by a wet 60-day period show large areas of windblown sand on which the vegetation values are very low, so a wet period immediately preceding image acquisition does not completely eliminate evidence of land degradation.

Although the amount of moisture in the soil is a factor in the amount of wind erosion which can occur, in most cases the most important effect of precipitation is its

effect on vegetation. As mentioned previously, the plant cover is dependent on the rainfall. This is especially true of the desert grass with its shallow roots which are unable to tap deep water sources. The grasses will gradually die out over a period of extensive drought. The grass is very important to the wind erosion problem, since it tends to provide sand trapping (Bagnold, 1942) over larger contiguous areas than the more isolated shrubs. If there is insufficient water for the grass to continue to grow, it can then be overwhelmed by blowing sand, and be completely buried (Bagnold, 1942). When wetter periods return, the grass can reestablish itself as a protection against wind erosion.

The death and burial of the downwind vegetation is the factor that allows the regions of blowing sand to continue to grow. Under conditions of strong mobilization, the mobilizable sand in the source region may be depleted. The source area ceases to supply sand as the easily erodible particles are removed. In addition, as observed in the field, deflation ripples of coarse material build up which increases the non-erodible surface roughness and decreases the ability of the wind to mobilize sand over that area. However, even if the original source area turns off, the downwind destruction of vegetation by the blowing sand can create a new source. The wetter period which has occurred since 1991 may have shut off the process before irretrievable damage had occurred to the downwind vegetation.

The preceding analysis shows the importance of the local conditions of wind and precipitation on the investigation of land degradation. Extrapolations based on the local meteorological data are only useful near to the point of data collection, and it would be a mistake to expect that the sand mobilization conditions observed in the Manix Basin area

to be present across a NOAA climatological region like the Southeastern California Desert Basins region which contains the Manix Basin. Likewise, composite meteorological data for a climatological region will generally not be useful to predict the potential for wind erosion at any specific locality in the region, and such composite data may not even be informative of potential wind erosion on a regional basis. The difficulty of predicting potential or estimating actual wind erosion from non-local or regionally-averaged meteorological data further supports the need for frequent satellite remote sensing to monitor the state of wind erosion in areas with poor local weather information.

The preceding inferences made from the remote sensing temporal series have been confirmed by on-site observations. This was supplemented by discussions with the local residents who mentioned sand drifting onto many of the roads in the areas downwind of abandoned fields during 1988–1990. Observations in 1990 and early 1991 revealed drifted sand and heavily wind-rippled and barren abandoned fields. During the recent wetter period extensive regrowth of grass and small shrubs has been observed; however, given the high mortality of young desert shrubs (Mabry *et al.*, 1977), this does not yet mark a recovery of the area.

Based on the evidence of low vegetation levels in the areas of windblown sand inferred from the AVIRIS and RESOURCE data that were collected after recent significant rains, some conclusions about the process of recovery from wind erosion can be made. First, an area which has experienced extensive wind erosion tends to lack the organic matter and nutrients for the rapid growth of ephemeral plants or the establishment of perennials. Second, this lack of nutrients may be compounded by the continual

sweeping of seeds from the area by the wind, leaving few seeds available for germination after the rainfall. When rains do occur, the vegetation outside of the area of blown sand experiences a significant increase. Upwind, the increased vegetation robs more energy from the wind, reducing its ability to mobilize sand. Downwind, the increased vegetation acts as predicted by Bagnold (1942), continually trapping windblown sand and stopping its spread. In the absence of an extended period of drought the area of blown sand is probably reclaimed by vegetation invading from the downwind edge and the sides of the area of windblown sand. The vegetation downwind would tend to invade much more slowly, since most of its growth effort is expended in staying alive under continual inundation by sand and the fact that its seeds would tend to spread downwind. Shrubs such as creosote bush grow very slowly (Barbour *et al.*, 1977a, Barbour *et al.*, 1977b), so most of the initial invasion is by ephemerals and grass with relatively shallow roots. This reclamation is susceptible to the return of a drought period until the slow-growing shrubs reclaim the area, a process taking centuries (Vasek *et al.*, 1975a; Vasek *et al.*, 1975b; Vasek, 1979/80; Carpenter *et al.*, 1986).

Part 6.7: *A Quantification of Soil Loss*

The flood irrigation system discussed in chapter 2 provides an opportunity to make a quantitative assessment of soil loss from that specific area. The tops of the vertical pipes in the irrigation system would have been flush with the surface of the ground when the field was in operation. Today, the irrigation system has been partially excavated by

erosion. The vertical distance from the top of the stand to the bottom of the horizontal pipe is 54 cm. Assuming that the original soil slope from the irrigation system was 5%, which is the typical maximum slope reported in this area by Tugel and Woodruff (1986), a triangular wedge of soil 54 cm in height by 1080 cm in length must have been removed from each side of the irrigation system. For each meter of irrigation system so exposed, 5.83 cubic meters of soil would be removed. The entire length of the irrigation system is 695.7 m, so this would mean that 4057.4 cubic meters of soil would have been removed from the field. However, not all of the irrigation system is completely excavated, and a conservative estimate is that the average excavation along the entire system is about half of the total height of the system. This leads to a final estimate of 2028.7 cubic meters of soil. If this volume of soil were spread over the 98.1 hectare area of blown sand west of field 12 in which this system is located, it would represent a layer 2 mm thick.

Part 6.8: *The Edge of Destruction*

A notable feature which can be seen in vegetation index images computed from the 1988 Landsat MSS data is the bright downwind edge of some of the areas of blowing sand, as shown in figure 120. The average NDVI in the enhanced region downwind of fields 6 and 7 is 0.0910, while the undisturbed desert gives an average value of 0.0871. The higher vegetation index values for these edges as compared to the undisturbed desert suggests that the downwind edges of the regions of blowing sand are zones of enhanced vegetation cover.

We generally expect that blowing sand will only decrease the vegetation cover through the burial and sandblasting of plants. Certain fast-growing plants in the desert do spread their seeds with the aid of the wind. The tumbleweed is a particularly good example of this, and we have seen that the growing tumbleweed is one of the "greenest" plants in the Manix Basin area under normal circumstances. These seeds could be trapped by the vegetation at the downwind edge of the area of blowing sand, and then a significant rain would cause a green bloom at the downwind edge of the field. However, the evidence shown in figures 116–119 indicates that the period preceding the 1988 image was not a period of relatively high precipitation.

The answer to this question lies in the problem of non-linear mixing discussed earlier. We showed previously in this thesis and in, Ray and Murray (1995), that non-linear mixing can produce as much as a 50% increase in apparent plant cover as one goes from a dark non-reflective background to a background of bright desert soil. The enhancement in this case is only 0.0041 as opposed to the more extreme case discussed earlier which gave an NDVI which was 0.0166 higher for the bright background than the dark. This is reasonable, since there is almost certainly a smaller contrast between the background soils in the image than between the dark Krylon-coated background and the soil.

Consider that the downwind edge of a region of blowing sand is just beginning to feel the effects of the blowing sand. There has not yet been enough time for vegetation to have been disrupted by sandblasting and burial. However, the original soil surface is being

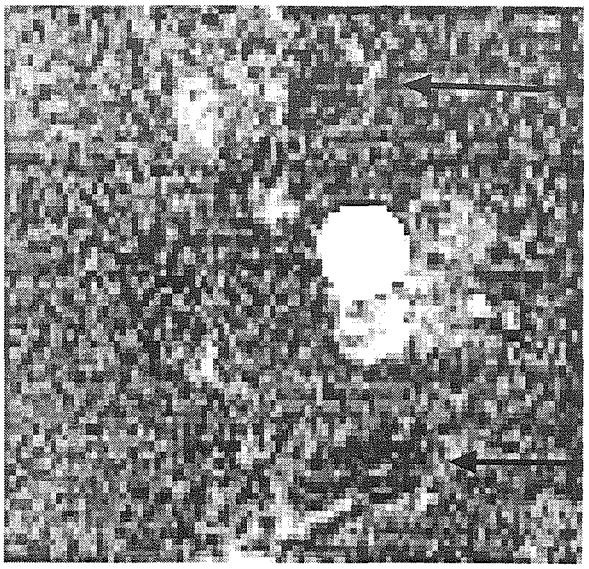

Figure 120: An enlargement of part of the 1988 MSS NDVI image. Notice the bright edges along the right (east) sides of the two dark patches of low NDVI (arrows).

covered by a thin veneer of sand which will tend to be more reflective than the original soil. In addition, we have seen that the short desert grass tends to be less reflective than the soil. We have photographic evidence that this grass disappears in regions of sand blowing even where there is still a significant cover of shrubs. This is reasonable, because the short grass will be buried more rapidly than the shrubs, especially the shrub tops, can be defoliated by sand blasting. This is an additional way to increase the reflectivity of the background.

The preceding analysis suggests that this region of slightly enhanced vegetation index values is an area which is just beginning to be effected by blowing sands. The area is the leading edge of an actively expanding area of blowing sand. For the vegetation enhancement discussed above to be caused by the presence of a more reflective background, enough sand must have been moved to cover the original soil, but the sand encroachment must be recent enough to have not adversely impacted the shrub vegetation.

Also, if part of the brightening of the background is due to the burial of the desert grass, the event must have occurred recently enough to deny the grass regrowth time. It is hypothesized that evidence for the recent strong mobilization of sand exists in the windspeed records from Daggett Airport.

In figure 121 we see a record of the number of hours each day that the windspeed exceeded the sand mobilization threshold of 5.56 m/s during the period from April through the end of June 1988. We see that there was a significant increase in the time that the winds exceeding the mobilization threshold during the period from late April through mid-June. During the month of May there were 10 days when the Daggett Airport list winds constantly above the sand mobilization threshold. The last week of May experienced nearly constant wind speeds sufficient to mobilize sand.

In figure 122 we can see that the wind speed exceeded the sand mobilization threshold for 459 hours. For the period from April through June 1988 there was a total of 1252 hours or 52 full days of erosive winds. This means that a period of sustained winds capable of blowing sand was just ending when the 1988 Landsat image was acquired, so that the conditions outlined above for a recent mobilization of large amounts of sand are met. This would cause the extreme downwind edge of the region of blowing sand appear to have enhanced vegetation cover due to enhanced non-linear spectral mixing caused by bright windblown sand.

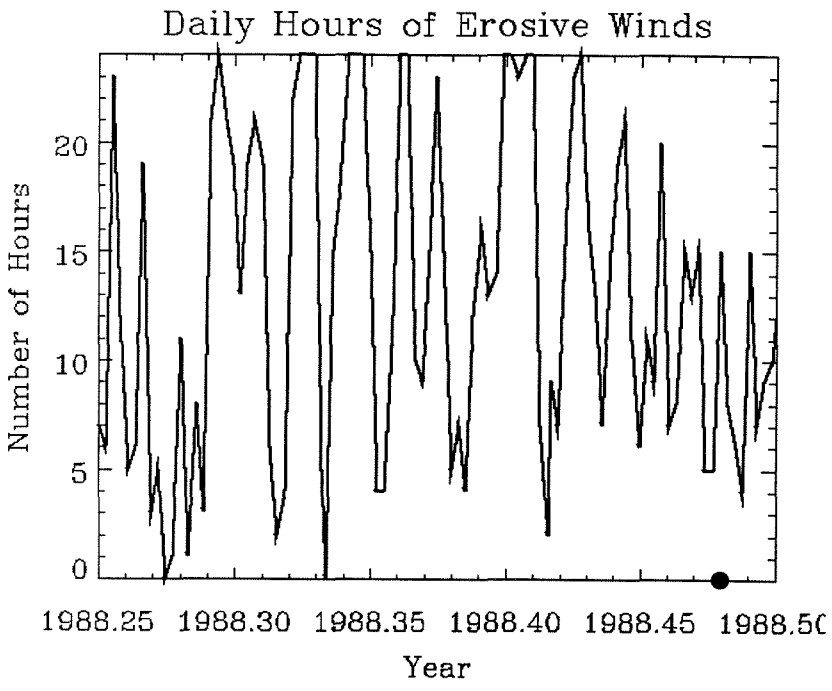

Figure 121: Number of hours each day that the wind speed exceeded the sand mobilization threshhold of 5.56 m/s from the beginning of April 1988 (1988.25) to the end of June 1988 (1988.5). The black dot shows the date when figure 120 was collected.

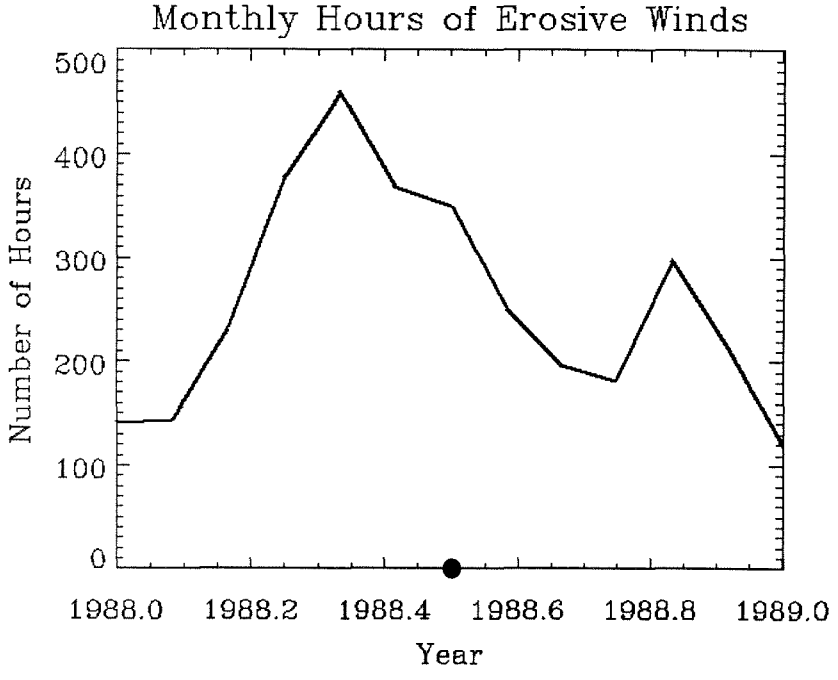

Figure 122: Plot of the number of hours each month that the wind exceeded the threshhold mobilization speed of 5.56 m/s. Notice that the April through June period was dominated by high winds. The black dot shows the date when figure 120 was collected.

Part 6.9: *AIRSAR and AVIRIS Revisited*

A particular inconsistency observed in both the AIRSAR and AVIRIS data is the consistently more degraded appearance of field 2 as compared to field 1. In Table 6.3, it was shown that field 2 was used for twice as many years between 1973 and 1990 as was field 1. As discussed earlier in this chapter, much land degradation occurs during the actual cultivation of the field, and this degradation may enhance degradation which occurs after the abandonment of the field. The degradation that occurred during the cultivation of the field would also tend to make the biological reclamation of the field more difficult.

Consider the lower vegetation index value for field 2 as compared to field 1. This may be due to a depletion of soil resources during cultivation. This would include any wind erosion of fines, a further destruction of soil structure through cultivation, and a longer-term pursuit of the use of herbicides to eliminate desert plants occurring as weeds on the field. However, figure 75 indicated that the area closer to the river, which includes field 1, tended to have higher levels of vegetation cover than areas further north of the river, which includes field 2. This lower vegetation cover on field 2 as compared to field 1 may be simply due to this factor.

This chapter has shown the power of temporal remote sensing to the study of land degradation. Such temporal remote sensing is the key to monitoring. This chapter has shown how the discontinuous temporal pattern of degradation requires long-term observation for accurate assessment of degradation. We have seen how areas of blowing sand appear and grow during periods of low rainfall and high winds. The satellite data ties closely with local meteorlogical data, and this shows how regionally averaged rainfall and

wind data does not accurately predict land degradation in specific locations within the region. Finally, this chapter has shown the power of remote sensing for quickly viewing and quantifying the extend of degradation in an arid region under observation.

Chapter 7: *Monitoring Arid Lands*

Land degradation is a complex ensemble of surface processes including wind erosion, water erosion, soil compaction, salinization, and soil waterlogging. When these processes, directly triggered by human activity, increase the barrenness of the lands, the resulting degradation is referred to as "desertification." As the ever-increasing world population places more and more demands on land for food production and other uses, many marginal arid and semiarid lands will be at risk of degradation. The need to maintain sustainable use of these lands will require that they be monitored for the onset of land degradation so that the problem may be addressed in its early stages. Monitoring will also be required to assess the effectiveness of measures to control land degradation. This chapter will summarize the need for affordable satellite monitoring of arid lands and outline the parameters of a future system for satellite monitoring. Near-future technique development and verification opportunities will also be outlined.

Part 7.1: *The Need for Affordable Satellite Monitoring*

Land degradation is a global problem, but is specific to localities. It progresses in a discontinuous manner in both time and space, responding to both natural climatic changes and to generally increasing anthropogenic causes. It begins as isolated patches scattered across an area, and, if the problem is not addressed in a timely manner, these spots will expand and coalesce. The degradation becomes more obvious during periods of drought, whereas rainy periods temporarily obscure the damage. This discontinuous

nature of land degradation means that on-site surveys, which can quickly reveal that some specific spot has been degraded, nevertheless cannot easily assess the pattern and extent of degradation scattered over an area. The temporally discontinuous nature of land degradation means that the only way to accurately assess land degradation is through a long-term program of repeated observations referenced to a common baseline or, to put it more simply, a monitoring program.

Airborne remote sensing is not an efficient tool suitable for such monitoring for many reasons. First, airborne sensors, even those flown in very high-altitude aircraft such as the ER-2 or NASA SR-71, can only provide a relatively local view. Each acquisition of data using an airborne system requires an active decision to fly the instrument over the target area. It is extremely difficult to accurately reproduce flight lines in terms of ground track, altitude and aircraft attitude, which dramatically increases the difficulty of analyzing and interpreting the monitoring data. Airborne instruments suffer through flight stresses each time that the instrument is flown, and the accessibility of the instrument to ground-based engineers often leads to continual tinkering and "improvements" to the instrument, which can compound the difficulty of comparing data acquired at different times. The operating expenses for an airborne instrument (aircraft maintenance, ground and flight crew pay, airfield expenses, aviation fuel, etc.) are very high.

Although the up-front costs of launching a satellite instrument are also quite high, the operational costs are significantly lower than for an aircraft per unit of data. Satellite systems provide automatically repeating coverage along predictable flight paths with little variance compared to aircraft flight lines. The repeating coverage of satellites provides

the ability to track seasonal changes and, over a longer time scale, changes related to climatic variability. This capability enables differentiation between anthropogenic land degradation and natural variations. Repeated coverage also provides the ability to use differential analysis of relatively unchanging targets for local target calibration and to provide information on atmospheric variability to compensate for atmospheric effects on the surface signatures. A satellite system also provides automatic coverage of much of the entire globe, and therefore, potentially, may enable some degree of global generalization. Lastly, a satellite system monitoring drylands on a global scale has a greater potential for producing data useful for currently unanticipated needs than does dedicated airborne data collection.

Part 7.2: *Spectral Choices: Polarimetric Radar vs. Visible and Near Infrared*

The highly visible flights of SIR-C (Shuttle Imaging Radar C) in the space shuttle and its emphasis on environmental study suggests that polarimetric SAR systems would be an important component of global monitoring. Specifically, polarimetric SAR can provide information about surface roughness produced by human scratching at the Earth's surface (e.g., furrows), and it can use this to provide information about processes acting on the Earth's surface such as wind erosion. The information about surface roughness provided by polarimetric SAR can also provide information about the presence and degree of wind erosion, and measures of surface roughness can provide information about the potential for wind erosion (Greeley *et al.*, 1988). This detailed characterization of the surface

roughness with polarimetric SAR gives information on features which are significantly smaller than the pixel resolution. The strongest advantage of radar is the fact that it works day and night under both clear and cloudy conditions. However, polarimetric SAR is intrinsically complex technically leading to large mass and power requirements on orbit. Polarimetric SAR also requires extensive and intensive ground processing before the data can be utilized.

Even though this research shows that distintive polarization signatures arise from surfaces covered by ripples formed through wind erosion, this only shows where wind erosion has occurred and it does not supply information about the area affected by windblown sand. If the ripples which form in regions under observation tend to have wavelengths significantly different than the observing SAR, the polarization signatures of wind ripples will not be apparent in the SAR data. The resonance features observed from concentric cultivation are interesting, but the obliteration of such features over time could be due to either further land degradation or the reclaimation of the field by the natural ecosystem. The radar also gives little useful information about vegetation cover.

Visible and near-infrared (V/NIR) sensing provides information about vegetation cover and also human scratching. There is a longer history of satellite V/NIR data than there is for satellite radar data, which makes the extension of V/NIR observations into the past much simpler. The implementation of polarimetric SAR in a satellite system is difficult compared to visible and near-infrared sensors. The time delay between the V and H pulses in a polarimetric system is significant for a satellite instrument, and this greatly increases the difficulty of ground processing. The processing of visible and near-infrared

data is much simpler than polarimetric SAR data. Gathering in-situ field V/NIR data with modern field spectrometers is very simple, while measurements of the dielectric constants of living shrubs in the field is a problem with no practical technical solution at present (JoBea Way, 1995, personal communication). Furthermore, the V/NIR part of the electromagnetic spectrum contains most of the important spectral features of vegetation. These considerations suggest that V/NIR sensing should be the primary focus of a monitoring system, although the inclusion of a polarimetric SAR system would be useful if sufficient resources were available.

Part 7.3: *Future Development Opportunities*

There are a series of remote sensing instruments to be launched in the near future which may provide opportunities for incremental definition and development of the technical characteristics of a future dedicated, affordable arid region monitoring system. The characteristics of these upcoming instruments are shown in table 25. In order to consider the suitability of these instruments for arid region monitoring, we must first consider the features which the system will be required to measure in order to provide useful information about arid region land changes.

Table 25: Characteristics of Upcoming V/NIR Satellite Systems

Instrument	Launch Date	Surface Resolution	Repeat Coverage	Bands (μm)
SeaWIFs	October 1995	1 km	Daily	0.402–0.422; 0.433–0.453 0.480–0.500; 0.500–0.520 0.545–0.565; 0.660–0.680 0.745–0.785; 0.845–0.885
Lewis & Clark	June 1996	30 m	16 days	0.4–2.5 (in 384 bands)
		5 m	16 days	0.5–0.7
MODIS	1998	250 m; 500 m; 1000 m	1–2 days	0.4–3.0 (in 20 bands)
???????				
ADEOS (OCTS)	1996	700 m	3 days	0.402–0.422; 0.433–0.453 0.480–0.500; 0.510–0.530 0.555–0.575; 0.655–0.675 0.745–0.785; 0.845–0.885
ADEOS (AVNIR)	1996	16 m	14 days	0.420–0.500; 0.520–0.600 0.610–0.690; 0.760–0.890
	1996	8 m	14 days	0.52–0.69

Part 7.4: *The Vital VNIR Spectral Features to Monitor*

This research shows how areas of blowing sand can be easily identified and monitored with satellite remote sensing. The area affected by windblown sand can be easily quantified from remotely sensed images. The relationship of drought and land degradation was clearly shown by the temporal MSS data. Abandoned fields produced large areas of windblown sand during periods of drought, and these areas of windblown sand became inactive and difficult to see during periods of higher rainfall. When drought conditions again occurred, the same areas reactivated and expanded in area compared to the previous active period. In all of these cases, no areas of windblown sand unrelated to abandoned or active agricultural fields were observed. This sort of observation of areas of windblown sand will be an important aspect of a monitoring system.

However, the most vital single parameter for monitoring is the signature of vegetation cover. Vegetation provides protection against degradation processes such as wind erosion, and subtle changes in vegetation are likely to be a precursor of wind erosion. Decreasing vegetation cover, and changes in the population of the vegetation cover, e.g., from creosote bush to bursage in the Manix Basin, are sensitive indicators of land degradation. Vegetation reflects the hydrological aspects of arid regions, and provides an indicator of current and recent hydrological fluxes.

The 0.4–1.0 μm part of the electromagnetic spectrum contains the red edge feature of the green vegetation reflectance spectrum which is exploited by standard vegetation indices. A key result of this thesis is to emphasize that there are other spectral features of arid vegetation in this spectral range which have not been exploited in remote sensing and

must be used for an effective sensing system. Laboratory and field spectra of some desert plants indicates that there are also interesting features in the 2.0–2.5 μm range related to leaf coatings, but these features will probably not be key in measuring arid vegetation cover while the visible wavelength pigment features will be key.

Current techniques of remotely measuring vegetation cover are based on the characteristics of humid vegetation with large leaf area, fairly continuous canopies, high chlorophyll content, and thin, translucent leaves. As shown in chapter 5, arid vegetation has special adaptations to the water and thermal stresses which occur in these regions. The inability of arid region vegetation to regulate temperature through transpiration leads to small leaves and open canopies to improve the efficiency of cooling the leaves by moving air. The small leaves reduce the amount of leaf area in arid vegetation, and the open canopies mean that a great deal of soil is visible through most arid vegetation canopies. Further compounding the problem is the fact that arid plants tend to have vertically oriented leaves to avoid direct sunlight during midday, which is when remote sensing observations are generally made in order to have the brightest lighting and the fewest shadows. The edge-on view of these leaves means that little of the small amount of leaf area present in arid plants can be seen with remote sensing. Other plants change the orientation of their leaves by rolling and unrolling or steering the leaves which has the same effect of reducing the leaf area visible to remote sensing. Many arid region plants have leaf hairs and coatings which alter the spectral properties of the leaves, and they often have less chlorophyll concentration than humid plants.

On a larger scale, desert shrubs, which are the dominant plant type in the vast majority of deserts around the world, are sparsely distributed. This sparse distribution of shrubs, coupled with the open canopies of the shrubs means that variability of the soil background will be very significant in the reflected spectrum in arid regions. The nature of the soil "noise," which is partially due to non-linear spectral mixing, will be different than that observed in humid regions because very little light physically passes through the leaves in arid plants, while significant amounts pass through humid plant leaves (Roberts *et al.*, 1994). There is high variability in the nature, appearance, and behavior of arid vegetation with respect to recent rainfall. There are also significant variations in the appearance of plants due to seasonal effects. Lastly, spectral characteristics differ significantly between shrub types.

Thus, standard remote sensing vegetation indices are unsuitable for the accurate measurement of vegetation cover in arid regions. Monitoring vegetation in arid regions will require vegetation indices specifically designed for use in arid regions. In addition, the large degree of variability in the spectral characteristics of different types of arid shrubs requires that the vegetation indices be designed and used in conjunction with knowledge of the vegetation in the area being monitored. This knowledge is best gathered through the collection of in-situ spectra of plants which occur in the area of interest and of various plant components such as leaves and twigs. An index designed for use in the Southwestern U. S. in areas dominated by bursage and creosote bush may perhaps not be directly suitable in the Sahel, which has a different plant community; indeed, this is an important question for subsequent research.

In areas which are dominated by two types of shrubs, such as the Manix Basin Area, two complementary vegetation indices are desired. The first index would be relatively insensitive to changes in the type of vegetation, and this index would provide a gross estimate of the plant cover. The second index would be one sensitive to the two different types of plants, and it would be used in conjunction with the first index to determine the changes in the percentage abundance of dominant type of plant in the area being observed. In the case of the creosote bush—bursage community which occurs in the Manix Basin Area (and a great deal of the Mojave desert), a narrow-band version of the Modified Soil-Adjusted Vegetation Index (MSAVI) with additional narrow bands emphasizing the difference between the reflectance on either side of the chlorophyll bump at 0.55 μm would probably satisfy the requirements for the first index. The smaller difference between the chlorophyll absorption at 0.675 μm and the pigment absorption between 0.45 and 0.50 μm for creosote bush compared to bursage will counterbalance the higher MSAVI values for creosote bush compared to bursage. This index would be relatively insensitive to both season and rainfall because both bursage and creosote bush exhibit similar changes from their respective baseline spectra during the dry season. Thus, smaller values of the difference between the pigment absorptions for creosote bush than bursage would be maintained irrespective of season and rainfall. A complementary vegetation index which differs markedly for bursage and creosote bush, such as an augmented NDVI, would then be used to estimate the level of cover by each plant type. Repeated analyses could then be used to determine of the relative abundance of each plant type has changed.

Monitoring over the growing season will enable the signature of ephemeral plants to be untangled from measurements of changes in the cover of perennials. Many annuals, such as Russian Thistle in the Southwestern U. S., are extremely green during their peak growing phase. The vegetation cover measured when they are active will confuse the effects of degradation on the perennials. More importantly, areas experiencing degradation may become dominated by these annual invader species. Thus, the unraveling of annual plant signatures from that of perennials, will identify areas where annuals dominate and where degradation is indicated. Observations which occur within the first few weeks after a rain will identify the effects of the re-greening of vegetation during wet periods, and allow this type of "noise" to be eliminated from the measurements.

The non-linear mixing which can occur in the spectra of arid region plants also requires attention. Although this may only lead to a few percent of error in measurements over the size of an AVIRIS or Landsat pixel, the very small changes which must be observed in the satellite data to detect subtle changes in vegetation cover requires that this error be further reduced. In order to achieve this, spectra of the various components of the plants present in the field area must be coupled with the spectra of soil in the area under observation to develop models of the light scattering within the plant canopies and between the plant canopies and the soil. In addition to the spectra of the various components, statistical studies of the canopies of various plant types will be needed to improve the modeling of non-linear effects. However, much useful monitoring can be performed before accurate non-linear modeling has been completed as part of a mature monitoring effort.

Part 7.5: *Monitoring System Requirements*

The vegetation indices outlined in the previous section are a key technical component of an arid region monitoring system. However, the essential preliminary need is an up-front commitment to monitoring (Rodenberg, 1991; Murray *et al.*, 1994). Simply having a satellite in orbit spewing out data will not provide for monitoring arid regions. The motivation must be both philosophical and financial. Although an improved understanding of the surficial processes would be one of the dividends provided by a satellite remote sensing system producing data for arid regions around the world, the driving reason for the existence of the monitoring satellite must be to provide useful information for individuals and organizations whose decisions and actions affect both current renewable resources and also the future potential of arid regions. Additionally, financial support must be available to groups and organizations which will use the data for monitoring. Data and information produced by the monitoring system must be made widely and readily available to all users. The powers of multimedia computers and other means of scientific visualization, such as the production of videos, should be used to broadly disseminate the results of the monitoring.

The satellite instrument used for the monitoring system must be very well calibrated. Accurate measurement of arid vegetation cover makes calibration to with 5% absolute reflectance a necessity. Spatial resolution at the level of Landsat MSS or slightly coarser (between 50 and 200 m) will be needed. At least a weekly repeat cycle is desired in order to provide useful (cloud-free) repeat coverage comparable to the Landsat repeat

cycle (21 days). Although an imaging spectrometer covering the spectral range from 0.4–1.0 μm at the 10 nm spectral resolution of AVIRIS would be most highly desirable, an efficient system providing narrow bands centered at 0.45, 0.475, 0.5, 0.55, 0.59, 0.615, 0.675, 0.75, and 0.85 μm are the minimum requirements to monitor the key pigment features in vegetation.

The satellite instruments outlined in part 7.3 do not meet these requirements. Although SeaWIFs and the ADEOS OCTS (Ocean Color and Temperature Scanner) provide a number of narrow spectral bands between 0.4 and 1.0 μm, their spatial resolution of 1 km (SeaWIFs) and 700 m (OCTS) are too coarse. Furthermore, these instruments have been designed to look at the ocean, which is a dark and fairly homogeneous surface. In contrast, the bright land surface will either blind these instruments or be incorrectly measured due to non-optimum gain settings such as those of SeaWIFs. However, SeaWIFs and ADEOS OCTS provide bands which can be used for research to help develop a remote sensing vegetation index utilizing the pigment absorptions. ADEOS AVNIR (Advanced Visible and Near-Infrared Radiometer) is designed to look at the land surface and has more than adequate spatial resolution (16 m in multispectral mode), but the spectral resolution of this instrument is not much greater than what is provided by Landsat Thematic Mapper. MODIS provides good spectral resolution and it is designed to look at the land surface, but the spatial resolution of no better than 250 m is inadequate for monitoring arid regions. The Lewis & Clark system is the best of the upcoming systems, providing 30 m spatial resolution and a large number of bands in the VNIR. The repeat cycle of 16 days is only adequate if the target under

observation has clear sky conditions the vast majority of the time. Lewis & Clark also has the advantage of being a pushbroom scanner which simplifies the co-registration task by avoiding cross-track scanning distortions. The 5 m panchromatic band provides the ability to do very precise measurements of the size of areas of active windblown sand.

Satellite data alone are not enough to perform adequate monitoring. Focused and continuing on-site observations will be required to provide ground truth for the satellite remote sensing system, and certain well-studied areas will be necessary as "calibration" sites. Local rainfall and wind data must be incorporated into the monitoring system in order to help identify changes in both the remotely sensed and in-situ data due to rainfall variations and changes in the wind regime. Additionally, the solar data collected by stations such as those operated by the National Renewable Energy Laboratory, especially the broad-band optical depth measurements, would be an addition helpful to the calibration of the satellite data.

Table 26: Characteristics of Satellite for Arid Region Monitoring	
Characteristic	**Desired Values**
Spectral Region	Visible/Near-Infrared (0.4–1.0 μm)
Repeat Cycle	Weekly
Spatial Resolution	50–200 m
Spectral Band Centers (μm)	0.450, 0.475, 0.500, 0.550, 0.590, 0.615, 0.675, 0.750, 0.850
Spectral Band Width (μm)	0.010
Calibration	<5% Absolute Apparent Reflectance
Precision	~1% within band
Positional Knowledge (Georeferenced)	50–200m
Duration	Indefinite, or Replaced

Part 7.6: *From Science Process Study to Monitoring*

The research presented in this thesis is a beginning of the evolution from traditional process studies to affordable monitoring. The next step required is further work on the development of a vegetation index suitable for arid regions. This requires the further analysis of field spectral data of plants and plant materials such as those discussed in chapter 5. The work presented in this thesis indicates that an index based on the difference between the reflectance on either side of the 0.55 μm chlorophyll bump coupled with a narrow-band version of MSAVI is the best possibility for an index to measure the level of vegetation cover. Investigations to further refine arid region vegetation indices should focus on the combined use of the red edge and the pigment features in the visible wavelengths.

Further analysis of the non-linear mixing problem is also required. The procedure for doing this was outlined in part 7.5. From the modeling of individual shrubs models or pixels dotted by scattered shrub canopies can be developed to allow the prediction of the spectrum observed for a given level of vegetation cover.

In-situ measurements of plant cover in control regions through either numerous surface traverses or a smaller number of surface traverses augmented by low-level aerial photography can be combined with laboratory spectra and the non-linear mixture model above to predict what a remote sensing system will observe. These predictions must be compared with the remote sensing observations to calibrate the vegetation indices and assess whether the model-based indices will work with real remote sensing data. This may

be combined with overflights of airborne systems, such as AVIRIS, whose calibration may be better understood than that of the satellite observing system.

Historical remote sensing data should be used to gain an understanding of the temporal changes which have occurred in the areas being monitored. This will help to establish the baseline required for comparison with future monitoring data. The identity and nature of the processes of land degradation at work in the areas will be revealed by the historical data, and this will help focus both in-situ observations and the analysis of future remote sensing data. This use of historical remote sensing data should be combined with historical meteorological data to understand how the remote observations are affected by rainfall and wind.

These observations will establish the baseline required for monitoring. Areas suitable for use as "unchanging" targets for calibration must also be identified in the region under observation, and in-situ spectra of these targets should be collected periodically. A set of identifiable targets which can be used for co-registration should be identified and an effective algorithm should be developed to locate them in the remote images. This effort in identifying and automatic location of tiepoints will reduce the human labor required for co-registration.

The co-registered and calibrated monitoring data can be combined with the vegetation indices designed for the areas being monitored to measure changes in vegetation cover related to degradation. These changes in vegetation cover can then be related to the processes of land degradation identified for the area from the use of in-situ observation and historical data. This information may then be used by the people making

decisions about how the land is to be used. Such a monitoring system will enable better maintenance of the land's productive capacity and enable the continued support of the Earth's population.

Appendix A: *MSS X-format Tapes*

Pre-1978 MSS data are released in a format referred to as X-format. This format is rather obscure and the documentation available from the EROS Data Center take this confusing format and explain it in the most confusing way possible. Although there are a few software programs still available for dealing directly with these data, e.g. VERTSLOG in the JPL VICAR image processing system, most usually the user is confronted with a confusing format and opaque documentation. Also, if the few existing programs for use with X-format data run into an unexpected problem, the user is confronted with either deciphering and understanding a 1970's vintage computer program (VERTSLOG was originally written in assembly language in 1972) or puzzling out the format. The data tapes consist of five variable-block data files. The first four files are image files, and the remaining file consists of various ancilliary data. Most modern computer programs for reading tapes assume that the tapes are fixed-block tapes (each tape record or block is a set number of bytes). In the image files, all but the first two records (the first two tapes records are the header) are 3320 bytes long, and most programs for reading tapes can be ordered to pad all records to a fixed number of bytes.

To understand how the four image files are laid out, imagine taking a stack of four photographs, and cutting the stack into four vertical strips of equal width. The first image file consists of the leftmost vertical strips of each image interleaved by pixel pair (BIP-2), the second image file is the set of vertical strips immediately to the right of the first set, etc. BIP-2 format means that each 8-bit sequence in the image files contains the DN

values in each of the four bands for a pair of adjacent pixels. Starting with the first of the 8 bits, we have: DN(Band5,pixelA), DN(Band4,pixelB), DN(Band5,pixelA), DN(Band5,pixelB), DN(Band6,pixelA), DN(Band6,pixelB), DN(Band7,pixelA), DN(Band7,pixelB). The files are then arranged into lines (one line per tape block) which are 3320 bytes long. The basic idea is to read through the image file sequentially and separate the pixel pairs into four single-band image strips.

There are some catches. First, sometimes the header records will sometimes be completely absent. Second, there are 56 extra bytes at the end of each line in the tape image file. These last 56 pixels are engineering calibration data and synthetic pixels, which are not generally of use to the user. Third, X-Format Landsat pixels are NOT square, they are oblong. An X-format pixel nominally covers 79 m in the line dimension (top to bottom of image) and 57 m in the sample direction (left to right). Finally, the image formed using the four image strips are rectangular, but the rotation of the Earth beneath the satellite causes a one pixel displacement every 18 image lines, making the actual image boundary a parallelogram.

Basic Procedure: Take image file 1. Skip the header records (0 to 2 of them). The first byte is the first pixel of the first quarter-line of the Band 1 image. The second byte is the second pixel of the first quarter-line of the Band 1 image. The third byte is the first pixel of the first quarter-line of the Band 2 image, etc. By following this pattern, the first strip of the image (816 samples by 2340 lines) can be built. Then follow the same scheme for each image file. Then use some matrix operation to lay the strips next to each other.

This yields a 3264 by 2340 rectangular image. Make the pixels 79m square by compressing the image in the x-direction (left to right). This results in an image about 2305 samples by 2340 lines. Now add 130 blanks (0 bytes) to the start of the first line. Add this same number of blanks to each of the first 18 lines. Add 129 blanks to the start of line 19 and one blank at the end. Do this to each of lines 19 through 36. On line 37 add 128 blanks to the start and 2 to the end, etc. The finalt result is a 2435 by 2340 Landsat MSS image with a nominal pixel resolution of 79 m.

Appendix B: *A FAQ on Vegetation in Remote Sensing*

The following document is an internet FAQ (frequently asked questions) list which was written after several questions on the topic were raised on the internet mailing list IMAGRS-L which is a mailing list concerned with image processing and remote sensing. This document is produced in its entirety as it appears on the internet including its reference list. This document was revised based on comments from members of the mailing list and discussion with A. Chehbouni at ORSTOM. Requests for permission to republish parts or all of this document have been received from remote sensing newsletters in Spain and Great Britain and from the publishers of the ERDAS image processing software system for inclusion in a handbook distributed with their software.

A FAQ on Vegetation in Remote Sensing

Written by Terrill W. Ray
Div. of Geological and Planetary Sciences
California Institute of Technology

email: terrill@mars1.gps.caltech.edu

Snail Mail: Terrill Ray
Division of Geological and Planetary Sciences
Caltech
Mail Code 170-25
Pasadena, CA 91125

THIS FAQ AVAILABLE VIA ANONYMOUS FTP AT:

kepler.gps.caltech.edu - /pub/terrill/rsvegfaq.txt

Version 1.0: 10/13/1994

Acknowledgements: Thanks to the following people for comments and
suggestions (listed in no particular order)

A. Chehbouni - ORSTOM
Martin Hugh-Jones - Louisiana State University
Kjeld Rasmussen -

Revision History:
Version 1.0 - major revision. Discussion of radiance vs. reflectance added. Addition of vegetation indices designed to minimize atmospheric noise (GEMI, ARVI, etc.). Addition of SPOT HRV bands. Numerous minor changes. Cautions regarding the use of SAVI, MSAVI, etc. added.
Version 0.7 - numerous minor non-substantive typos fixed. Addition of question 14a. Some stylistic and grammatical problems dealt with.
Version 0.6 - major typo in TSAVI equation fixed and minor typo in MSAVI2 fixed.
Version 0.5 - original version posted

Conventions:
In most cases, reflectance, apparent reflectance and radiance can be used interchangeably in this FAQ. (But see question #5 for some important considerations about this.)
Wavelengths are given in nanometers (nm).
The "origin" is the point of zero red reflectance and zero near-infrared reflectance.
The abbreviation SPOT refers to the Systeme Pour l'Observation de la Terre which has five bands of interest (the bandpasses may not be precisely correct since the document I am looking at lists the "proposed" bands)
SPOT1 covers 430-470 nm
SPOT2 covers 500-590 nm
SPOT3 covers 610-680 nm
SPOT4 covers 790-890 nm
SPOT5 covers 1580-1750 nm
The abbreviation AVHRR refers to the Advanced Very High Resolution Radiometer which has two bands of interest:
AVHRR1 covers 550-700 nm
AVHRR2 covers 700-1000 nm
The abbreviation TM refers to the Landsat Thematic Mapper which has six bands of interest:
TM1 covers 450-520 nm
TM2 covers 520-600 nm
TM3 covers 630-690 nm
TM4 covers 760-900 nm

TM5 covers 1550-1750 nm
TM7 covers 2080-2350 nm

The abbreviation MSS refers to the Landsat MultiSpectral Scanner.

MSS bands are referred to by the old system:
MSS4 covers 500-600 nm
MSS5 covers 600-700 nm
MSS6 covers 700-800 nm
MSS7 covers 800-1100 nm

NIR is used to indicate a band covering all or part of the near-infrared portion of the spectrum (800-1100 nm or a subset of these wavelengths). Examples: MSS7, TM4, AVHRR2

R is used to indicate a band covering all or part of the portion of the visible spectrum perceived as red by the human eye (600-700 nm). Examples MSS5, TM3, AVHRR1

Questions:

GENERAL

1) What are the important spectral characteristics of vegetation that I should know about?
2) I have some remote sensing data, what bands will show vegetation best?
   2a) TM data
   2b) MSS data
3) I want to use band ratioing to eliminate albedo effects and shadows. What band ratios are best?
   3a) TM data
   3b) MSS data
4) Why is vegetation usually shown in red by remote sensing people?
5) What is the difference between radiance and reflectance?

VEGETATION INDEX

6) What the &*(^ is a vegetation index?
7) What are the basic assumptions made by the vegetation indices?
8) What is the soil line and how do I find it?

BASIC INDICES

9) What is RVI?
10) What is NDVI?
11) What is IPVI?
12) What is DVI?
13) What is PVI?
14) What is WDVI?

INDICES TO MINIMIZE SOIL NOISE

15) What is Soil Noise?
16) What is SAVI?
16a) Why is there a (1+L) term in SAVI?
17) What is TSAVI?
18) What is MSAVI?
19) What is MSAVI2?

INDICES TO MINIMIZE ATMOSPHERIC NOISE

20) What is Atmospheric Noise?
21) What is GEMI?

GENERAL

1) What are the important spectral characteristics of vegetation that I should know about?
A: The cells in plant leaves are very effective scatterers of light because of the high contrast in the index of refraction between the water-rich cell contents and the intercellular air spaces. Vegetation is very dark in the visible (400-700 nm) because of the high absorption of pigments which occur in leaves (chlorophyll, protochlorophyll, xanthophyll, etc.). There is a slight increase in reflectivity around 550 nm (visible green) because the pigments are least absorptive there. In the spectral range 700-1300 nm plants are very bright because this is a spectral no-man's land between the electronic transitions which provide absorption in the visible and molecular vibrations which absorb in longer wavelengths. There is no strong absorption in this spectral range, but the plant scatters strongly as mentioned above.

From 1300 nm to about 2500 nm vegetation is relatively dark, primarily because of the absorption by leaf water. Cellulose, lignin, and other plant materials also absorb in this spectral range.

SUMMARY: 400-700 nm = dark
700-1300 nm = bright
1300-2500 nm = dark (but brighter than 400-700 nm)

2) I have some remote sensing data, what bands will show vegetation best?
A: Basically a band covering part of the region from 700-1300 nm if you want the vegetation to be bright. (Using a band covering part of 400-700 nm would make vegetation dark, but this isn't the way we generally do things.)
2A) For TM data, either TM4 or TM5
2B) For MSS data, either MSS6 or MSS7 (MSS7 is usually better since

it avoids the transition near 700 nm).

3) I want to use band ratioing to eliminate albedo effects and shadows. What band ratios are best?
A: If you want the vegetation to turn out bright (which is usually the most sensible approach) ratio a band covering part of the range 700-1300 nm with a band covering either 400-700 nm or 1300-2500 nm. Ratioing a near-infrared band to a visible band is the traditional approach. Usually a visible band covering 650 nm is preferred since this is near the darkest part of the vegetation spectrum usually covered by remote sensing instruments. Basically you want a band where vegetation is bright on the top of the ratio, and a band where vegetation is dark on the bottom.

Although vegetation is more highly reflective in green than in red, early work showed that near-infrared-red combinations were preferable to green-red combinations (Tucker, 1979).

3A) TM: The traditional ratio is TM4/TM3
TM5/TM7 is also good, but many clays will also be fairly bright with this combination.
I see no immediate reason why TM5/TM3 or TM4/TM7 wouldn't work, but they usually aren't used.

3B) MSS: The traditional ratio is MSS7/MSS5
MSS6/MSS5 is also used.

4) Why is vegetation usually shown in red by remote sensing people?
A: This is one of the apparently silly things done in remote sensing. There are three reasons for it:
The first (and rather pointless) reason is TRADITION. People in remote sensing have been doing this a long time and virtually everyone who has spent much time working with remote sensing will instinctively interpret red splotches as vegetation. Bob Crippen (not the astronaut) at JPL said that he spent some time trying to break this tradition by showing vegetation in green, but he was ultimately beaten into submission. (Consider it this way: you are a remote sensing professional, you usually give talks to remote sensing professionals. They expect vegetation in red so you don't have to add an explanation that "vegetation is shown as green." This simplifies your life.)

The second reason is the fact that the human eye perceives the longest visible wavelengths to be red and the shortest visible wavelengths to be blue. This is an incentive for remote sensing images to be set up so that the shortest wavelength is shown as blue and the longest one is shown as red. Usually a near-infrared band is the longest wavelength being displayed (this is especially true for MSS and aerial color infrared photography). Since vegetation is brightest in the near-infrared, vegetation turns out red. Using red for vegetation in digital data makes the digital data color scheme similar to that for color infrared film. This can make it easier for a person familiar with color infrared film pictures to adjust to the interpretation of digital remote sensing data.

The third (and only sensible) reason is to remind the audience that they are not seeing real colors. If vegetation is shown as green, the audience is more likely to subconsciously think that the image is true color, while if vegetation is red they will immediately

realize that the image is false color.

5) What is the difference between radiance and reflectance?
A: Radiance is the variable directly measured by remote sensing instruments. Basically, you can think of radiance as how much light the instrument "sees" from the object being observed. When looking through an atmosphere, some light scattered by the atmosphere will be seen by the instrument and included in the observed radiance of the target. An atmosphere will also absorb light, which will decrease the observed radiance. Radiance has units of watt/steradian/square meter.

Reflectance is the ratio of the amount of light leaving a target to the amount of light striking the target. It has no units. If all of the light leaving the target is intercepted for the measurement of reflectance, the result is called "hemispherical reflectance."

Reflectance (or more specifically hemispherical reflectance) is a property of the material being observed. Radiance, on the other hand, depends on the illumination (both its intensity and direction), the orientation and position of the target and the path of the light through the atmophere. With effort, many of the atmospheric effects and the solar illumination can be compensated for in digital remote sensing data. This yields something which is called "apparent reflectance," and it differs from true reflectance in that shadows and directional effects on reflectance have not been dealt with. Many people refer to this (rather inaccurately) as "reflectance."

For most of the vegetation indices in this FAQ, radiance, reflectance, and apparent reflectance can be used interchangibly. However, since reflectance is a property of the target material itself, you will get the most reliable (and repeatable) vegetation index values using reflectance. Apparent reflectance is adequate in many cases.

VEGETATION INDEX

6) What the &*(^ is a vegetation index?
A: A vegetation index is a number that is generated by some combination of remote sensing bands and may have some relationship to the amount of vegetation in a given image pixel. If that sounds sarcastic or even insulting, it's meant to. Jim Westphal at Caltech pointed out to me one day that vegetation indices seemed to be more numerology than science. This may be an overly harsh assessment, since there is some basis for vegetation indices in terms of the features of the vegetation spectrum discussed above; however, the literature indicates that these vegetation indices are generally based on empirical evidence and not basic biology, chemistry or physics. This should be kept in mind as you use these indices.

7) What are the basic assumptions made by the vegetation indices?
A: The most basic assumption made is assuming that some algebraic combination of remotely-sensed spectral bands can tell you something useful about vegetation. There is fairly good empirical evidence that they can.

A second assumption is the idea that all bare soil in an image will form a line in spectral space. This is related to the concept

of the soil line discussed in question number 7. Nearly all of the commonly used vegetation indices are only concerned with red-near-infrared space, so a red-near-infrared line for bare soil is assumed. This line is considered to be the line of zero vegetation.

At this point, there are two divergent lines of thinking about the orientation of lines of equal vegetation (isovegetation lines):

1) All isovegetation lines converge at a single point. The indices that use this assumption are the "ratio-based" indices, which measure the slope of the line between the point of convergence and the red-NIR point of the pixel. Some examples are: NDVI, SAVI, and RVI

2) All isovegetation lines remain parallel to soil line. These indices are typically called "perpendicular" indices and they measure the perpendicular distance from the soil line to the red-NIR point of the pixel. Examples are: PVI, WDVI, and DVI.

8) What is the soil line and how do I find it?

A) The soil line is a hypothetical line in spectral space that describes the variation in the spectrum of bare soil in the image. The line can be found by locating two or more patches of bare soil in the image having different reflectivities and finding the best fit line in spectral space. Kauth and Thomas (1976) described the famous "triangular, cap shaped region with a tassel" in red-NIR space using MSS data. They found that the point of the cap (which lies at low red reflectance and high NIR reflectance) represented regions of high vegetation and that the flat side of the cap directly opposite the point represented bare soil.

THE SIMPLE WAY OF FINDING THE RED-NIR SOIL LINE: Make a scatterplot of the red and NIR values for the pixels in the image. I recommend putting red on the x-axis and NIR on the y-axis (the rest of the instructions assume this). There should be a fairly linear boundary along the lower right side of the scatterplot. The straight line that best matches this boundary is your soil line. You can either select the points that describe the boundary and do a least squares fit, or you can simply made a hardcopy and draw in the line that looks like the best fit. (You have to make a lot of judgment calls either way.)

9) What is RVI?

A) RVI is the ratio vegetation index which was first described by Jordan (1969). This is the most widely calculated vegetation index, although you rarely hear of it as a vegetation index. A common practice in remote sensing is the use of band ratios to eliminate various albedo effects. Many people use the ratio of NIR to red as the vegetation component of the scene, and this is in fact the RVI.

SUMMARY: ratio-based index

isovegetation lines converge at origin

soil line has slope of 1 and passes through origin.

range 0 to infinity

CALCULATING RVI:

$$RVI = \frac{NIR}{red}$$

10) What is NDVI?
A) NDVI is the Normalized Difference Vegetation Index which is ascribed to Rouse et al. (1973), but the concept of a normalized difference index was first presented by Kriegler et al. (1969). When people say vegetation index, this is the one that they are usually referring to. This index has the advantage of varying between -1 and 1, while the RVI ranges from 0 to infinity. RVI and NDVI are functionally equivalent and related to each other by the following equation:

$$NDVI = \frac{RVI-1}{RVI+1}$$

SUMMARY: ratio-based index
isovegetation lines converge at origin
soil line has slope of 1 and passes through origin
range -1 to +1
CALCULATING THE NDVI:

$$NDVI = \frac{NIR-red}{NIR+red}$$

11) What is IPVI?
A) IPVI is the Infrared Percentage Vegetation Index which was first described by Crippen (1990). Crippen found that the subtraction of the red in the numerator was irrelevant, and proposed this index as a way of improving calculation speed. It also is restricted to values between 0 and 1, which eliminates the need for storing a sign for the vegetation index values, and it eliminates the conceptual strangeness of negative values for vegetation indices. IPVI and NDVI are functionally equivalent and related to each other by the following equation:

$$IPVI = \frac{NDVI+1}{2}$$

SUMMARY: ratio-based index
isovegetation lines converge at origin
soil line has a slope of 1 and passes through origin
range 0 to +1
CALCULATING IPVI:

$$IPVI = \frac{NIR}{NIR+red}$$

12) What is DVI?
A) DVI is the Difference Vegetation Index, which is ascribed in some recent papers to Richardson and Everitt (1992), but appears as VI (vegetation index) in Lillesand and Kiefer (1987). [Lillesand and Kiefer refer to its common use, so it was certainly introduced earlier, but they do not give a specific reference.]
SUMMARY: perpendicular index
isovegetation lines parallel to soil line
soil line has arbitrary slope and passes through origin
range infinite.

CALCULATING DVI:

DVI=NIR-red

13) What is PVI?

A) PVI is the Perpendicular Vegetation Index which was first described by Richardson and Wiegand (1977). This could be considered a generalization of the DVI which allows for soil lines of different slopes. PVI is quite sensitive to atmospheric variations, (Qi et al., 1994) so comparing PVI values for data taken at different dates is hazardous unless an atmospheric correction is performed on the data.

SUMMARY: perpendicular index

isovegetation lines are parallel to soil line

soil line has arbitrary slope and passes through origin

range -1 to +1

CALCULATING PVI:

PVI = sin(a)NIR-cos(a)red

a is the angle between the soil line and the NIR axis.

14) What is WDVI?

A) WDVI is the Weighted Difference Vegetation Index which was introduced by Clevers (1988). This has a relationship to PVI similar to the relationship IPVI has to NDVI. WDVI is a mathematically simpler version of PVI, but it has an unrestricted range. Like PVI, WDVI is very sensitive to atmospheric variations (Qi et al., 1994).

SUMMARY: perpendicular index

isovegetation lines parallel to soil line

soil line has arbitrary slope and passes through origin

range infinite

CALCULATING WDVI:

WDVI = NIR-g*red

g is the slope of the soil line.

INDICES TO MINIMIZE SOIL NOISE

15) What is Soil Noise?

A) Not all soils are alike. Different soils have different reflectance spectra. As discussed above, all of the vegetation indices assume that there is a soil line, where there is a single slope in red-NIR space. However, it is often the case that there are soils with different red-NIR slopes in a single image. Also, if the assumption about the isovegetation lines (parallel or intercepting at the origin) is not exactly right, changes in soil moisture (which move along isovegetation lines) will give incorrect answers for the vegetation index. The problem of soil noise is most acute when vegetation cover is low.

The following group of indices attempt to reduce soil noise by altering the behavior of the isovegetation lines. All of them are ratio-based, and the way that they attempt to reduce soil noise is by shifting the place where the isovegetation lines meet.

WARNING: These indices reduce soil noise at the cost of decreasing the dynamic range of the index. These indices are slightly

less sensitive to changes in vegetation cover than NDVI (but more sensitive than PVI) at low levels of vegetation cover. These indices are also more sensitive to atmospheric variations than NDVI (but less so than PVI). (See Qi et al. (1994) for comparisons.)

16) What is SAVI?
A) SAVI is the Soil Adjusted Vegetation Index which was introduced by Huete (1988). This index attempts to be a hybrid between the ratio-based indices and the perpendicular indices. The reasoning behind this index acknowledges that the isovegetation lines are not parallel, and that they do not all converge at a single point. The initial construction of this index was based on measurements of cotton and range grass canopies with dark and light soil backgrounds, and the adjustment factor L was found by trial and error until a factor that gave equal vegetation index results for the dark and light soils was found. The result is a ratio-based index where the point of convergence is not the origin. The convergence point ends up being in the quadrant of negative NIR and red values, which causes the isovegetation lines to be more parallel in the region of positive NIR and red values than is the case for RVI, NDVI, and IPVI.

Huete (1988) does present a theoretical basis for this index based on simple radiative transfer, so SAVI probably has one of the better theoretical backgrounds of the vegetation indices. However, the theoretical development gives a significantly different correction factor for a leaf area index of 1 (0.5) than resulted from the empirical development for the same leaf area index (0.75). The correction factor was found to vary between 0 for very high densities to 1 for very low densities. The standard value typically used in most applications is 0.5 which is for intermediate vegetation densities.

SUMMARY: ratio-based index
isovegetation lines converge in negative red, negative NIR quadrant
soil line has slope of 1 and passes through origin.
range -1 to +1

CALCULATING SAVI:

$$SAVI = \frac{NIR-red}{NIR+red+L}(1+L)$$

where L is a correction factor which ranges from 0 for very high vegetation cover to 1 for very low vegetation cover. The most typically used value is 0.5 which is for intermediate vegetation cover.

16a) Why is there a (1+L) term in SAVI?
A) This multiplicative term is present in SAVI (and MSAVI) to cause the range of the vegetation index to be from -1 to +1. This is done so that both vegetation indices reduce to NDVI when the adjustment factor L goes to zero.

17) What is TSAVI?
A) TSAVI is the Transformed Soil Adjusted Vegetation Index which

was developed by Baret et al. (1989) and Baret and Guyot (1991). This index assumes that the soil line has arbitrary slope and intercept, and it makes use of these values to adjust the vegetation index. This would be a nice way of escaping the arbitrariness of the L in SAVI if an additional adjustment parameter had not been included in the index. The parameter "X" was "adjusted so as to minimize the soil background effect," but I have not yet been able to come up with an a priory, non-arbitrary way of finding the parameter. The value reported in the papers is 0.08. The convergence point of the isovegetation lines lies between the origin and the usually-used SAVI convergence point (for L = 0.5)

SUMMARY: Ratio-based index
isovegetation lines converge in negative red, negative NIR quadrant
soil line has arbitrary slope and intercept.
range -1 to +1

CALCULATING TSAVI:

$$TSAVI = \frac{s(NIR - s*red - a)}{(a*NIR + red - a*s + X*(1+s*s))}$$

where a is the soil line intercept, s is the soil line slope, and X is an adjustment factor which is set to minimize soil noise (0.08 in original papers).

18) What is MSAVI?

A) MSAVI is the Modified Soil Adjusted Vegetation Index which was developed by Qi et al. (1994). As noted previously, the adjustment factor L for SAVI depends on the level of vegetation cover being observed which leads to the circular problem of needing to know the vegetation cover before calculating the vegetation index which is what gives you the vegetation cover. The basic idea of MSAVI was to provide a variable correction factor L. The correction factor used is based on the product of NDVI and WDVI. This means that the isovegetation lines do not converge to a single point.

SUMMARY: ratio-based index
isovegetation lines cross the soil line at different points
soil line has arbitrary slope and passes through origin
range -1 to +1

CALCULATING MSAVI:

$$MSAVI = \frac{NIR - red}{NIR + red + L}(1+L)$$

where L = 1 - 2*s*NDVI*WDVI
and s is the slope of the soil line.

19) What is MSAVI2?

A) MSAVI2 is the second Modified Soil Adjusted Vegetation Index which was developed by Qi et al. (1994) as a recursion of MSAVI. Basically, they use an iterative process and substitute 1-MSAVI(n-1) as the L factor in MSAVI(n). They then inductively solve the iteration where MSAVI(n)=MSAVI(n-1). In the process, the need to

precalculate WDVI and NDVI and the need to find the soil line are eliminated.

SUMMARY: ratio-based
isovegetation lines cross the soil line at varying points.
soil line has arbitrary slope and passes through origin
range -1 to +1

CALCULATING MSAVI2:

MSAVI2 = (1/2)*(2(NIR+1)-sqrt((2*NIR+1)^2-8(NIR-red)))

where ^2 signifies the squaring of the value and sqrt() is the square-root operator.

INDICES TO MINIMIZE ATMOSPHERIC NOISE

20) What is Atmospheric Noise?

A) The atmosphere is changing all of the time and all remote sensing instruments have to look through it. The atmosphere both attenuates light passing through it and scatters light from suspended aerosols. The atmosphere can vary strongly across a single scene, especially in areas with high relief. This alters the light seen by the instrument and can cause variations in the calculated values of vegetation indices. This is particularly a problem for comparing vegetation index values for different dates. The following indices try to remedy this problem without the requirement of atmospherically corrected data.

WARNING: These indices achieve their reduced sensitivity to the atmosphere by decreasing the dynamic range. They are generally slightly less sensitive to changes in vegetation cover than NDVI. At low levels they are very sensitive to the soil background. (See Qi et al. (1994) for comparisons.)

NOTE: I seldom work with data without performing an atmospheric correction, so I have made no significant use of any of the indices in this section (T. Ray).

21) What is GEMI?

A) GEMI is the Global Environmental Monitoring Index which was developed by Pinty and Verstraete (1991). They attempt to eliminate the need for a detailed atmospheric correction by constructing a "stock" atmospheric correction for the vegetation index. Pinty and Verstraete (1991) provide no detailed reasoning for this index other than that it meets their requirements of insensitivity to the atmosphere empirically. A paper by Leprieur et al. (1994) claims to find that GEMI is superior to other indices for satellite measurements. However, A. Chehbouni (who happens to be the fourth author of Leprieur et al. (1994)) showed me some examples using real data (the analysis in the paper was based on a model) which strongly contradicted the Leprieur et al. (1994) conclusions. Qi et al. (1994) shows a violent breakdown of GEMI with respect to soil noise at low vegetation covers. I understand that there are several ongoing studies to evaluate GEMI, and I think that the jury is still out.

SUMMARY:
Non-linear
Complex vegetation isolines
Range 0 to +1

CALCULATING GEMI:

$$GEMI = eta*(1-0.25*eta)- \frac{red - 0.125}{1 - red}$$

where :

$$eta = \frac{2*(NIR^2-red^2)+1.5*NIR+0.5*red}{NIR + red + 0.5}$$

22) What are the atmospherically resistant indices?
A) The atmospherically resistant indices are a family of indices with built-in atmospheric corrections. The first of these was ARVI (Atmospherically Resistant Vegetation Index) which was introduced by Kaufman and Tanre (1992). They replaced the red reflectance in NDVI with the term:

$$rb = red - gamma (blue - red)$$

with a value of 1.0 for gamma. Kaufman and Tanre (1994) also suggested making the same substitution in SAVI which yields SARVI (Soil adjusted Atmospherically Resistant Vegetation Index). Qi et al. (1994) suggested the same substitution in MSAVI2 which yields ASVI (Atmosphere-Soil-Vegetation Index). Obviously the same substitution can also be made in MSAVI or TSAVI.

Qi et al. (1994) showed that this class of indices were very slightly more sensitive to changes in vegetation cover than GEMI and very slightly less sensitive to the atmosphere and the soil than GEMI for moderate to high vegetation cover. The atmospheric insensitivity and the insensitivity to soil break down violently for low vegetation cover.

SUMMARY:

ratio-based
isovegetation lines cross as assumed by parent index
soil line as assumed by parent index
range -1 to +1

CALCULATING ARVI:

$$ARVI = \frac{NIR-rb}{NIR+rb}$$

with rb defined as:

$$rb = red - gamma*(red - blue)$$

and gamma usually equal to 1.0

The parent index of ARVI is NDVI. The substitution of rb for red in any of the ratio-based indices gives the atmospherically resistant version of that index.

[NOTE: I view these indices for reducing atmospheric noise as late-evolving dinosaurs. The utility of a good atmospheric correction for remotely-sensed data is so high as to make the effort of performing

a proper atmospheric correction worthwhile. These end runs around this problem may serve a useful purpose at present while better atmospheric corrections for data collected over land are being developed. However, the move towards atmospheric correction of remote sensing data is underway, and it is almost certainly the wave of the future. - Terrill Ray]

OTHER INDICES

23) What is GVI?
A) GVI stands for Green Vegetation Index. There are several GVIs. The basic way these are devised is by using two or more soil points to define a soil line. Then a Gram-Schmidt orthogonalization is performed to find the "greenness" line which passes through the point of 100% (or very high) vegetation cover and is perpendicular to the soil line. The distance of the pixel spectrum in band space from the soil line along the "greenness" axis is the value of the vegetation index. The PVI is the 2-band version of this, Kauth and Thomas (1976) developed a 4-band version for MSS, Crist and Cicone (1984) developed a 6-band version for TM, and Jackson (1983) described how to construct the n-band version.
SUMMARY: perpendicular vegetation index using n bands
isovegetation lines are parallel to soil line.
soil line has arbitrary orientation in n-space
range -1 to +1
CALCULATING GVI:
Default version for MSS
GVI = -0.29*MSS4 - 0.56*MSS5 +0.60*MSS6+0.49*MSS7

Default version for TM
GVI = -0.2848*TM1-0.2435*TM2-.5436*TM3+0.7243*TM4+0.0840*TM5-
0.1800*TM7

24) Are there vegetation indices using other algebraic functions of the bands?
A) Yes. Rouse et al. (1973, 1974) proposed using the square root of NDVI+0.5, Goetz et al. (1975) proposed log ratios, Wecksung and Breedlove (1977) proposed arctangent ratios, and Tuck (1979) discussed the square root of the NIR/red ratio. These seem to have been generally abandoned. They make the same assumptions about the isovegetation lines and the soil lines as made by RVI and NDVI, and they have neither the value of common use or of ease of calculation. You will probably never see these, and there is really no good reason to bother with them.

25) Are there vegetation indices that use bands other than the red and NIR bands?
A) Yes. First, the various GVIs make use of more than just the NIR and red bands. In general, the GVI for a given multispectral sensor system uses all of the available bands. Secondly, there have been attempts to develop vegetation indices based on green and red bands as discussed in the next question.

Mike Steven at the University of Nottingham has recently informed me of some work on an index using NIR and mid-infrared

bands. More on this will be included when I have received a paper from him.

26) Plants are green, why isn't the green chlorophyll feature used directly.
A) There are several reasons for this. First, the reason that plants look so green is not because they are reflecting lots of green light, but because they are absorbing so much of the rest of the visible light. Try looking at an area of bare dry soil and compare that to a grassy field. You will immediately notice that the grassy field is generally darker. It is generally easier to detect things when they are bright against a dark background.

Second, this was tried early in the history of satellite remote sensing by Kanemasu (1974) and basically abandoned after a study by Tucker (1979) which seemed to demonstrate that the combinations of NIR and red were far superior than combinations of green and red. The idea of using red and green with MSS data was resurrected in recent years by Pickup et al. (1993) who proposed a PVI-like index using MSS bands 4 and 5 which they called PD54 (Perpendicular Distance MSS band 5 MSS band 4). They claimed a tassel cap like pattern in the scatterplot for these two bands, but most of the MSS data I have looked at doesn't show this pattern. A significant point for PD54 was that it detected non-green vegetation (dry grass).

Third, many soils have iron oxide absorption features in the visible wavelengths. As the soil gets obscured by vegetation cover, this feature becomes less apparent. It is likely that a great deal of the variance measured by the green-red indices is due to this instead of the plant chlorophyll feature (which is why PD54 might appear to be sensitive to non-green plant material). This is fine if you know that the iron oxide absorption in the soil is uniform across the image, but if the iron oxide absorption is highly variable, then this will confuse green-red indices.

PROBLEMS

27) How well do these vegetation indices work in areas with low vegetation cover?
A) Generally, very badly. When the vegetation cover is low, the spectrum observed by remote sensing is dominated by the soil. Not all soils have the same spectrum, even when fairly broad bands are being used. Both Huete et al. (1985) and Elvidge and Lyon (1985) showed that the soil background can have a profound impact and vegetation index values with bright backgrounds producing lower vegetation index values than dark backgrounds. Elvidge and Lyon (1985) showed that many background materials (soil, rock, plant litter) vary in their red-NIR slope, and these variations seriously impact measurements of vegetation indices. Then there is the problem of non-linear mixing.

28) What the ^&*(*&^ is "non-linear" mixing?
A) A lot of remote sensing analysis has been based on the concept of the Earth as spots covered by differently-colored paint. When the spots of paint get too small, they appear to blend together to

form a new color which is a simple mixture of the old colors. Consider an area covered by 50% small red spots and 50% small green spots. When we look at the surface from far enough away that we can't see the individual dots, we see the surface as yellow. Different proportions of red and green dots will produce different colors, and if we know that the surface is covered by red and green dots we can calculate what the proportions are based on the color we see. The important thing to know is that any light reaching the observer has only hit one of the colored dots. That is linear mixing.

Non-linear mixing occurs when light hits more than one of the colored dots. Imagine a surface with a lot of small, colored bumps which stick out varying distances from the surface. We can now image that light could bounce from one colored bump to another and then to the observer. Now some of the light coming from the green bump bounced off of a red bump first, and this light will have characteristics of both the red and green bumps. There is also light coming directly from the green bump that only bounced from the green bump. If we could see this individual green bump, it would not look as green as it should. Now, when the light from all of the bumps reaches the observer, the light looks different than when the bumps were simple spots even through the proportion of the area covered by each color is unchanged. (We are assuming that there are no shadows.)

A second way for non-linear mixing to happen is if light can pass through one material and then reflect off of another. Imagine a piece of translucent plastic with half of the area covered by randomly placed translucent green spots placed on top of a red surface. Now light can pass through a green spot on the plastic and then reflect off of the red below before returning to the observer. Once again, the interaction of the light with multiple spots along its path changes the character of the light coming from each spot. Once again the color looks different than the linear case, which is just the case when light cannot pass through green spots.

The basic point is that non-linear mixing twists the spectra of the materials being observed into different spectra which do not resemble any of the targets. This can magnify the apparent abundance of a material. Consider the piece of translucent plastic with the translucent green dots. If we put it on top of a low-reflectivity surface, very little of the light that passes through the green dots will be reflected back, so all we see is the light directly reflected from the green dots. Now we put a highly reflective surface behind it, and we see a brighter green because we now see both the light directly reflected from the dots and most of the light which has passed through the green dots (which is green) is reflecting back from the highly-reflective background. If we didn't know better, we might think that we just had more green dots instead of a brighter background.

29) Is the variation in the soil the only problem?
A) No. Many of the commonly studied areas with low vegetation cover are arid and semi-arid areas. Many plants which grow in such areas have a variety of adaptations for dealing with the lack of water and high temperatures. (Even plants growing in areas with

relatively cool air temperature have problems with heat regulation in dry climates since transpiration is the main way they keep cool.) These adaptations often decrease the amount of visible light absorbed by the plants and/or decrease the amount of sunlight striking the plants (hence the plants do not reflect as much light). These inherent qualities make arid and semi-arid vegetation hard to detect unless it is observed during periods of relatively abundant water when a whole new set of adaptations to maximize plant productivity takes effect.

30) What if I can't get a good soil line from my data?
A) If you're working in an area with high plant cover, this can be common. This makes it virtually impossible to use the perpendicular indices or things like TSAVI and MSAVI1. However, NDVI is at its best with high plant cover, so it is still available to you. The correction factor L for SAVI should be near 0 for this sort of situation, which makes SAVI equivalent to NDVI. MSAVI2 also need no soil line. If you really want to use an index which requires a soil line, you will need to construct it with field and laboratory spectra, but this is not an easy task, and really not advisable.

31) How low a plant cover is too low for these indices?
A) These are rules of thumb, your mileage may vary:

RVI, NDVI, IPVI = 30%
SAVI, MSAVI1, MSAVI2 = 15%
DVI = 30%
PVI, WDVI, GVI = 15%

The more uniform your soil, the lower you can push this.

FUTURE DIRECTIONS

32) I hear about people using spectral unmixing to look at vegetation, how does this work?
A) See 22 for a thumbnail description of linear mixing. Basically, you assume that the given spectrum is a linear combination of the spectra of materials which appear in the image. You do a least squares fit to find weighting coefficients for each individual material's spectrum which gives the best fit to the original spectrum. The weighting coefficients are considered to be equal to the abundances of the respective materials. For detailed discussions of this see Adams et al. (1989), Smith et al. (1990), Roberts et al. (1994) and Smith et al. (1994). There is also the highly sophisticated convex geometry technique discussed in Boardman (1994).

33) Are there any indices which use high spectral resolution data?
A) Yes. Elvidge and Chen (1994) have developed indices of this kind. They depend on the fact that when you take a derivative of the red edge in the vegetation spectrum you get a bump at about 720 nm. It is known that the red edge in be seen in high spectral resolution data down to about 5% cover (Elvidge and Mouat, 1988; Elvidge et al., 1993). Three indices were developed. The first used the integral of the first derivative of the reflectance

spectrum over the range 626-795 nm. The second took the first derivative of the reflectance spectrum, subtracted the value of the derivative at 625 nm and integrated the result over the range 626-795 nm. The third index used the integral of the absolute value of the second derivative of the reflectance spectrum integrated over the range from 626-795 nm. Of these three indices, the first one was found to have greater predictive power than RVI or NDVI, but less predictive power than SAVI or PVI. The index which used the second derivative has greater predictive power than SAVI and PVI. The index which used the difference between the first derivative and the value of the first derivative at 625 nm had the greatest predictive power.

FINAL QUESTION

34) What vegetation index should I use?

A) NDVI.

Nearly everyone who does much with the remote sensing of vegetation knows NDVI, and its often best to stick to what people know and trust. NDVI is simple. It has the best dynamic range of any of the indices in this FAQ and it has the best sensitivity to changes in vegetation cover. It is moderately sensitive to the soil background and to the atmosphere except at low plant cover. To just take a quick qualitative look at the vegetation cover in an image, you just can't beat NDVI unless you are looking at an area with low plant cover.

PVI is somewhat less common in its use, but it is also widely accepted. It has poor dynamic range and poor sensitivity as well as being very sensitive to the atmosphere. It is relatively easy to use, and finding the soil line is important for using some of the other indices. It sometimes is better than NDVI at low vegetation cover.

You really should probably use SAVI if you are looking at low vegetation cover, and if you use a correction factor which is not 0.5 you had better be prepared to cite the Huete (1988) paper and the fact the correction factor is larger than 0.5 for very sparse vegetation. MSAVI is also good, but it has seen very little use. If you have high spectral resolution data, you should consider the Elvidge and Chen (1994) indices.

Remember that many of the indices which correct for the soil background can work poorly if no atmospheric correction has been performed. If you are planning to seriously use vegetation indices for a multitemporal study, you should take a close look at the variability of the soil, and you should do an atmospheric correction. There is some concern about vegetation indices giving different values as you look away from the nadir, but this may not be terribly serious in your application.

SUMMARY: In order of preference for each type of sensor:

TM or MSS (or any broad-band sensor)

1: NDVI (or IPVI)
2: PVI
3: SAVI (top of list for low vegetation)
4: MSAVI2

High Spectral Resolution Data (e.g. AVIRIS)

1: First derivative index with baseline at 625 nm.

References

Adams, J.B., Smith, M. O., and Gillespie, A. R. (1989) Simple models for complex natural surfaces: a strategy for the hyperspectral era of remote sensing, in _Proc. IEEE Int. Geosci. and Remote Sensing Symp. '89_, IEEE, New York, 16-21.

Boardman, J. W. (1994) Geometric Mixture Analysis of Imaging Spectrometry Data, in _Proc. IEEE Int. Geosci. and Remote Sensing Symp. '94_, IEEE, New York, 2369-2371.

Baret, F., Guyot, G., and Major, D. (1989) "TSAVI: A vegetation index which minimizes soil brightness effects on LAI or APAR estimation," in _12th Canadian Symposium on Remote Sensing and IGARSS 1990_, Vancouver, Canada, July`10-14.

Baret, F. and Guyot, G. (1881) "Potentials and limits of vegetation indices for LAI and APAR assessment, _Remote Sensing of Environment_, vol. 35, pp. 161-173.

Clevers, J. G. P. W. (1988) "The derivation of a simplified reflectance model for the estimation of leaf area index, _Remote Sensing of Environment_, vol 35., pp. 53-70.

Crippen, R. E. (1990) "Calculating the Vegetation Index Faster," _Remote Sensing of Environment_, vol 34., pp. 71-73.

Crist, E. P. and Cicone, R. C. (1984) "Application of the tasseled cap concept to simulated thematic mapper data," _Photogrammetric Engineering and Remote Sensing_, vol. 50, pp. 343-352.

Elvidge, C. D. and Chen, Z. (1994) "Comparison of Broad-band and Narrow-band red versus near infrared vegetation indices," _Remote Sensing of Environment_, in review.

Elvidge, C. D. and Lyon, R. J. P. (1985) "Influence of rock-soil spectral variation on the assessment of green biomass," _Remote Sensing of Environment, vol. 17, pp. 265-269.

Goetz, A. F. H. and 7 others (1975) "Application of ERTS images and image processing to regional geologic problems and geologic mapping in northern Arizona," _JPL Technical Report 32-1597_, Jet Propulsion Laboratory, Pasadena, CA.

Huete, A. R., Jackson, R. D., and Post, D. F. (1985) "Spectral response of a plant canopy with different soil backgrounds, _Remote Sensing of Environment, vol. 17,, pp.37-53.

Huete, A. R. (1988) "A Soil-Adjusted Vegetation Index (SAVI)," _Remote Sensing of Environment_, vol. 25, pp. 295-309.

Jackson, R. D. (1983) "Spectral indices in n-space," _Remote Sensing of Environment, vol. 13, pp. 409-421.

Jordan, C. F. (1969) "Derivation of leaf area index from quality of light on the forest floor," _Ecology_, vol. 50, pp. 663-666.

Kanemasu, E. T. (1974) "Seasonal canopy reflectance patterns of wheat, sorghum, and soybean," _Remote Sensing of Environment_, vol. 3, 43-47.

Kaufman, Y. J., Tanre, D. (1992) "Atmospherically resistant vegetation index (ARVI) for EOS-MODIS, in _Proc. IEEE Int. Geosci. and Remote Sensing Symp. '92_, IEEE, New York, 261-270.

Kauth, R. J. and Thomas, G.S. (1976) "The tasseled cap--A graphic description of the spectral-temporal development of agricultural crops as seen by Landsat," _Proceedings of the Symposium on Machine Processing of Remotely Sensed Data_, Purdue University, West Lafayette, Indiana, pp. 41-51

Kriegler, F. J., Malila, W. A., Nalepka, R. F., and Richardson, W. (1969) "Preprocessing transformations and their effects on multispectral recognition, in _Proceedings of the Sixth International Symposium on Remote Sensing of Environment_, University of Michigan, Ann Arbor, MI, pp.97-131.

Leprieur, C., Verstraete, M.M., Pinty, B., Chehbouni, A. (1994) "NOAA/AVHRR Vegetation Indices: Suitability for Monitoring Fractional Vegetation Cover of the Terrestrial Biosphere," in _Proc. of Physical Measurements and Signatures in Remote Sensing_, ISPRS, 1103-1110.

Lillesand, T. M. and Kiefer, R. W. (1987) _Remote Sensing and Image Interpretation, 2nd edition_, John Wiley and Sons, New York, Chichester, Brisbane, Toronto, Singapore, 721 p.

Pickup, G., Chewings, V. H. and Nelson, O. J. (1993) "Estimating changes in vegetation cover over time in arid rangelands using Landsat MSS data," _Remote Sensing of Environment_, vol. 43, pp. 243-263.

Pinty, B. and Verstraete, M. M. (1991) "GEMI: A Non-Linear Index to Monitor Global Vegetation from Satellites," _Vegetatio_, vol. 101, 15-20.

Qi, J., Chehbouni, A., Huete, A. R., and Kerr, Y. H. (1994) "Modified Soil Adjusted Vegetation Index (MSAVI)," _Remote Sensing of Environment_, vol. 48, pp. 119-126.

Qi, J., Kerr, Y., and Chehbouni, A. (1994) "External Factor Consideration in Vegetation Index Development," in _Proc. of Physical Measurements and Signatures in Remote Sensing_, ISPRS, 723-730.

Richardson, A. J. and Everitt, J. H. (1992) "Using spectra vegetation indices to estimate rangeland productivity, _Geocarto International_, vol. 1, pp. 63-69.

Richardson, A. J. and Wiegand, C. L. (1977) "Distinguishing vegetation from soil background information," _Photogrammetric Engineering and Remote Sensing, vol. 43, pp. 1541-1552.

Roberts, D. A., Smith, M. O. and Adams, J. B. (1993) Green Vegetation, Nonphotosynthetic Vegetation, and Soils in AVIRIS Data, Remote Sensing of Environment, 44: 117–126.

Rouse, J. W., Haas, R. H., Schell, J. A., and Deering, D. W. (1973) "Monitoring vegetation systems in the great plains with ERTS," _Third ERTS Symposium, NASA SP-351_, vol. 1, pp.309-317.

Rouse, J. W., Haas, R. H., Schell, J. A., Deering, D. W., and Harlan, J. C. (1974) "Monitoring the vernal advancement and retrogradation (greenwave effect) of natural vegetation," _NASA/GSFC Type III Final Report_, Greenbelt, Md. 371 p.

Smith, M., Roberts, D., Hill, J., Mehl, W., Hosgood, B., Verdebout, J., Schmuch, G., Koechler, C. and Adams, J. (1994) A New Approach to Quantifying Abundance of Materials in Multispectral Images, in Proc. IEEE Int. Geosci. and Remote Sensing Symp. '94, IEEE, New York, 2372–2374.

Smith, M. O., Ustin, S. L., Adams, J. B. and Gillespie, A. R. (1990) Vegetation in Deserts: I. A Regional Measure of Abundance from Multispectral Images, Remote Sensing of Environment, 31: 1–26.

Tucker, C. J. (1979) "Red and Photographic Infrared Linear Combinations for Monitoring Vegetation," _Remote Sensing of Environment_, vol. 8, 127-150.

Wecksung, G. W. and Breedlove, J. R., Jr. (1977) "Some techniques for digital processing, display, and interpretation of ratio images in multispectral remote sensing," in _Applications of Digital Image Processing, Proceedings of Society of Photo-Optical Instrumentation Engineers,_ Bellingham, Washington, vol. 119, pp. 47-54.

Appendix C: *Minor Plants and Succulents.*

Part C.1: *Water Storage in Succulents*

Plants may also avoid water stress by storing water in their tissues. This is exemplified by the barrel cacti which store large amounts of water. Spalding (1905) showed that the distance between two points on opposite sides of a furrow on the side of a saguaro varied by more than an inch between dry and wet parts of the year. The storage of water for use during dry periods is a typical feature of desert succulents.

Many of the desert succulents also conserve water through the use of Crassulacean Acid Metabolism (CAM). In this specialized form of photosynthesis, the stomata are open for gas exchange only during the cool nighttime hours, which minimizes the water loss. The absorbed CO_2 is stored until the daytime when it is consumed by photosynthesis during the daylight hours with the stomata closed.

Part C.2: *Desert Succulents and Thermal Stress*

Although desert succulents such as agave has tissues which are resistant to heat stress, they still avoid reaching excessive temperatures by leaf orientation. The desert succulents, hold their large leaves within 30° of vertical and barrel cacti tend to have perfectly vertical sides (Gates, 1980).The example of the barrel cacti leads to another common adaptation of arid region plants for avoiding the absorption of excessive energy from sunlight. The barrel cacti often have rounded tops which are covered by especially thick layers of thorns which tends to enhance the reflectance of the top of the cactus in the visible and ultraviolet part of the spectrum which is where green plants have generally high

absorption (Gates *et al*, 1965). These spines have much the same effect as hairs on the leaves of some desert shrubs.

Part C.3: *Effect of the adaptations of Succulents on Remote Sensing*

Compared to their surface area, desert succulents have a larger volume of water-rich cellular material than do most other types of plants. This significant bulk of water-rich tissue will lead to an increased efficiency of reflection which could lead to a greater amount of near-infrared reflectance in these plants. However, many of the succulents to not appear strongly green to the eye which suggests that they are not as rich in chlorophyll and will not be quite as strongly absorbing in the visible as plants with stronger concentrations of chlorophyll. The succulents should also be relatively strong radar reflectors since their high water content should lead to an appreciable dielectric constant. Unlike desert shrubs, the succulent plants present a rather solid canopy (if you can apply the term to cacti with any accuracy) and appear just a green-plant as their laboratory leaf spectra.

Part C.4: *Minor Plant and Succulent Plant Spectra*

Minor species which have been observed using field and laboratory spectrometers are the small flowering plants chinchweed (*Pectis papposa*) and wooly daisy (*Eriophyllum wallacei*) as well as one example of an unidentified type of cactus.

There are several minor plants present in the field area which account for very little area covered by vegetation. The first of these is chinchweed (*Pectis papposa*), which is a small yellow wildflower. A PS2 spectrum of this plant is shown in figure C1. The spectrum is not quite as absorbing in the blue as the plants shown previously. There is a

distinct chlorophyll bump at 0.55 μm, and there are protochlorophyll and chlorophyll-a features clearly visible. Any chlorophyll-b absorption is very indistinct. The NIR reflectance is ratty, which may be partly due to the small amount of the FOV that the plant filled.

The PS2 spectrum of another yellow wildflower is shown in figure C2. This is a spectrum of wooly daisy (*Eriophyllum wallacei*) which gets its name in part from the fine white hairs which cover the green parts of the plant. The pigment features in the visible are very weak, with the 0.675 μm chlorophyll-a feature being the only distinctive feature in the visible. The absorptions due to xanthophyll or carotene are visible just short of 0.55 μm, but they are generally weaker than what has been seen in other plant spectra.

In figure C3, a PS2 spectrum of desert velvet (*Psathyrotes ramosissima*) against the soil background is shown. This plant has a purplish-gray appearance which leads to an expectation that the green bump at 0.55 μm should not be present, and this feature is quite flat in the figure. There is a definite absorption about 0.5 μm which is probably due to carotene and xanthophyll, and both chlorophyll absorptions can be seen at 0.625 and 0.675 μm. The protochlorophyll feature does appear to be absent.

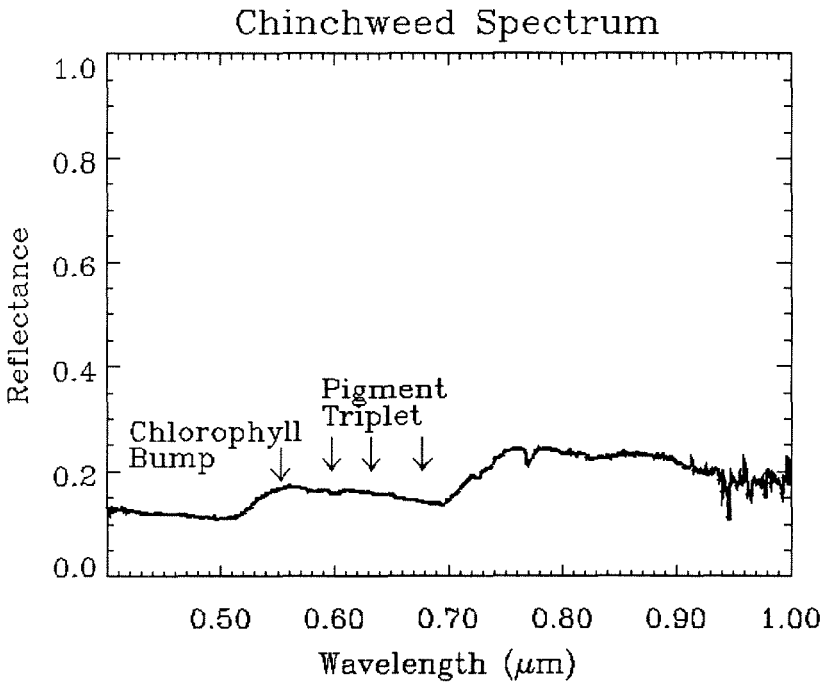

Figure C1: PS2 spectrum of chinchweed. Note the absence of a chlorophyll-b feature near 0.61 μm (middle arrow of pigment triplet).

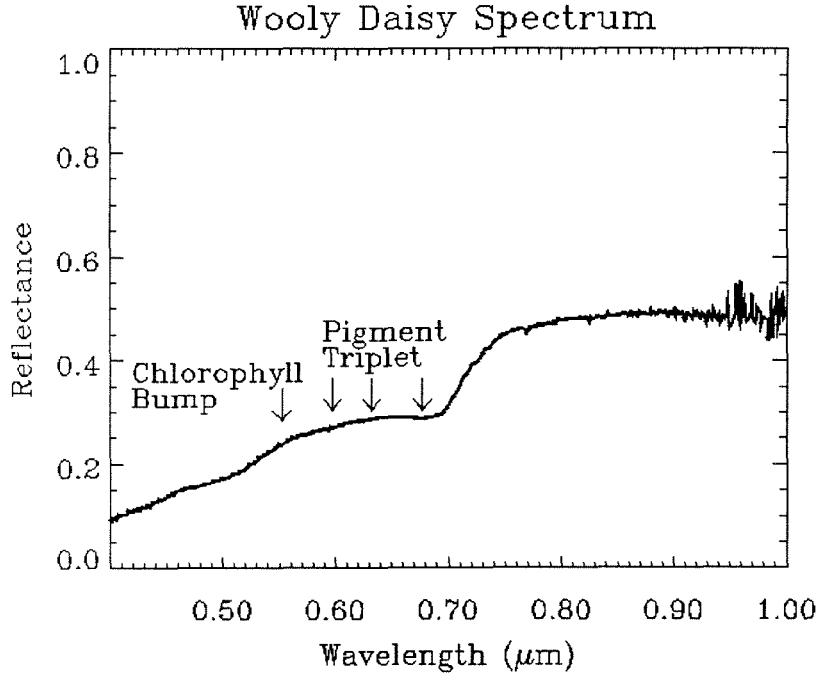

Figure C2: PS2 spectrum of wooly daisy. Note the lack of protochlorophyll and chlorophyll-b absorption (left and middle arrows of pigment triplet).

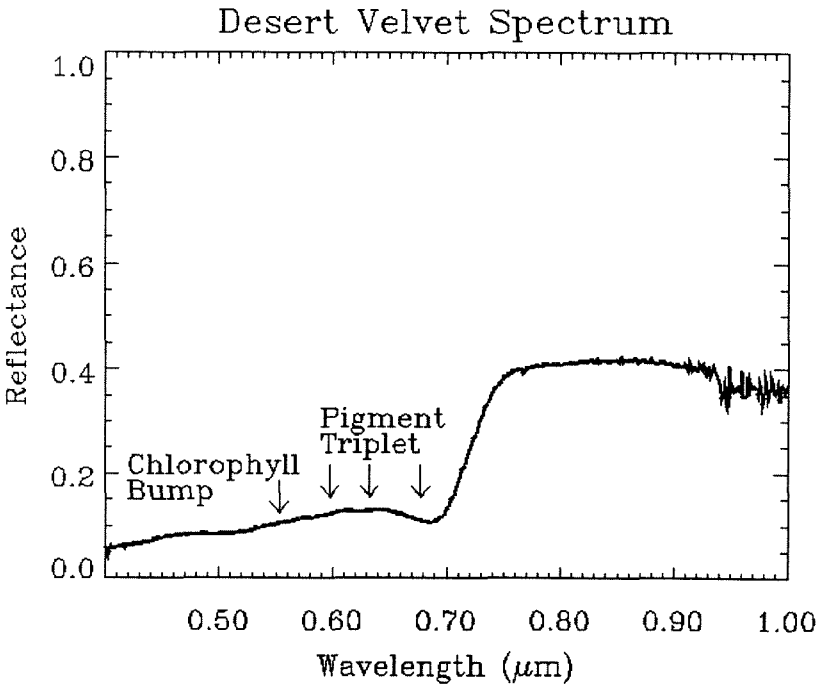

Figure C3: PS2 spectrum of desert velvet. Note the absence of protochlorophyll and chlorophll-b features (left and middle arrows of the pigment triplet).

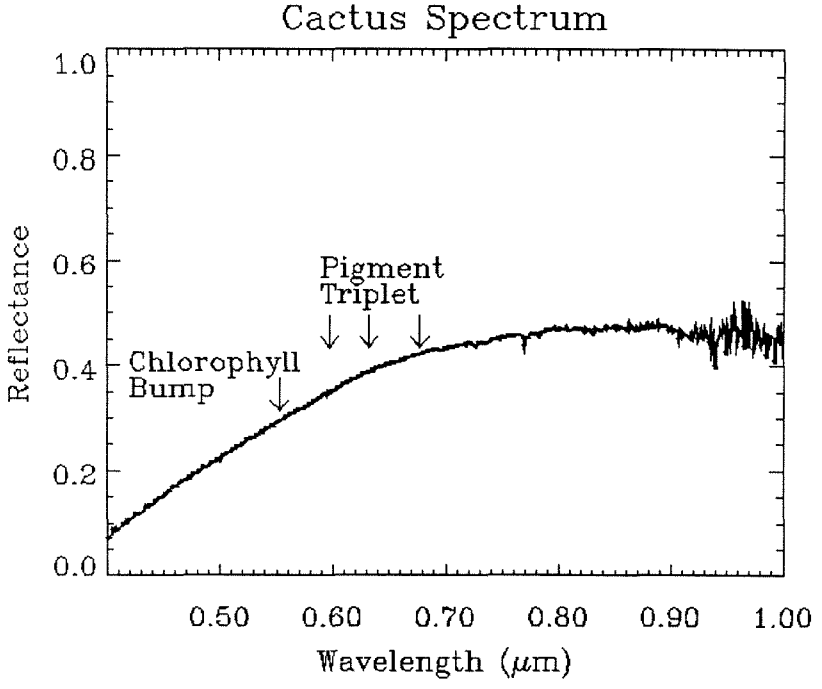

Figure C4: PS2 spectrum of a cactus. Note the lack of pigment features.

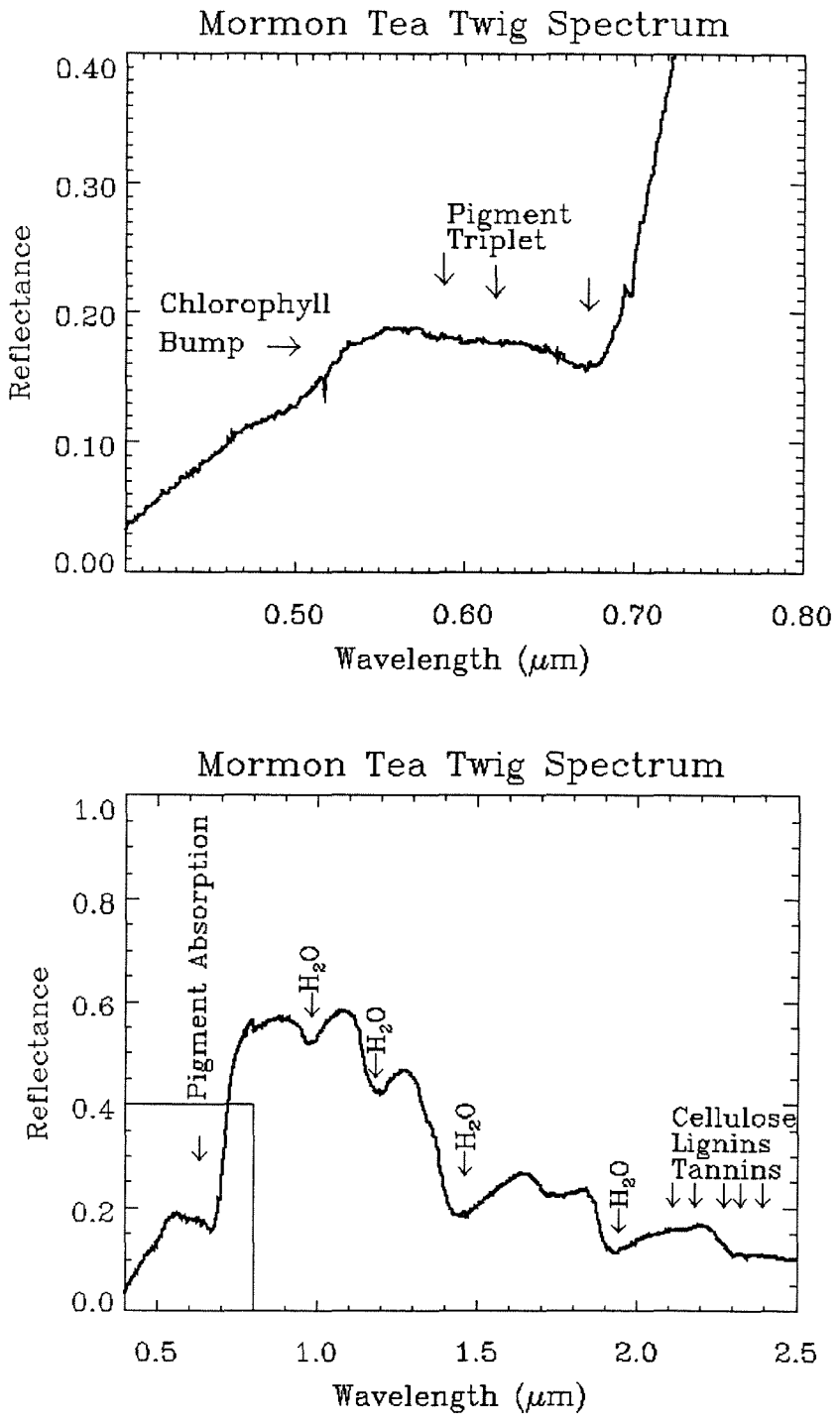

Figure C5: Beckman spectrum of fresh Mormon Tea twigs. The top plot is an enlargement of the boxed area in the bottom plot. Note the strong cellulose, lignin, and tannin absorptions between 2.2–2.5 μm.

Figure C4 is the PS2 spectrum of the single cactus observed in the field area. The spectrum is remarkably similar to that of the yellow desert grass. This seems to conflict with both the conclusion about the spectral characteristics of succulents expected from the earlier discussion. It should be noted that Gates (1980) does show that succulents have extremely large NIR reflectances.

The final minor plant examined was Mormon Tea (*Ephedra* spp.), which is shown in figure C5. This Beckman spectrum of green, fresh twigs. There is a pigment feature near 0.55 μm which is similar to what is seen in bursage whole plant spectra. The most definite absorption due to pigment is the chlorophyll-a absorption a 0.675 μm. In the NIR, there is a significant broad absorption near 2.3 μm which is probably due to a combination of lignin, tannin, and cellulose. These results are similar to those of Elvidge (1990), although his spectrum of fresh Mormon Tea stems had a stronger chlorophyll bump more like that in the Beckman leaf spectra of the other plants.

Appendix D: *The Video*

The video included with this thesis is JPL #AVC-95-075, and it runs for approximately 8½ minutes. The video opens with an animation of a rotating globe produced using images acquired by the Galileo spacecraft. The image of the United States was constructed by the USGS EROS Data Center from AVHRR data. Red areas are regions of high vegetation cover. This image was downloaded from the EROS Data Center World-Wide Web pages. The next image is an aerial view of the Caltech campus centered on the Millikan Library, and the image was provided by the Caltech Public Relations Office. The next image is a Landsat Thematic Mapper mosaic of the Southwestern United States. The boxed area is the approximate location of the Manix Basin. The next photograph is a ground-level photo of an irrigated alfalfa field in the study area. The three spectra in the subsequent plot were generated using IDL from in-situ field spectra collected using the PS2 spectrometer as discussed in Chapter 5. The subsequent photographs are pictures taken in the study area of an active alfalfa field, a desert landscape, a creosote bush, a bursage shrub, and a clump of yellow desert grass. This is followed by a plot of the reflectance spectra of alfalfa, creosote bush, bursage, and yellow desert grass generated with IDL using data collected with the PS2 spectrometer as discussed in Chapter 5. The next photograph shows the same abandoned flood irrigation system discussed in Chapter 2, and the partially buried pipe can be seen running across the center of the image. The view shifts back to the Landsat Thematic Mapper mosaic of the Southwestern United States. This is followed by the 1988 MSS image discussed in

Chapter 6 with MSS band 7 displayed as red, MSS band 5 as green, and MSS band 4 as blue. This is followed by a picture of an active alfalfa field. The next photograph is the color version of figure 15, which is a field abandoned for five years. Next, the color version of figure 27, a field abandoned for 17 years, is displayed. Next, is the series of MSS images discussed in Chapter 6, and the color scheme is identical to that discussed above. The AVIRIS image was constructed using the MSS bandpasses, as discussed in Chapter 4 from the three AVIRIS segments processed by JPL for this study. The last image in the series is the RESOURCE image discussed in Chapter 6. The next two images displayed are the MSS image synthesized from AVIRIS data, which is displayed as plate 18 in the main thesis text, and the color-coded NDVI image displayed as plate 17 in the main thesis text where white is very high vegetation cover. Lower levels of vegetation cover in the NDVI image are shown as colors near the blue end of the spectrum and higher levels of vegetation cover are shown as colors near the red end of the spectrum. These are followed by another photograph of the abandoned flood irrigation system, which clearly shows the effects of wind erosion. The synthetic MSS and NDVI images are repeated. The video concludes with the animation of the rotating Earth.

Appendix E: *More on Polarization Signatures*

Chapter 4 shows how unusual polarization signatures arise from fields covered by wind ripples. Figure E-1 shows two co-polarization signatures for a more "normal" natural surface. These are polarization signatures of the ocean surface in San Franciso Bay acquired in 1985 (van Zyl *et al.*, 1987b). Figure E-1a is the ocean at 20° incidence angle, and E-1b is the ocean at 50° incidence. In both cases, the maximum co-polarized return is at VV polarization (ψ=90°; χ=0°), which plots at the middle of the co-polarization signature, as shown by figure 18 in the main text. Note that the signature at the larger incidence angle peaks much more strongly at VV than does the signature at the smaller incidence angle. Notice also that the polarization signature for the smaller incidence angle also has a slight pedestal and never quite touches the base of the signature. The signature at the larger incidence angle (E-1b) also has a pedestal, but it is smaller than for figure E-1a. The first order small perturbation model discussed in chapter 3 was used by van Zyl *et al.* (1987b) to model the response from a surface with a Gaussian power spectrum. The model predicted the polarization signatures in figure E-1, with the exception of the pedestal height.

The second order small perturbation model discussed in chapter 4 was used by van Zyl *et al.* (1988) to model the observed polarization signature for part of the Pisgah lava flow in California's Mojave Desert. Figure E-2a shows the co-polarization signature for part of a pahoehoe lava flow. This is very similar to figure E-1b, with the maximum response occurring at VV, but the pedestal height is larger for figure E-2a, which suggests

a greater degree of surface roughness and multiple scattering is occurring from the pahoehoe flow than from the ocean surface. Figure E-2b shows the results obtained using the second-order small perturbation model. The model results closely resemble the observations, and the surface roughness used for this model agree with field measurements of the roughness of the flow. The first-order small perturbation model predicts no pedestal, but the second-order small perturbation model does predict the pedestal height. The ocean surface and the pahoehoe flow are examples of "normal" natural surfaces, and these signatures can be compared with the unusual signatures from many of the abandoned fields.

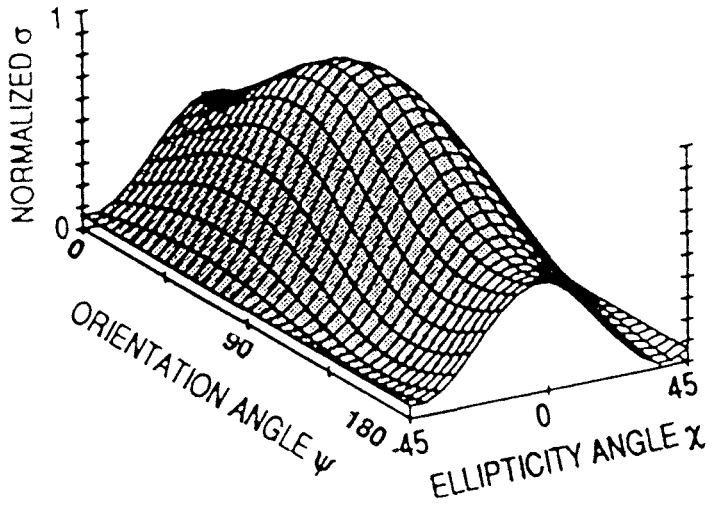

a)

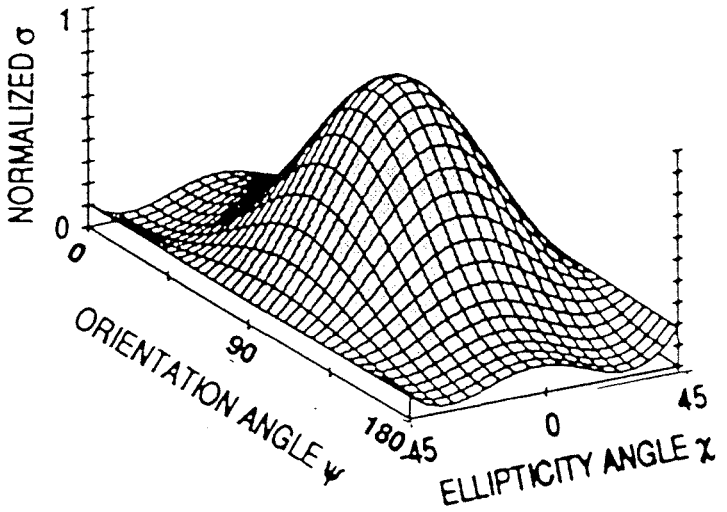

b)

Figure E-1: **a)** Co-polarization signature for the ocean surface at 20° incidence. **b)** Co-polarization signature for the ocean surface at 50° incidence. Note that the maximum response occurs at VV polarization (y=90°, c=0°) for both signatures. Notice how the polarization signature varies with incidence angle. The ocean surface can be regarded as a "normal" natural surface with isotropic, random roughness.

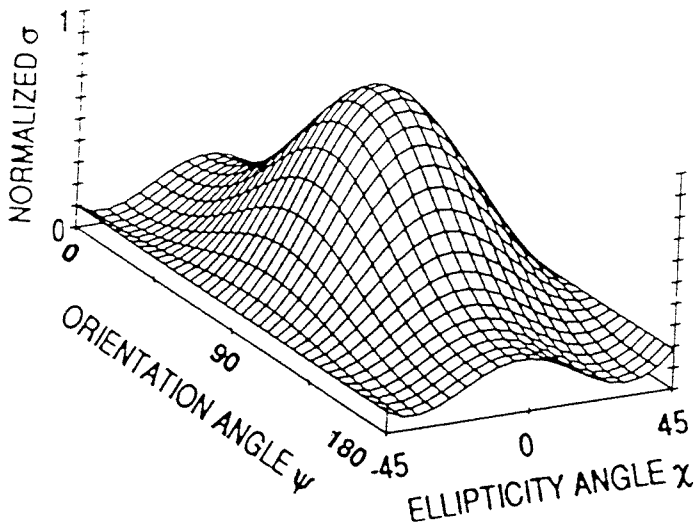

a)

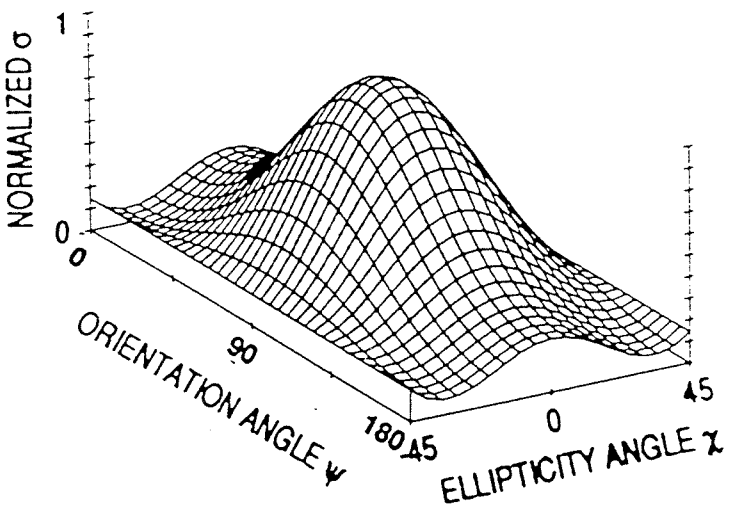

b)

Figure E-2: a) The co-polarization signature for a pahoehoe flow at Pisgah in California's Mojave Desert. Note the similarity to figure E-1b, and also notice that figure E-2a has a larger pedestal than figure E-1b. **b)** Model result using the second-order small perturbation model to predict the co-polarization signature of the lava flow. Note the strong similarity between figures E-2a and E-2b.

Bibliography

Abrams, L. (1944) **Illustrated Flora of the Pacific States, Volume 2**, Stanford University Press, Stanford, 635 p.

Abrams, L. (1951) **Illustrated Flora of the Pacific States, Volume 3**, Stanford University Press, Stanford, 866 p.

Abrams, L. (1960) **Illustrated Flora of the Pacific States, Volume 4**, Stanford University Press, Stanford, 732 p.

Adams, F. (1913) **Irrigation Resources of California and Their Utilization**, USDA, Office of Experiment Stations, Bulletin 254, 95 p.

Adams, J. B., M. O. Smith and P. E. Johnson (1986) "Spectral Mixture Modeling: A New Analysis of Rock and Soil Types at the Viking Lander I Site," **Journal of Geophysical Research, 91:** 8098–8112.

Adams, J. B., M. O. Smith, and A. R. Gillespie (1989), "Simple Models for Complex Natural Surfaces: A Strategy for The Hyperspectral Era of Remote Sensing," in **Proc. IEEE Int. Geosci. and Remote Sensing Symp. '89**, IEEE, New York, 16–21.

Alley, W. M. (1984) "The Palmer Drought Severity Index: Limitations and Assumptions," **Journal of Climate and Applied Meteorology, 23:** 1100–1109.

Aubreville, A. (1949) **Climats, Forêts et Désertification de l'Afrique Tropicale.** Soc d'Éditions Géographiques et Coloniales, Paris, 352p.

Bagnold, R. A. (1942) **The Physics of Blown Sand and Desert Dunes**, William Morrow & Co., New York, 265 p.

Barbour, M. G., G. Cunningham, W. C. Oechef, and S. A. Bamberg (1977a) "Growth and Development, Form and Function," in **Creosote Bush: Biology and Chemistry of *Larrea* in New World Deserts**, Mabry, T. J., J. H. Hunziker and D. R. Difeo, Jr. (eds.), Dowden, Hutchinson & Ross, Stroudsburg, 284 p.

Barbour, M. G., J. A. MacMahon, S. A. Bamberg and J. A. Ludwig (1977b) "The Structure and Distribution of *Larrea* Communities," in **Creosote Bush: Biology and Chemistry of *Larrea* in New World Deserts**, Mabry, T. J., J. H. Hunziker and D. R. Difeo, Jr. (eds.), Dowden, Hutchinson & Ross, Stroudsburg, 284 p.

Boardman, J. W. (1989) "Inversion of Imaging Spectrometry Data Using Singular Value Decomposition," **Proc. IEEE Int. Geosci. and Remote Sensing Symp. '89,** IEEE, New York, 2069–2072.

Boardman, J. W. (1990) "Inversion of High Spectral Resolution Data," **Proceedings SPIE, 1298:** 222–233.

Boardman, J. W. (1991), **Sedimentary Facies Analysis Using Imaging Spectrometry: A Geophysical Inverse Problem**, unpublished Ph.D. dissertation, University of Colorado, Boulder, 212 p.

Boardman, J. W. (1992) "Spectral Angle Mapping," unpublished manuscript.

Boardman, J. W. (1993) "Automating Linear Mixture Analysis of Imaging Spectrometry Data," **Proceedings International Symposium on Spectral Sensing Research '94,** 302–309.

Boardman, J. W. (1994) "Geometric Mixture Analysis of Imaging Spectrometry Data," in **Proc. IEEE Int. Geosci. and Remote Sensing Symp. '94**, IEEE, New York, 2369–2371.

Born, M. and E. Wolf (1980) **Principles of Optics, 6th corrected ed.**, Pergamon, Oxford, New York, Beijing, Frankfurt, São Paulo, Sydney, Tokyo, Toronto, 808 p.

Buwalda, J. P. (1914) "Pleistocene Beds at Manix in the Eastern Mojave Desert Region," **Bulletin of the Department of Geology, University of California - Berkeley, 7:** 443–464.

California Interstate Telephone Company (1961) **Romantic Heritage of Victor Valley, A Saga of Desert Exploration and Expansion**, 14 p.

Carpenter, D. E., M. G. Barbour and C. J. Bahre (1986) "Old Field Succession in Mojave Desert Scrub," **Madroño, 33:** 111–122.

Chepil, W. S. (1945) "Dynamics of Wind Erosion: I. Nature of Movement of Soil by Wind," **Soil Science, 60:** 305–320.

Clevers, J. G. P. W. (1988) "The Derivation of a Simplified Reflectance Model for The Estimation of Leaf Area Index," **Remote Sensing of Environment, 35:** 53–70.

Cody, M. L. (1989) "Growth-Form Diversity and Community Structure in Desert Plants," **Journal of Arid Environments, 17:** 199–209.

Conel, J.E., R. O. Green, G. Vane, C. J. Bruegge, R. E. Alley and B. J. Curtiss (1987) Airborne Imaging Spectrometer-2: Radiometric Spectral Characteristics and Comparison of Ways to Compensate for the Atmosphere," **Imaging Spectroscopy II, Proc. SPIE, 834:** 140-157.

Crippen, R.E. (1987) "The Regression Intersection Method of Adjusting Image Data for Band Ratioing," **Int. J. Remote Sens.: 8,** 137-155.

Crippen, R.E. (1990) "Calculating the Vegetation Index Faster," **Remote Sensing of Environment, 34:** 71-73.

Crist, E. P. and R. C. Cicone (1984) "Application of the Tasseled Cap Concept to Simulated Thematic Mapper Data," **Photogrammetric Engineering and Remote Sensing, 50:** 343–352.

Dregne, H. E. (1983) **Desertification of Arid Lands,** Harwood Academic Publishers, Chur, London, Paris, New York, 242pp.

Dregne, H. E. and C. J. Tucker (1988) "Desert Encroachment," **Desertification Control Bulletin,** Nairobi, Kenya, **16:** 16–19.

DuBois, P.C., E. Rignot and J.J. van Zyl (1992) "Direction Angle Sensitivity of Agricultural Field Backscatter with AIRSAR Data," **Proc. IEEE Int. Geosci. and Remote Sensing Symp. '92**, IEEE, New York, 1680–1682.

Ehleringer, J. R. and I. Forseth (1980) "Solar Tracking by Plants," **Science, 210:** 1094–1098.

Elachi, C. (1987) **Introduction to the Physics and Techniques of Remote Sensing**, John Wiley & Sons, New York, Chichester, Brisbane, Toronto, Singapore, 413 p.

El-Baz, F. (1988) "Origin and Evolution of the Desert," **Interdisciplinary Science Reviews, 13:** 331–347.

Elvidge, C. D. (1990) "Visible and Near Infrared Reflectance Characteristics of Dry Plant Materials," **International Journal of Remote Sensing, 11:** 1775–1795.

Elvidge, C. D. and Z. Chen (1995) "Comparison of Broad-band and Narrow-band Red Versus Near Infrared Vegetation Indices," **Remote Sensing of Environment,** in review.

Elvidge, C. D. and Z. K. Chen (1993) "Detection of Trace Quantities of Green Vegetation in 1990 AVIRIS Data," **Remote Sensing of Environment, 44:** 271–279.

Elvidge, C. D. and R. J. P. Lyon (1985) "Influence of Rock-Soil Spectral Variation on the Assessment of Green Biomass," **Remote Sensing of Environment, 17:** 265–269.

Elvidge, C. D. and D. A. Mouat (1989) "Analysis of Green Vegetation Detection Limits in 1988 AVIRIS Data," **Proceedings of the International Symposium of Remote Sensing of Environment, 7th Thematic Conference - Remote Sensing for Exploration Geology**.

Evans, D. L., T. G. Farr, J. J. van Zyl, H. A. Zebker (1988) "Radar Polarimetry: Analysis Tools and Applications," **IEEE Transactions on Geoscience and Remote Sensing, 26:** 774–789.

Fitter, A. H. and R. K. M. Hay (1987) **Environmental Physiology of Plants, 2nd ed.,** Academic Press, London, San Diego, New York, Berkeley, Boston, Sydney, Tokyo, Toronto, 423p.

Fonteyn, P. J. and B. E. Mahall (1978) "Competition Among Desert Perennials," **Nature, 275:** 544–545.

Ford, J. P., R. K. Dokka, R. E. Crippen and R. G. Blom (1990) "Faults in the Mojave Desert, California as Revealed on Enhanced Landsat Images," **Science, 248:** 1000–1003.

Fowler, N. (1986) "The Role of Competition in Plant Communities in Arid And Semiarid Regions," **Ann. Rev. Ecol. Syst., 17:** 89–110.

Frazer, R. W. (1972) **Forts of the West: Military Forts and Presidios and Posts Commonly Called Forts West of the Mississippi River to 1898**, Univ. of Oklahoma Press, Norman and London, 246 p.

Fryrear, D. W., J. Stubbendieck, W. G. McCully (1973) "Grass Seedling Response to Wind And Windblown Sand," **Crop Science, 113–116:** 622–625.

Gamon, J.A., Field, C.B., Roberts, D.A., Ustin, S.L., and Valentini, R. (1993) "Functional Patterns in an Annual Grassland During an AVIRIS Overflight," **Remote Sensing of Environment: 44,** 239-253.

Gates, D. M. (1980) **Biophysical Ecology,** Springer-Verlag, New York, Heidelberg, Berlin, 611 p.

Gates, D. M., Keegan, H. J., Schleter, J. C., and Weidner, V. R. (1965), "Spectral Properties of Plants," **Applied Optics, 4:** 11–20.

Gates, D. M., R. Alderfer and E. Taylor (1967) "Leaf Temperatures of Desert Plants," **Science, 129:** 994–995.

Goossens, R., M. D. Dapper and B. M. De Vliegher (1994) "A Model to Simulate and Predict Soil Salinity and Waterlogging. (Elaborated for the Nile Delta Fringes, Egypt)," **Proc. IEEE Int. Geosci. and Remote Sensing Symp. '94**, IEEE, New York, 773–775

Gorman, T., (1993) "Sand Trapped: Residents Along Part of Mojave River Dig in for Battle Over Drifting Dunes," **Los Angeles Times**, May 24, 1993, pages A3&A22.

Greeley, R., N. Lancaster, R. J. Sullivan, R. S. Saunders, E. Theilig, S. Wall, A. Dobrovolskis, B. R. White, and J. D. Iversen (1988) "A Relationship Between Radar Backscatter and Aerodynamic Roughness: Preliminary Results," **Geophysical Research Letters, 15:** 565–568.

Green, G. M. (1992) "Past, Present and Future Deforestation in Madagascar Using Satellite Images," **Association of American Geographers 88th Annual Meeting Abstracts**, 86–87.

Green, R. O., S. A. Larson, and H. I. Novack (1991) "Calibration of AVIRIS Digitized Data," **Proceedings of the Third Airborne Visible/Infrared Imaging Spectrometer (AVIRIS) Workshop,** 109–118.

Green, R. O., J. E. Conel, M. Helmlinger, J. van den Bosch, C. Chovit, and T. Chrien (1993) "Inflight Calibration of AVIRIS in 1992 and 1993," **Summ. of the 4th Ann. JPL Airborne Geoscience Workshop: AVIRIS Workshop:** 69–72.

Grove, C. I., S. J. Hook, and E. D. Paylor, II (1992) **Laboratory Reflectance Spectra of 160 Minerals, 0.4 to 2.5 Micrometers**, JPL Publication 92-2, 408 p.

Hapke, B. (1981) "Bidirectional Reflectance Spectroscopy 1, Theory," **Journal of Geophysical Research, 86:** 3039–3054.

Henderson, L. J. (1913) **The Fitness of the Environment**, Macmillan, London, 317 p.

Hillel, D. (1982) **Introduction to Soil Physics**, Academic Press, San Diego, New York, Boston, London, Sydney Tokyo, Toronto, 364p.

Hitchcock, A. S. (1935) **Manual of the Grasses of the United States**, United States Department of Agriculture, United States Government Printing Office, Washington, 1040 p.

Holý, M. (1980) **Erosion and Environment**, Pergamon Press, Oxford, New York, Toronto, Sydney, Paris, Frankfurt, 225 p.

Houk, I. E. (1951) **Irrigation Engineering, Vol. 1: Agricultural and Hydrological Phases**, John Wiley & Sons, New York, 545 p.

Huete, A. R. (1988) "A Soil-Adjusted Vegetation Index (SAVI)," **Remote Sensing of Environment, 25:** 295–309.

Huete, A. R., R. D. Jackson, and D. F. Post (1985) "Spectral Response of a Plant Canopy with Different Soil Backgrounds," **Remote Sensing of Environment, 17:** 37–53.

Hunziker, J. H., R. A. Palacios, L. Poggio, C. A. Naranto and T. W. Yang (1977) "Geographic Distribution, Morphology, Hybridization, Cytogenetics, and Evolution," in **Creosote Bush: Biology and Chemistry of *Larrea* in New World Deserts**, Mabry, T. J., J. H. Hunziker and D. R. Difeo, Jr. (eds.), Dowden, Hutchinson & Ross, Stroudsburg, 284 p.

IEEE (1979) **IEEE Standard Test Procedures for Antennas,** IEEE Press, New York.

Jacks, G. V. (1939) "Soil Erosion. The Rape of the Earth. A Survey of Soil Erosion." in **Soil Erosion and Its Control**, G. V. Jacks and R. O. Whyte (eds.), Faber, London, 313 p.

Jackson, J. D. (1975) **Classical Electrodynamics, 2nd ed.**, John Wiley & Sons, New York, Chichester, Brisbane, Toronto, Singapore, 848 p.

Jackson, R. D. (1983) "Spectral Indices in N-space," **Remote Sensing of Environment, 13:** 409–421.

Jefferson, G.T., J. R. Keaton, and P. Hamilton (1982) **Manix Lake and the Manix Fault Field Trip Guide: Quarterly San Bernardino Co. Museum Assoc., 29 (3-4):**1-47.

Johnson, P. E., M. O. Smith, S. Taylor-George, and J. B. Adams (1983) "A Semiempirical Method for Analysis of the Reflectance Spectra of Binary Mineral Mixtures," **Journal of Geophysical Research, 88:** 3557–3561.

Jordan, C. F. (1969) "Derivation of Leaf Area Index From Quality of Light on the Forest Floor," **Ecology, vol. 50:** 663–666.

Kaufman, Y. J., D. Tanré (1992) "Atmospherically Resistant Vegetation Index (ARVI) for EOS-MODIS," in **Proc. IEEE Int. Geosci. and Remote Sensing Symp. '92**, IEEE, New York, 261–270.

Kauth, R. J. and G. S. Thomas (1976) "The Tasseled Cap--A Graphic Description of the Spectral-Temporal Development of Agricultural Crops as Seen by Landsat," **Proceedings of the Symposium on Machine Processing of Remotely Sensed Data,** Purdue University, West Lafayette, Indiana, pp. 41–51

Kuga, Y., M. W. Whitt, K. C. McDonald, and F. T. Ulaby (1987) "Scattering Models for Distributed Targets," in **Radar Polarimetry for Geoscience Applications**, F. T. Ulaby and C. Elachi (eds.), Artech House, Norwood, 111–190.

Leakey, L. S. B. and R. D. Simpson (1972) **Pleistocene Man at Calico; a Report on the International Conference on the Calico Mountains Excavations, San**

Bernardino County, California, San Bernardino County Museum Association, 82 p.

Leprieur, C., M. M. Verstraete, B. Pinty and A. Chehbouni (1994) "NOAA/AVHRR Vegetation Indices: Suitability for Monitoring Fractional Vegetation Cover of the Terrestrial Biosphere," **ISPRS Proceedings on Physical Measurements and Signatures in Remote Sensing**, 1103–1110.

Li, L., C. H. Chan and L. Tsang (1994) "Numerical Simulation of Conical Diffraction of Tapered Electromagnetic Waves from Random Rough Surfaces and Applications to Passive Remote Sensing," **Radio Science, 29:** 587–598.

Lillesand, T. M. and R. W. Kiefer (1987) **Remote Sensing and Image Interpretation, 2nd ed.**, John Wiley & Sons, New York, Chichester, Brisbane, Toronto, Singapore, 721 p.

Lowdermilk, W. C. (1935) "Man-Made Deserts," **Pacific Affairs, University of British Columbia, 8:** 409–419, in **Soil Erosion and Its Control**, R. P. C. Morgan (ed.), Van Nostrand Reinhold, New York, 311 p.

Mabry, T. J., D. R. Difeo, Jr., M. Sakakibara, C. F. Bohnstedt, Jr. and D. Seigler (1977a) "The Natural Products Chemistry of *Larrea*," in **Creosote Bush: Biology and Chemistry of *Larrea* in New World Deserts**, Mabry, T. J., J. H. Hunziker and D. R. Difeo, Jr. (eds.), Dowden, Hutchinson & Ross, Stroudsburg, 284 p.

MacDougal, D. T. (1908) **Botanical Features of North American Deserts,** Carnegie Institution, Washington, DC, 111 p.

Mahall, B. E. and R. M. Callaway (1991) "Root Communication Among Desert Shrubs," **Proceedings of the National Academy of Sciences of the United States of America, 88:** 874–876.

Mainguet, M. (1994) **Desertification: Natural Background and Human Mismanagement, 2nd ed.**, Springer-Verlag, Berlin, Heidelberg, New York, London, Paris, Tokyo, Hong Kong, Barcelona, Budapest, 314p.

Markham, B. L. and J. L. Barker (1985) "Spectral Characterization of the Landsat Thematic Mapper Sensors," **International Journal of Remote Sensing, 6:** 697–716.

Martin, J. T. and B. E. Juniper (1970) **The Cuticles of Plants,** Arnold, London, 347 p.

McIntire, H. D. (1986a) "History and Development (of the Mojave River Area)," in **Soil Survey of San Bernardino County, California: Mojave River Area**, A. J. Tugel and G. A. Woodruff (eds.), U. S. Government Printing Office, 1–2.

McIntire, H. D. (1986b) "Water (of the Mojave River Area)," in **Soil Survey of San Bernardino County, California: Mojave River Area**, A. J. Tugel and G. A. Woodruff (eds.), U. S. Government Printing Office, 3–4.

Mead, E. (1901) **Report of Irrigation Investigations in California**, USDA, Office of Experiment Stations, Bulletin 100, 409 p.

Meek, N. (1989) "Geomorphic and Hydrologic Implications of the Rapid Incision of Afton Canyon, Mojave Desert, Califronia," **Geology, 17:** 7–10.

Millar, C. E., L. M. Turk, and H. D. Foth (1951) **Fundamentals of Soil Science, 3rd ed.**, John Wiley & Sons, New York, 526 p.

Murray, B.C., Hammond, A., and Rodenburg, E. (1994) **Global Environmental Monitoring: Pathways to Responsible Planetary Management**, World Resources Institute.

Nash and Conel (1974) "Spectral Reflectance Systematics for Mixtures of Powdered Hypersthene, Labradorite, and Ilmenite," **Journal of Geophysical Research, 79:** 1615–1621.

NCDC (National Climatic Data Center) (1986a) "Climate (of Mojave River Area)," in **Soil Survey of San Bernardino County, California: Mojave River Area**, A. J. Tugel and G. A. Woodruff (eds.), U. S. Government Printing Office, 4–6.

NCDC (National Climatic Data Center) (1990a) **National Climate Information Disc, Volume 1,** National Climatic Data Center, Asheville, NC.

NCDC (National Climatic Data Center) (1972–1991) **Climatological Data: California**, National Climatic Data Center, Asheville, NC, **75–95**.

Nelson, R. (1988) "Dryland management: the 'desertification' problem," **The World Bank Planning and Research Staff, Environmental Department, 8:** 42.

Newton, I. (1704) **Opticks**, Dover, New York, 408 p.

NREL (National Renewable Energy Laboratory) (1991a) **Solar and Meteorological Surface Observation Network, 1961–1990, Volume 3, Western U.S.,** National Renewable Energy Laboratory, Golden, CO.

NREL (National Renewable Energy Laboratory) (1991b), **National Solar Radiation Data Base (1961–1990), User's Manual,** National Renewable Energy Laboratory, Golden, CO.

Orshan, G. (1963) "Seasonal Dimorphism of Desert and Mediterranean Chamaephytes and its Significance as a Factor in Their Water Economy," **Symposium of the British Ecological Society, 3:** 206–222.

Paisley, E. C. I., N. Lancaster, L. R. Gaddis and R. Greeley (1991) "Discrimination of Active and Inactive Sand from Remote Sensing: Kelso Dunes, Mojave Desert, California," **Remote Sensing of Environment, 37:** 153–166.

Palmer, W. C. (1965) "Meteorologic Drought," **U.S. Weather Bureau, Res. Pap. No. 45,** 58 p.

Papoulis, A. (1962) **The Fourier Integral and Its Applications**, McGraw-Hill, New York, San Francisco, London, Toronto, 318 p.

Pickup, G., V. H. Chewings and D. J. Nelson (1993) "Estimating Changes in Vegetation Cover over Time in Arid Rangelands Using Landsat MSS Data," **Remote Sensing of Environment, 43:** 243–263.

Pinty, B. and M. M. Verstraete (1991) "GEMI: A Non-Linear Index to Monitor Global Vegetation from Satellites," **Vegetatio, 101:** 15–20.

Powell, J. W. (1879) **Report on the Lands of the Arid Region of the United States**, U.S. Government Printing Office, Washington, D.C., 195 p.

Qi, J., A. Chehbouni, A. R. Huete, Y. H. Kerr (1994a) "Modified Soil Adjusted Vegetation Index (MSAVI)," **Remote Sensing of Environment, 48:** 119–126.

Qi, J., Y. Kerr and A. Chehbouni (1994b) "External Factor Consideration in Vegetation Index Development," **ISPRS Proceedings on Physical Measurements and Signatures in Remote Sensing,** 723–730.

Ray, T. W., T. G. Farr and J. J. van Zyl (1991) "Polarization Signatures for Abandoned Agricultural Fields in the Manix Basin Area of the Mojave Desert," **Proceedings of the Third AIRSAR Workshop**, 117–125.

Ray, T. W., T. G. Farr and J. J. van Zyl (1992a) "Polarization Signatures for Abandoned Agricultural Fields in the Manix Basin Area of the Mojave Desert: Can Polarimetric SAR Detect Desertification?" **Proc. IEEE Int. Geosci. and Remote Sensing Symp. '92**, IEEE, New York, 947–949.

Ray, T. W., T. G. Farr and J. J. van Zyl, (1992b) Detection of Land Degradation with Polarimetric SAR, **Geophysical Research Letters, 19:** 1587-1590.

Ray, T. W., T. G. Farr, R. G. Blom and R. E. Crippen (1993) "Monitoring Land Use and Degradation Using Satellite and Airborne Data," **Summaries of the 4th Annual JPL Airborne Geoscience Workshop: AVIRIS Workshop:** 145–148.

Ray, T. W., J. J. van Zyl and E. M. DeJong (1994) "Polarization Effects in Radar Reflection from Surfaces with Periodic Roughness," **Proc. IEEE Int. Geosci. and Remote Sensing Symp. '94**, IEEE, New York, 1133–1135.

Ray, T. W. and B. C. Murray (1994) "Arid Vegetation and Remote Sensing," **AGU 1994 Fall Meeting.**

Ray, T. W. and B. C. Murray (1995) "Non-Linear Spectral Mixing in Desert Vegetation," **Remote Sensing of Environment**, (in review).

Rhoades, D. F. (1977) "The Antiherbivore Chemistry of *Larrea*," in **Creosote Bush: Biology and Chemistry of *Larrea* in New World Deserts**, Mabry, T. J., J. H.

Hunziker and D. R. Difeo, Jr. (eds.), Dowden, Hutchinson & Ross, Stroudsburg, 284 p.

Richardson, A. J. and Everitt, J. H. (1992) "Using Spectral Vegetation Indices to Estimate Rangeland Productivity," **Geocarto International, 1:** 63–69.

Richardson, A. J. and Wiegand, C. L. (1977) "Distinguishing Vegetation from Soil Background Information," **Photogrammetric Engineering and Remote Sensing, 43:** 1541–1552.

Roberts, D.A. (1991) **Separating Spectral Mixtures of Vegetation and Soils**, unpublished Ph. D. dissertation, Univ. of Washington, 180 p.

Roberts, D. A., Smith, M. O., and Adams, J. B. (1993), Green Vegetation, Nonphotosynthetic Vegetation, and Soils in AVIRIS Data, **Remote Sensing of Environment, 44:** 117–126.

Roberts, D. A., R. O. Green, J. B. Adams, J. S. Cothern, D. E. Sabol and M. O. Smith (1994) 'Temporal and Spatial Relationships Between Topography, Atmospheric Water Vapor, Liquid Water and Vegetation Endmember Fractions Determined Using AVIRIS," **Proceedings IGARSS '94**, IEEE, 2366–2368.

Robinson, A. R. and A. S. Humpherys (1967) "Water Control and Measurement on the Farm," in **Irrigation of Agricultural Lands,** R. M. Hagan, H. R. Haise, and T. W. Edminster, American Society of Agronomy, Madison, 828–864.

Rodenberg, E. (1991) **Eyeless in Gaia: The state of global environmental monitoring,** World Resources Institute, 101 p.

Schuler, D. L. and J. S. Lee (1992) "Improved Microwave Measurements of Ocean Wave Spectra," **Proceedings of the Topical Symposium on Combined Optical-Microwave Earth and Atmosphere Sensing,** IEEE, 47–50.

Sharp, R. P. (1963) "Wind Ripples," **Journal of Geology, 71:** 617–626.

Sharp, R. P. (1976) **Southern California**, Kendall/Hunt, Dubuque, 208 p.

Sheridan, D. (1981) **Desertification of the United States**, U.S. Government Printing Office, 142 p.

Singer, R. B. (1981) "Near-Infrared Spectral Reflectance of Mineral Mixtures: Systematic Combinations of Pyroxenes, Olivine, and Iron Oxides," **Journal of Geophysical Research, 86:** 7967–7982.

Smith, M., D. Roberts, J. Hill, W. Mehl, B. Hosgood, J. Verdebout, G. Schmuch, C. Koechler, and J. Adams (1994) "A New Approach to Quantifying Abundance of Materials in Multispectral Images," in **Proc. IEEE Int. Geosci. and Remote Sensing Symp. '94**,IEEE, New York, 2372–2374.

Smith, M. O., S. L. Ustin, J. B. Adams and A. R. Gillespie (1990) "Vegetation in Deserts: I. A Regional Measure of Abundance from Multispectral Images," **Remote Sensing of Environment, 31:** 1–26.

Solbrig, O. T. (1977) "The Adaptive Strategies of *Larrea*," in **Creosote Bush: Biology and Chemistry of *Larrea* in New World Deserts**, Mabry, T. J., J. H. Hunziker and D. R. Difeo, Jr. (eds.), Dowden, Hutchinson & Ross, Stroudsburg, 284 p.

Spalding, E. S. (1905) "Mechanical Adjustment of the Sahuaro (*Cereus giganteus*) to Varying Quantities of Stored Water," **Bulletin of the Toronto Botanical Club, 32:** 57–68.

Spalding, V. M. (1909) **Distribution and Movements of Desert Plants,** Carnegie Institution, Washington, DC, 144 p.

Stallings, J. H. (1957) **Soil Conservation,** Prentice-Hall, 575 p.

Stegner, W. (1954) **Beyond the Hundredth Meridian,** Houghton Mifflin, Boston, 430 p.

Timmermann, B. N. (1977) "Practical Uses of *Larrea*," in **Creosote Bush: Biology and Chemistry of *Larrea* in New World Deserts**, Mabry, T. J., J. H. Hunziker and D. R. Difeo, Jr. (eds.), Dowden, Hutchinson & Ross, Stroudsburg, 284 p.

Tugel, A. J. and G. A. Woodruff (1986) **Soil Survey of San Bernardino County, California: Mojave River Area**, U. S. Government Printing Office, 211 p.

Ulaby, F. T., R. K. Moore, and A. K. Fung (1982) **Microwave Remote Sensing, Active and Passive,** Artech House, Norwood, 2162 p.

Ulaby, F. T. and J. J. van Zyl (1987) "Wave Properties and Polarization," in **Radar Polarimetry for Geoscience Applications**, F. T. Ulaby and C. Elachi (eds.), Artech House, Norwood, 1–16.

UNEP, [United Nations Environment Programme] (1978) **United Nations Conference on Desertification: Roundup, Plan of Action and Resolutions**, United Nations, New York, 1978.

UNEP [United Nations Environment Programme] (1991) **Financing Ani-Desertification Programmes**, UNEP, Nairobi, 82p.

UNEP [United Nations Environment Programme] (1992) **Status of Desertification and Implementation of the United Nations Plan of Action to Combat Desertification**, UNEP, Nairobi, 88p.

USDA [United States Department of Agriculture] (1993) **Soil Survey Manual**, USDA Handbook No. 18, U. S. Government Printing Office, 437 p.

Van de Hulst, H. C. (1981) **Light Scattering by Small Particles**, Dover, New York, 470 p.

van Zyl, J. J. (1985) **On the Importance of Polarization in Radar Scattering Problems,** Ph.D. Thesis, Caltech Antenna Laboratory Report No. 120, California Institute of Technology, Pasadena, CA, 152 pp.

van Zyl, J. J. (1990) "Calibration of Polarimetric Radar Images Using Only Image Parameters and Trihedral Corner Reflector Responses," **IEEE Trans. on Geosci. and Rem. Sens., 28:** 337–348.

van Zyl, J. J., P. C. Dubois, T. G. Farr, and H. A. Zebker (1988) "Inference of Geologic Surface Parameters from Polarimetric Radar Observations and Model Inversion," **Proc. IEEE Int. Geosci. and Remote Sensing Symp. '88,** IEEE, New York, 51–52.

van Zyl, J. J. and F. T. Ulaby (1987) "Scattering Matrix Representation for Simple Targets," **Radar Polarimetry for Geoscience Applications**, F. T. Ulaby and C. Elachi (eds.), Artech House, Norwood, 17–52.

van Zyl, J. J., H. A. Zebker and C. Elachi (1987a) "Polarimetric SAR Applications," **Radar Polarimetry for Geoscience Applications**, F. T. Ulaby and C. Elachi (eds.), Artech House, Norwood, 315–360.

van Zyl, J. J., H. A. Zebker and C. Elachi (1987b) "Imaging Radar Polarization Signatures: Theory and Observation," **Radio Science, 22:** 529–543.

Vasek, F. C. (1979/80) "Early Successional Stages in Mojave Desert Scrub Vegetation," **Israel Journal of Botany, 28:** 133–148.

Vasek, F. C., H. B. Johnson and G. D. Brum (1975a) "Effects of Power Transmission Lines on Vegetation of the Mojave Desert," **Madroño, 23:** 114–130.

Vasek, F. C., H. B. Johnson and D. H. Eslinger (1975b) "Effects of Pipeline Construction on Creosote Bush Scrub Vegetation of the Mojave Desert," **Madroño, 23:** 1–64.

Warren, A. and C. Agnew (1988) "An Assessment of Desertification and Land Degradation in Arid and Semi-Arid Areas," **International Institute for Environmental Development, Drylands Programme,** University College, London, 72 p.

Webb, W. P. (1957) "The American West: Perpetual Mirage," **Harper's Magazine, 24(1284):** 26.

Weir, J. E. (1962) "Large Ripple Marks Caused by Wind Near Coyote Lake (Dry), California," **Geological Society of America, Special Paper 73:** 72.

Wells, P. V. (1961) "Succession in Desert Vegetation on Streets of a Nevada Ghost Town," **Science, 134:** 670–671.

Willstätter, R. and A. Stoll (1918) **Untersuchunger über die Assimilation der Kohlensäure**, Springel-Verlag, Berlin, 448 p.

Woodruff, N. P. and Siddoway, F. H. (1965) "A Wind Erosion Equation." **Proc. Soil Soc. Am., 29:** 602–608.

Woodburne, M. O., S. T. Miller, R. H. Telford (1985) "Stratigraphy and Geochronology of Miocene Strata in the Central Mojave Desert, California," in **Geologic Investigations Along Interstate 15, Cajon Pass to Manix Lake, California**, R. E. Reynolds (ed.), San Bernardino County Museum, 79–104.

World Meteorological Organization (1983) **Meteorological aspects of certain processes affecting soil degradation – especially erosion,** Technical Note No. 178, WMO No. 591:149.

World Resources Institute (1992) **World Resources 1992-1993**, Oxford University Press, Oxford. 385p.

World Resources Institute (1993) **World Resources 1993-1994**, Oxford University Press, Oxford. 385p.

Yuhas, R. H. and A. F. H. Goetz (1994) "Monitoring and Modeling Semi-Arid Landscape Response to Climate Change," **Proceedings IGARSS '94**, IEEE, 1036–1038.

Zebker, H. A. and L. Norikane (1987) "Radar Polarimeter Measures Orientation of Calibration Corner Reflectors," **Proceedings of the IEEE, 75:** 1686–1688.

Zebker, H. A., J. J. van Zyl and C. Elachi (1987a) "Polarimetric Radar System Design," **Radar Polarimetry for Geoscience Applications**, F. T. Ulaby and C. Elachi (eds.), Artech House, Norwood, 273–314.

Zebker, H. A., J. J. van Zyl and D. N. Held (1987b) "Imaging Radar Polarimetry From Wave Synthesis," **J. Geophys. Res. 92:** 683–701.